Surfaces of the icosahedral Ag-In-Yb quasicrystal: structure, reactivity and thin film growth

Thesis submitted in accordance with the requirements of
the University of Liverpool for the degree of Doctor in Philosophy

by Peter John Nugent

06/2011

Viva completed on the 02/11/2011

Internal examiner - Prof. P. Weightman, University of Liverpool

External examiner - Prof. D.P Woodruff, University of Warwick

Acknowledgements

The preparation of this Thesis has been a long, hard, but ultimately fun and satisfying journey, which would not have been possible without the support of some excellent people at the Surface Science Research Center. These people include Dr. Joseph Smerdon, whose patience and dedication helped me stay motivated throughout this project, including the long nights in the lab beating him at shareware Quake. I would also like to thank Dr. Sam Haq whose expertise with UHV systems enabled me to become autonomous when conducting experiments.

The support of great friends, both new and old, has made my time at the SSRC an enjoyable one. A special thanks to Dr. Chris Mansley, who has been around since day one of undergrad. I would also like to thank Jackie and Tony who have been on the scene for days innumerable, Helen and Gareth whom I became good friends with during my masters, and my co-workers Kirsty, Joe, Lisa and Ian.

It has been an immense honour to work with my supervisor Dr. Hem Raj Sharma, who allowed me to undertake this project. This is limited not only to the work we have undertaken, but also included the opportunity to travel to many places where I have met many incredible people. This includes several trips to Japan, where I was graciously hosted by Dr Masahiko Shimoda. My thanks also to Prof. Ronan McGrath, who offered me my initial quasicrystal project, and whose insight and guidance has been of great help.

My final thanks lies with that of my family, who have constantly supported me throughout my life. My brothers Scott and Matthew, my sister Sally, and my step dad Rich have encouraged me and supplied perspective during this project. Also to Tim, whose love over the past eight years has made the world a brighter place. And last, but by no means least, to my Mum, without whom I would have never considered myself capable of going to University, let alone complete a project as prestigious as this.

Mum, this is for you.

Peter Nugent, 2011

"Eyn chaya kazo!"

Prof. Daniel Shechtman, upon observing the 10 fold diffraction pattern from Al-Mn.

Roughly translates as "There can be no such creature!"

Contents

Abstract

Quasicrystals are intermetallic alloys which exhibit long range order but lack periodicity. While, until recently, all stable quasicrystal species discovered are ternary alloys, consisting of 3 elemental species, recent studies have developed the binary system i-Cd-Yb, which in turn has led to the inception of a new family of ternary quasicrystals, of which one is i-Ag-In-Yb. This thesis documents studies performed on the high symmetry surfaces of the i-Ag-In-Yb quasicrystal using a variety of techniques such as STM, LEED, XPS, UPS, MEIS and thin film deposition.

The five, three and twofold high symmetry surfaces of i-Ag-In-Yb have been characterised in terms of their atomic structure and composition. All three surfaces produce surfaces that are atomically flat and composed of a stepped and terraced structure. All three surfaces are found to be formed along atomic planes that intersect the centers of the rhombic triacontahedral (RTH) clusters, the building blocks of this material. By comparing the results from STM, LEED, XPS and MEIS, the structure and composition of the these surfaces are determined to be bulk truncated. Each surface also possesses comparable stabilities.

The deposition of Sb on the fivefold surface creates a quasiperiodic overlayer expressing long range order. The thin film grows firstly as a monolayer with Sb atoms forming fivefold features on top of the truncated RTH clusters. It then forms a partial second layer before growing in a disordered manner. The first layer Sb atoms settle in adsorption sites similar to those recorded for the Pb monolayer on the same surface. The second layer of Sb adsorps in sites forming pentagonal features that are τ scaled in size in respect to the monolayer features. Depositing C_{60} on both the clean surface and the clean surface modified by a predeposition of Sb yields a thin film expressing no ordering.

Behaviours that are expressed when exposed to oxygen for all three high symmetry surfaces are identical, with each constituent species also behaving in a similar manner to each element in

its pure form. Upon oxidising the fivefold surface in vacuum, atmospheric conditions, and water, it was found that water is the most effective oxidising agent due to a greater concentration of oxygen.

List of abbreviations

i	Icosahedral
d	Decagonal
RTH	Rhombic Triacontahedral
UHV	Ultra High Vacuum
STM	Scanning Tunneling Microscopy
LEED	Low Energy Electron Diffraction
MEIS	Medium Energy Ion Scattering
XPS	X-ray Photoelectron Spectroscopy
UPS	Ultraviolet Photoelectron Spectroscopy
FFT	Fast Fourier Transform
L	Langmuir

Chapter 1

Introduction

With the discovery of quasicrystals in 1982 and their subsequent publication in 1984 [1], forbidden symmetries in crystal structures became an intense area of research. This new type of material expressed long range order but no periodicity, which led to a reclassification of the definition of a crystal from a material that has translational invariance, to a material that produces a discrete diffraction pattern [2]. Since the documentation of the icosahedral phase of the meta stable Al-Mn system, many materials of differing structures have been created. Materials expressing five, eight, ten and twelvefold symmetries have been discovered. These include, but are not limited to, *i*-Al-Pd-Mn, *d*-Al-Ni-Co, *i*-Al-Cu-Fe, *i*-Cd-Yb and *i*-Ag-In-Yb.

Quasicrystals pose an interesting mathematical and structural challenge. The consideration of aperiodic order in a two dimensional plane was broached by Sir Roger Penrose [3] in which he constructed an aperiodic tiling consisting of 4 unique tiles. Further work produced simpler sets of tiles with specific selection rules. The formulation of their structures also requires the consideration of more spacial dimensions than the typical three that express periodic systems. Also, quasicrystals have interesting physical properties, such as low surface friction, non sticking behaviour, hardness, and unexpected thermal and electrical conductivities [4–9]. Such properties offer a wide variety of potential applications, such as the coatings of moving parts in mechanical engines.

Many studies have been conducted on quasicrystals, with several having the aim of determining their surface and bulk structures. The surfaces of these materials are important for a variety of reasons. For instance, the differences to periodic crystals can help explain why and

how the surface properties of quasicrystals originate. Determining not just the structure, but also the chemical compositions and distributions are pivotal in understanding the behaviour of such surfaces. For more complicated studies such as epitaxial growth, without knowledge of the substrates surface the characterisation of any formed structures would be impractical.

The three most studied quasicrystals, *i*-Al-Pd-Mn, *d*-Al-Ni-Co and *i*-Al-Cu-Fe, have been investigated with a wide variety of techniques. Techniques such as STM and LEED [10–29] have discovered that specific preparation conditions produce surfaces that exhibit bulk structures and hence are not reconstructed. Further studies, including work such as the epitaxial growth of different elements, have found that these materials interact with the adsorpates in such a way that form quasicrystalline single element overlayers [5, 30–43]. Such overlayers can grow as islands where multiple orientations of the adsorpates lattice occur with common directions related to the high symmetry axes of the substrate. This is known as rotational epitaxy, and has been observed in several systems [32, 33, 44, 45]. Interest in these novel structures lies with how the quasiperiodic ordering imparted by the substrate onto these films has affected their physical, electrical and chemical properties. A recent study has analysed the surface of the clean Al-Pd-Mn quasicrystal in regards to the amounts of features that relate to truncated Bergman and Mackay clusters, known as dark stars and white flowers, and are two potential candidates for adsorption sites of metals and semi metals, and how they differ in terms of structure and chemical decorations [46].

A great deal of work has been done to gain a better understanding of these materials, but several inherent difficulties continue to arise. One of these issues is that a quasicrystal is chemically complex; all stable quasicrystals contain three elemental species which makes the calculation of their structures using techniques such as X-ray diffraction problematic, as similarities between certain element's Bragg peaks do not contrast well with each other. Although each atomic position can be determined, the specific atomic species cannot always be estimated to a degree of sufficient accuracy.

In 2000 Tsai *et al.* discovered a stable binary quasicrystal [47]. This new species was created by reducing the amount of Mg in the Cd-Mg-Yb quasicrystal. The result was an icosahedral phase from which a perfect structural solution could be calculated [48]. The structure of this new material differs from that of Al based quasicrystals. A quasicrystal can be considered to be a three dimensional intersection of a six dimensional periodic lattice [49]. This forms an

atomic model that can be considered as an aperiodic packing of atomic clusters. For example, the i-Al-Pd-Mn quasicrystal can be considered to be created from Bergman and pseudo Mackay clusters [50, 51]. Structure calculations have determined that the i-Cd-Yb material is created by the packing of a different structure of cluster. This cluster is constructed by placing atomic shells within a larger rhombic triacontahedron, creating the rhombic triacontahedral, or RTH cluster. There are also differences in the higher order concepts where their aperiodicity can be envisioned using periodic lattices. However, unlike i-Al-Pd-Mn, i-Cd-Yb is unsuitable for study in ultra high vacuum due to the high vapour pressure of its Cd component. To rectify this the Cd was replaced by equal amounts of Ag and In to produce an isostructural stable ternary alloy which was suitable for study under vacuum [52].

This new structure makes this family of quasicrystal significantly different from existing well studied families of quasicrystals, and presents an excellent opportunity to test how and why its different structure and composition affects its properties. The difference in structure creates many opportunities for further studies into thin film growth and the search for novel surface structures, such as discovering single element quasicrystals which can be grown upon i-Ag-In-Yb.

Chapter Breakdown

Chapter 2 introduces the basics of quasicrystals and how mathematics can be employed to describe their aperiodic structures. The i-Cd-Yb and i-Ag-In-Yb systems are also introduced, as well as a review of the work into their creation and the calculation of their atomic structure.

Chapter 3 summarises previous studies on the i-Al-Pd-Mn surface, a prominent icosahedral quasicrystal which has been studied extensively. The clean surface's characterisation is described, as well as several epitaxy experiments conducted upon it.

Chapter 4 details the experimental methods that have been utilised for the work in this thesis. Ultra High Vacuum is introduced with an explanation as to why it is employed for surface studies, as well as crystal growth used to grow the studied samples and crystal cleaning routines. Experimental techniques are described for Scanning Tunneling Microscopy (STM), Low Energy Electron Diffraction (LEED), X-ray Photoelectron Spectroscopy (XPS), Ultraviolet Photoelectron Spectroscopy (UPS), Medium Energy Ion Scattering (MEIS) and thin film growth.

Chapter 5 presents the first in depth study into the fivefold surface of *i*-Ag-In-Yb. The studies employed in its characterisation include STM, LEED, MEIS and XPS. Through the collective results of these four techniques while referring to the model structure of *i*-Cd-Yb, the surface structure has been understood and its surface planes characterised.

Chapter 6 introduces the other two high symmetry surfaces that exist for the *i*-Ag-In-Yb material. STM, LEED and XPS have been conducted on these two surfaces and the results compared to the model structure as for the five fold case.

Chapter 7 explores the epitaxial growth of thin films on the quasicrystal surface of *i*-Ag-In-Yb, concentrating primarily on Sb. Through the study of STM, the structure of the growing film is explained, with a complimentary XPS study assisting in the determination of the films growth mode. A smaller study involving the growth of a C_{60} film on the fivefold *i*-Ag-In-Yb surface is also included.

Chapter 8 looks at the behaviour of the three high symmetry surfaces when exposed to oxygen. XPS is employed to monitor surface composition and core level behaviour as the three surfaces as slowly oxidised in UHV. Pure metal forms are also oxidised for comparisons. The stability of the oxide layer on the fivefold layer was then tested, as well as the oxide layer thickness being calculated. Further to oxidation in UHV, conditions such as atmosphere and pure water were also employed to see if the presence of greater amounts of oxygen modified *i*-Ag-In-Yb's oxidation behaviour.

Finally, chapter 9 provides a summary of this thesis, and suggests possible studies for the improvement of data presented and future areas of research.

Chapter 2

An introduction to Quasicrystals

2.1 Introduction

Our universe has been dominated by matter ever since a primordial asymmetry at the beginning of the universe. Matter has changed and evolved to create everything we can see and touch, from the planets and stars suspended in the cosmos, to the food we eat. Matter exists in several forms, the more common of which are Solids, Liquids and Gases. These three types of matter have particular behaviours and physical laws associated with them. Solids can exhibit several different structures, which are known as amorphous, crystalline and quasicrystalline.

Introduced in this chapter is a form of solid known as quasicrystals. Also, the mathematics behind aperiodicity is explored. The binary quasicrystal i-Cd-Yb and the discovery of i-Ag-In-Yb is also presented, with a brief summary of the work carried out on the structure of this material.

2.2 The discovery and history of quasicrystals

Until the end of the last century, crystallography defined a crystal structure as exhibiting 2-, 3-, 4- and 6-fold symmetries, with such materials possessing periodic long range order. Any other symmetries in a crystal were thought forbidden, and as such could not exist. This can be demonstrated using tiles of certain shapes and tiling them to infinity. On an infinite surface, a tiling of rectangles, triangles, squares or hexagons will cover it completely with no gaps or overlaps. If this is attempted with pentagons, heptagons, octagons or decagons, the pattern

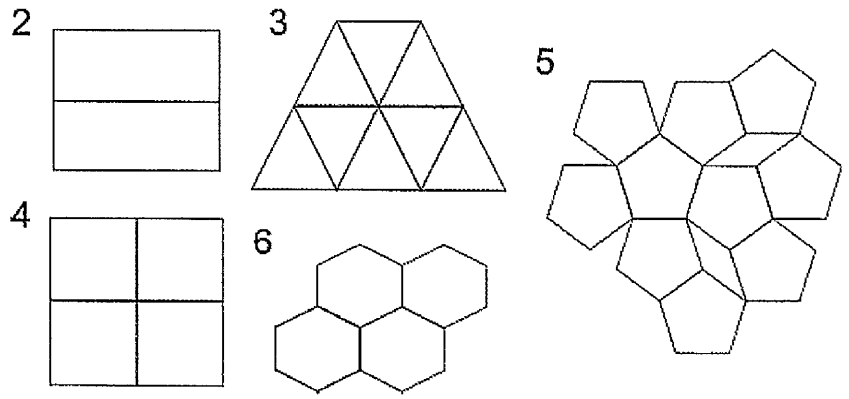

Figure 2.1: Arrangements of 2-, 3-, 4-, 5- and 6-fold tilings comparing the issues with tiling a pentagonal pattern.

will be incomplete and feature faults. These examples can be seen in figure 2.1. Because of the occurrence of such gaps and overlaps, it was thought that these configurations would not create stable structures, and hence would not exist in nature.

In 1982 Dan Shechtman, a visiting scientist at the National Bureau of Standards in America, discovered a material that would place the original definition of Crystal structure into doubt. While studying varying amounts of Mn in an AlMn alloy, Shechtman discovered icosahedral patterns while probing these crystals using Transmission Electron Spectroscopy (TEM). This material contained 25% Mn and was created by rapid cooling. It was polycrystalline, being made up of grains of up to 2μm in size. This material was found to exhibit an icosahedral structure, containing six fivefold, ten threefold and fifteen twofold axes. This materials was a metastable phase.

This discovery faced many challenges after its publication in 1984 [1], being dismissed by many scientists, including the well known chemist Linus Pauling, who stated the findings were caused by multiply twinned cubic crystals [53]. The controversy surrounding these materials eventually diminished as more and more thermodynamically stable quasicrystalline species were discovered, and their existence became irrefutable. Since then a wide variety of stable quasicrystals have been discovered, taking one of two possible forms; axial quasicrystals exhibiting ten fold symmetry in 2 dimensions while the 3rd dimension features a periodic stacking of aperiodic planes, or fivefold materials which are aperiodic in every direction.

With the discovery of an icosahedral polycrystalline material, it was only a matter of time

before materials that were more appropriate for surface sensitive studies became available. In 1986, the first single grain quasicrystal was grown [54]. With careful study into the phase diagrams of suspected quasicrystalline materials, it has become possible to grow single grain crystals of many differing species.

As well as five and tenfold species [55–57], eight [58–60] and twelvefold [61,62] quasicrystalline materials have been discovered. Quasicrystals exhibiting eight or twelvefold order are also axial, but they are metastable.

Around 80% of discovered thermodynamically stable quasicrystals are composed of Al along with 2 or more other elements. Some well studied families include, in the icosahedral phase, Al-Pd-RE (RE = Rare Earth), Al-Cu-Fe and RE-Mn-Zn, and in the decagonal phase, Al-Ni-Co and Al-Co-Cu [63]. These crystals are good candidates for study due to the ability to grow these materials as single grains of satisfactory size, and their stability in vacuum conditions, with the exception of RE-Mn-Zn. The alloy containing no Al exhibits a high vapour pressure which makes its preparation in such an environment problematic.

There has been a great deal of research conducted into the surface structures of quasicrystals. While bulk studies are important in characterising the structure of solids, in efforts to understand their physical properties, surface studies are important as surfaces have strong influences on the physical and chemical properties, and behaviour of materials. Some of the studies are listed in table 2.1

Table 2.1: List of various quasicrystal studies, performed using various surface sensitive techniques.

Quasicrystal	Technique	Reference
i-Al-Pd-Mn	STM	[10–14]
	LEED	[22–24]
i-Al-Cu-Fe	STM	[15–18]
	LEED	[25, 26]
i-Ag-In-Yb	STM/RHEED	[64]
d-Al-Ni-Co	STM	[19–21, 27]
	LEED	[27, 28]

More recent discoveries include the binary quasicrystal i-Cd-Yb [47]. This material is unique amongst quasicrystals due to it being thermodynamically stable, and composed of only two elements. This material then led to the discovery of a new family of ternary quasicrystals, which includes i-Ag-In-Yb.

This new family of quasicrystals is significantly different from existing well studied families of quasicrystals, and presents an excellent opportunity to test how and why its different structure and composition effects its properties. Such properties include low surface friction, extreme hardness and electrical and thermal conductivities [9]. The difference in atomic structure, and hence the surface structure, creates many opportunities for further studies into thin film growth and the search for novel surface structures, such as discovering single element quasicrystals which can be grown upon i-Ag-In-Yb.

While all studied quasicrystals are materials that can be synthesised in the laboratory under controlled conditions, there is a recent documented occurrence of a quasicrystal having formed naturally [65]. The material is an alloy of aluminium, copper and iron, and occurs as micrometer sized grains associated with khatyrkite (with a nominal composition of $(Cu,Zn)Al_2$) and cupalite (with a nominal composition of (Cu,Zn)Al). This mineral was reportedly taken from the the Koryak Mountains, northeast of the Kamchatka Peninsula in Russia. The complex assembly of mineral phases suggest that the grains were formed naturally under geological conditions, and not as a result of human activity.

2.3 Simple forms of long range order

2.3.1 Periodicity

Solid matter was classically thought to exist in one of two structures. It is possible to differentiate these two forms by looking at how the atomic arrangements of these materials differ over small and long distances. The first type of solid is commonly referred to as amorphous. These materials have no ordering in their arrangement of atoms; they are akin to a liquid that has been flash frozen in time. Types of amorphous solids include materials such as ceramics. The second form are known as crystals, previously thought to be formed by a periodic arrangement of atoms. It is possible to model a periodic crystal by first creating an array of lattice points $\mathbf{r}$ that can be

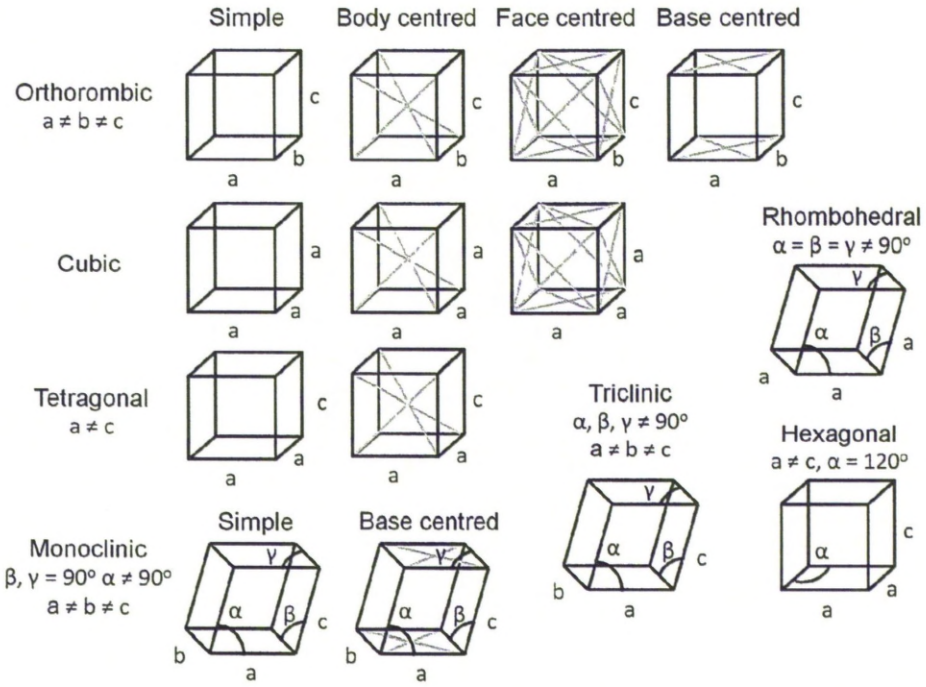

Figure 2.2: All 14 possible 3 dimensional spacial arrangements that can take the form of a unit cell in crystallography.

explained by;

$$\mathbf{r} = n_1\mathbf{a} + n_2\mathbf{b} + n_3\mathbf{c} \tag{2.1}$$

where n_1, n_2 and n_3 are integers, and $\mathbf{a}$, $\mathbf{b}$ and $\mathbf{c}$ are fundamental units of translational symmetry. This describes the materials primitive cell. There are only 14 unique ways in which to arrange these lattice points and create a periodic structure in 3D space. These primitive cells are known as the Bravais Lattices and are shown in figure 2.2. Simple solids can be constructed from these frameworks by placing a basis, or a collection of atoms, at every single lattice point. Collectively the primitive cell and the basis form the Unit Cell, and this can be used to describe the structure of a solid.

Defining a crystal in such a way would dictate that only certain rotational symmetries can exist. Those that are based on intervals of 60° and 90° and as such materials exhibiting only 2-, 3-, 4- and 6- fold symmetries can be described as a crystal. Such configurations will provide discrete diffraction patterns associated with Bragg Scattering. This means some other kind of order must be responsible for the fivefold diffraction patterns observed in 1982. If periodic

Table 2.2: Fibonacci sequence as created by S and L segments

S	(1)
L	(1)
LS	(2)
LSL	(3)
LSLLS	(5)
LSLLSLSL	(8)
LSLLSLSLLSLLS	(13)
LSLLSLSLLSLLSLSLLSLSL	(21)
:	

ordering cannot be responsible for the diffraction patterns, then it must be due to aperiodic ordering.

2.3.2 The Fibonacci sequence

The Fibonacci sequence is a one dimensional arrangement of numbers that has segments that are familiar through out its sequence, but over an infinite length, none of these segments ever repeat. The first form of this consists of a sequence of numbers, where every new number is the sum of the previous two numbers such that;

$$x_n = x_{n-2} + x_{n-1} \tag{2.2}$$

This produces the sequence of numbers 1, 1, 2, 3, 5, 8, 13, 21... etc. It is possible to construct the same sequence by using two segments, named S and L, and using the simple rules S $\rightarrow$ L ; L $\rightarrow$ LS when constructing the next term of the sequence. The sum of the letters occurring mirrors the number progression generated by equation 2.2. This creates the sequence seen in table 2.2.

For this sequence, if successive terms are taken and divided by the preceding term and the mean of this ratio is taken as the successive term approaches infinity, $\lim_{n\to\infty} x_n/x_{n-1}$, an irrational ratio is obtained. This ratio is known as the golden mean or golden ratio. This value is also the ratio of L to S segments in the second form of the Fibonacci sequence presented. The ratio can

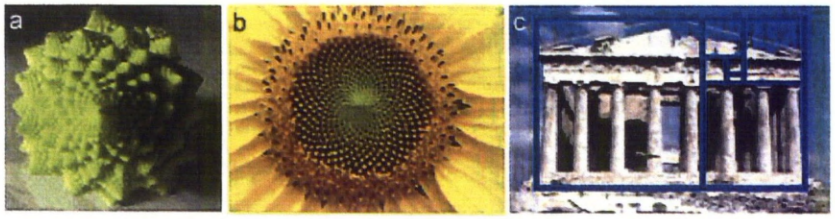

Figure 2.3: The Golden Ratio in nature, (a) A cauliflower/broccoli hybrid. (b) The inside of a sunflower. (c) The Parthenon in Greece.

be calculated by:

$$\frac{\sqrt{5}+1}{2} = \tau = 1.618034... \tag{2.3}$$

The golden mean τ and the Fibonacci sequence also appear in nature. The Fibonacci sequence features in the patterns of seeds observed in pinecones, sunflowers and other plants. Figure 2.3 (a) and (b) show examples of Fibonacci ordering in plants, where the numerus of clockwise and anti-clockwise spirals are consecutive terms in the Fibonacci sequence. Our art has also been influenced by this ratio and sequence, with ratios of arches seen on the Parthenon in Greece being equal to τ (figure 2.3 (c)).

2.3.3 Penrose tilings

While the Fibonacci sequence can describe long range aperiodicity over a single dimension, a manifestation of such ordering in two dimensions was presented by Sir Roger Penrose. First consider an infinitely large table. It is possible to cover this table with identically sized rectangles, triangles, squares or hexagons, and create a pattern that features no overlaps or gaps. This is not possible with other shapes, such as pentagons, heptagons, or octagons etc. However, Roger Penrose deduced a way of tiling two or more shapes using specific matching rules, to create patterns that exhibited 5, 7, 8 and other higher orders of symmetry [3]. The five and tenfold patterns formed in this way show the aperiodicity of the Fibonacci sequence in two dimensions, and this becomes important when discussing the atomic arrangements of the surfaces of quasicrystals. Patterns such as these were conceived a decade before Shechtman *et al.* published their findings.

The first pattern to be constructed is known as the P1 tiling shown in 2.4 (a). This pattern involves 4 differently shaped tiles; boat, star, pentagon and rhomb. These are used to construct

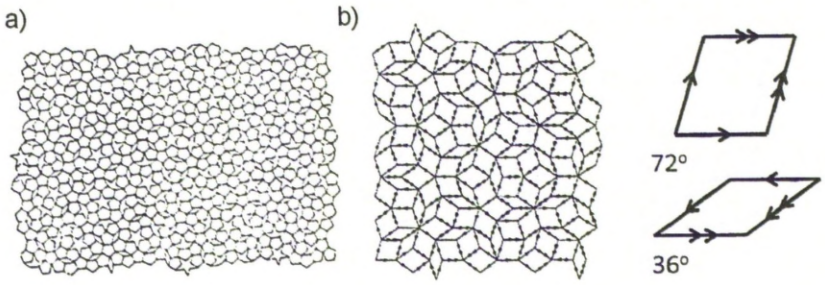

Figure 2.4: The two more famous Penrose tiling patterns. (a) Demonstrates a P1 tiling, consisting of 4 tile shapes; a rhomb, a star, a boat and a pentagon. (b) shows a P3 tiling, with appropriate matching rules.

an aperiodic arrangement that stretches to infinity, although to keep the aperiodicity of the pattern while avoiding any spaces or overlaps, matching rules are be applied. One of Penrose's tilings, the P3 tiling, is constructed using just two shapes; the fat and skinny rhombs, as shown in figure 2.4 (b). These rhombs, with internal angles of 108°and 72°, and 114°and 36°, can again be tiled to infinity to form either a periodic structure, or a five fold aperiodic structure when the correct matching rules are used. Each polygon has a number of arrows pointing in a specific direction along its sides. To get a perfectly aperiodic pattern, polygon sides may only be joined if they have the same number of arrows and if the arrows point in the same direction. A P2 tiling features two different shapes of tiles, namely kites and darts, and is not described.

The relationship of the Fibonacci sequence and τ are intrinsic to the aperiodic versions of these patterns. By drawing lines down the common edges of tiles in the P3 tiling, a Fibonacci sequence can be created. The ratio of areas of the two rhombs is equal to τ, as is the ratio of the occurrence of both tiles within the pattern.

Penrose tilings are important in the world of quasicrystals due to their mathematical origins and their relationship to theoretical atomic models that are generated using hyperspace. It is possible to superimpose a Penrose tiling onto quasicrystal atomic models [29, 66], as well as experimental data [27]. In such cases it may be possible to superimpose Penrose tilings onto atomic positions. Examples of such superimposing are shown in figure 2.5. Such a technique is invaluable when characterising quasicrystal surfaces and the thin films grown upon them.

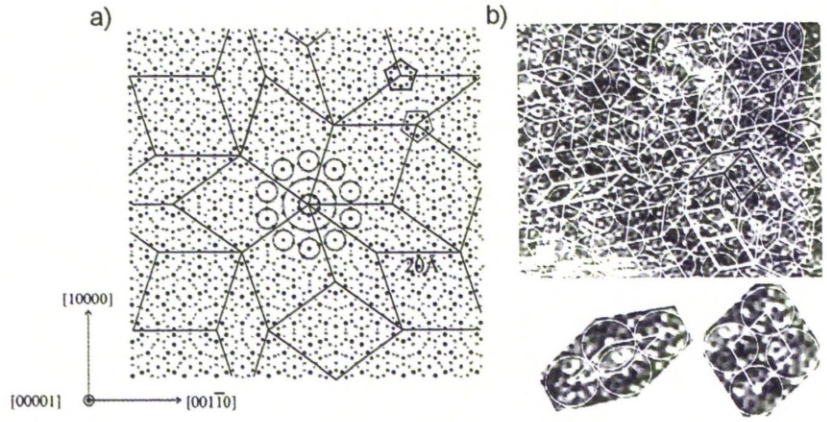

Figure 2.5: (a) A P3 tiling super imposed onto the atomic structure of d-Al-Ni-Co projected along the tenfold axis, with dark and grey dots denoting transition metals and Al respectively, and larger dots denoting atoms at $z = 0$ and smaller dots at $z \sim 2\mathring{A}$. Structure reprinted from [66], superimposition reprinted from [29]. (b) A P3 tiling superimposed on a high resolution STM image from d-Al-Ni-Co. It is possible to see mismatches in the tiling caused by surface defects, indicated by tiles with a thicker edge. Reprinted from [27].

2.4 Generating aperiodicity from higher dimensions

While it is relatively simple to produce a periodic sequence in three dimensions by identifying a segment, or group of segments, and repeating them to infinity, generating a sequence which never features any repeating segment is a more complex task. To construct an aperiodic system in one, two or three dimensions, it is necessary to utilise the concept of higher dimensionality [67].

In an effort to construct an aperiodic structure in three dimensions, which is required to describe quasicrystallinity, a basic one dimensional system must first be considered.

2.4.1 Section Method

To generate a one dimensional aperiodic sequence, it is necessary to consider a two dimensional arrangement of lattice points. A periodic lattice can be defined by $\mathbf{r} = n_1\mathbf{a} + n_2\mathbf{b}$, where $n_1 = n_2 = d$. An infinitely long line, R_{par}, is projected from the origin at a specific angle θ. Every lattice point will then have a line projected from it, $\mathbf{R}_{perp}$, which is oriented perpendicular to $\mathbf{R}_{par}$. The length this line, Δ, is defined as

$$\Delta = d(\cos\theta + \sin\theta) \tag{2.4}$$

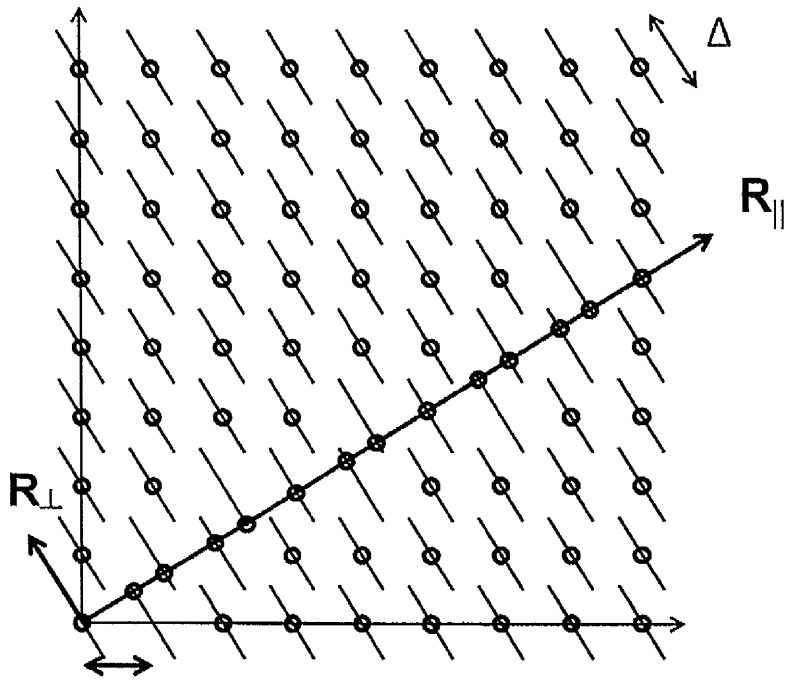

Figure 2.6: A schematical representation of the section method.

and centered on the lattice point. Any lattice point whose R_{perp} component intersects with R_{par} is then projected onto R_{par}. The angle at which the R_{par} is oriented will dictate what kind of sequence is projected upon it. If the angle is irrational, it will never intersect a coordinate of integer values other than at the origin. If the angle of R_{par} is related to the golden mean $\cot\theta = \tau$, then a sequence of points corresponding to the Fibonacci sequence will be generated. For such a sequence, the longer separations (L) will have length $d\cos\tau$ and the shorter separations (S) will have length $d\sin\tau$.

Using such a method, the original two dimensional lattice is considered to be a hyper dimensional construct, from which real space can be obtained. For the case of the Section method, R_{par} is considered real, or parallel or external space, while R_{perp} is considered perpendicular or internal space.

This method can then be expanded to create aperiodicity in three dimensions. Firstly, a lattice in six dimensions must be considered. Lattice vectors are specified by:

$$\mathbf{d}_1 = \frac{1}{2ca^*}\begin{pmatrix} 0 \\ 0 \\ c \\ 0 \\ 0 \\ 1 \end{pmatrix}, \quad \mathbf{d}_i = \frac{1}{2ca^*}\begin{pmatrix} c\sin\theta\cos\frac{2\pi i}{5} \\ c\sin\theta\sin\frac{2\pi i}{5} \\ c \\ -\sin\theta\cos\frac{4\pi i}{5} \\ -\sin\theta\sin\frac{4\pi i}{5} \\ c\cos\theta \end{pmatrix}, \quad i = 2, ..., 6 \tag{2.5}$$

Where $c = 1$ for a hypercubic lattice and $\tan\theta = 2$. From this lattice, three dimensional real space $\mathbf{H}^{\parallel}$ can be obtained with the first 3 terms of the matrix $\mathbf{d}_i$ forming realspace coordinates. The remaining three terms form the virtual space $\mathbf{H}^{\perp}$. The lattice points can then be decorated with occupational domains (OD's), which are three dimensional constructs and oriented with respect to $\mathbf{H}^{\perp}$. Lattice points from the OD's that fall upon the real space plane will be equivalent to the atomic positions of the crystal structure that is being derived.

A simple cubic 6D reciprocal lattice gives rise to a primitive type structure, or *P-type*. By giving each lattice coordinate a basis of 3 points, a face centered structure can be constructed, or *F-type*. Aluminium based quasicrystals are based upon an F-type 6D reciprocal lattice, with Al-Pd-Mn having the space group $Fm\overline{3}5$ [6,68], while the binary *i*-Cd-Yb quasicrystal is based on the P-type lattice [47] and has the space group $Pm\overline{3}5$.

The notation used for indexing the space groups is known as the Hermann-Manguin notation and is used to represent the symmetry elements in point groups, plane groups and space groups [69], and is adequate to describe the symmetries of the higher dimensional groups used to create quasicrystals [70]. A cube, which has three point groups and a mirror axis, is denoted as *m3*. However the quasicrystal is formed in higher dimensions, for which 5 point groups can exist, denoted by a 5. These two sets of point groups may also be inverted to generate themselves, which is denoted by overlining. The initial symbol denotes the type of cubic lattice used. *P* denotes a primitive cube, while *F* denotes a face centered cube.

2.4.2 Indexing methods for aperiodic diffraction

For indexing purposes, generalised Miller indices are used as introduced by Elser [71], and take the form $< h_1, h_2, h_3, h_4, h_5, h_6 >$ for 6D space. These indices are utilised in a similar way to Miller indices for a periodic crystal, in that h_i corresponds to a lattice vector. However an

aperiodic crystal is not limited to symmetry in three dimensions, hence more than three terms are required.

To understand the indexing method, first consider the reciprocal of the 6D lattice used to create the bulk quasicrystal. Lattice points in reciprocal space are given by:

$$\mathbf{d}_1^* = a^* \begin{pmatrix} 0 \\ 0 \\ 1 \\ 0 \\ 0 \\ c \end{pmatrix}, \quad \mathbf{d}_i^* \begin{pmatrix} \sin\theta\cos\frac{2\pi i}{5} \\ \sin\theta\sin\frac{2\pi i}{5} \\ 1 \\ -c\sin\theta\cos\frac{4\pi i}{5} \\ -c\sin\theta\sin\frac{4\pi i}{5} \\ -c\cos\theta \end{pmatrix}, \quad i = 2, ..., 6 \tag{2.6}$$

With $c = 1$ and $\tan\theta = 2$. The vectors $\mathbf{a}_i^*$, $i = 1, ..., 6$ can then be considered real space projections of the basis vectors $\mathbf{d}_i^*$, $i = 1, ..., 6$, where:

$$\mathbf{a}_1^* = (0, 0, 1),\ \mathbf{a}_i^* = \mathbf{a}^*(\sin\theta\cos\frac{2\pi i}{5}, \sin\theta\sin\frac{2\pi i}{5}, \cos\theta),\ a^* = \| \mathbf{a}_i^* \|,\ i = 2, ..., 6 \tag{2.7}$$

These lattice vectors can be envisioned as vectors of an icosahedron, with the vectors being directed towards the corners of an icosahedron as shown in figure 2.7 (a). These vectors can then be projected onto a real space diffraction plane in order to create a diffraction pattern as seen in 2.7 (b). The vector $\mathbf{a}_1^*$ is perpendicular to the projected plane and hence its magnitude is not measurable.

For a periodic crystal, diffraction spots are limited in their distribution in that the distance between the spots must be at least $\frac{2\pi}{a}$, ie. the minimum separation of the atoms in a periodic lattice is a. However an aperiodic diffraction pattern is different. Combining certain vectors as shown in figure 2.7 (c) creates new vectors of magnitude less than a^*. As the combination of vectors can create new vectors that have irrational angles, this leads to a diffraction pattern composed of an infinitely dense set of diffraction spots, and in experiment would create diffraction patterns that could not be discerned. However, the intensity of each diffraction spot in the infinitely dense pattern is not uniform. This enables an aperiodic crystal to generate a diffraction pattern that consists of discrete diffraction spots.

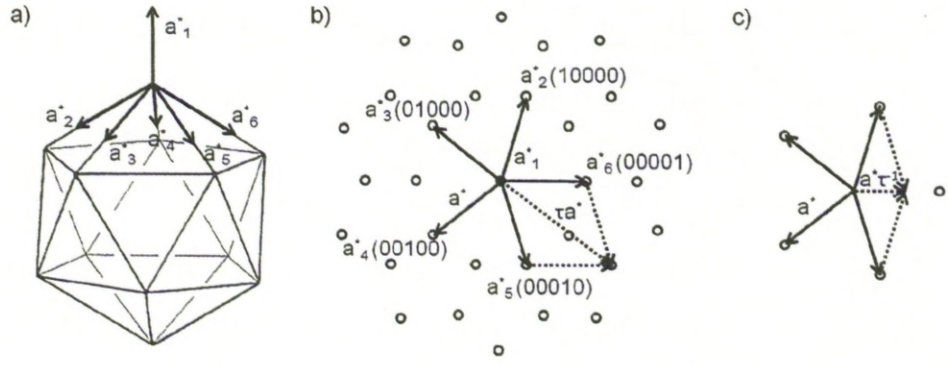

Figure 2.7: (a) The orientation of the reciprocal lattice vectors a_i^*. (b) Physical space projection of the reciprocal lattice vectors, and how the vectors are labeled with generalised Miller indices. (c) Example of how diffraction spots for an aperiodic crystal can occur with separations less than $\frac{2\pi}{a^*}$.

2.5 The discovery of *i*-Cd-Yb and subsequent ternary alloys

For the 16 years after the publication of Dan Shechtman's discovery, the majority of subsequently discovered stable quasicrystals were ternary alloys usually consisting of Al and two other constituents. Several binary quasicrystals were discovered, such as the dodecagonal quasicrystal Ta-Te [72], but their lack of abundance and stability made them difficult to study. In 2000, An Pang Tsai published the discovery of the first thermodynamically stable binary quasicrystal [47].

Tsai *et al.* have been able to prepare quasicrystal alloys made from Cd-Mg-RE (where RE is a rare earth) [73]. This family of quasicrystal was discovered taking an *i*-Zn-Mg-RE and replacing the Zn component with Cd. Quasicrystals can be considered to be a Hume-Rothery electron compound with a definite valence concentration (valence electron to atom ratio or e/a) of roughly 2 [74]. The e/a ratio may be calculated by;

$$e/a = Z_A(1 - c_B) + Z_B c_B \tag{2.8}$$

Where Z is the valency of species A and B and c_B is the concentration of species B.

The e/a ratio is an important determinant crystal structures due to its indication of how full the structures Brillouin zones are. If a Brillouin zone is filled but more electrons are present, it is energetically favourable to change4 the shape of the Brillouin zone to accommodate more (resulting in a structure change) then to promote electrons across the band gap to the next

empty or partially filled Brillouin zone.

This makes it possible to predict what compounds may make quasicrystals when swapping constituents from existing quasicrystals to make new materials. Stable Al-transition metal quasicrystals have an e/a of around 1.75, while i-Zn-Mg-Al quasicrystal has an e/a ratio of 2.1-2.2. By replacing the Zn with Cd in the Zn-Mg-Dy quasicrystal, a new stable compound was discovered with stoichiometry $Cd_{66}Mg_{21}Dy_{13}$ and an e/a of 2.15. The Dy component can be replaced with several rare earth materials. By adjusting the composition to $Cd_{65}Mg_{20}RE_{15}$ to maintain an e/a of 2.15, new icosahedral materials including Cd-Mg-Yb and Cd-Mg-Ca, can be created. Cd-Mg-Yb is of note as it is the most stable material from this family of quasicrystals. This ultimately means that a quasicrystal of this composition can be grown as a large crystal relatively easily.

Other conditions to construct a stable quasicrystal include size of the constituent atoms, and electronegativity [74]. The difference in size of atomic species present in a material may be calculated by;

$$\delta = \frac{r_A - r_B}{r_A} \tag{2.9}$$

Where r is the atomic radius of species A and B. If the size of the constituent species differs by more than 15%, even at low concentrations, a quasicrystalline structure is unstable. The constituents must also have a significant difference in their electronegativity, ensuring bonds with some ionic character are formed. In terms of the most important factors for forming a quasicrystal, e/a is the most stringent rule, with even the smallest change in composition of a quasicrystal giving a large change in e/a. In materials where species can be exchanged freely because they are divalent, atomic size is the next important factor. Electronegativity is a comprehensive rule for forming any ionic compound, and must also be adhered to strictly.

In this system it is found that Cd and Mg form a mutual continuous solid solution over a wide temperature range, implying that the two elements are interchangeable without affecting the solids structure. So by systematically eliminating the Mg component of the alloy, a brand new quasicrystalline phase was discovered at a composition of $Cd_{5.7}Yb$ [47,73]. X-ray diffraction reveals diffraction peaks that can be attributed to icosahedral symmetry using the indexing method proposed by Elser [71], exhibiting a primitive icosahedral lattice. Both Cd and Yb are divalent, with the e/a of the quasicrystal being 2.0, adhering to the valence concentration

condition. Also, the difference in size of the two species is 2%, so the size condition is also adhered to.

The surface study of the Cd-Yb system is however hindered by the high vapour pressure of Cd. The study of this material in an Ultra High Vacuum (UHV) environment is problematic, as upon heat treatment the Cd component of the material evaporates from the surface. To solve this issue *i*-Cd-Yb is modified so that a new species of quasicrystal is created, *i*-Ag-In-Yb.

2.6 The icosahedral Ag-In-Yb quasicrystal

Guo *et al.* replaced the Cd component with equal amounts of Cd's neighbours in the periodic table, namely Ag and In [52]. Substituting Cd in this way creates a compound that still adheres to the Hume-Rothery conditions above. Silver is monovalent while In is trivalent, so in equal parts the new material will have 2 free electrons per atom. In regards to atomic sizes, $d_{Cd} = 0.314$ nm, $d_{Ag} = 0.290$ nm and $d_{In} = 0.332$ nm with $d_{0.5Ag+0.5In} = 0.311$ nm, so that the overall difference in size between the original constituent and its substitutes is 1%. Only the Cd species is replaced and the amount of Yb is unchanged in this new quasicrystal. This gives a material with a composition of $Ag_{42}In_{42}Yb_{16}$. This process can also be used to produce a sister material $Ag_{42}In_{42}Ca_{16}$.

X-ray diffraction of this material reveals diffraction peaks that can be attributed to icosahedral symmetry with an estimated quasilattice parameter of 0.559 nm. Selected-area electron diffraction of this material, shown in figure 2.8, confirms it to have six fivefold, ten three fold and fifteen twofold axes. The composition of this material cannot be modified to the same extent of that of its progenitor, Cd-Mg-Yb. To remain in the quasicrystalline phase, the amount of Yb can only be changed by 1 at.%. If the concentration of Yb is fixed at 16 at.%, the amounts of Ag and In can be modified by a few at.% and still produce a stable quasicrystal, showing that this material is a Hume-Rothery electron compound.

One of the prominent comparisons between *i*-Cd-Yb *i*-Ag-In-Yb and *i*-Ag-In-Ca are that these materials are isostructural; the atomic structure of *i*-Cd-Yb is the same as *i*-Ag-In-Yb. The similarity of their structures can be seen by comparing the X-ray diffraction peaks as shown in figure 2.9, and by comparing their selected-area electron diffraction patterns (which are not shown).

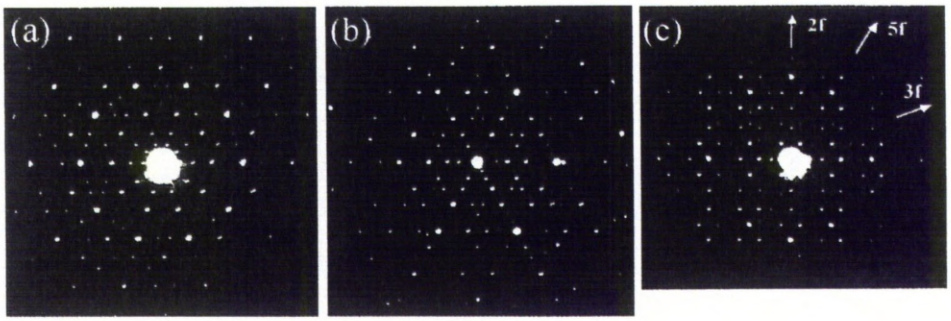

Figure 2.8: Selected-area electron diffraction patterns of *i*-Ag-In-Ca, which has the same structure as Ag-In-Yb and displays the same diffraction pattern. (a) Fivefold symmetry pattern, (b) threefold symmetry pattern, (c) twofold symmetry pattern. Reprinted from ref. [52].

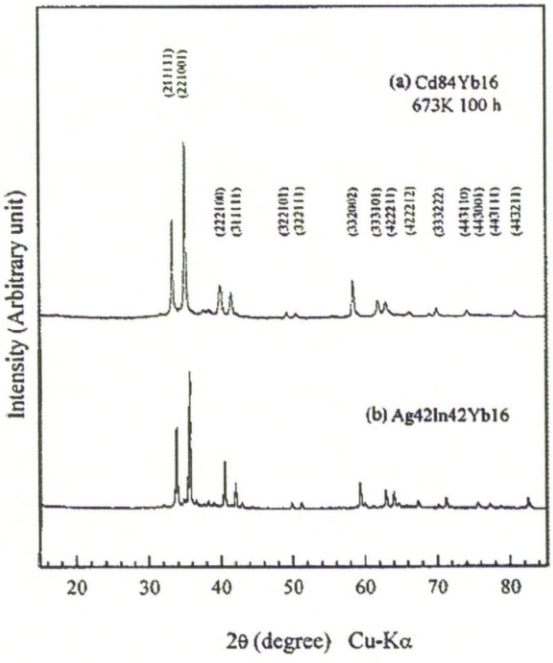

Figure 2.9: X-ray diffraction spectra from *i*-Cd-Yb and *i*-Ag-In-Yb. Spectrum (a) reprinted from ref. [73] and spectrum (b) reprinted from ref. [52].

Bulk structure determination of *i*-Cd-Yb and *i*-Ag-In-Yb

Determination of a crystal structure is an essential part in understanding the crystals physical properties, and predicting how the crystal will behave under certain conditions. Takakura *et al.* [48] have calculated a complete model structure for *i*-Cd-Yb, which also supplies a model structure for *i*-Ag-In-Yb. This is the first time such a complete model has been calculated for any species of quasicrystal.

Unlike periodic crystals and ten fold quasicrystals, icosahedral quasicrystals are aperiodic in all three spatial dimensions. Due to this, it is not possible to use two dimensional imaging techniques such as High Resolution Electron Microscopy (HREM) to determine their structures. For previous icosahedral quasicrystals progress has been made on their structure determination, as is the case for *i*-Al-Pd-Mn [75], but due to the chemical disorder it is difficult to determine the contrast between diffraction spots, and hence detail the exact species of the atoms present. However, as *i*-Cd-Yb is binary, the contrast between the two constituents is enough to tell them apart. *i*-Cd-Yb also has the benefit of having two approximants, 1/1 Cd_6Yb and 2/1 $Cd_{5.8}Yb$, for which detailed structural analysis has also been achieved [76,77]. The approximant materials are useful for the determination of the quasicrystals structure, as they have similar compositions to the quasicrystal but are periodic, having very large unit cells.

The structures of previously discovered quasicrystals, such as Al-Mn and Al-Zn-Mg, have been deduced by considering their respective approximant materials. The structure of Al-Mn was deduced by studying the structure of 1/1 α-Al-Mn-Si, which has a large unit cell that features a three dimensional Penrose tiling similar to that of Al-Mn [71]. The structure of Al-Zn-Mg was also discovered in a similar way [78].

Both approximants of the Cd-Yb system are constructed by a packing Rhombic Triacontrahedral (RTH) clusters which exhibit well-defined chemical order. These approximants exhibit a cubic packing of clusters, the 1/1 having clusters stacked in a body centered structure, and the 2/1 approximant having a more complex packing. The cell parameters of 1/1 and 2/1 approximants are related to each other as $b = 1.566$ nm and $\tau b = 2.533$ nm respectively. The cluster units are linked along the twofold access at a distance of b (b-linkages), and along the threefold axes by a distance of $c = b\sqrt{3/2}$ (c linkages). The structure of the RTH clusters is shown in figure 2.10. The individual atomic shells are placed inside each other in a manner similar to a Russian doll.

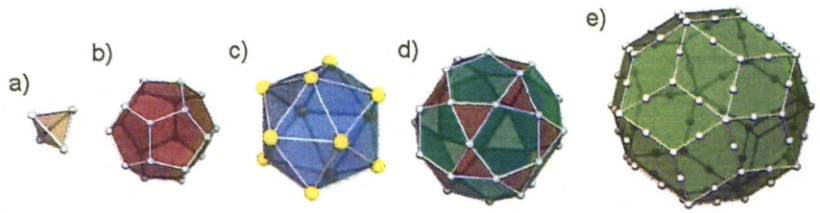

Figure 2.10: Atomic structure of the 5 shells responsible for the atomic clusters present in i-Cd-Yband it's 1/1 and 2/1 approximants, and their radii (r). These shells include (a) tetrahedron of 4 Cd atoms (b) dodecahedron of 20 Cd atoms ($r = 0.46$ nm) (c) icosahedron of 12 Yb atoms ($r = 0.56$ nm) (d) icosidodecahedron of 30 Cd atoms ($r = 0.65$ nm) (e) rhombic triacontrahedron of 92 Cd atoms ($r = 0.78$ nm along its twofold direction). Grey atoms signify Cd, while yellow signifies Yb. Reprinted from ref. [48]

To determine the structure of the quasicrystal, X-ray diffraction spectra were obtained at varying angles [48]. Synchrotron radiation was used due to the resolution obtainable, on a single grain of high structural quality and low mosaic spread. This determined the space group of the quasicrystal to be $Pm\overline{3}5$ with an icosahedral lattice constant of $a = 0.5689$ nm. For the first step of structure determination, a phase reconstruction for Fourier synthesis was achieved by applying a low-density elimination method. The obtained phases and Fourier amplitudes were then used to generate the electron densities within the 6D unit cell of the quasicrystal. The densities clearly concentrate at the three high symmetry planes, and allow the chemical decoration to be identified due to the contrast between Cd and Yb atoms, with the higher electron densities observed being attributed to Yb atoms. From a detailed analysis of this map, atomic clusters of identical structure and chemical decoration to that observed in the approximant crystals are also present in the quasicrystal.

The density maps calculated are not detailed enough to achieve a structural description similar to those achieved for periodic crystals. Hence it is necessary to design a structural model with a reasonable number of parameters that can be tested and refined using experimental data. This process is simplified by using the approximant crystals structures and the 6D electron density map. It is shown that a subset of vertices can be derived from a three dimension Penrose tiling (3DPT), of edge length a, and connected by b linkages and c linkages. The resulting structure generates a model with no unreasonably small interatomic distances (apart

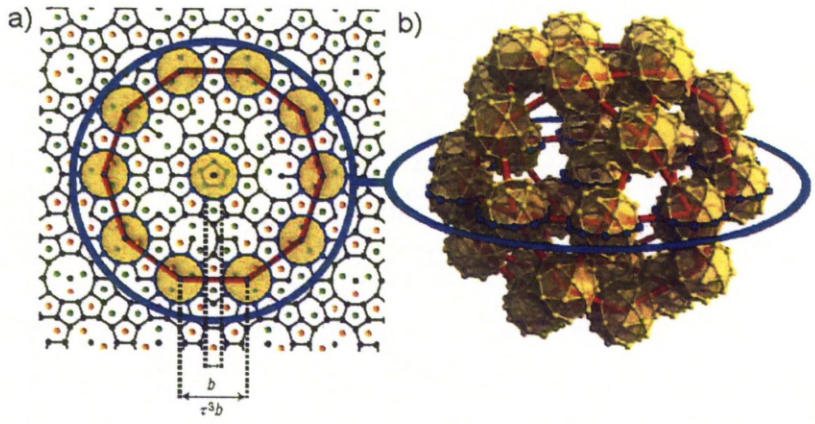

Figure 2.11: Demonstration of a τ^3 inflation of the i-Cd-Ybmodel. Yellow dots represent RTH units which grey dots represent c-linkages. (a) Demonstrates the inflation in 2D space, while (b) shows this in 3D. Reprinted from ref. [48]

from those seen in the disordered Cd_4 tetrahedron) and a composition of $Cd_{83.7}Yb_{16.3}$ which is in agreement with experimental data. Another way of describing the structure is through inflation, in that a set of specific points when scaled up by a specific factor, for the case of this model the factor is τ^3, can be seen to occur again in an identical arrangement, as shown in figure 2.11. Inflation in this sense also occurs within a P1 Penrose tiling and is also know as self similarity.

Atomic surfaces can then be determined by taking slices from the atomic model perpendicular to the five, three or two fold axis, depending on which surface is required. Figure 2.12 demonstrates a plane of atoms taken perpendicular to the five fold axis. This figure also illustrates the possibility of superimposing a P1 tiling upon the atomic structure by using the centres of the RTH clusters as vertices. These atomic planes can then be compared to experimental results and their validity of potential bulk terminations determined.

To modify this model for use for i-Ag-In-Yb, the replacement of Cd with Ag and In must be considered. As the Yb component is unchanged the positions of the Yb atoms will not be modified. However, the species of atom that replaces each Cd atom position is ambiguous, and cannot be known with certainty. However, this model provides an excellent tool for comparison with experimental results.

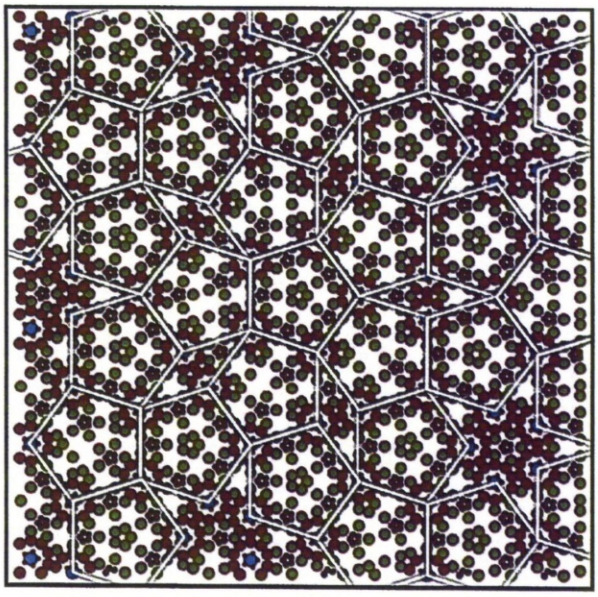

Figure 2.12: A Penrose tiling superimposed upon a plane of atoms perpendicular to the five fold axis of the i-Cd-Yb atomic model. The red dots indicate the positions of Cd, green dots the positions of Yb, and the blue dots the position of the cluster center. The smaller darker red dots indicate Cd atoms on a lower atomic plane.

2.7 Comparisons of the bulk physical and electrical properties of i-Ag-In-Yb to Al based quasicrystals

Until the discovery of i-Cd-Yb, the majority of icosahedral quasicrystal structures were composed of a combination of atomic clusters; the Mackay cluster for the Al-Mn class of quasicrystals, and the Bergman cluster for the Al-Zn-Mg class of quasicrystal. The former cluster consists of an icosahedron of 12 atoms within a larger icosahedron, while the latter of these clusters is made from an icosahedron surrounded by a rhombic triacontrahedral. The i-Cd-Yb and i-Ag-In-Yb quasicrystals are constructed by an aperiodic packing of rhombic triacontrahedral clusters. Because of this it is possible to underpin the chemical ordering of the i-Cd-Yb, and to a degree, the chemical ordering for i-Ag-In-Yb. For Al based quasicrystals it is not possible to overcome the chemical disorder. Reasons for this include lack of contrast on X-ray diffraction spectra, and the inability for certain experimental techniques to identify the species of any observed atoms, and an inherent chemical disorder present in quasicrystals.

Electronically, icosahedral quasicrystals are interesting due to a drop in the density of states

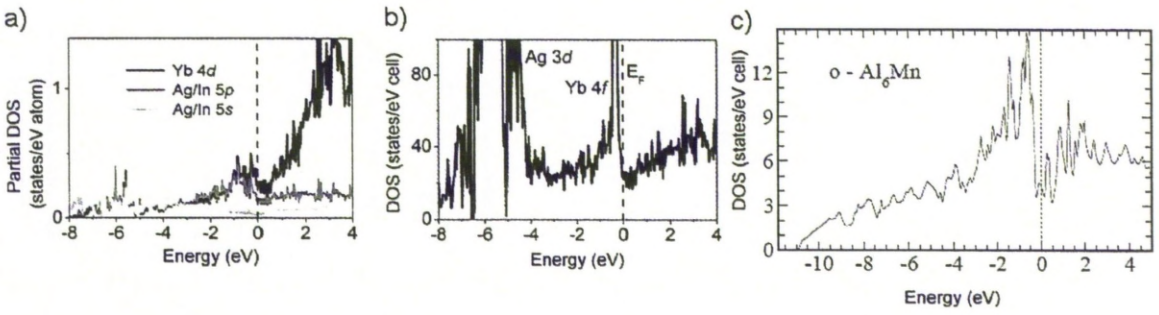

Figure 2.13: Density of state calculations for i-Ag-In-Yb and i-Al_6Mn. (a) shows the individual DOS of all 3 metals in i-Ag-In-Yb while (b) shows the total DOS (both spectra reprinted from ref. [83]). (c) Total DOS of Al_6Mn (Reprinted from ref. [80])

(DOS) at the Fermi level, as seen from first principle calculations. This pseudogap separates the bonding and anti-bonding states. For example in i-Al-Cu-Fe the drop in the DOS about the Fermi level is $\sim 1/3$, while in i-Al-Cu-Ru the drop in the DOS is $\sim 1/10$ [79]. First principle calculations indicate that a hybridisation of the s, p and d orbitals of the materials leads to the pseudogap, as well as a contribution from the Hume-Rothery mechanism responsible for the valence electron concentration condition e/a [80, 81].

Unlike Al based quasicrystals, i-Cd-Yb does not exhibit sp-d hybridisation, but instead exhibits p-d hybridisation, as seen in the DOS calculations around the Fermi level (figure 2.13). It is determined that for i-Cd-Yb, the pseudogap is caused primarily by the hybridisation of the Yb $5d$ band with the Cd $5p$ band [82].

The i-Cd-Yb quasicrystal exhibits physical and electronic properties expected from a quasicrystalline material. However, due to the inclusion of a rare earth in the Cd-RE family of quasicrystals, other physical and electronic properties are observed, such as large electronic specific heat coefficients and high magnetoresistance [6–8].

Chapter 3

Surface studies of quasicrystals

3.1 Introduction

While bulk studies of materials are important for characterising the structure of such solids, surface studies play an important role in discovering their physical and chemical properties. Since quasicrystals exhibit properties not observed for periodic crystals, it is of interest to explore how the aperiodic structures of these materials has modified them to have these characteristics.

Several species of quasicrystalline materials have been discovered and have been utilised in further surface studies such as epitaxy. It is important to consider these previous studies while examining new materials so that their behaviour can be compared, and how the differences in these materials influence such reactions.

Introduced below is a brief summary of work completed on the clean surface of the icosahedral quasicrystal Al-Pd-Mn. This quasicrystal is considered due to it being an already established field of study, and also due to several key similarities and differences between *i*-Al-Pd-Mn and *i*-Ag-In-Yb. Both quasicrystals are tri-metallic and exhibit an icosahedral symmetry. However there are several differences including properties, atomic structure and behaviour of epitaxially grown elements that makes the *i*-Al-Pd-Mn system a good comparative tool when studying the *i*-Ag-In-Yb quasicrystal.

The first elements that were found to create aperiodic overlayers on a quasicrystal were Sb and Pb, having been deposited on the *i*-Al-Pd-Mn and *d*-Al-Ni-Co quasicrystals [30]. This discovery has led to the growth of many more single element quasicrystalline thin films. One system

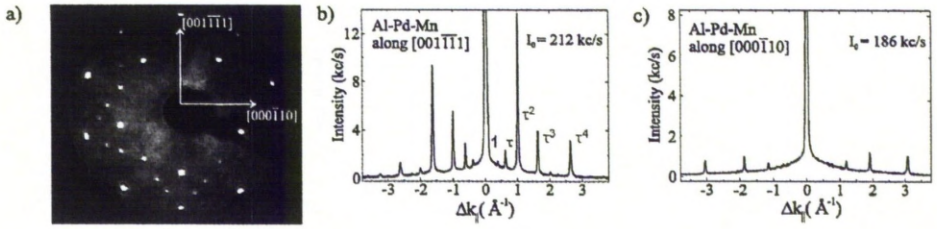

Figure 3.1: (a) LEED pattern taken from the fivefold surface of *i*-Al-Pd-Mn. (b) and (c) HAS spectra taken along two high symmetry directions. Reprinted from [84]

that has been extensively studied is that of Bi on *i*-Al-Pd-Mn, which forms a quasicrystalline monolayer followed by the growth of islands. This epitaxial investigation is briefly detailed to show how quasicrystals can be used as a template for other quasicrystalline structures. Finally, the first surface study into *i*-Ag-In-Yb is reviewed, and a brief comparison of both systems is included.

3.2 Determination of the surface structure of the *i*-Al-Pd-Mn quasicrystal

Icosahedral Al-Pd-Mn is one of the most studied quasicrystals to date. Its ease of preparation and suitability for surface studies makes it an excellent choice for exploring the effects of aperiodicity of a surface, and a prime candidate for epitaxial studies.

As well as various techniques, the fivefold surface has also been explored in terms of preparation conditions. It is found that the anneal temperature plays an important role in determining the type of surface plane that is observed. This surface has been studied at anneal temperatures of 700 K up to anneal temperatures of 1050 K. Anneal temperatures below 900 K produce a surface that is covered in protrusions [13]. An anneal temperature of 900 K or more for a sufficient period of time will produce an atomically flat, step terrace structure, while greater anneal temperatures modify the surface further. A surface prepared using an anneal temperature of 900 K $\sim$ 950 K is presented first, while studies using higher anneal temperatures are explained later.

The long range ordering of *i*-Al-Pd-Mn is examined by using a combination of Low Energy Electron Diffration (LEED) [22] and Helium Atom Scattering (HAS) [84], the latter of which

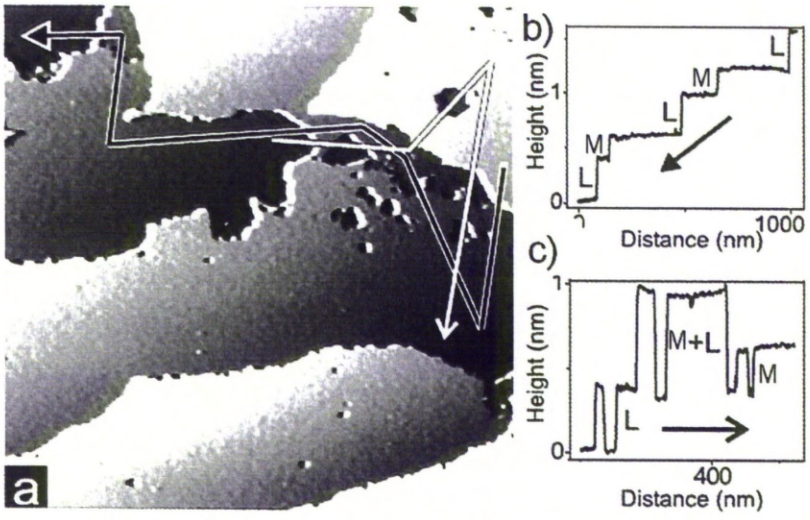

Figure 3.2: (a) An STM image of the clean fivefold surface of i-Al-Pd-Mn (600 nm $\times$ 600 nm), with two line profiles with (b) from the black line and (c) from the white line. Reprinted from [85].

is extremely surface sensitive providing information from the topmost layer of atoms. LEED shows a diffraction pattern of sharp spots conforming to a fivefold diffraction pattern (figure 3.1 (a)), while HAS displays a τ scaling of maxima (figure 3.1 (b)), indicating the presence of aperiodic ordering.

Probing the local surface structure using STM displays a surface that is atomically flat and arranged in a step terrace structure [13], which is shown in figure 3.2 (a). The step heights encountered depends on the anneal temperature used. An anneal temperature of 900 K will produce a surface exhibiting steps of three heights, $S = 2.4 \pm 0.2$ Å, $M = 4.1 \pm 0.2$ Å and $L = 6.5 \pm 0.2$ Å. The medium step height is not encountered often, indicating that terraces featuring an M step are less preferred. Also, the step heights are related by τ such that $M/S \approx L/M \approx \tau$.

The sequence of step heights also forms a Fibonacci sequence shown in figure 3.2 (b). This feature shows with greater clarity the importance of this sequence and the golden mean in the understanding of aperiodic order. There are also occurrences of pits on terraces. These pits have depths that are the same as step heights, or combinations of step heights, as shown in figure 3.2 (c).

The structure on these terraces can be resolved using STM, with the structure of 2 adjacent terraces shown in figure 3.3 (a) and (b) [86]. The terraces are atomically flat and are dominated

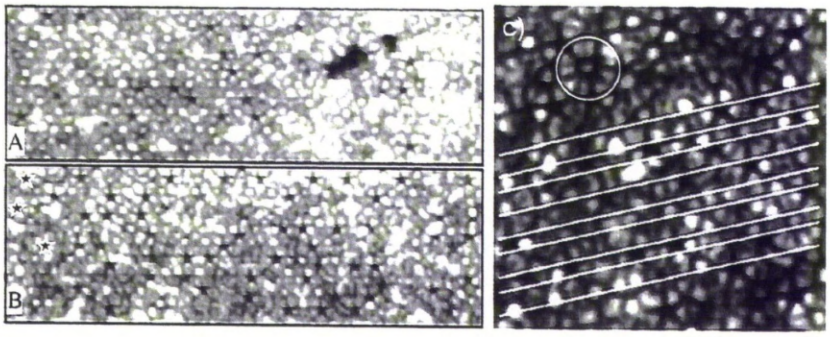

Figure 3.3: (a) and (b) 30 nm × 10 nm atomic resolution images of the fivefold surface of *i*-AlPdMn, showing the different density distribution of holes on consecutive terraces. (c) A 10 nm × 10 nm STM image with white lines super imposed running through specific points of the dark stars demonstrating the Fibonacci sequence exhibited by the surface. Reprinted from [86].

by a surface depression in the shape of a 'dark star' (three of these have been highlighted in figure 3.3 (b)), and a formation of protrusions known as a white flower (one of which is highlighted in figure 3.3 (c)). The dark stars all have the same orientation while the white flowers are oriented parallel to the dark stars or at 36° to them. The spacings between the points of the dark stars are related by τ and by drawing lines through these points it is possible to form a Fibonacci sequence, which is demonstrated in figure 3.3 (c).

However the two adjoining terraces have different densities of these features, with the terrace displayed in (b) having roughly 3 times more of the amount of dark stars than the terrace displayed in (a). It has been suggested that there are only two differing bulk terminations that constitute surface planes for *i*-Al-Pd-Mn; a plane which features many dark star features, and a plane that has few dark star features [12].

These results may then be related to the model structure of *i*-Al-Pd-Mn, which has undergone several refinements [50,75,87]. Firstly the step heights, or terrace separations, are considered [16]. The three major contributing factors to the selection of a surface plane have been recognised as the surface free energy of the elements present [23], the atomic density [88], and the gap size between subsequent atomic planes above and below the surface [89]. While for periodic systems a higher atomic density is believed to be the prevailing factor in surface plane selection, for quasicrystals there is evidence that a combination of all three conditions play a role in what atomic planes become surfaces.

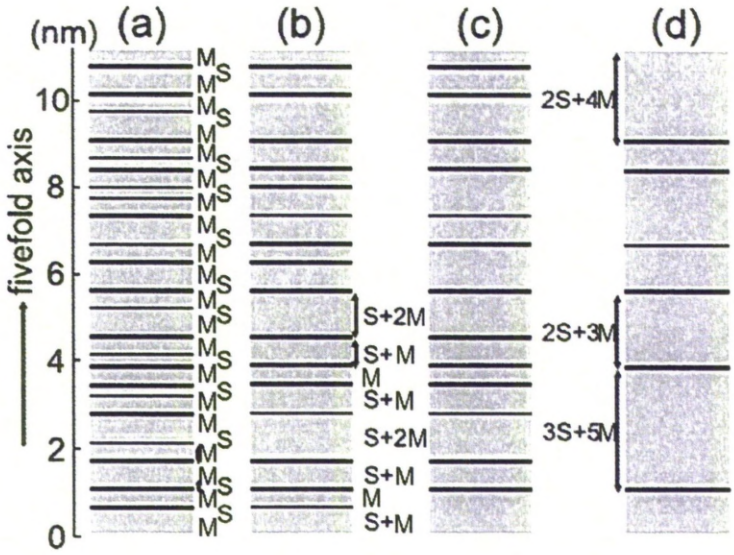

Figure 3.4: Schematic view of the refined structure of i-Al-Pd-Mn projected normal to the fivefold axis. Grey and black rectangles depict blocks of layers and gaps, respectively. Schematics showing (a) small and medium gaps, (b) only larger gaps, (c) larger gaps above regions of a moderate or high density, and (d) larger gaps above regions of a high density. Reprinted from [16].

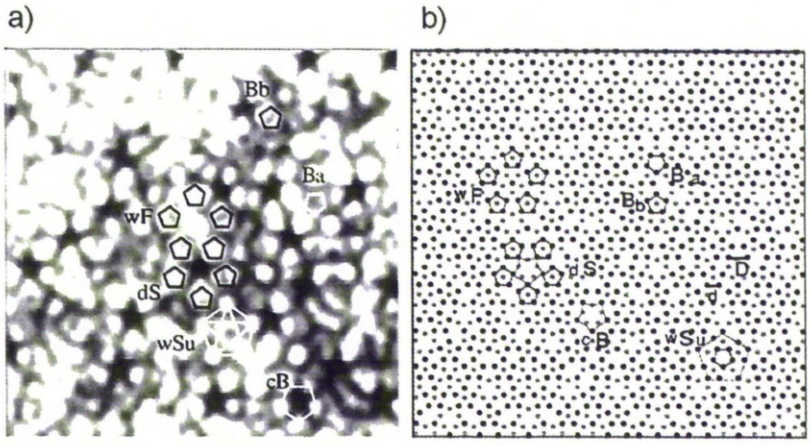

Figure 3.5: (a) A 10 nm × 10 nm STM image of one of the two possible surface planes on the fivefold *i*-Al-Pd-Mn quasicrystal, and (b) a termination from the model structure. Several features have been highlighted including dark stars (dS), white flowers (wF), upwards pointing white stars (wSu) as well as Bergman cluster below the terrace (Bb), above the terrace (Ba) and dissected by the terrace (cB). Reprinted from [12].

Gierer *et al.* has selected specific atomic planes from the model that match the experimental results [22]. However, the layers selected feature another atomic plane in very close proximity to the initially selected plane. These layers are close enough that they have been considered to be a single buckled layer. This produces atomic planes that have atomic densities similar to that of an fcc Al(111) crystal, and are also contain a high concentration of Al. This produced possible surface terminations which were separated by distances similar to the step heights observed by STM. Next, Sharma *et al.* have considered the gaps between atomic planes [16] using a refined structure model of *i*-Al-Pd-Mn [75, 87]. The projection normal to the fivefold axis is displaying as a distribution of atoms along the fivefold axis is shown in figure 3.4. By considering certain termination rules potential surfaces are selected from atomic planes that occur after large gaps within the refined model structure (figure 3.4 (b)) on planes that have a high Al content. However it is coincidental that the bulk terminations occur on atomic planes that exhibit a high atomic density, are composed mostly by Al, and occur after or before large gaps.

The features and motifs expressed by the terraces can themselves be related directly to the model structure also. Papadopolos *et al.* have compared the two different terraces observed by STM, an example of which is shown in figure 3.5 (a) to specific planes within the model structure,

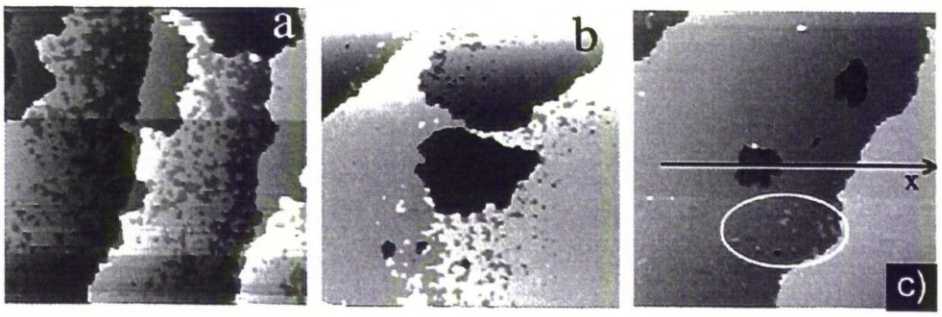

Figure 3.6: STM images of the fivefold surface of i-Al-Pd-Mn, illustrating the change in terrace morphology in respect to anneal temperature. (a) 500 nm × 500 nm, after annealing at 900 K. (b) 500 nm × 500 nm, after annealing at 915 K. (c) 500 nm × 500 nm, after annealing at 925 K. Reprinted from [14].

with the atomic plane corresponding to (a) shown in figure 3.5 (b) [50]. Specific features have been identified, such as the dark star depressions which are formed from truncated Bergman clusters, with these features then being identified on the theoretical atomic planes (figure 3.5 (b) and (d)). Due to the similarities between the experimental results and model structure, the surfaces expressed by this material are considered to be bulk terminated.

Annealing at temperatures higher than 900 K induces a change in the observed structure of the surface. As the anneal temperature is increased, terraces start to exhibit more voids [14]. However these voids are only observed on specific terraces, while other terraces appear to be free of such features. Terraces that exhibit voids are bordered by S steps. By increasing the anneal temperature, the terraces that sport voids begin to evaporate off the surface, until at temperatures above 925 K where these terraces have seemingly been removed. This evolution is shown in figure 3.6. At such preparation conditions, the terraces continue to exhibit previously identified features such as dark stars. However, the evaporating terraces also exhibit ten fold rings. These rings are not found on void free terraces.

Annealing the surface to 1050 K produces step heights that no longer feature the S step [90]. However, steps of heights greater than the M and L steps are observed. 'Step bunching' gives steps a height that can be considered combinations of the original three step heights [85]. An example of this is shown in figure 3.7 (a) with a line profile shown in (b). A linear combination of these three original heights can produce the height of a 'bunched step'. For example step heights consisting of $S+2L$, $2S+3L$ and $3S+5L$ are observed, although the occurrences of these

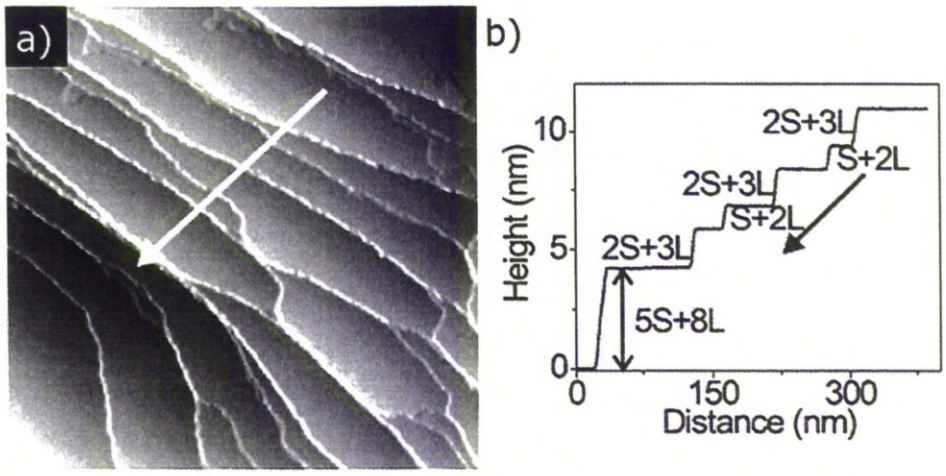

Figure 3.7: (a) An Al-Pd-Mn surface after an anneal at high temperature. (b) A line profile taken from (a), down several successive steps. Reprinted from [85].

heights varies, with some bunched heights being less frequent than others. This phenomena is not restricted just to the surface of *i*-Al-Pd-Mn, as it is also observed in other systems such as *i*-Al-Cu-Fe [17], *i*-Al-Cu-Ru [49] and *i*-Ag-In-Yb [91].

3.3 Epitaxially grown single element overlayers on the fivefold *i*-Al-Pd-Mn quasicrystal

With the clean fivefold surface of *i*-Al-Pd-Mn understood, further studies featuring the aim to grow a single element quasicrystal using *i*-Al-Pd-Mn have been accomplished. The first instance of Bi and Sb forming a quasicrystalline ordering on the fivefold *i*-Al-Pd-Mn surface was documented by Franke *et al.* [30]. The materials were deposited on the surface at 300°C, with the Sb layer being subsequently annealed to 550°C. LEED patterns taken from the clean surface and the subsequent depositions are shown in figure 3.8. The LEED patterns from Bi (figure 3.8 (b)) and Sb (figure 3.8 (c)) show more diffraction spots. This does not indicate the existence of a super structure, but instead is caused by the higher electron cross scattering of the heavier elements which allows for the detection of more diffraction maxima.

Helium atom scattering has also been employed to test the structure of the grown over layers, and spectra along two different high symmetry directions are shown in figure 3.9 (a) and (b).

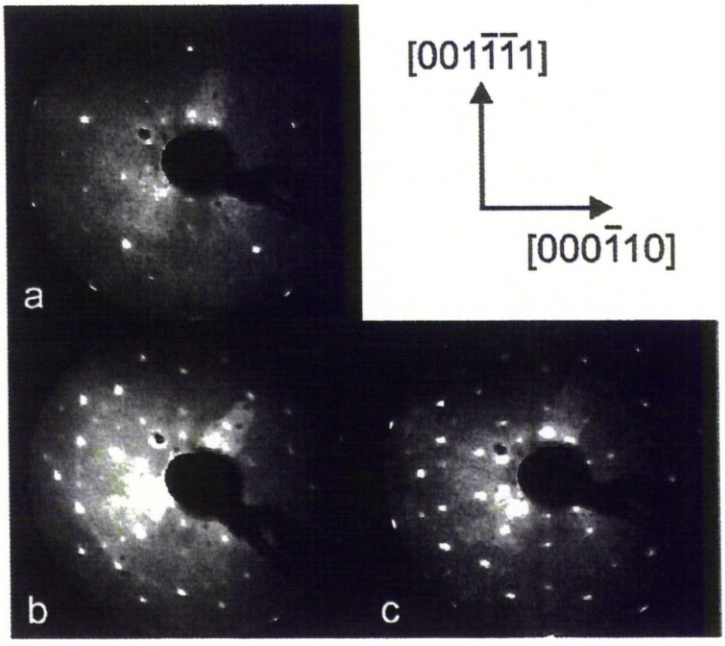

Figure 3.8: LEED patterns taken from (a) the clean surface of *i*-Al-Pd-Mn, (b) After a deposition of Bi and (c) after a deposition of Sb. Reprinted from [30].

The diffraction spectra of the clean surface demonstrates τ scaling as expected. The overlayers also show this scaling, as well as more intense peaks. The peak intensity indicates that the films that have been grown have a very low defect density.

Smerdon *et al.* have investigated the formation of the Bi overlayer by studying its growth from a fraction of a monolayer up to a coverage close to a complete monolayer [92]. Sub monolayer growth is shown in figure 3.10. Growth begins with the nucleation of several pentagonal Bi clusters shown in figure 3.10 (a). FFT patterns of STM images show τ scaling, indicating the presence of quasicrystalline ordering. Further growth leads to a roughening of the overlayer leading to a loss of resolution. At this level of deposition, preferential absorbtion sites are limited to either the nucleation of clusters in sites that are still vacant, or to fill any remaining vacancies in an already forming cluster. At a coverage of 0.54 ML (figure 3.10 (c)) the islands begin to coalesce, and the overall resolution of the film reduces further. At near monolayer levels (figure 3.10 (d)) it is still possible to resolve the structures of the Bi pentagons, but their orientation cannot be discerned. It is still possible to obtain fivefold FFT patterns from the surface at these levels of coverage, which indicates that even though the overlayer is difficult to resolve, it still

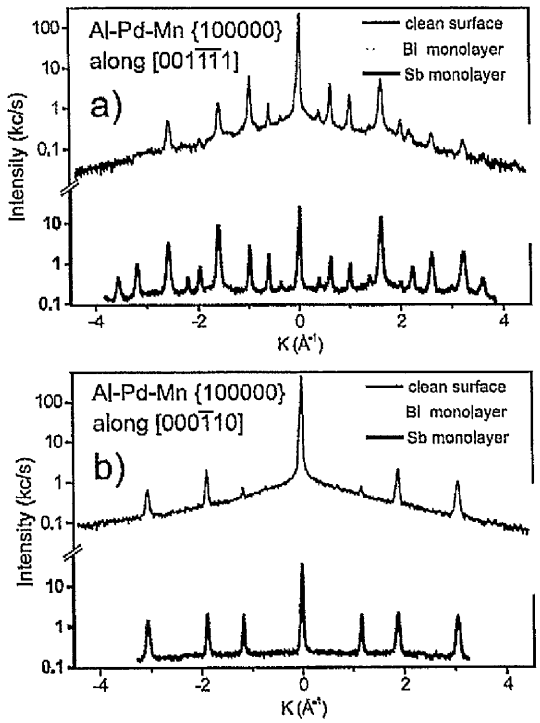

Figure 3.9: HAS spectra of the clean surface, Bi overlayer and Sb overlayer, taken along two high symmetry directions. Reprinted from [30].

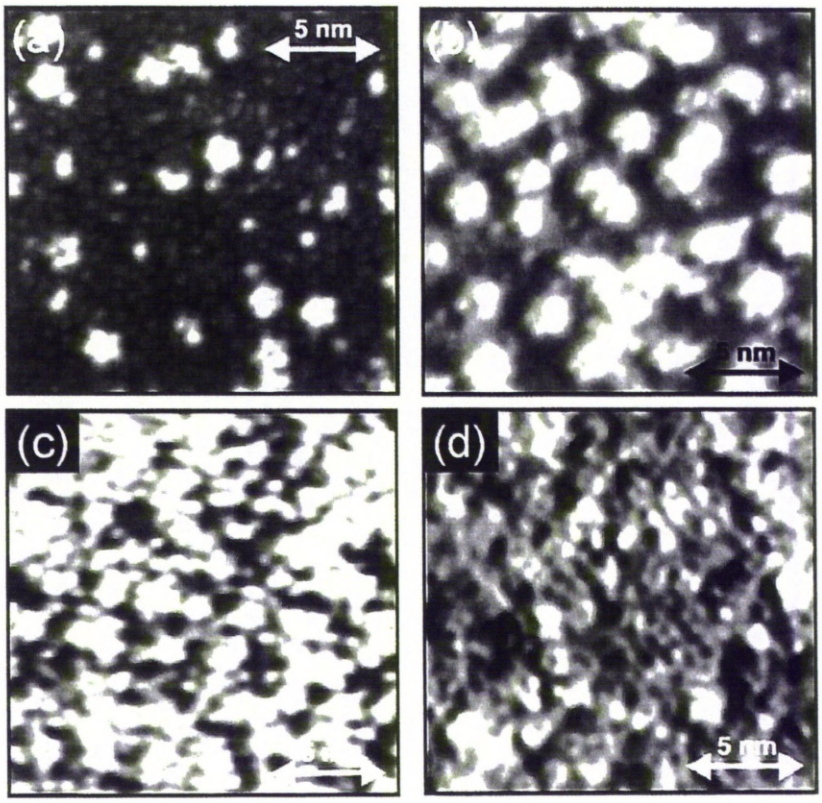

Figure 3.10: Several STM images taken at varying coverages of Bi on the clean *i*-Al-Pd-Mn quasicrystal. (a); 0.13 ML,(b) 0.38 ML, (c) 0.54 ML and (d) 0.9 ML. Reprinted from [92].

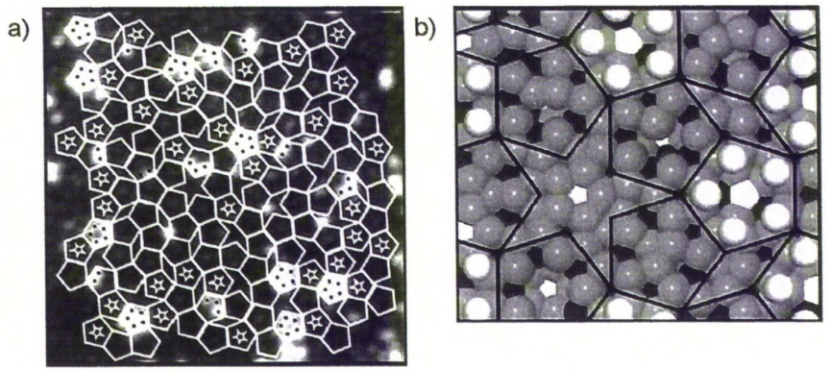

Figure 3.11: (a) STM image of the fivefold i-Al-Pd-Mn surface after a 0.13 ML deposition of Bi, with a P1 Penrose tiling superimposed upon it. The tiling is of edge length 7.8 Å. Bottom pentagons contain a dark star depression and are highlighted as such, while Bi atoms are only present in the top pentagons. (b) A DFT simulation of the fivefold i-Al-Pd-Mn surface with a P1 Penrose tiling of edge length 7.76 Åsuperimposed. Light grey atoms represent Al, dark grey atoms represent Pd and white atoms represent Mn. Bi atoms are shown in off white and form pentagons sitting on top of the substrate layer in the top pentagonal tiles. Reprinted from [92].

exhibits quasicrystalline order. When the monolayer is complete, it is not possible to resolve the overlayer. However, LEED images still indicate that the surface is quasicrystalline.

A nucleation site has thus been proposed by Smerdon *et al.* [92]. DFT calculations by Krajč *et al.* [5] have led to the interpretation of the i-Al-Pd-Mn quasicrystal surface being composed of truncated Bergman and psuedo-MacKay clusters [93]. A P1 Penrose tiling has been placed on the 0.13 ML deposition STM image, shown in figure 3.11 (a). This image indicates that Bi atoms are only forming in clusters within one orientation of pentagon, namely the pentagon that contains the white star feature. The white star pentagon is formed from the intersection of a pseudo-MacKay cluster, and features a Mn atom in the center of the substrate plane. Smerdon *et al.* hence proposes that the pseudo-MacKay clusters must have a Bi pentagonal cluster form upon it before other nucleation sites can be considered for adsorption.

Further growth has been investigated by Sharma *et al.* [45], in which coverages of 1.02 ML and 4.5 ML were investigated. Growth further than the original wetting layer forms as islands of irregular size that have specific heights of four atomic heights or multiples of this number, shown in figure 3.12 (a). These islands have a [012] rhombohedral axis (ie. pseudocubic [100]) parallel to the surface normal, with the structure of these islands displayed clearly in figure 3.12 (b).

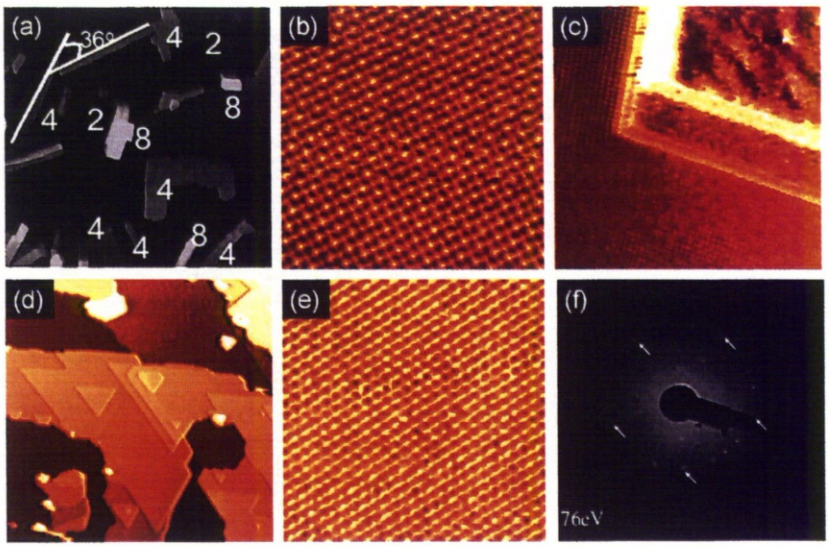

Figure 3.12: (a) STM images of a deposition of 4.5 ML of Bi on the surface of fivefold *i*-Al-Pd-Mn at room temperature (400 nm × 400 nm). (b) 10 nm × 10 nm STM image showing the surface of a pseudocubic island. (c) 30 nm × 30 nm STM image of a domain boundary of a twinned pseudocubic island. (d) 300 nm × 300 nm STM image showing hexagonal islands. (e) 10 nm × 10 nm STM image showing the structure of the hexagonal islands. (f) LEED pattern from the monolayer with hexagonally oriented Bi islands. Arrows indicate the contribution to the pattern from the substrate. (a) Reprinted from [45], (b) - (e) reprinted from [44].

These islands can grow along five different orientations with respect to the surface, at angles of $\frac{n\pi}{10}$. Such relative orientations are shown in figure 3.12 (a).

The specific heights (or magic heights) of the islands can be explained by influence of a quantum size effect (QSE), where the nanometre sized scale of the system becomes comparable to an electron's Fermi wavelength [94, 95]. This confines electrons at the film/subtrate and film/vacuum interfaces, which leads to the formation of quantum well states which depend on the films thickness [96]. Hence, certain thicknesses of a thin film will be more stable than others, preferentially growing to these magic heights. This effect has been reported in several other surfaces, such as Ag, Bi and Pb on Si(111) [97–99].

Smerdon *et al.* investigated the structure of the Bi islands [44]. They document that after a time scale of several hours, the islands of irregular size transform into long and thin islands while maintaining their magic height condition. They also document the twinning of islands, where two islands are joined along their respective edges. Figure 3.12 (c) demonstrates the joining of two islands at the atomic scale, showing the domain boundary.

Increasing the amount of deposited material increases the sizes of the pseudocubic islands. As the size of the single domain islands increases, the island's morphology undergoes a change which exposes a hexagonal plane (rhombohedral (111)) parallel to the surface. These islands are shown in figure 3.12 (d), with their atomic structure detailed in figure 3.12 (e). Unlike the pseudocubic islands, that have had reported heights of 24 layers, the hexagonal islands are restricted to a size of 6 layers.

As well as discrete island heights, their widths can be measured in excess of of 0.25 μm^2, which is in contrast to the pseudocubic islands, where if the island was of a size of 200 nm^2 or greater it would possess at least two domains. The persistence of the pseudocubic structure indicates that some of these islands are stable enough to resist the transformation into a hexagonal structure.

The LEED pattern displayed in figure 3.12 (f) also demonstrates the rotational symmetry imparted onto the islands from the substrate. The diffraction from the hexagonal island domains is shown to have five possible directions of orientation indicating that the islands are rotationally aligned with the substrate, known as rotational epitaxy. The islands taking on a periodic structure indicates that the adsorbate-adsorbate interaction is stronger than the adsorbate-substrate interaction. If the converse were true, the islands would adopt a quasicrystalline order.

The formation of this structure is dependent on the flux used to create it. A flux of 0.16 ML/sec exhibits 30 hexagonal domains per μm^2, while doubling that flux led to 900 domains per μm^2 which are not hexagonal.

3.4 Other surface studies on Al based quasicrystal

The studies on Al based quasicrystals are by no means limited to the short review of literature included here. A Pb overlayer has been grown upon *i*-Al-Pd-Mn [100] and *d*-Al-Ni-Co [101] and has been shown that the first atomic layer of a deposited thin film mimicks the quasicrystalline structure of the substrate. Another study has shown Sn growing several fivefold features on the *i*-Al-Cu-Fe quasicrystal [39].

A more recent study onto the growth of single element quasicrystal thin films features Ag on the fivefold surface of *i*-Al-Pd-Mn [102–104]. This element was deposited at 325 K and grows as islands. The initial growth mode sees the formation of a Ag monolayer that adopts the same structure as the substrate, expressing dark star motifs. Islands quickly grow to a height of three atomic layers, after which they prefer to grow laterally. The structures exhibited by the two and three atomic height Ag islands consist of periodic atomic arrangements. This was observed previously by Fournée *et al.* [103].

Other studies have also led to the discovery of novel structures, such as films with fivefold-twinned structure [29], films with magic heights influenced by quantum size effects [45, 96, 105] and quasiperiodically modulated multilayer Cu structures [32, 33, 106].

3.5 First UHV Surface Studies of Single-Grain Icosahedral Ag-In-Yb Quasicrystal

As *i*-Ag-In-Yb is relatively new, few studies have been conducted on the surface of this material. Studies completed on the quasicrystal have aimed to prove its quasicrystalline nature. The most in depth surface study conducted before the work shown in this thesis was initiated, was that of Sharma *et al.* [64]. For this study, the crystal was grown using the Bridgman method, after which it was polished using diamond paste of 0.25 μm, and prepared using cycles of sputtering with Ar^+ ions at an energy of 3 KeV, and subsequent annealing up to a temperature 620 K.

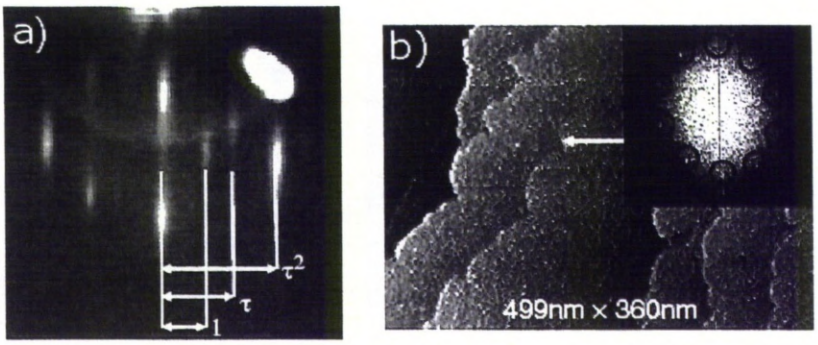

Figure 3.13: Summary of results from the first surface study of *i*-Ag-In-Yb from ref. [64]. (a) RHEED pattern after annealing the surface to 470K. (b) STM image and corresponding FFT pattern of the surface, with a surface defect highlighted.

Reflection High Energy Electron Diffraction (RHEED) was performed on the annealed surface and a five fold pattern produced. Scanning Tunneling Microscopy was the final technique to be employed in this study and resultant images are obtained after annealing at 670 K. The surface appears to exhibit a step-terrace morphology as shown in 3.13 (c). Analysis of step heights indicate that steps tend to have height values of 0.22 to 0.29 nm, 0.70 to 0.74 nm or 0.94 to 0.96 nm. The terraces are atomically flat, having a roughness of 0.05 nm. It is also possible to generate an FFT pattern from the STM images, which displays 10 spots, emphasising the fivefold order present.

The studies presented in this thesis aim to extend this work by characterising the surfaces of the five, three and twofold planes of *i*-Ag-In-Yb, as well as observing the behaviour of these surfaces when subjected to epitaxy techniques and oxygen.

Chapter 4

Experimental methods and techniques

4.1 Introduction

To study a surface there are many factors that must be taken into consideration. Chemical species in the atmosphere prohibit the study of materials that may be reactive to small quantities of these contaminants. To remove the presence of this factor, Ultra High Vacuum is introduced as a principle tool for use in the following studies. Surface sensitive techniques which are used to probe such surfaces are also introduced and explained.

4.2 Experimental Methods

4.2.1 Ultra High Vacuum (UHV)

It has been understood for some time that surfaces are an important aspect of the physical and chemical properties of a material. Although a considerable amount of theoretical work was conducted on this issue, experimental work was hindered by a key fact; at a pressure of $10^{-6}\tau$ (τ, torr, of which 1 mbar = 0.76τ = 100 Pa) a clean surface will accumulate one monolayer of impurities from a residual gaseous environment in roughly 1 second. This time frame is far too short for any experiment to be conducted. Surface impurities have a dramatic effect on a surface's physical and chemical properties. For example, oxygen can rapidly change the chemical

Low vacuum	Medium vacuum	High vacuum	Ultra high vacuum	Extreme high vacuum
1 mbar	$> 10^{-3}$ mbar	$> 10^{-7}$ mbar	$> 10^{-12}$ mbar	$< 10^{-12}$ mbar

Table 4.1: Different levels of vacuum and what pressure applies to each description

composition and structure of a metallic surface. Impurities also represent unknown quantities on a surface, which may change or inhibit any techniques used to collect data from the surfaces. The rate at which a surface will be covered by impurities can by deduced from kinetic theory;

$$rate = \frac{bP}{M_r T^{\frac{1}{2}}} \tag{4.1}$$

Where b is a universal constant ($2.63 \times 10^{26} \mathrm{m^{-2} s^{-1} K^{1/2} mbar^{-1}}$), P is the residual pressure, M_r is the relative molecular mass of the contaminant and T is the temperature. So, for an atmosphere of N_2 molecules at a pressure of 10^{-6} torr (or 1.31×10^{-5} mbar) at 300 K a material's surface will suffer a surface impact rate of 3×10^{18} atoms $\mathrm{m^{-2} s^{-1}}$. If every N_2 molecule sticks, this will cover the surface in around 3 seconds (assuming the number of atoms in a $\mathrm{m^2}$ is 10^{19}). Although this is an ideal case, there will be some modification of the sticking rate due to the sticking coefficients of N_2 to the substrate, and the rate at which clean substrate is covered by the impurities.

However, technology has improved and since the 1960s and 1970s new pumps and vacuum systems have been developed that can create a vacuum several million times better than 10^{-5} mbar. At a pressure of 10^{-10} mbar the time for a surface to become coated in N_2 will be 97 hours, giving plenty of time between preparation cycles to conduct meaningful experiments without fear of a surface becoming contaminated. With a long experimental window, and the relative ease of attaining such pressures, ultra high vacuum is a desirable environment in which to conduct surface studies.

Vacuum chamber

To obtain an ultra high vacuum environment, a few things must be considered. Firstly, how does one obtain such a low pressure? Secondly, how does one maintain this pressure, keeping it stable over long periods of time? To obtain such low pressures, a vacuum chamber is constructed

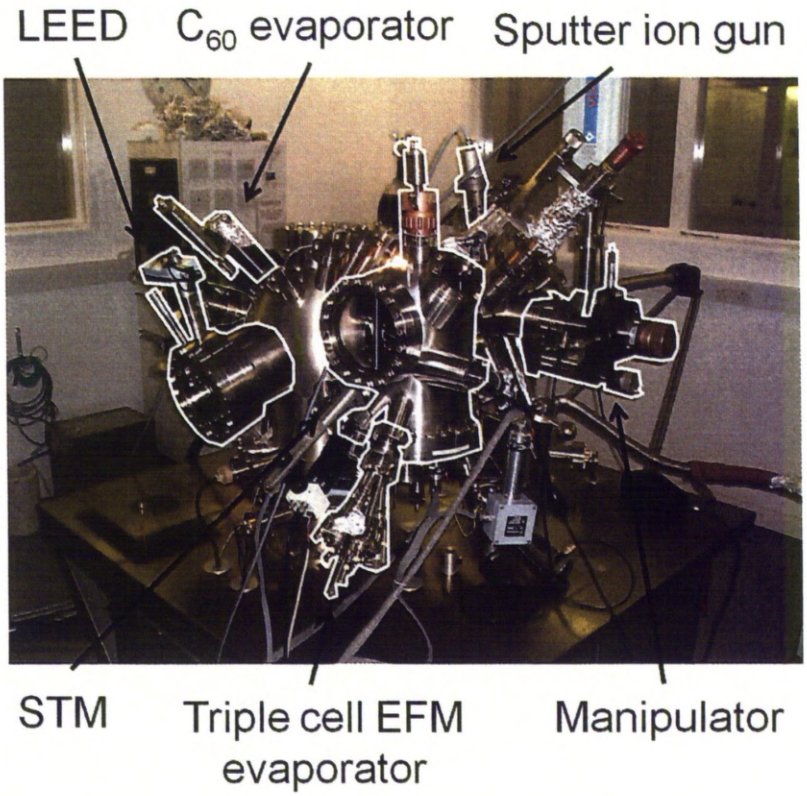

Figure 4.1: The UHV chamber that facilitated the majority of data collection presented in this thesis.

in which a vacuum may be maintained and monitored, which also includes the ability to house apparatus required for experimental techniques. It is important that all materials inside the vacuum chamber are made from materials which have low vapour pressures, to stop them from evaporating when vacuum pressures are achieved.

A vacuum chamber is constructed from many interconnecting parts made from stainless steel, and a typical chamber is shown in figure 4.1. The thickness of the stainless steel walls is roughly 1.5 mm thick. This means that common highly reactive gases in the atmosphere, such as oxygen and carbon dioxide, cannot permeate into the vacuum. Although these gases cannot enter the chamber, hydrogen can diffuse through the steel walls, although this only occurs in trace amounts and does not affect experimental results. The quantities that do diffuse through are removed through the pumping mechanisms described below. Although it is essential to protect the encompassed vacuum, it is also a requirement to be able to look inside the chamber,

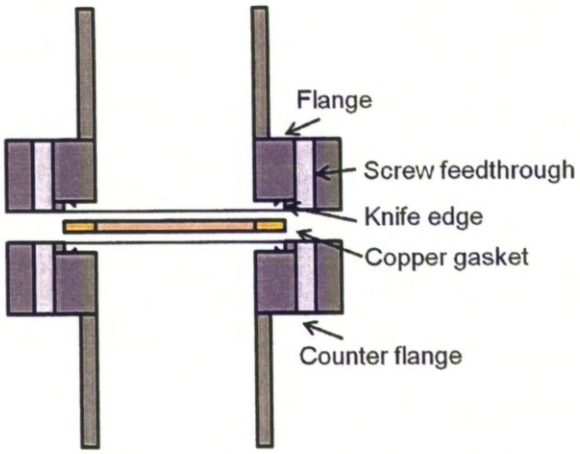

Figure 4.2: Representation of the formation of an air tight seal using a copper gasket and a knife edge.

so that apparatus may be manipulated and samples moved. For this purpose, several blank ends have glass windows placed inside them. These windows are sealed so that no atmospheric gases can enter the chamber.

Sections of chamber and blanks are secured by simple nuts and bolts. The parts that interconnect to each other sport a small knife edge rim. A schematic is shown in figure 4.2. This allows a copper gasket to be placed between the 2 chamber pieces and when they are affixed to each other a seal is formed. Since copper is malleable, as the knife edge is forced into the copper gasket it is deformed, creating an air tight seal. Rubber can also be used as a gasket and at some times may be favourable due to its reusability. Ceramics are also used to allow wires to enter the chamber without breaking containment and without earthing them through the walls of the chamber. These feed-throughs are ceramic sleeves that create a buffer between wire and metal chamber, and also create an air tight seal.

It is often required that a vacuum chamber needs be opened to atmosphere so that equipment can be moved, replaced or repaired. During this time the inside of the chamber, which is kept clean by the presence of vacuum, is exposed to contaminants. To minimise any exposure, instead of venting the chamber to air it can be vented to an atmosphere of pure nitrogen. To reduce the contamination by macroscopic impurities work on the chamber is carried out quickly. Gloves are used by the operator to stop oils, dead skin and hair from hands and arms from falling into the chamber. If a chamber needs to be opened for a lengthy amount of time, areas open

to atmosphere can be covered using tin foil to stop dust from falling into it. Although these methods are not 100% guaranteed to stop contaminants from entering the chamber, they do stop the majority. Any contaminants that do enter can then be removed without problem, although if a chamber has been open for a long time, it will take longer for the system to attain suitable UHV.

One contaminant that is not easy to avoid is water. Since the atmosphere consists of 1% water, it is inescapable that the inside of the vacuum chamber will accumulate a significant amount on its internal surfaces. Water is notoriously difficult to pump away using the methods described below, as in UHV it will freeze. To remove the bulk of water in the system, the entire chamber can be baked to a temperature slightly higher than that of water. This causes any present water and ice on the chamber walls and equipment to vapourise and be removed. This process does have its drawbacks however. The chamber's main constituents are the stainless steel of the walls and the ceramics of the windows and feed-throughs for equipment. These two materials will have different heat capacities. This will mean that the materials will cool at different rates, and hence undergo thermal contraction at different rates and can cause breaches or cracks in the ceramics. To alleviate this issue, metal foil can be placed over any exposed ceramics to slow down their rate of cooling by trapping in hot air, and making the rate of thermal contraction similar to the rest of the chamber.

Other considerations in a vacuum arise from active filaments. Filaments within a UHV chamber will usually be constructed of a thin wire of metal, usually Ta. Some techniques require more specific filaments, such as LaB_6 for a Low Energy Electron Diffraction (LEED) optic. While it is active, the surface atoms of the filament will react with any contaminants in the chamber and sublimate. This means that filaments must be treated with extreme care. The gradual increase and decrease of current to a filament over a prolonged period of time will help increase its lifetime. If a filament sublimes in vacuum, it is no longer possible to utilise that technique until the chamber is vented so that it may be repaired. The process of venting, baking and pumping back down to UHV can take several days so it is not desirable to vent often.

Vacuum pumps

With a chamber to hold and maintain a stable vacuum, it is necessary to use a pump or pumping system to obtain a UHV pressures. A system of many kinds of pumps that all work in tandem is

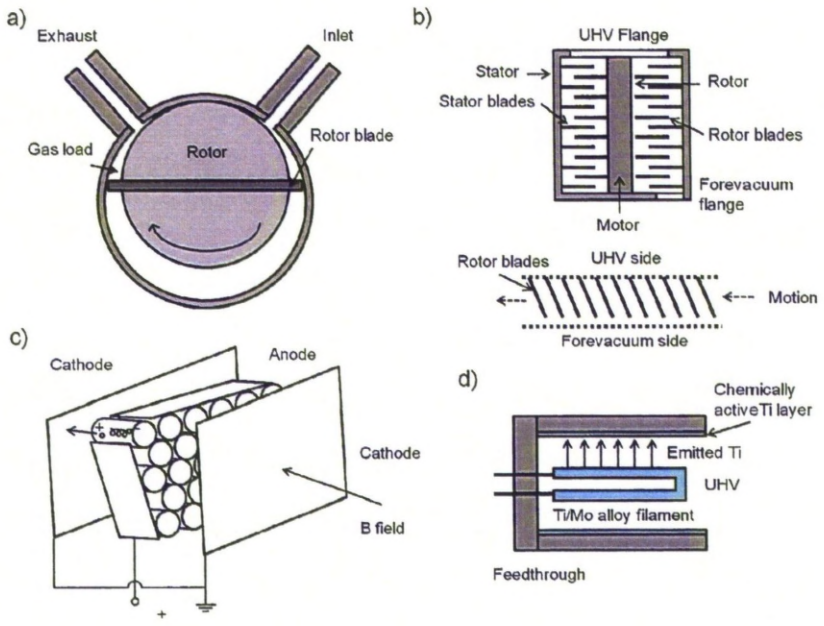

Figure 4.3: Schematics of the most used pumps employed for studies presented in this Thesis. (a) Rotary vane pump. (b) Turbomolecular pump. (c) Sputter ion pump. (d) Titanium sublimation pump.

used in the majority of chambers, and pumps encountered during studies featured in this thesis are detailed here [107].

Rotary vane pump

A rotary pump (figure 4.3 (a)) is used to obtain pressures in the region of 1×10^{-3} and as such functions to prepare the chamber for more delicate pumps that can reach better vacuum pressures, as well as evacuate those pumps of residual atmosphere. These pumps may also be used to remove the exhaust from the more powerful pumps, and as such are referred to as backing pumps. A rotary vane pump consists of a rotor mounted off centre in a chamber surrounded by a stator. The pump functions on a basis of changing gas volumes produced by the rotation of an eccentric motor which has two blades in a diametric slot. During the gas inlet phase, the open volume near the inlet expands until after further rotation this volume is separated from the inlet. Then, during the compression phase, the gas is compressed and forced through the exhaust valve. Due to the requirement of oil for this pump, a zeolite trap between it and the previous UHV pumping stage will prevent any oil contaminating the clean system.

Turbomolecular pump

A turbomolecular pump (figure 4.3 (b)) can be used to sustain a pressure of 1×10^{-9} mbar and in many UHV systems is the main pump for the system. It cannot be activated above a pressure of 1×10^{-2} mbar due to the delicate nature of how it functions. A turbo molecular pump consists of several bladed fans, of which the blades are densely packed. These are attached to a rotor, with each successive fan having blades oriented and moving in the opposite direction and are usually suspended within the pumps casing using a magnetic field. The blades are then made to spin at high speeds (90,000 rpm is an optimal speed). Any gas molecules that are within the volume swept by the first set blades undergo a collision that then forces the gas molecule into the path of the next set of blades and so on. Since this pump is mechanical and undergoes many rotations in a short amount of time, it needs to be regularly maintained.

Diffusion pump

This pump can be used instead of a turbo molecular pump, although it can be used in tandem if the vibrations caused by the turbo molecular pump are counter productive to any techniques being performed but pumping is still required. It can be used to sustain pressures of 1×10^{-10} mbar and can be used from a base pressure of 1×10^{-1} mbar. A reservoir of oil is heated and directed as a jet of heated gaseous molecules. This is then deflected into the path of gas molecules from the UHV system. The collisions then force the flow from the UHV chamber into the the bottom of the chamber, while the heated oil particles return to the liquid reservoir they originated from. This creates a greater gas pressure at the bottom of the diffusion pump, which is then removed using a backing pump. Cooling is required along the sides of the pump to oppose any back streaming of molecules, and is supplied using a liquid nitrogen reservoir. As this has no moving parts, it is a long lived pump, but requires the coolant to be replaced at regular intervals.

Titanium sublimation pump

The titanium sublimation pump (figure 4.3 (d)) is an additional pump used to correct any bursts of pressure that might occur during an experimental process (for example, recovering the base pressure after sputtering) and cannot be used as a stand alone pump. It functions by passing a current of 40 amps through a thick Ti based filament. This causes Ti to sublimate and

coat the inside of the chamber wall around it. The Ti film is highly reactive to gaseous species and forms stable chemical bonds with any stray contaminants, binding them to the wall of the chamber. As some Ti molecules may find there way into the experimental parts of the chamber, it is important not to use this pump if samples are reactive to Ti atoms. Titanium sublimation pumps are usually activated for a minute once over a certain period (usually between 4 to 8 hours) and after a clean and stable vacuum is obtained, are rarely used afterwards.

Sputter ion pump

To obtain a pressure of 1×10^{-11} mbar a sputter ion pump (figure 4.3 (c)), more commonly known as an ion pump, is used. The pump is usually operated from a pressure of 1×10^{-8}. This pump operates by ionising gases and then trapping them using a strong electric potential between 3kV to 8kV. Electrons are produced in hollow cells which ionise free atoms, and then cause them to become trapped within the crossed electric and magnetic fields. These ions then swirl around until the positive ions come in contact with a chemically active cathode, usually composed of Ti, inducing a sputter effect. The sputtered Ti atoms then travel to the anode, forming a 'getter' film. The Ti atoms then react with the active gases present, forming stable compounds which become buried under successive sputtered Ti atoms that form a new active film over captured impurities. Since this pump contains no moving parts and causes no vibrations, it needs little maintenance, and can be used to maintain a good UHV environment during vibration sensitive experiments.

Pressure monitoring

Although it's possible to guess how good a vacuum is by monitoring the efficiency of any used pumps, it is imperative to monitor the pressure of a vacuum during an experiment to ensure that results taken are not being altered by any unexpected contaminants. It is also a requirement to know the pressure in case of sudden leaks, so that pumps may be shut down or isolated before they become damaged.

Between a pressure range of 1×10^{-6} to 1×10^{-12}, an ion gauge is used. This gauge consists of 3 electrodes; a filament, a grid and a collector plate. An electron emitted by the filament will move into the grid. During the travel time, there is a chance it may collide with a gaseous atom, causing the gaseous atom to become ionised. These ions are then captured by the collector plate,

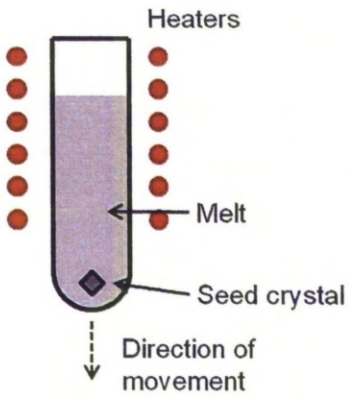

Figure 4.4: A simple representation of the Bridgman method.

from which an ion current is formed. The current will be proportional to the amount gaseous atoms present in the system, and hence a pressure can be calculated.

4.2.2 Sample cleaning

Ex situ preparation

Samples used in these studies were grown at IMRAM at Tohoku University in Sendai, Japan. They were grown using the Bridgman method [108] shown in figure 4.4. This process involves heating a polycrystalline material above its melting point, and slowly cooling it from one end where a seed crystal is located. A single crystal can then be grown along the length of the container. The sample is then cut (spark-etched) perpendicular to the required axis, which is determined using Laue backscattering.

Once a crystal is grown and cut to the required size, the surface intended for study needs to be prepared. The surface is roughly polished using a suspension of diamond granules of different sizes in the micrometer range. The greater the granule size, the rougher the treatment. Diamond granules can be suspended in several mediums, although for crystal polishing these mediums tend to be a paste or an oil. The suspension is held by using a polishing pad of specific roughness. The roughnesses of pads vary from sand paper-esque to delicate fibres. Larger granule sizes benefit from rougher polishing pads. While it is possible to polish a crystal using paste on a polishing pad affixed to a turn table, due to the brittleness of quasicrystals, polishing by hand is preferred to minimise potential damage.

With a clean and polished crystal, it is now possible to prepare the sample for insertion into UHV. Since crystals come in a variety of shapes and sizes, a standardised plate shape and size is introduced onto which a crystal can be affixed. These plates are made from either Mo, Ta or stainless steel. Since sudden thermal gradients can cause crystals to undergo structural changes or break along grain boundaries, the crystals are affixed to the plate by using thin tantalum straps that hold the crystal to the plate by the straps tension. Upon affixing to a plate, the crystal and plate are cleaned in a sonic bath while submerged in methanol to remove as much excess polishing material as possible. The crystal is then kept submerged in methanol until it is ready to be placed into the chambers load lock.

In situ preparation

Once inserted into a UHV environment, it is no longer possible to directly manipulate the crystal or its surface. Any adjustments must now be made via apparatus pre inserted into the the chamber. With treatment detailed above, the crystal surface will be clean and smooth to the naked eye. On the atomic scale this is not the case, as even though the crystal has been immersed in methanol, there will still be residual amounts of diamond paste remaining, as well as any contaminants picked up while transferring the sample to the chambers load lock. To further clean the crystal and eventually prepare an atomically flat surface, it is exposed to cycles of ion bombardment, or sputtering, and subsequent heat treatment, or annealing.

Sputtering is the process of bombarding the surface with energetic ions in an attempt to remove the top-most atomic layers from the surface. This will remove any impurities such as oxides that accumulate over a long period and any structures which may have been grown on the sample in a previous study that are no longer required. This process involves ionising an inert atomic species such as a Argon. Although any noble gas can be used, one of sufficient mass is preferred. The sputtering is done by use of an electron gun, which utilises free electrons to remove electrons via elastic collisions from the valence bands of the noble gas. This leaves the noble gas with a positive charge.

Next, the ions are subject to an electric field. This will then accelerate the ions to a specified energy, which is aimed at the surface of the crystal to be cleaned. The resulting collisions with the crystals surface will knock the surface atoms off of the bulk, 'etching' away at the surface. This processes may be carried out for varying periods of time, depending on the condition of

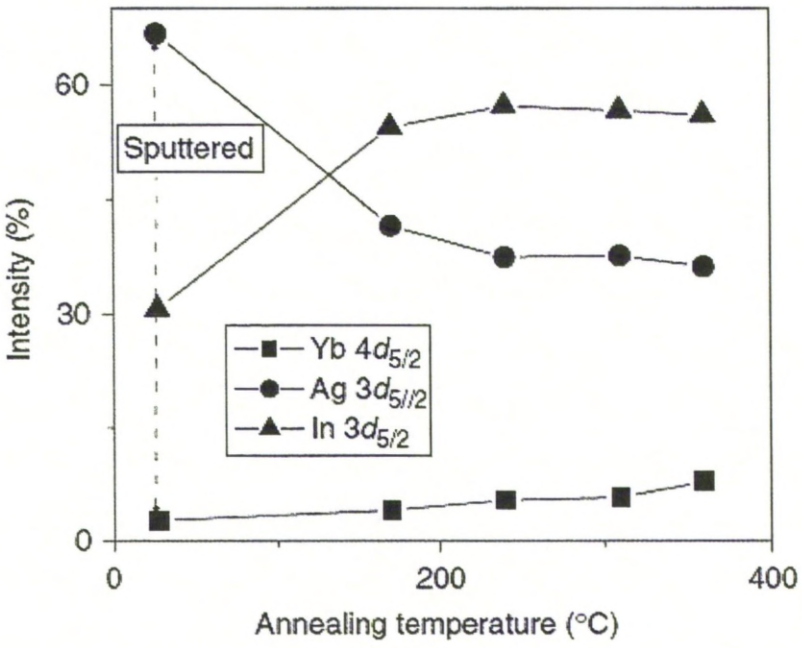

Figure 4.5: Concentrations of atomic species on the *i*-Ag-In-Yb surface as a function of anneal temperature as observed by XPS. Reprinted from [64].

the surface.

The effect of sputtering on *i*-Ag-In-Yb has been studied by Sharma *et al.* [64]. By utilising X-ray Photoelectron Spectroscopy (XPS), which is explained below, the relative amounts of the surfaces constituents were measured as a function of anneal temperature. The resulting concentrations shown in figure 4.5 shows that sputtered surface is chemically different to that of the annealed surface. During ion bombardment, In is preferentially sputtered away leaving a Ag rich surface of composition $Ag_{71}In_{24}Yb_5$. As heat is applied, the concentrations shift so that the resulting surface has a composition similar to the bulk of the material, of $Ag_{40}In_{45}Yb_{15}$.

Reflection High Energy Electron Diffraction (RHEED) was also performed at several temperatures. After sputtering no pattern was discernable, indicating no surface structure. This is in contrast to Al base quasicrystals that adopt a periodic structure after surface bombardment. Upon heating to 470 K diffraction streaks were observed, with the pattern not changing as anneal temperatures approached 670 K.

After sputtering, the surface is reduced to a rough structure. For some Al based quasicrystals

the resulting rough structure is periodic [24]. This is caused by the preferential removal of Al from the surface, which adjusts the surfaces composition to a phase which exhibits a periodic structure. For *i*-Ag-In-Yb the sputtered surface shows no structure [64], with the change in composition shifting the material to an amorphous phase. While these rough structures may be suitable for some surface techniques, for techniques such as Scanning Tunneling Microscopy (STM) a rough surface may actively damage the apparatus.

To smooth the surface to make it suitable for several surface sensitive techniques, the crystal is annealed. The process of annealing requires the crystal to be heated up to a temperature just below the surface melting point. This allows atoms from the bulk to diffuse to the surface and create an energetically favourable termination. Heat treatments can last for a varied amount of time. Long treatments are used on newly cut samples in an attempt to remove bulk impurities [109]. Samples that have already experienced several preparation cycles may only need a couple of hours of heat treatment to re-correct for the damage done during sputtering. The temperature of the crystal can be measured using an optical pyrometer set to the emissivity of the annealing material, or by using a thermocouple.

4.3 Experimental techniques

There are a wide variety of experimental techniques that can be performed on a crystal in efforts to determine its structure and composition. Work undertaken for this thesis is specifically tailored to the determination and characterisation of the surface of a quasicrystalline surface, as well as structures grown upon it. For this task the following surface sensitive techniques are used.

4.3.1 Scanning Tunneling Microscopy (STM)

Scanning Tunneling Microscopy (STM) is a technique in which the spatial dependence of the Local Density of States (LDOS) of a surface are probed to estimate the positions of surface atoms. This technique makes use of the physical phenomena known as quantum tunneling. This refers to the behaviour of an electron in a non-classical system. In classical physics, an electron can only exist where it has the energy to do so. This means that if a potential barrier has 'walled off' a certain area of space, if the electron does not have sufficient energy to overcome

the potential barrier, it cannot exist in the space occupied by the barrier or on the opposite side of the barrier. However, in the quantum world an electron can behave like a particle and a wave. This means its wave form can penetrate into a potential barrier even if it does not have the energy to overcome it, as described by the Schrödinger equation, with the probability of its existence diminishing exponentially the further into the potential barrier it tunnels.

The first evidence of metal-vacuum-metal tunneling was documented in 1971 by Young *et al.* [110]. A tungsten field emitter was positioned within a few hundred angstroms of a platinum surface. Movement was induced using 3 piezoelectric controllers so that very fine adjustments in position were possible. Upon maintaining a constant field between tip and surface, a current was measured and a topographical map was created.

The relation governing STM is;

$$J_T \propto e^{A\phi^{1/2}S} \tag{4.2}$$

Where J_T is the current, ϕ is the average barrier height, S is the distance between tip and sample and A is a constant equal to 1.025 $A^{-1}eV^{-1/2}$ for tunneling through a vacuum. The exponential dependence on the width of the potential gap and the flow of electrons that permeate it give rise to the resolution of the technique, with very subtle changes in separation of tip to the corrugated nature of a surface at the atomic level giving rise to significant changes in the tunneling current. This technique was perfected in 1982 by Binning and Roher, which eventually led to them winning the Nobel Prize for physics for demonstrating the technique on $CrIrSn_4$ [111]. We can now expect atomic measurements from such a device due to improvements in damping thermal and vibrational effects.

It is possible to control the direction in which electrons tunnel in respect to the surface and the tip by controlling the bias voltage across the gap between surface and tip. If the surface is biased negative with respect to the tip, or $V_B < 0$, electrons will tunnel from the surface to the tip and hence filled states of the surface are probed. If the surface is biased positive with respect to the tip, or $V_B > 0$, electrons tunnel from the tip to the surface, and unfilled states of the surface are probed.

The precise nature of STM stems from the use of piezo-electric drives. These mechanisms are created using tubes of piezo-ceramic materials. To create such a material, a piezo-ceramic tube is heated to a high temperature and then exposed to a voltage generated using tubular

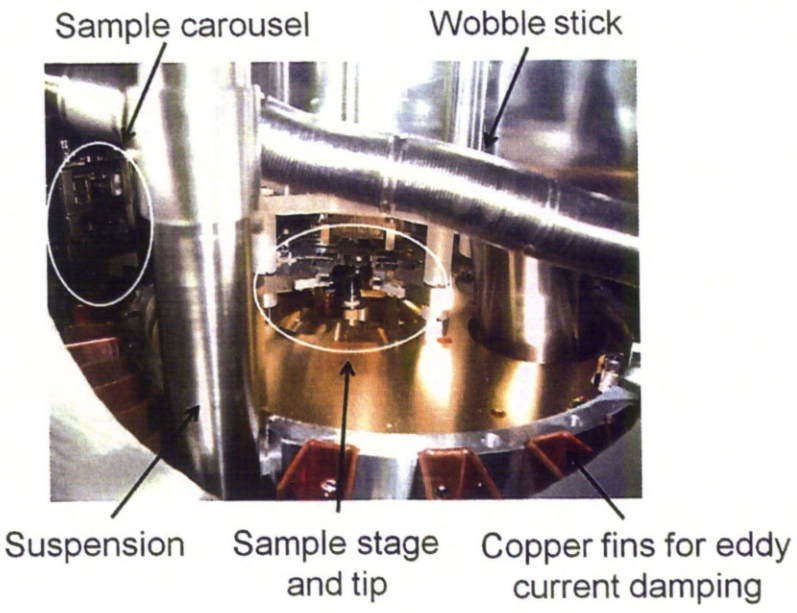

Figure 4.6: An Omicron variable temperature scanning tunneling microscopic stage.

electrodes running outside and through the centre of the tube. This aligns the polar molecules within the material with the electric field, and as the tube is cooled the radial polarisation is preserved. If the tube is exposed to a potential, the tube will contract or expand rapidly due to the electrostatic interaction. By utilising a tripod of these materials it is possible to obtain precise movement on the nanoscale in three dimensions.

STM Device and UHV chamber

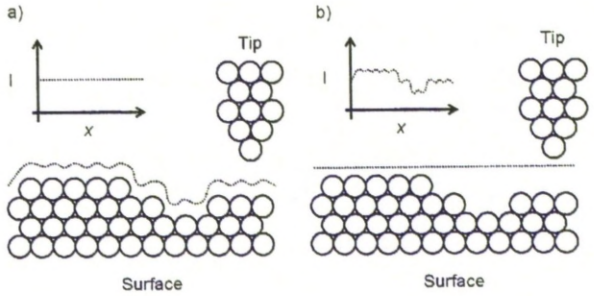

Figure 4.7: Operation of an STM in the two most common modes; (a) Constant current and (b) constant height.

The majority of data acquired from STM presented in this thesis has been taken using an Omicron VT-STM, shown in figure 4.6. This figure shows the position of the tip relative to the sample, the sample stage, copper fins used for eddy current damping, a carousel for sample storage and a wobble stick to manipulate samples *in situ*. There are two possible modes of operation for this type of STM shown in figure 4.7; constant height or constant current modes. Constant height fixes the tip at a defined height and measures the tunneling current as the tip is raster scanned across the surface. This mode can create images quickly, but has the draw back that the sample's surface must be very flat, as a rough surface would cause the tip to crash. As prepared quasicrystal surfaces are composed of steps and terraces, constant current mode is preferred. For this mode the tunneling current is maintained, which will also maintain a constant tip-surface separation. A feedback loop is used to adjust the z-piezo controlling the position of the tip. The z-motion of the sample may then be used to create a topographical image.

STM Tips

An STM tip can be made from any conducting material. To produce well resolved images that can detail atomic features, a tip must be tailored to have specific attributes. A tip that approaches within one atomic nearest neighbour distance of a surface will undergo a large increase in current measured, therefore an atomically sharp tip is the most effective at gathering atomic scale images.

Commonly a tungsten tip was used. These are produced by chemically etching a tungsten wire. A meniscus of a concentrated potassium hydroxide solution is created on a stainless steel plate across an aperture of radius 2 mm. A tungsten wire is placed through this hole and meniscus, so that the wire does not touch the metal plate and so that there is an equal distance between the holes edge and the wire in all directions. A potential is then applied across the wire and plate. The tip will be etched away around the meniscus until the wire breaks. When viewed through a microscope, the severed ends of the wire will appear vanishingly sharp. A tip that appears hooked or malformed at this stage is then discarded. Successful tips will then be washed in pure water to remove any hydroxide residue.

When entered into UHV, several *in situ* preparation techniques can be applied to ensure cleanliness and further improve on the sharpness of the tip. Sputtering will remove the oxide layer from the surface of the tip, and the tip may also be annealed to remove other impurities.

Figure 4.8: Example of a double tip encountered on C_{60} deposited on the fivefold surface of *i*-Ag-In-Yb after surface modification by a small deposition of Sb (75 nm × 75 nm).

Sometimes asymmetric or multiple tips can be formed, the effect of which can be seen in figure 4.8. For the case of a multiple tip, every feature is imaged multiple times. This is caused by the existence of several areas of the tip which are roughly the same distance to the surface and encourages multiple paths for electron tunneling. This can come about from the tip absorbing atoms from the surface or impurities from the environment. To correct this, it is possible to apply a sudden high voltage pulse (15nA, 10V) between tip and surface which will eject material from the tip.

Image processing and analysis

Image processing and analysis presented in this thesis was performed on the `WSxM` software package [112]. This package allows for the easy manipulation of images into a workable format by means of flattening the image with respect to separate terraces, the ability to remove information occurring at specific heights (height filtering) and to recolour the image with respect to specific heights. The analysis tools provided by this package include Fast Fourier transforms, auto correlations and line profiles.

4.3.2 Low Energy Electron Diffraction (LEED)

Diffraction is a common tool used to discover the overall physical structure and ordering of a material. William Henry Bragg and William Lawrence Bragg were the first to use X-ray diffraction to determine the structures of crystals, such as diamond, and in the process ascertained the interactions of waves with an ordered crystal lattice, which is commonly known as Bragg's law. This led to father and son winning the Nobel prize in 1915. Braggs law provides the condition for which a diffraction peak is produced for X-rays permeating into a surface, which occurs when the scattered waves interact constructively;

$$n\lambda = 2dsin\theta \tag{4.3}$$

Where n is an integer, λ is the wavelength, $d = (h^2 + j^2 + k^2)^{1/2}$ and θ is the angle between the incident beam and the scattering plane.

The method employed to study the structure of a surface employs the diffraction of electrons, and only concerns itself with the first layer of atoms. As electrons have mass, they were thought to behave as particles until Louis de Broglie theorised wave particle duality in 1924. This states that all matter with momentum p has a wavelength λ;

$$\lambda = \frac{h}{p} \tag{4.4}$$

Where h is Planck's constant. This would allow electrons to diffract from a surface and produce a pattern if that surface was ordered over a long distance. Electron diffraction was first reported by Davisson and Germer in 1927, where they accidently produced an electron diffraction pattern from a Ni (111) crystal [113]. An incident beam has a wavevector $\mathbf{K}$ and the scattered beam has a wavevector of $\mathbf{K}'$ [114]. In three dimensions the conservation of momentum gives [115];

$$\mathbf{K} + \Delta\mathbf{K} = \mathbf{K}' \tag{4.5}$$

where $\mathbf{K}$ and $\mathbf{K}'$ is the wavevector for the incident and reflective beams respectively and $\Delta\mathbf{K}$ is the change in wavevector. A wavevector is a measure of momentum given by;

$$\mid \mathbf{K} \mid = \frac{2\pi}{\lambda} \tag{4.6}$$

The amplitude of the incident and reflected waves is given by;

$$\mid \mathbf{K} \mid = \mid \mathbf{K}' \mid \tag{4.7}$$

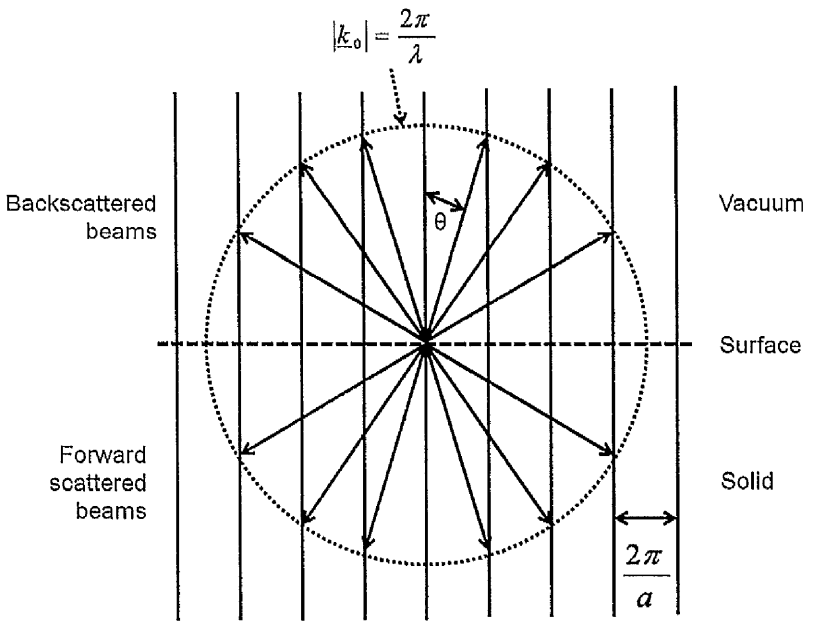

Figure 4.9: A graphical representation of an Ewald circle superimposed onto a periodic surface.

The diffraction condition may also be expressed by;

$$\mathbf{K}' = \mathbf{K} + \mathbf{g}_{hkl} \tag{4.8}$$

with the reciprocal lattice $\mathbf{g}_{hkl} = h\mathbf{a}^* + k\mathbf{b}^* + l\mathbf{c}^*$. As diffraction will originate from the surface, this can be simplified to only include conservation of momentum parallel to the surface;

$$\mathbf{K}'_{\parallel} = \mathbf{K}_{\parallel} + \mathbf{g}_{hk} \tag{4.9}$$

and;

$$\mathbf{g}_{hk} = h\mathbf{a}^* + k\mathbf{b}^* \tag{4.10}$$

If $\Delta\mathbf{K} = G$ and $\mathbf{K} + G = \mathbf{K}'$ the diffraction condition can be expressed as;

$$2\mathbf{k} \cdot \mathbf{G} + G^2 = 0 \tag{4.11}$$

Which gives the central result in the theory of elastic scattering of waves in a periodic lattice. If **G** is a reciprocal vector, then so is **-G** and hence the Bragg condition can be written as

$$2\mathbf{k} \cdot \mathbf{G} = G^2 \tag{4.12}$$

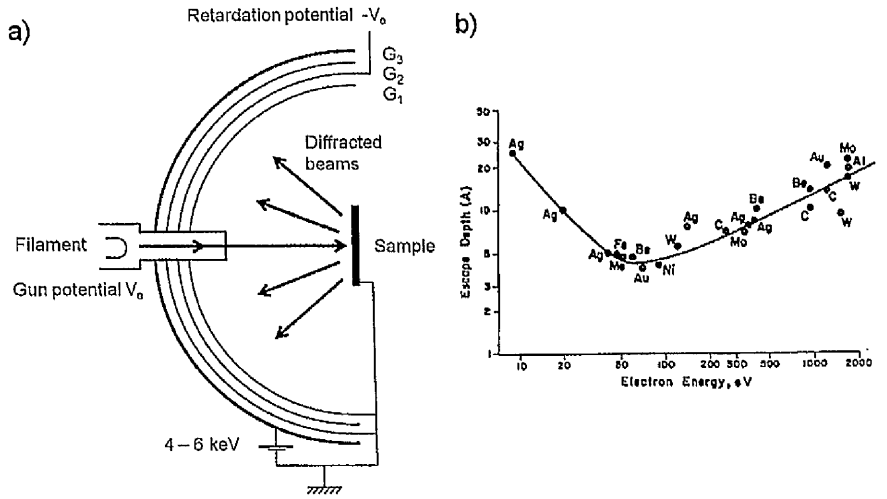

Figure 4.10: (a) A schematical representation of a LEED optic. (b) The 'Universal Curve' showing the escape depth of an electron in relation to its energy.

A graphical representation of the process of diffraction from a surface is called an Ewald circle and is represented in figure 4.9. This was conceived by Paul Peter Ewald, a German born physicist and crystallographer who pioneered X-ray diffraction techniques. While bulk diffraction would require an array of dots and a sphere construct, LEED only measures the surface and instead a series of lines and a sphere construct is used.

A circle is placed on the surface at an origin, and the radius of the circle is defined by **K** (or $2\pi/\lambda$). At every point the circle generated by **K** cuts a rod, the condition for diffraction is satisfied. Scattered beams that emerge into the vacuum will be detected, while beams directed into the solid will not. It should be noted that the representation in figure 4.9 is for a periodic crystal. For an aperiodic crystal, the rods will be separated by τ scaled spacings.

The LEED system widely used in the following experiments is an Omicron SpectaLEED source, and a schematic is shown in figure 4.10 (a). Electrons of high scattering cross section have energies of 1 keV or lower. According to the 'Universal Curve', shown in figure 4.10 (b), using electrons of an energy in the range of 60 eV to 300 eV is considered to be surface sensitive. The basics of the apparatus consists of an electron gun pointed at the sample, which can fire an electron beam of specific energy (and hence wavelength) with a collection of grids and a phosphorous screen behind it. The volume between sample and the electron gun is field free, provided by the first and third grids G_1 and G_3 which are earthed. The second grid G_2 is set to a

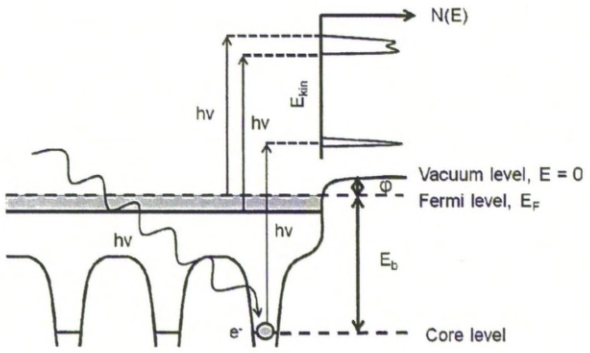

Figure 4.11: Energy level diagram of the photoemission process encountered in XPS. A photon excites an electron so that it escapes the surface. This electron is then detected by an electron analyser.

positive potential similar to that of the original potential used at the electron source. This retards any inelastic backscattered electrons, allowing only those that have been elastically scattered to pass through it. Although not shown in the schematic, the Omicron SpectaLEED uses two grids for the retardation of backscattered electrons. The screen is then used to accelerate the electrons is set at 4 - 6 keV. This causes the screen to emit a photon where an electron collides with it, allowing for a visible diffraction pattern to be observed.

4.3.3 X-ray Photoelectron Spectroscopy (XPS)

X-ray Photoelectron Spectroscopy is a technique that uses photons that interact with the core level electrons of atoms on the surface to determine what those atoms are. The penetration depth of the X-rays will be determined by their energy. However, not every electron the incident photons interact with will escape the bulk to be detected, as the ejected photoelectrons will undergo several collisions with adjacent atoms leaving them with not enough energy to escape. This means each photoelectron will have a mean free path which is dictated not only by the incident photons energy, but also the kinetic energy of the electron before it is ejected. Hence, only photoelectrons from atoms in the surface and near surface region have sufficient energy to escape the material for detection, making XPS a surface sensitive technique.

The electrons that interact with the incident photons are emitted with specific energies that are collected and analysed. Each element will emit electrons of specific energies, enabling them to be identified. The amount of emitted electrons will also relate to the amount of that

species present, so by studying the relative intensities of electrons of specific energies allows for the determination of the studied surfaces composition. Firstly, a photon of specific energy is considered;

$$E = h\nu \tag{4.13}$$

which is then adsorbed by an electron at an energy level E_b. If the energy is just enough, or greater than the energy required to excite the electron to the vacuum, then electron is emitted from the surface. An electron must not just have enough energy to overcome its binding energy, E_b, it must also have enough energy to overcome the work function, ϕ. This is the energy required to liberate an electron from the Fermi level to the vacuum level. The electron will be emitted with kinetic energy;

$$KE = h\nu - E_b - \phi \tag{4.14}$$

This is the simplest case which involves a single electron bound to an atom.

To calculate the binding energy of the electron;

$$E_{binding} = E_{photon} - (E_{kinetic} + \phi) \tag{4.15}$$

For this simple case, the energy distribution of photoemitted electrons should be the energy distribution of the electron states in the solid surface, shifted by the photons energy $h\nu$. However, the probability that a photon will be absorbed by varying electronic states is different. The photoionisation cross section can be calculated by using the Golden rule that the emission rate is proportional to the square of the matrix element;

$$< f|\mathbf{H}'|i > \tag{4.16}$$

Where $\mathbf{H}'$ is the interaction between the photon and electron or electromagnetic field, and f and i are the final and initial states of the electron respectively. $\mathbf{H}'$ is given by;

$$\mathbf{H}' = -\frac{e}{2mc}(\mathbf{p}\cdot\mathbf{A} + \mathbf{A}\cdot\mathbf{p}) \tag{4.17}$$

where $\mathbf{p}$ is the electron momentum operator (-i∇) and $\mathbf{A}$ is the vector potential field. This describes the difference of photoionisation cross section between different electron bands. Hence in calculations of composition, a 'sensitivity' factor is used to determine the amount of an element that is detected.

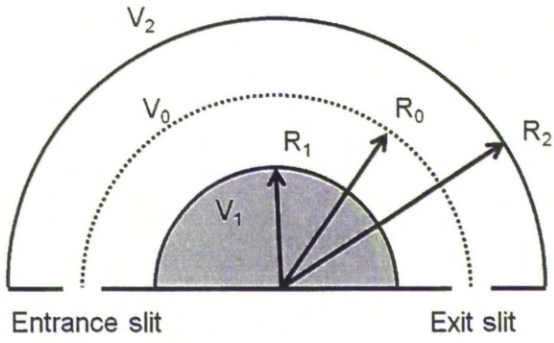

Figure 4.12: Schematic of an hemispherical analyser.

As mentioned above, photons may penetrate into the near surface region before interacting with an electron. Typical photons used for XPS have a penetration depth of the order of 10 μm. However, energy loss caused by inelastic scattering prevents electrons emitted from atoms 10 atomic layers deep from being detected, making this technique surface sensitive [116]. Selecting the photon energy for spectroscopy is important, as the photon energy must be greater than that of the work function ($hv - \theta$) of the solid so that the emitted electron may escape. For this purpose, this restricts the use of photons with radio, visible and near ultraviolet wavelengths. For the purposes of XPS the photon energy range is usually restricted to two lines (or group of lines); Al_α and Mg_α X-ray emissions at 1486.6 eV and 1253.6 eV respectively. Synchrotron radiation sources ($hv < 10$ keV) can also be used as it is provided in an intense polarised continuum narrowly defined in the plane of the accelerator used to produce it.

Analysers and Lenses

To detect electrons emitted from a surface under study, there are several types of analyser available. For the work presented in this thesis, a hemispherical deflector has been used with its schematic shown in figure 4.12. This device utilises two plates of radius $R_1 < R_2$ with a potential placed between them, such that

$$V_1 = V_0(\frac{2R_0}{R_1} - 1), V_2 = V_0(\frac{2R_0}{R_2} - 1) \tag{4.18}$$

Where V_1 and V_2 is the potential at R_1 and R_2 respectively, and V_0 is the potential at R_0, the midpoint between R_1 and R_2. This allows the selection of electrons of energy eV_0 which will travel along the central trajectory R_0. Electrons with energy greater or less than eV_0 will end

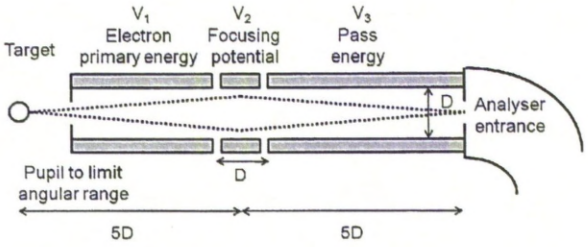

Figure 4.13: Schematic representation of a triple cylinder electron lens.

up with a trajectory of radius greater or less than R_0, and will collide with the walls of the analyser and will not be detected. Electrons that manage to travel through the exit slit will then encounter a photomultiplier, which will enhance the signal into a readable current which is then fed to a computer for display. To gather a complete spectrum, the potential of the analyser is changed so that every required energy is studied.

The incoming beam of electrons at a normal angle to the analyser slit is a small percentage of the yield of electrons being emitted from the surface. The yield of electrons is proportional to the solid angle, so for a surface to analyser separation of 25 mm and a 0.5 mm sample to lens entrance slit separation:

$$Yield \sim \frac{\pi(0.5)^2}{4\pi(25)^2} \sim 0.01\% \tag{4.19}$$

To increase this yield an electron lens is used. A lens of diameter 8mm increases this yield to 0.16%. A lens will also allow the ability to analyse at lower energies. A detectors resolution is given by;

$$\Delta E \sim E_0 \frac{w}{2R_0} \tag{4.20}$$

Where w is the apertures width. With no lens and electrons being emitted isotropically with an energy of 10 eV, an aperture width of 0.01 mm and $R_0 = 1$ m, the resolution is ~ 0.1 eV. Introducing a similar lens in the yield example above improves this resolution to 0.01 eV. An example of a lens, called a triple cylinder lens, is shown in figure 4.13.

There are two modes of operation for an analyser and lens pair. The first mode of operation has the lens purely focussing the incoming electrons into the analyser. The analyser then varies the voltage of its two plates to select which energy of electrons should be scanned. The second mode of operation uses the lens to retard the electrons to the required energy for scanning, while the analyser works at a constant energy (known as the pass energy) to ensure that a constant

resolution is maintained. For the studies mentioned later, the second mode of operation was employed.

Spectra analysis

Peak intensities and binding energies are determined using the CASA XPS software package [117]. Peak intensities were determined by creating a fixed region, which is set between two specific energies to enclose a core level peak. The background was considered linear and subtracted from the signal, and the remaining intensity recorded as the intensity due to the presence of the element being investigated.

Binding energies can be determined using one of two techniques. The least accurate way is to highlight the top most part of a peak and read the energy levels associated with the cursors position. The second and more accurate method of determining binding energies can be accomplished by fitting a curve onto the core levels, and then reading off the calculated peak height. Fitted curves can be created using a convolution of Lorentzian and Gaussian line forms [118,119]. Typically, for the following studies, the line forms are generated by convoluting 60% Gaussian and 40% Lorentzian.

While determining which elements are present on a surface requires the comparison of measured binding energies with that of known values, calculating the composition requires the analysis of the relative intensities of all the elemental species present. To determine the amount of a specific element, C_A, present on the surface;

$$C_A = \frac{I_A/(S_A\lambda_A)}{\sum_n I_n/(S_n\lambda_n)} \tag{4.21}$$

Where I is the intensity of the measured XPS signal, S is the sensitivity factor of the element, n denotes each species present on the surface in turn, and λ is the mean free path of the ejected electrons. λ is calculated using the Tanuma-Powell-Penn equation [120];

$$\lambda = \frac{E}{{E_p}^2(\beta \ln(\gamma E) - \frac{C}{E} + \frac{D}{E^2})} \tag{4.22}$$

Where E_p is the plasmon energy $E_p = 28.8\sqrt{U}$, E_g is the band gap in eV,

$$\beta = -0.1 + \frac{0.944}{\sqrt{{E_p}^2 + {E_g}^2 + 0.069\rho^{0.1}}} \tag{4.23}$$

$$\gamma = 0.191\rho^{-0.5} \tag{4.24}$$

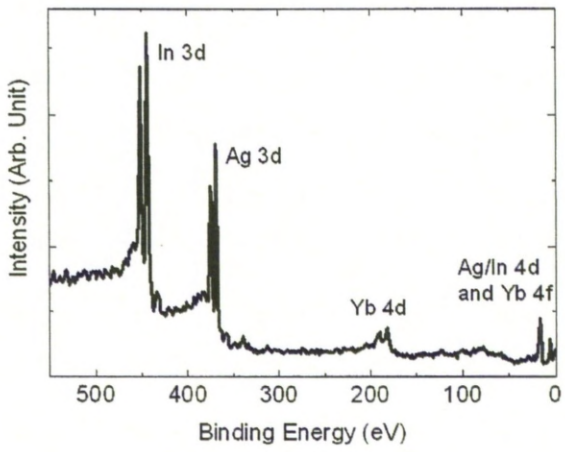

Figure 4.14: A typical XPS spectrum taken from the clean surface of *i*-Ag-In-Yb.

$$C = 1.97 - 0.91U \tag{4.25}$$

$$D = 53.4 - 20.8U \tag{4.26}$$

$$U = \frac{N_v \rho}{M} \tag{4.27}$$

Where N_v is the number of valence electrons, ρ is the density in g/cm^{-3} and M is the atomic mass. The error associated with the intensities measured, N, is considered to be a counter error, or $\sqrt{N}$.

Figure 4.14 demonstrates a typical spectrum that can be obtained from the *i*-Ag-In-Yb quasicrystal. It shows characteristic peaks at energies of 452 eV (In $3d_{3/2}$), 444 eV (In $3d_{5/2}$), 374 eV (Ag $3d_{3/2}$), 368 eV (Ag $3d_{5/2}$) and 182 eV (Yb $4d$ doublet). From this spectrum information such as surface composition and alloying between materials can be quantified.

4.3.4 Ultraviolet Photoelectron Spectroscopy (UPS)

Ultraviolet Photoelectron Spectroscopy (UPS) is a similar technique to XPS in that it uses photons of specific energies which interact with a surface, with the energy of the emitted electrons collected and analysed. While XPS can be used to calculate compositions, UPS can be utilised to study the effects of reactions with other materials.

For UPS, a different energy of photon source is utilised compared to XPS. Photons used for XPS not only excite electrons in the core levels, they also excite the electrons within the valence band. However the valence band is typically 10 eV in size, and because of the energy spread

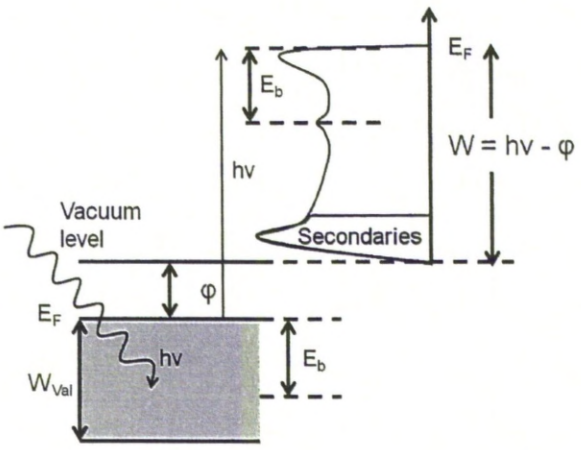

Figure 4.15: Energy level diagram of the photoemission process encountered in UPS.

of the photons used for XPS (usually 1 eV), this leads to poor resolution for detecting valence band electrons. The photons used for UPS are generated using a He gas discharge line source, which can be operated to maximise the output of HeI or HeII, producing photons of 21.2eV and 40.8 eV respectively. As the photon energies are much lower they will be unable to excite core levels as in XPS, and instead will primarily excite valence band electrons that lie close to the Fermi Edge.

As with XPS, incoming photons are absorbed by electrons and are then emitted from the surface, with a measurable kinetic energy of $KE = hv - E_b - \phi$. Electrons are collected and analysed using a hemispherical analyser and lens as described above. This will then give information about the density of states (DOS) of the solid being studied.

4.3.5 Medium Energy Ion Scattering (MEIS)

Unlike the above techniques, Medium Energy Ion Scattering (MEIS) has the ability to measure both composition and structure of a surface. This is accomplished by shining an incident beam of ions at a surface at differing angles and measuring how many ions are scattered back. The intensity of the scattered ions will depend largely on how far they penetrate into a surface, and hence will be dependent on the structure of the surface. By measuring the energy of the scattered ions it is also possible to determine what kind of element they have scattered from.

This technique provides structural data due to the basic physical principle that an ion that

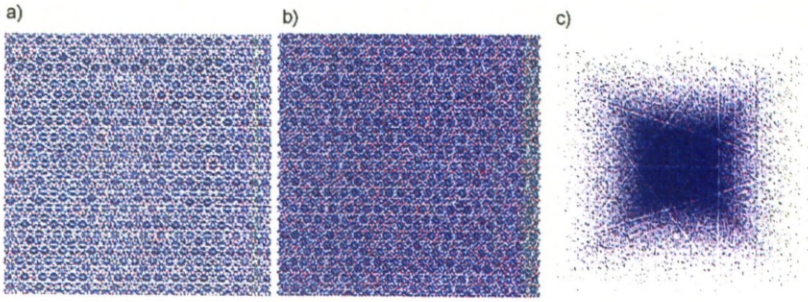

Figure 4.16: (a) A 3nm slice of the i-Ag-In-Yb model aligned along a channeling direction. (b) The same model at an angle offset from a channeling direction. (c) A perspective view of the model, where it is possible to identify the 5 fold symmetry of the crystal.

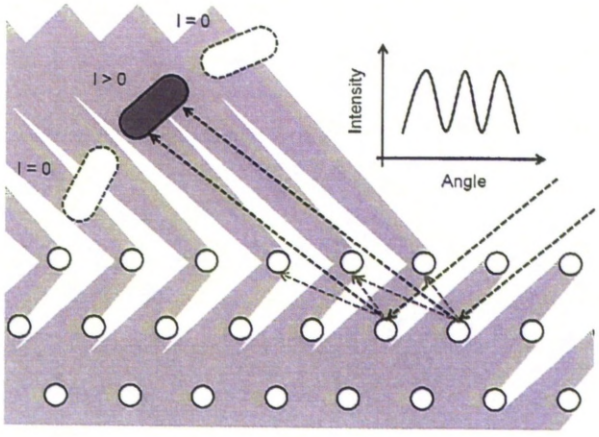

Figure 4.17: An example of double alignment geometry.

has penetrated into a solid will have an increasing probability that it will not escape that solid the further it has penetrated. An easy way to envision this is to consider a small section of an atomic model. Figure 4.16 (a) and (b) shows such a model at two different orientations. In this figure, the model is presented without perspective, similar to what a collimated beam would 'see'. Even though the model is opaque at a certain orientation, if the model is approximately aligned along a crystal plane, it almost vanishes. These are known as channeling directions, named so because ions with incident angles nearly but not exactly aligned may be channeled along it due to interactions with atoms in the structure. When viewed along one of these directions with perspective, as shown in figure 4.16 (c) it is possible to see the inherent symmetries in the surface.

However, this treatment is insufficient to describe this technique, as the detector does not

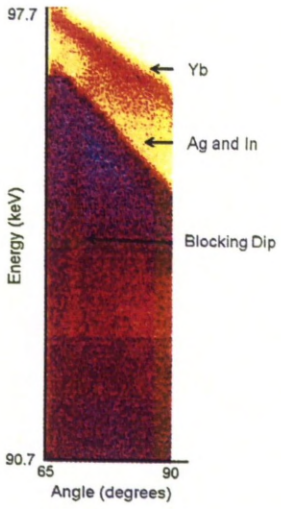

Figure 4.18: Two dimensional MEIS spectra obtained from the clean i-Ag-In-Yb surface.

measure the reflected component of the ion beam along its incident direction. A double alignment geometry is achieved when the beam is incident along a major crystallographic direction, shown in figure 4.17, and the detector is scanned over a range of angles including the opposite crystallographic direction. In this way, the impinging ions are first scattered from the top few layer of atoms, and are then subjected to blocking, due to the atoms that may scatter them on the way out of the surface. If the sample is well ordered these dips will only occur at well-defined angles relative to the scattering atoms and the coinciding drop in intensity is indicated by a blocking dip. By using a two dimensional detector, a two dimensional spectrum displaying both the reflected ions intensity and scattering angle can be obtained.

Two-dimensional spectra

Two-dimensional data, of which an example is shown in figure 5.20 provides information about the energy intensity dependent on the angle of the analyser to the sample. The spectra can be used immediately to analyse the surface being studied. Each diagonal streak of high intensity corresponds to an elemental species that is present on the surface. The width of these streaks also gives information on how thick the layer is. The constant signal encountered at lower energies gives information about the bulk of the crystal. Vertical lines of lower intensity in this region are known as blocking dips, and occur at angular positions dependent on the structure of the sample. This information can be used in conjunction with Monte Carlo simulations to provide picometer resolution. However, due to the aperiodic nature of the surfaces studied

in this thesis, this resolution is somewhat lower due to assumptions made in the Monte Carlo simulations used.

Data analysis

To be able to gain quantitative data from this technique, the spectra must be modified. Compressing the angle resolved data from a specific region into a 1 dimensional line form will give you information about the structure of the region highlighted. If information about the bulk is required, then that region is compressed into a one dimensional spectrum. This may then be analysed by performing a Monte Carlo simulation which is carried out by the `VEGAS` program. This program simulates a specified amount of ions impacting a model structure, and then produces the theoretical angle resolved data. The process is then repeated, adjusting the model used until a match is made with the MEIS data gathered.

To undertake a compositional analysis, the energy resolved data is utilised. This provides information on what species, and how much of that species is present on the surface. For this method `SIMNRA` is used, which allows the user to create a model based on the composition of a surface. The program allows you to create different atomic layers of varying thickness, from which a one dimensional energy spectrum is produced. This is then compared to MEIS results, and the model changed until a good match is made. The relative intensities of each element are modified by the size of the elemental species being detected. The composition can then be calculated thus:

$$C_A = \frac{I_A/Z_a^2}{\sum_n I_n/Z_n^2} \tag{4.28}$$

Where I is the intensity of the measured MEIS signal (with A denoting the elemental species in question and n each elemental species present on the surface in turn) and Z is the atomic number of each elemental species.

Technical specifications

The ions used for this technique have an average penetration depth of 10 Å and as such this technique provides information of the surface and near surface regions. The equipment used for MEIS measurements demonstrated in this thesis was utilised at Daresbury CCLRC and is represented in figure 4.19. Data from this technique is gathered in a two-dimensional manner

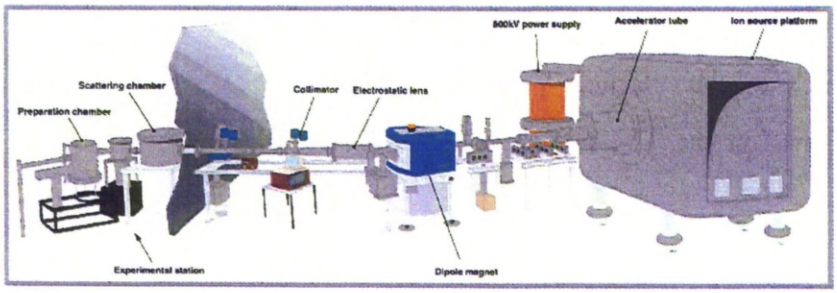

Figure 4.19: The MEIS system at Daresbury CCLRC

with an energy scale on the y-axis and an angular scale on the x-axis. A two-dimensional set is created by collecting data in stages (tiles) which are then joined together.

The experimental apparatus includes many interconnected UHV components which facilitate the *in situ* transfer and storage of samples being studied. There are several UHV chambers to accomplish this; a load lock, a storage chamber, a preparation chamber and a scattering chamber. The load lock is used to insert samples into UHV without the need to pump down auxiliary chambers which may eV housing sensitive equipment, while the storage chamber is self explanatory. The preparation chamber is used to prepare the samples surface, and includes sputtering and annealing facilities, LEED and Auger so that the surface may be characterised, and gas dosing for any experiments that may require it. The scattering chamber houses the ion analyser, sample goniometer and two dimensional (energy and angle) position sensitive detector. Data acquisition is handled by the `MIDAS` software package, which was originally created for the nuclear physics EUROGAM programme.

The ion beam is composed of either H^+ or He^+ ions, at an energy range of 50 to 400 keV. The beam has a divergence less than 0.1° and a spot size of 1 mm horizontal by 0.5 mm vertical, and results in a current at the sample of 0.1 to 1.0 μA, dependent on beam energy and species. This technique is destructive due to the nature of the incoming energy beam, and hence the sample must be moved regularly so that damaged areas of the surface are not being studied. The toroidal electrostatic analyser has an analysing (pass) energy of 0 - 400 keV and can move 140° in the horizontal plane. The chevron array anode detector with micro channel plates has an energy window of 2% and a resolving power of $dE/E = 2.4 \times 10^{-3}$. The angular window is 27° and has an angular resolution of 0.3°.

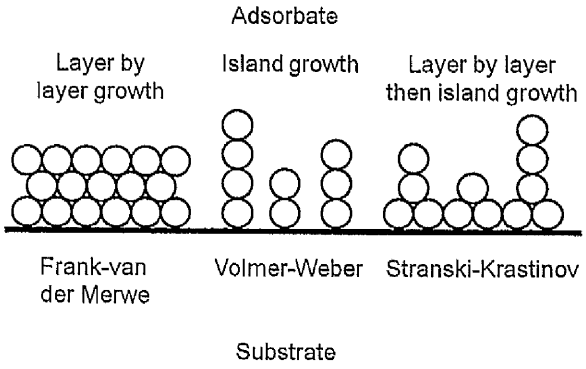

Figure 4.20: The three growth modes encountered during epitaxy.

Sample preparation

Preparation of a sample used for MEIS is the same for other techniques. However, a larger crystal will provide a larger amount of surface to collect data from, and hence a longer collection time during experimentation due to the need to continually move the beam and reduce physical damage to the surface. Due to this fact, the surface being studied must not be polycrystalline, as movement across a grain boundary will give different results due to a change in surface structure.

The crystal is mounted onto a unique sample holder. This sample holder contains a filament which is then used for direct heating in the *in situ* preparation of the surface. The crystal is secured onto the holder with Mo screws and plates.

4.3.6 Thin film growth and epitaxy

Thin film growth modes and epitaxy play an important role in many branches of industry, such as electronics, and are a main pathway to discovering novel small scale structures that can be exploited to create new nano-scale frameworks. Deposited overlayers are also used to modify the physical and electrical properties of the substrate for example, decreasing surface friction for mechanical applications.

Thin film growth can be categorised into 3 different growth modes, shown in figure 4.20. If the affinity of the adsorbate to the substrate is high, then two dimensional islands of atoms will begin to form, with additional atoms favouring sites around the already nucleated growth. This continues until a two dimensional layer is completed, after which a second layer will begin to form in the same fashion. This is commonly known as Frank van der Merwe growth mode.

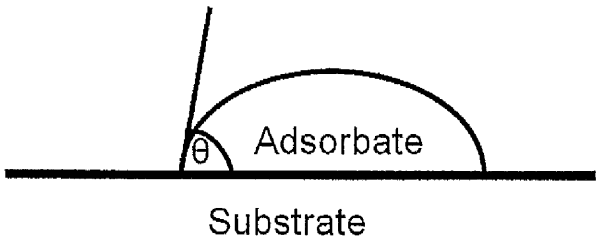

Figure 4.21: Representation of Youngs equation.

If the opposite is true, and the adsorbate and substrate interact weakly, then there will be no preferential adsorption sites, and three dimensional islands will form. Additional atoms will prefer to settle upon the growing adsorbate structure rather than the substrate itself. This is known as the Volmer-Weber growth mode. The final mode is known as Stranski-Krastanov growth, and usually occurs when there is a strong affinity between substrate and adsorbate, but there are lattice mismatches present between the film and substrate. This will cause significant strain on the overlayer. After the first few monolayers have been formed, the growth converts to island growth in an attempt to alleviate this strain.

The mode of growth encountered when depositing a material onto a surface depends heavily on the surface free energies of the adsorbate and the substrate (where the surface free energy is the increase in free energy caused by exposing a surface plane), and the tendency for thermodynamically stable films to attain the lowest surface free energy they can. The surface free energies or the substrate and adsorbate are related by Youngs equation:

$$cos\theta = \frac{\gamma_{sv} - \gamma_{sf}}{\gamma_{fv}} \tag{4.29}$$

Where γ denotes the surface energy between a substrate and film (sf), substrate and vapour (sv) and film and vapour (fv). θ denotes the angle the adsorbate droplet makes with the surface (figure 4.21).

Youngs equation can be used to express the conditions for different growth modes in terms of free energy. For layer by layer growth, where $\theta = 0$;

$$\gamma_{sv} \geq \gamma_{sf} + \gamma_{fv} \tag{4.30}$$

and for island growth where $\theta > 0$;

$$\gamma_{sv} < \gamma_{sf} + \gamma_{fv} \tag{4.31}$$

In general, adsorbates with a low surface energy will wet the substrates with high surface free energies resulting in layer by layer growth, while adsorbates with high surface free energies being deposited on substrates with low surface energies will result in island growth. While calculating the free energy of certain materials is difficult, it is often possible to predict what kind of growth mode will occur.

There are several other factors that can dictate the growth of a thin film upon a surface. The flux rate denotes how many adsorbate atoms are incident on the surface at any one time. A higher flux will cause a large amount of atoms to arrive per unit time, reducing the ability for an adsorbing atom to find a preferable adsorption site. A low flux will allow atoms to diffuse across the surface, if possible, in an attempt to settle in the most preferred adsorption site. Applying external thermal energy will also allow the adsorbate to diffuse, if the substrate - adsorbate interaction can be overcome by the increased thermal energy of the system.

Quasicrystal modulated epitaxy

The cases listed above demonstrate the most basic examples of epitaxial growth. These three growth modes can be heavily influenced by the stability of the interface between the substrate and adsorbate [121–123]. For the example of a system featuring a periodic substrate and periodic adsorbate, a stable interface will require the substrate and adsorbate to have a common unit cell, which can be determined if both materials have at least two common reciprocal lattice vectors, of which $\mathbf{G} \neq 0$, oriented in different directions. If both periodic crystals are incommensurate and hence unable to form an epitaxial interface, there is no possibility of them forming any type of epitaxial structure. A quasicrystal does not possess a unit cell and hence is incommensurate with any periodic system. However thin films with stable interfaces have been observed, and as such present an opportunity to study the physical principles governing the interactions between substrates and adsorbates.

For the consideration of a classically periodic material growing on top of a quasicrystal, the resulting thin film would contain a great deal of lattice mismatches, and hence would be unstable. To avoid this issue a quasicrystal and periodic material may be linked together with an interlayer. An interlayer exhibits a structure which is commensurate with both substrate and adsorbate.

For the majority of epitaxial studies conducted on *i*-Al-Pd-Mn, the deposited material forms

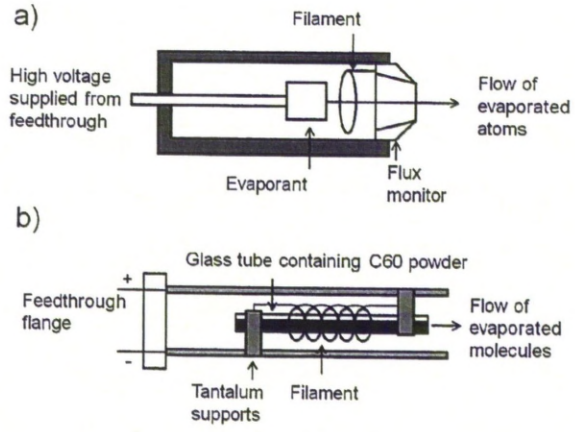

Figure 4.22: Schematical views of (a) A single cell evaporator, (b) A C_{60} evaporator.

a structure that is heavily modified by the presence of the quasicrystalline substrate. This includes, but is not limited to the monolayer growth followed by the growth of islands of Bi [44, 45], and the nucleation of 3D islands of Ag [102–104]. The behaviour of these deposited metals demonstrate that quasicrystalline materials present candidates as templates for growth of new types of materials.

One type of growth encountered is known as rotational epitaxy (which should be noted is not a behaviour exclusive to aperiodic systems). For this growth mode, islands of a crystalline structure normally encountered for the deposited material are aligned along high symmetry axes of the quasicrystalline material below. This has been observed in several systems, such as Bi [44, 45] and Cu [32, 33] on *i*-Al-Pd-Mn, and Pb on *i*-Ag-In-Yb (not yet published).

Growth of certain elements may also induce alloying on the substrate. Such an example is seen when depositing Bi on a Ag(111) crystal which induces the formation of a $BiAg_2$ alloy adopting a long range $\sqrt{3} \times \sqrt{3}$ structure [124]. Alloying is observed on a quasicrystal when depositing sub monolayer Au on the fivefold *i*-Al-Pd-Mn surface [125], where upon annealing a multiply twinned $AuAl_2$ crystalline layer formed. To induce this structure for a multilayer system, In was used as a surfactant.

Evaporators

To aid in surface characterisation and in the search for novel structures, thin film growth is an exploitable method that can be used in tandem with the above experimental techniques.

The process of adsorbing a single element upon a surface requires the use of an evaporator. Evaporator designs differ from producers and by method of evaporation. A typical design is utilised in the Omicron triple EFM evaporator. This triple cell evaporator is essentially 3 single cells combined into one piece of equipment, to allow more than one element to be used concurrently or for use in succession. This evaporator features a water cooled copper shroud, a retractable evaporant holder and a shutter to allow for precise evaporation times.

A single cell evaporator schematic is shown in figure 4.22 (a). It consists of a filament wound around a small chamber in which the evaporant is placed. The form of the evaporant depends on how it behaves in UHV upon heating; some materials sublimate, for example Fe or Sb, and so a rod of the material is acceptable. Some elements like Bi and Pb melt, so a rod form is not acceptable. Instead, elements that melt and then evaporate are contained in a Mo crucible. Heat is applied by the filament, and is enhanced by applying a potential of several hundred volts across the evaporant and filament. This induces the electrons emitted from the filament to strike the evaporant or crucible housing the evaporant and increase its temperature, causing it to sublimate, or melt and then evaporate. The now vapourised material is then directed out of an aperture and towards its intended target.

As well as depositing metals and semi metals, it is also possible to expose gases to the surface. This is done by connecting up a canister of the required pure gas, and then letting the gas directly into the chamber. The exposure can be measured by recording the pressure and the time at which that pressure is maintained, and then converted to Langmuir. 1 Langmuir is equivalent to 1 second at a pressure of 1×10^{-6} torr. However for this thesis the definition of 1 Langmuir is taken as 1×10^{-6} mbar instead, as the unit of pressure torr is not used.

It is also possible to deposit molecules. This is done in a similar way as a single element, although the evaporants can be slightly more unwieldy. C_{60} for example exists in a powdered form, and sublimates upon heating. It is therefore advantageous to create a custom built evaporator for molecular deposition. For example, a glass tube with an aperture at one end is filled with C_{60} and a filament wound around it. This filament is connected to the outside of the chamber via a feed through. This allows the filament to directly heat the C_{60} powder and enable it to evaporate. Such an evaporator is shown in figure 4.22 (b).

Chapter 5

Structure and chemical composition of the fivefold surface of the *i*-Ag-In-Yb quasicrystal

5.1 Introduction

The first binary quasicrystal, *i*-Cd-Yb, provides an excellent opportunity to study the physical and chemical properties of quasicrystals, by providing a system that does not suffer from chemical disorder. However this material cannot be studied in UHV. Instead, a daughter quasicrystal *i*-Ag-In-Yb is suitable for UHV conditions and possess the same structure as its progenitor.

This chapter details the first in depth surface characterisation study conducted on the fivefold *i*-Ag-In-Yb surface [91, 126–128]. The process of characterisation of this surface by means of study and comparison with the model structure of *i*-Cd-Yb will prove invaluable for further studies using this material, such as epitaxy, where information of the substrate will facilitate the characterisation of more complex structures.

To characterise the surface, STM has been employed to detect features on the surface at the atomic level. Comparisons of any discovered features with the *i*-Cd-Yb model will allow for the identification of the surfaces structure. This can be further tested by employing LEED to determine what surface symmetries are present on the surface, identify any long range order, and measure the materials k-vector for comparison with the bulk lattice constant. MEIS can

then be used to determine how a quasicrystal's surface structure relates to that of the model, by comparing experimental diffraction data with spectra generated by an ideal theoretical surface. Finally, XPS is used to study the composition of the surface.

During the experiments and analysis of characterising the fivefold surface, the valence band structure of the fivefold surface of *i*-Ag-In-Yb was investigated [83]. Although not included in this thesis, this study concluded that the near Fermi region is dominated by Yb $4f$ states, which is in agreement with calculations. It was also found that the valence band structure of *i*-Ag-In-Yb is very similar to that of *i*-Cd-Yb.

5.2 Samples

The growth of quasicrystals is a process that is being constantly improved upon. Such an improvement was accomplished part way through the commencement of this project and better quality crystals became available. An ingot of *i*-Ag-In-Yb which clearly displays facets of all three possible symmetries of an icosahedral geometry is shown in figure 5.1 (a). This sample shows the many different symmetries that exist in an icosahedron geometry; five, three and twofold symmetries. In terms of stability it is generally accepted that high symmetry surfaces that contain high atomic density planes will form the most stable surfaces. This is observed in the Al-Pd-Mn system [88,129] where the twofold and threefold surfaces are less stable. The two and threefold *i*-Ag-In-Yb surfaces are explored in a later chapter.

For this study two samples were used, both grown using the Bridgman method. At the beginning of this project, the growth of a single crystal of significant size had yet to be accomplished. This meant that available samples contained many grains and grain boundaries. The original crystal used for this study is shown in figure 5.1 (b) and is hereafter referred to as sample 1. Sample 1 was extracted from its Bridgman furnace at a rate of 0.2 mm/h and is the slower grown sample [130]. The crystal in figure 5.1 (c) was used for further STM studies, and is hereafter referred to as sample 2. This sample was extracted from its Bridgman furnace at a rate of 0.8 mm/h.

Both samples have several characteristics in common. They both take the form of a silvery metal that is hard and brittle, indicated by the edges of the sample having the tendency to break off. They then took a mirror finish after polishing treatment. Upon annealing, sample 1

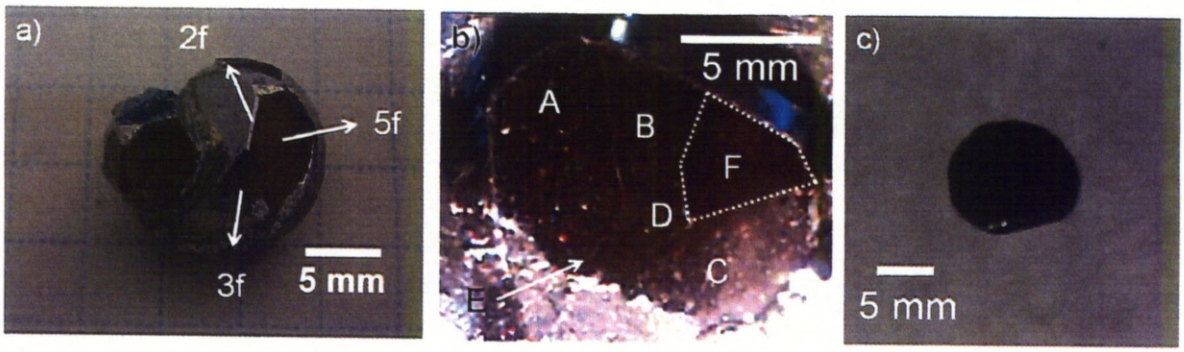

Figure 5.1: (a) A larger ingot showing planes related to the three high symmetry surfaces present in an icosahedron. (b) The original crystal used at the beginning of the studies presented in this thesis, known as sample 1. (c) The crystal used for the majority of studies presented in this thesis, known as sample 2.

(figure 5.1 (b)) would exhibit different domains formed at the surface. These domains presented differing structures, apart from domain F. The crystal had taken damage after this picture was taken and before studies began, and domain F was no longer present. The composition of these domains were determined using an electron probe microanalyser, and are given in table 5.1. Domains A - D all present a composition similar to the bulk crystal. However, each domain has a different structure [128].

Domain A is quasicrystalline and exhibits aperiodic STM and LEED results. Domain B was the same phase, although the fivefold plane is oriented differently with respect to the cut surface plane. This resulted in STM images featuring a large concentration of steps and narrow terraces, and a LEED pattern where the specular beam was off center in comparison to domain A. Both features indicate that domain B is vicinal. Due to the preparation conditions, the formation of this vicinal surface was most likely to have originated during the crystals growth or post annealing treatments. Domains C and D were structurally poor and gave weak LEED patterns. Local structures were detected by STM. These structures were periodic, and are explored in more detail in a later section.

The grain boundaries have different compositions and structures to the larger domains. The boundaries contained greater amounts of Yb, but it was not possible to explore their structure using surface sensitive techniques due to the small surface area they present.

During the initial study, the opportunity to study a new *i*-Ag-In-Yb crystal became available

Table 5.1: The composition of the domains featured on the crystal shown in figure 5.1 (b). Compositions given in percentage of total contribution as determined by an electron probe micro-analyser.

Domain	Ag	In	Yb	Resulting structure
A	42.2	42.9	14.9	QC
B	41.7	43.1	15.2	QC, Vicinal
C	41.7	43.3	14.9	Periodic
D	41.7	43.4	14.8	Periodic
E	40.0	38.2	21.8	Domain Boundary

[131]. Sample 2 took the appearance of the first sample, but annealing did not expose multiple grains. It produces good quality LEED and STM results from all areas of the sample. Several other samples were cut from the same ingot and sent to other laboratories. All samples exhibited good structural quality. Previous STM and LEED results were verified on the new sample and shown to be identical to those seen before, albeit easier to obtain due to having more area to experiment upon, and, in the case of LEED, giving clearer patterns. The longevity of the crystals during experimental sessions was also improved; after a certain amount of hours being annealed, a sample surface would begin to degrade. A similar behaviour has been recorded in *i*-Al-Pd-Mn [132] where upon long periods of heat treatment, bulk vacancies migrate to the surface. This phenomena could also be occurring for *i*-Ag-In-Yb during anneal treatments. When a sample degraded sufficiently, it would need to be repolished. Two and threefold samples were cut from the same ingot, producing samples of the same size as the fivefold. These samples also exhibit a single domain and good structural quality, and are explored in a later chapter.

5.3 Experimental Details

The crystals used in this study were grown using the Bridgman technique [52,130,131] at IMRAM in Tohoku University, Sendai, Japan, and provided to us for surface study. Pure elements of Ag (99.99 wt%), In (99.99 wt%) and Yb (99.9 wt%) were placed in an alumina crucible with a sharp end, and sealed under an Ar atmosphere. This was then placed in a Bridgman furnace and heated to 1073K. After 2 days of heating the crucible was extracted from the furnace.

Sample 1 was extracted from its Bridgman furnace at a rate of 0.2 mm/h [130], while sample 2 was extracted at a rate of 0.8 mm/h [131]. This produced a crystal with multiple grains in the case of sample 1, and a single grain crystal in the case of sample 2. These samples have a bulk composition of $Ag_{42}In_{42}Yb_{16}$. The ingot was then cut perpendicular to the fivefold axis as determined by Laue backscattering [130, 131].

The cut samples were then mechanically polished using a turn-table and a rough polishing pad to remove the residue left behind by the cutting process. When this residue was removed and a shiny surface obtained, the sample underwent manual polishing using a variety of diamond pastes containing granules of size 6 μm, 1 μm and 0.25 μm. Polishing was conducted by smearing diamond paste onto a polishing pad and then moving the crystal through a figure of eight motion, periodically changing the orientation of the crystal. This ensures that no direction is preferentially polished. Excess paste is removed using methanol before the next phase of polishing is undergone, and a non-abrasive tissue paper is used to remove excess methanol.

After polishing the crystal is mounted upon a suitable plate, and then submerged in methanol and subjected to 30 minutes in a sonic bath. This is to ensure any embedded diamond molecules are dislodged and dissolved in the solvent. After this process the sample is not exposed to air until it is ready for insertion into UHV. This preparation technique was carried out prior to all work presented in this chapter, regardless of the subsequent experimental techniques.

Atomically flat terraces were obtained through cycles of 2.5 KeV Ar^+ sputtering (30 - 60 minutes) at room temperature followed by annealing at 715 K (2 - 4 hrs) at a pressure of 1.4×10^{-10} mbar. Temperatures were monitored using an infra-red pyrometer set at an emissivity of 0.35. An emissivity of 0.35 is selected as an arbitrary value, and is also the value used when measuring the temperature of *i*-Al-Pd-Mn. The emissivity has not been calculated for the *i*-Ag-In-Yb sample, however using this value produces good agreement in temperature measurements of both the pyrometer and a thermocouple. The samples were then left to cool for 15 minutes after annealing.

STM experiments in Liverpool were performed in Ultra High Vacuum (UHV) using an Omicron variable temperature STM operating at room temperature. Experiments previous to the work carried out for this thesis were performed in Tsukuba, Japan, with a Unisoku low temperature STM operating at 78 K. The stated bias refers to to the potential applied to the sample relative to the tip. The bias relates to the direction of the tunneling electrons.

MEIS experiments were conducted at Daresbury CCLRC, by delivering 100 KeV He^+ ions to the surface at an angle incident 31.8°. The intensity was then recorded by a 2D array that was rotated around the crystal. The damage to the sample at an ion flux used in previous experiments with quasicrystals [34, 133] was significant, and as such $\frac{1}{8}$th of the flux (resulting in a flux of 0.25 C/mm) of that which was used for a study into Au on *i*-Al-Pd-Mn [134] was used on the *i*-Ag-In-Yb samples.

LEED experiments were performed using an Omicron Specta LEED optic and source. The electrons are supplied from a LaB_6 filament and were measured by viewing a spherical phosphorescent screen. For the comparative study, LEED patterns were taken from a Cu(111) crystal. LEED was performed in a different chamber then the STM studies.

Surface composition of the *i*-Ag-In-Yb crystal was monitored by XPS with unmonochromatised AlK_α radiation ($h\nu = 1486.6$ eV) using a PSP Vacuum Technology hemispherical electron-energy analyser. For studies of the pure elements, 99.9% pure In and Yb foils and a Ag(111) single crystal were used to calibrate the core levels detected form the quasicrystal. Each sample was cleaned by Ar^+ sputtering with XPS used to monitor their cleanness. The Yb foil was difficult to prepare, with a trace amount of oxygen detectable by XPS after many cycles of sputtering. These reference samples were used to calibrate the XPS core-level binding energies. XPS was carried out in a chamber separate from those used to record STM and LEED results.

5.4 Results

5.4.1 STM

Step Heights

Sputter and annealing yields a stepped and terraced surface, with terrace widths ranging from sub-100 nm to 500 nm widths, with an example shown in figure 5.2 (a) and (b). The terraces are atomically flat. The heights of over 400 steps were measured from STM images. There are two methods of determining the height of a step. The first method involves selecting a significant portion of two adjacent terraces bordering a step. A histogram plotting the height of each pixel of the image is then created, shown in figure 5.2 (e), from which distinct height values can be determined. The difference in these two heights will equal the step height between the two terraces originally selected. The second method is conducted by creating a line profile across

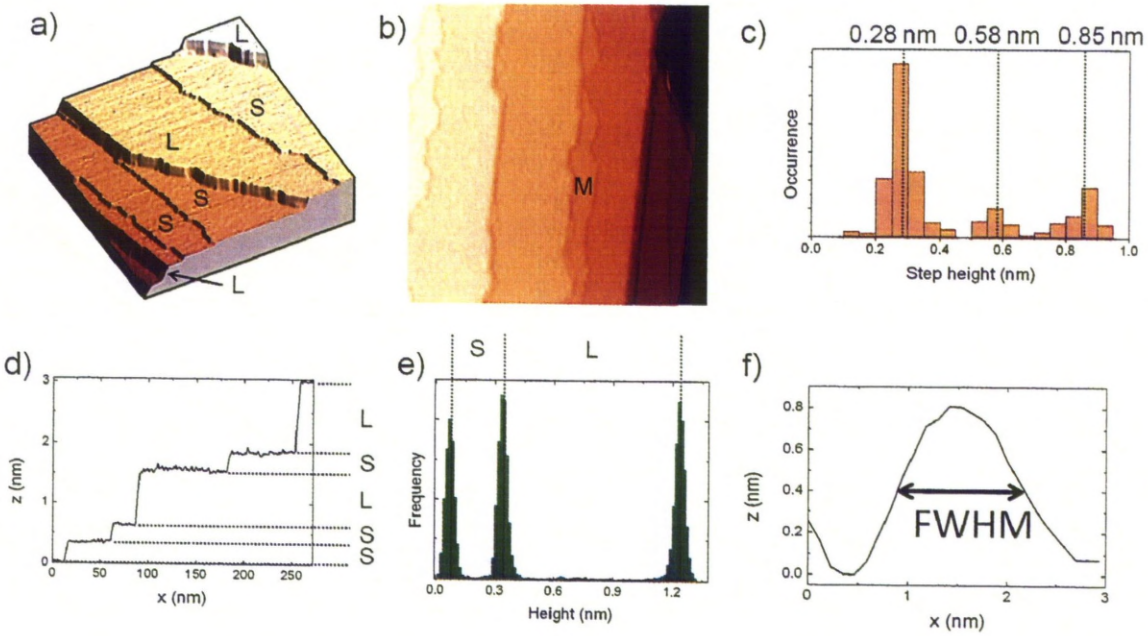

Figure 5.2: (a) Large scale STM image enhanced to distinguish step edges. (250 nm × 250 nm) of the fivefold *i*-Ag-In-Ybsurface represented in 3D to detail the step-terrace structure. (b) Example of a thin terrace resulting from a M step height (150 nm × 150 nm). (c) Histogram of step height values with a bin width of 0.05 nm, with the S, M and L step heights indicated. (d) An example of a line profile extracted from an STM image taken from (a), with different step heights highlighted. (e) An area-height histogram with two different steps shown. (e) A line profile measuring the FWHM of a protrusion.

a step, shown in figure 5.2 (c), and measuring the difference in the z axis between two adjoining terraces. While the first method is more accurate, the second method is quicker. However, the results of both methods are in agreement.

A distribution of step heights is presented in figure 5.2 (d). There are 3 major occurring step heights; a small step $S = (0.28 \pm 0.04)$ nm, a medium step height $M = (0.58 \pm 0.03)$ nm, and a larger step height $L = (0.85 \pm 0.05)$ nm. The step heights are not τ scaled such that $\frac{M}{S} \neq \frac{L}{M} \neq \tau$. Larger step heights also occur, but it is possible to assign these heights as combinations of the former 3 heights. 'Step bunching' has been observed in other species of quasicrystals, such as Al-Pd-Mn [85], Al-Cu-Ru [49] and Al-Cu-Fe [17, 135]. Step bunching occurs in greater frequency with higher anneal temperatures. However the anneal temperature used for i-Ag-In-Yb is already close to the melting point of the bulk, and as such it is not possible to extensively study the effects of step bunching on this material.

The relative occurrence of the S, M and L step heights is 66%, 12% and 22% respectively at the nominal surface preparations specified above. The low occurrence of M step heights, highlighted in figure 5.2 (b), as well as the tendency for terraces arising from this height being very narrow. For example in 5.2 (b) the M step terrace only contributes to 5.91% of the image, while the above terrace which borders an L step occupies 29.34% of the image. This suggests that the surface termination arising from the M step is less preferred.

High resolution STM images

Images taken by STM indicate that observations of surface depend on the applied bias voltage, V_b. Figure 5.3 (a) - (d) shows images taken on the same terrace but at differing bias voltages. Images taken at $V_B < 0$ are characterised by large protrusions which are locally arranged into pentagons (highlighted in figure 5.3 (a)). These pentagons have an edge length of 2.40 ± 0.15 nm and two different orientations rotated at 36° from each other. The diameter of the protrusions is estimated at 1.30 ± 0.04 nm by measuring the full width at half maxima of their height profiles, of which one is shown in figure 5.2 (f). At $V_B > 0$ the protrusions do not appear as shown in figure 5.3 (b). Instead, rings are observed at the vertices of the previously described pentagons. The diameter of these rings is 1.80 ± 0.05 nm.

It is found that the protrusions from negative bias images are composed of Ag and In, while the rings from positive bias images are composed of Yb. This is explained in more detail below.

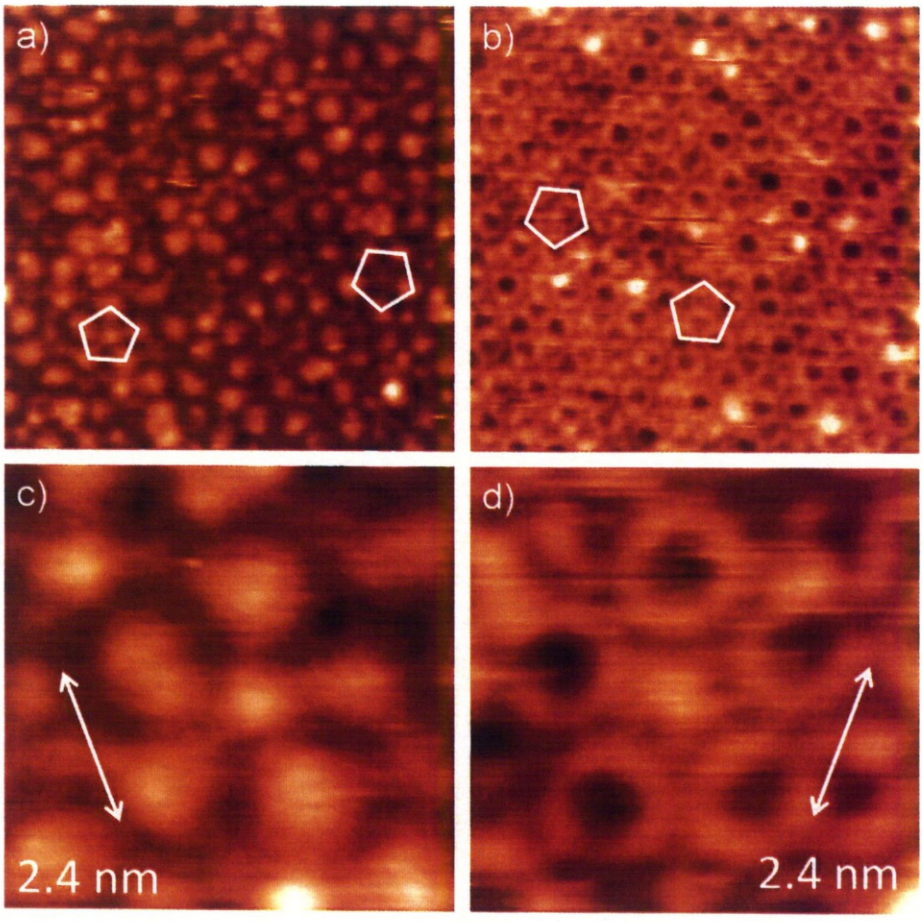

Figure 5.3: (a) Negative bias STM image of a terrace (-0.81V, 30 nm × 30 nm). (b) Positive bias STM image of a different terrace (-2.6V, 30 nm × 30 nm). (c) and (d) Close up images of the pentagonal arrangements taken from (a) and (b) respectively.

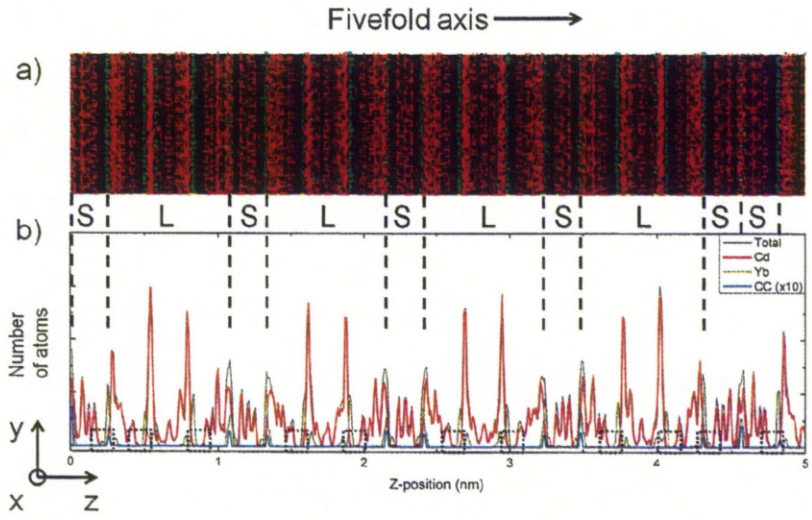

Figure 5.4: (a) The atomic structure of i-Cd-Yb projected normal to the fivefold axis. (b) Variation in the atomic density per 0.01 nm layer perpendicular to the fivefold axis. Red indicates Cd, green indicates Yb, blue indicates cluster centers (for which (b) has this amount increased by a factor of 10) and the grey line represents the overall atomic density. Broken black boxes indicate significant gaps in the atomic density distribution.

Comparison with the i-Cd-Yb model

Comparing STM results to the theoretical model enables the identification of bulk terminations and surface planes. For this purpose the i-Cd-Yb model is used due to both materials being isostructural. This model is created from the placements of RTH clusters as described by Takakura *et al.* [48] and has been displayed as a distribution of atomic planes perpendicular to the fivefold axis. The variation of atomic density along the fivefold axis is shown in figure 5.4 calculated from a 10 nm $\times$ 10 nm $\times$ 5 nm section of the i-Cd-Yb model. The gaps between high density regions of atoms is consistent with the electron density analysis of the same system reported by de Boissieu *et al.* [136].

Experimental evidence indicates that the surface observed by STM is formed at high density regions which intersect cluster centers. Obeying this rule, there are three separation distances between the high density layers encountered in the model, 0.25 nm (S), 0.57 nm (M) and 0.82 nm (L). The step heights are not τ scaled. These three distances are similar to the S, M and

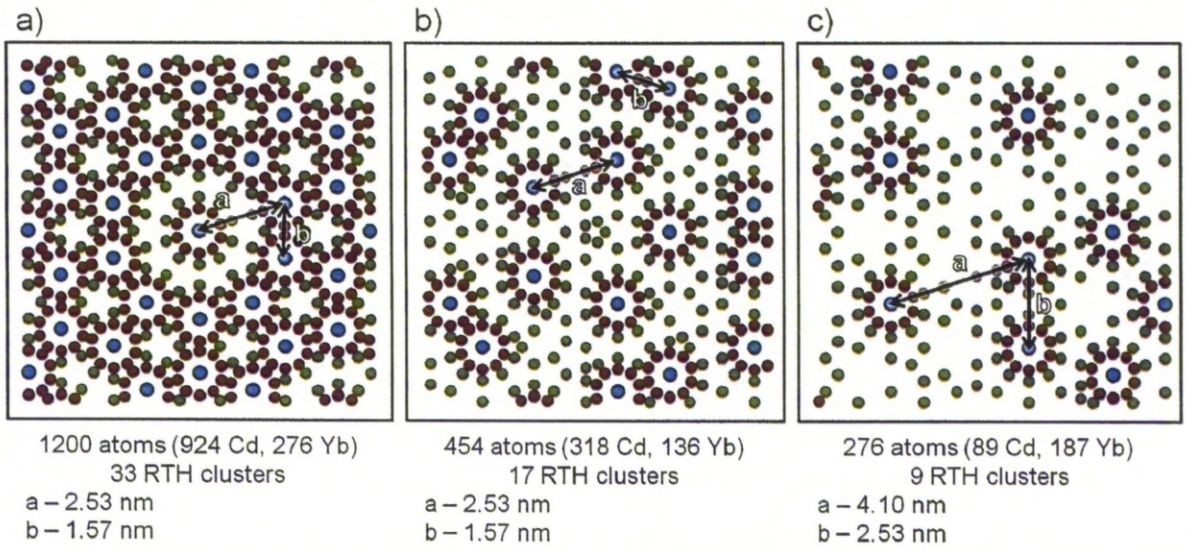

Figure 5.5: The 3 common atomic planes that intersect the RTH cluster centers perpendicular to the fivefold axis. (10 nm × 10 nm)

L steps observed by STM. The occurrence of S, M and L steps in a 10 nm section projected normal to the fivefold direction of the i-Cd-Yb model (of which 20 steps are present) is 55%, 5% and 40% respectively, which is again similar to the occurrences of these steps as observed by STM.

A sequence in cluster separations of $LSLSS$ is observed within the z distribution of atoms which matches the previously seen sequence observed by STM (figure 5.2 (a) and (d)). If a surface were to form at every high density plane and not just the corresponding planes that contain cluster centers (which can be seen in figure 5.4) the only step size that would be produced is the S step. This would not agree with the occurrence of the L step as seen by STM. This indicates that the surface selection rules for this material are not determined by atomic density alone [88].

There are also significant gaps occurring alongside each high atomic density plane, indicated in figure 5.4 (b) by broken black boxes. As these gaps accompany atomic planes that are not a preferential choice for a surface, it can be concluded that this factor does not influence the selection of a bulk termination either.

By specifying the condition that a surface termination must lie upon a plane of atoms that intersect the RTH cluster centers, and by considering the atomic density, it is possible to categorise each surface plane into one of three uniqu groups. A dense plane contains 20 - 40

cluster centers per 10 nm × 10 nm, a moderately dense plane contains 10 - 20 cluster centers per 10 nm × 10 nm, and a low density plan contains less than 10 cluster centers per 10 nm × 10 nm. These three planes all exhibit similar features of concentric Cd and Yb rings. The size of a cluster can be considered to be bound by the radius of its largest atomic shell, the Triacontahedron. The radius of this shell is 0.78 nm along its two fold direction, which is parallel to the fivefold surface. This gives a cluster an area of 1.91 nm^2, and hence gives a cluster density from (a), (b) and (c) of 0.63, 0.32 and 0.17 clusters per nm^2 respectively.

Each atomic plane is related to each other by the process of inflation and deflation by a factor of τ. The densest plane is a deflation of the moderately dense atomic plane, while the moderately dense atomic plane is a deflation of the least dense plane.

Figure 5.5 (a) shows the densest plane selected. This plane exhibits two cluster separations of 2.53 nm and 1.57 nm. Both of these cluster separations are observed in experimental results. Figure 5.5 (b) shows the second densest plane. This plane also exhibits the smaller cluster separation but its occurrence is rare. Figure 5.5 (c) shows the sparsest layer. This layer exhibits a larger cluster separation of 4.10 nm which is also observed directly from experimental results. The cluster separations are related by τ, in that $\frac{2.53}{1.57} \approx \frac{4.10}{2.53} \approx \tau$.

As studies progressed, it became possible to obtain atomic resolution of these rings, which was accomplished by Sharma *et al.*in Ecole des Mines in Nancy, France. During the course of these studies, initial STM experiments allowed us to resolve the ring like structures previously presented. This increment of resolution has enabled both dense and moderately dense terraces to be identified. Figure 5.6 demonstrates some of the smaller cluster separations. These occur when clusters take the shape of a rhomb and a smaller scale pentagon. Such features are highlighted by white shapes. For comparison, a pentagon of edge length $\sim$ 2.53 nm is highlighted in black.

If the densest plane intersecting cluster centers was chosen as a surface plane, the step sizes produced by this new selection would not match those observed by STM. These step sizes would now be combinations of the S, M and L steps. Step bunching with a frequency to allow this selection of atomic planes to be considered for surface terminations has not been observed on this surface. This detail, as well as the comparison of STM from Nancy with the model indicates that both high density and moderate density planes can occur as a stable surface.

The atomic density of each potential surface is shown in figure 5.7. The denser atomic planes (corresponding to figure 5.5 (a)) contain more Cd than Yb, while the moderately dense

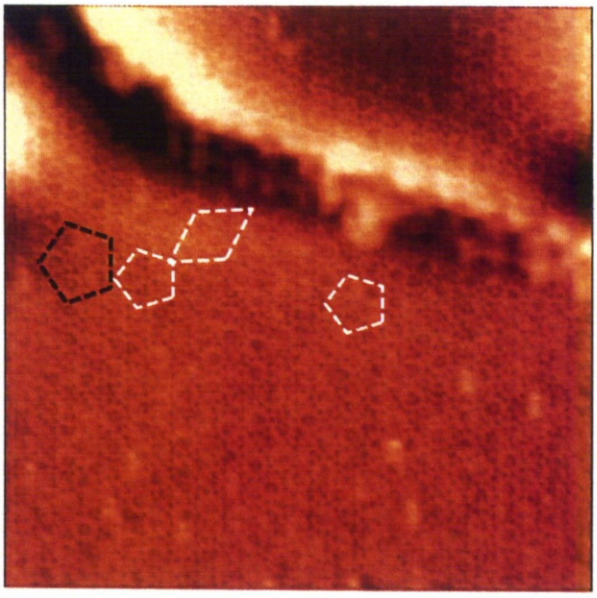

Figure 5.6: High resolution positive bias image of the clean fivefold surface of *i*-Ag-In-Yb. This image details cluster formations that feature separations of 2.53 nm (black shapes) and 1.57 nm (white shapes). Courtesy of Dr V. Fourne of Ecole des Mines, Nancy.

atomic planes are characterised by containing more Yb than Cd (refer to figure 5.7 (b)). The distribution of the atomic planes in reference to their density does not dictate the sequence of step heights. An M step accompanies a lower density plane. However, due to the limitations of the model and the lack of examples of M steps and low density planes, it cannot be conclusively proven that these low density planes are always accompanied by an M step.

Further evidence for these atomic planes being selected for surface terminations can be obtained by comparing the positions of protrusions and rings with the positions of features from the *i*-Cd-Yb model. A pentagonal tiling of edge length 2.53 nm can be superimposed on atomic planes that intersect the center of the RTH clusters, taken from the *i*-Cd-Yb model structure, and is shown in figure 5.8 (a). This atomic plane features Yb atoms from the 3rd shell of the RTH cluster, and Ag/In atoms from the 4th shell of the RTH cluster. 80% of the 4th shell is populated by In [137]. However, this calculation has been conducted for the 1/1 Approximant, but it is assumed that the RTH clusters from the quasicrystal and its approximants are similar in composition [48]. Each vertex of this tiling coincides with the position of a cluster center. A similar pentagonal tiling can be superimposed onto the STM images with the same criteria for

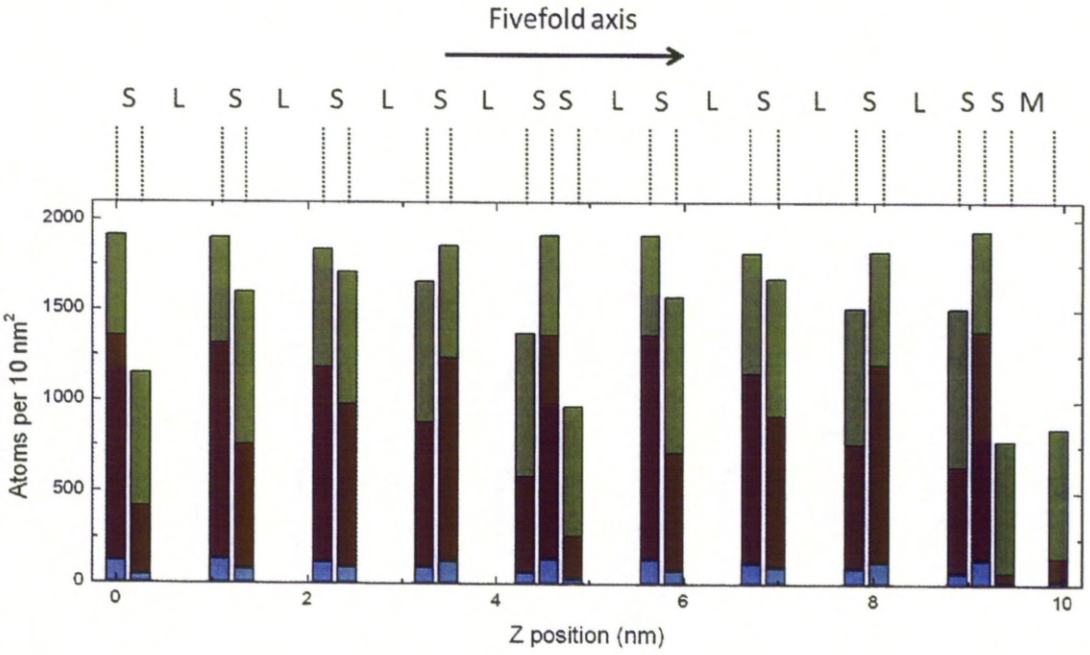

Figure 5.7: The atomic density of viable surface terminations along the direction normal to the fivefold axis using a step size of 0.01 nm. Blue indicates the amount of cluster centers, red indicates the amount of Cd and green indicates the amount of Yb.

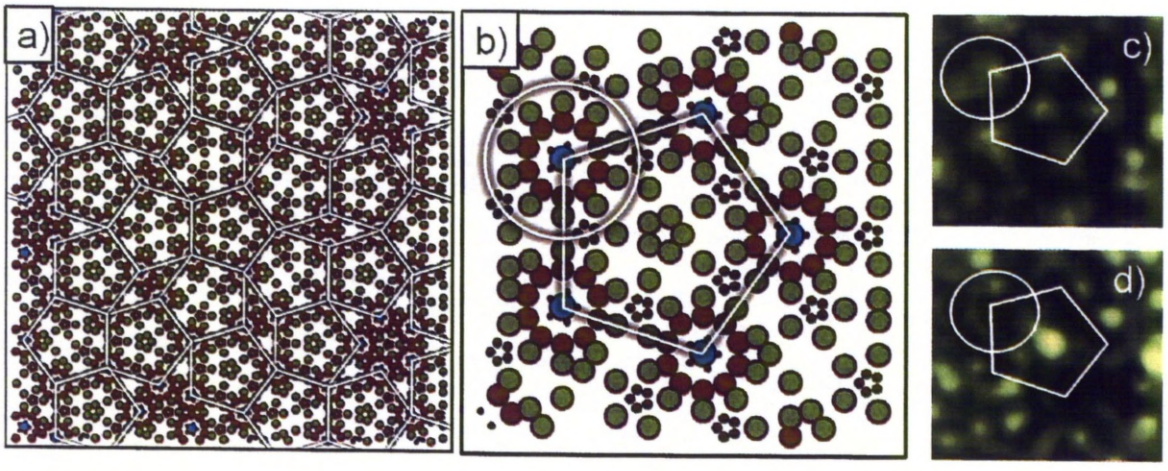

Figure 5.8: (a) The projected structure of the atomic planes that intersect the cluster centers (20 nm × 20 nm). (b) A close up of a pentagonal arrangement of clusters from the same atomic plane highlighting the pentagonal motif of the superimposed tiling and the position of the atomic cluster (7 nm × 7 nm). STM images at (c) a negative bias and (d) a positive bias, highlighting the pentagonal formation of protrusions and rings, as well as their position in relation to the tiling.

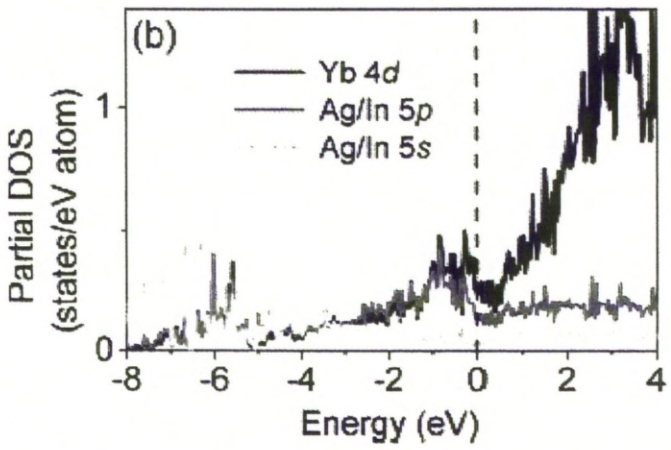

Figure 5.9: Partial DOS's about the Fermi level for the 1/1 approximant of *i*-Ag-In-Yb [83]. Partial density of states for Yb 4*d* (black), Ag/ In 5*p* (grey), and Ag/In 5*s* (light grey).

the positions of the vertices.

Comparing the sizes of the protrusion from negative biased images (figure 5.8 (c)) and the ring from positive biased images figure 5.8 (d)) from the model allow us to identify what the features are. These features are highlighted from the model shown in figure 5.8 (b). The first ring around the cluster center, a red ring composed of Cd (or Ag/In for the ternary alloy) corresponds to the cross section of an icosidodecahedron (the fourth shell of the RTH cluster) which has a diameter of 1.30 nm. This matches the diameter of the protrusions observed at negative bias, and indicates a bias of $V_B < 0$ enhances the Ag and In sites. The second ring from the center of the RTH cluster has a diameter of 1.94 nm and belongs to different RTH clusters or the linkages between these units. This diameter is similar to that of the observed ring at a positive bias $V_B > 0$ and indicates that a tunneling current at $V_B > 0$ enhances at the Yb sites. The choice of this atomic plane as a surface would indicate that the surface of *i*-Ag-In-Yb is rich in In and Yb.

From calculations performed for the 1/1 approximant of *i*-Ag-In-Yb [83] it is shown that unoccupied states just above the Fermi level are dominated by Yb 4*d* levels. This is also seen for the ternary alloy and is shown in figure 5.9 which displays the partial DOS's around the fermi level. While the states above the Fermi level are dominated by Yb 4*d*, the states just below the Fermi level are combinations the Yb4*d* and Ag/In 5*p* states. Levels around -6 eV are

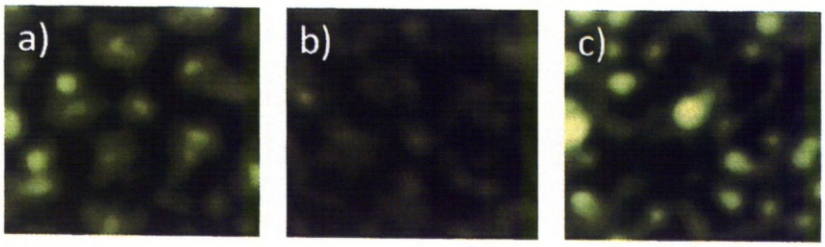

Figure 5.10: Pentagonal feature of the clean surface of *i*-Ag-In-Yb at varying bias'. Images (a, b, c) taken at -1.0V, +0.1V and +1.2V respectively.

a combination of all three elements, Ag/In $5s$, Ag/In $5p$ and Yb $4d$ levels, although for STM measurements this is not a consideration as STM measurements primarily focus on potentials between ± 2 V. The states just below the Fermi level are a combination of Ag/In $5p$ and Yb $4d$ levels with negligible contributions from the Ag and In $3s$ levels. This represents the presence $p-d$ hybridisation for this material. The occurrence of Ag, In and Yb states at various energies about the Fermi level explains protrusions of Ag and In are visible at a negative bias, while rings of Yb atoms are visible at a positive bias. The coupling of Ag and In states also explains the difficulty in obtaining atomic resolution of the clusters.

Figure 5.10 shows in greater detail the changes that occur as the bias is changed from negative to positive. These images feature the pentagonal motif described above. As the bias is changed, it is possible to resolve the inside of the protrusions. This is a rare occurrence and is not observed often. At a +0.1V bias atoms can be resolved in a protrusion. The exact distribution of Ag and In atoms in the central ring is currently unknown. Specific arrangements of these different elemental species could cause the local density of states (LDOS) being concentrated about an atom, which in turn would allow that specific atom to be imaged clearly by STM. For example, the inclusion of a pentagon of Ag within the Ag/In ring could cause such a feature to be resolved by STM given appropriate tunneling conditions.

Step and terrace morphology

There are also features that occur in the STM images, that are directly comparable to the model, that exist on step edges. At the edge of 0.28 nm high steps it is possible to observe protruding clusters from STM images taken at a negative bias. These protruding clusters can yield a Fibonacci sequence of A and B segments, extending for several tens of nanometers. This

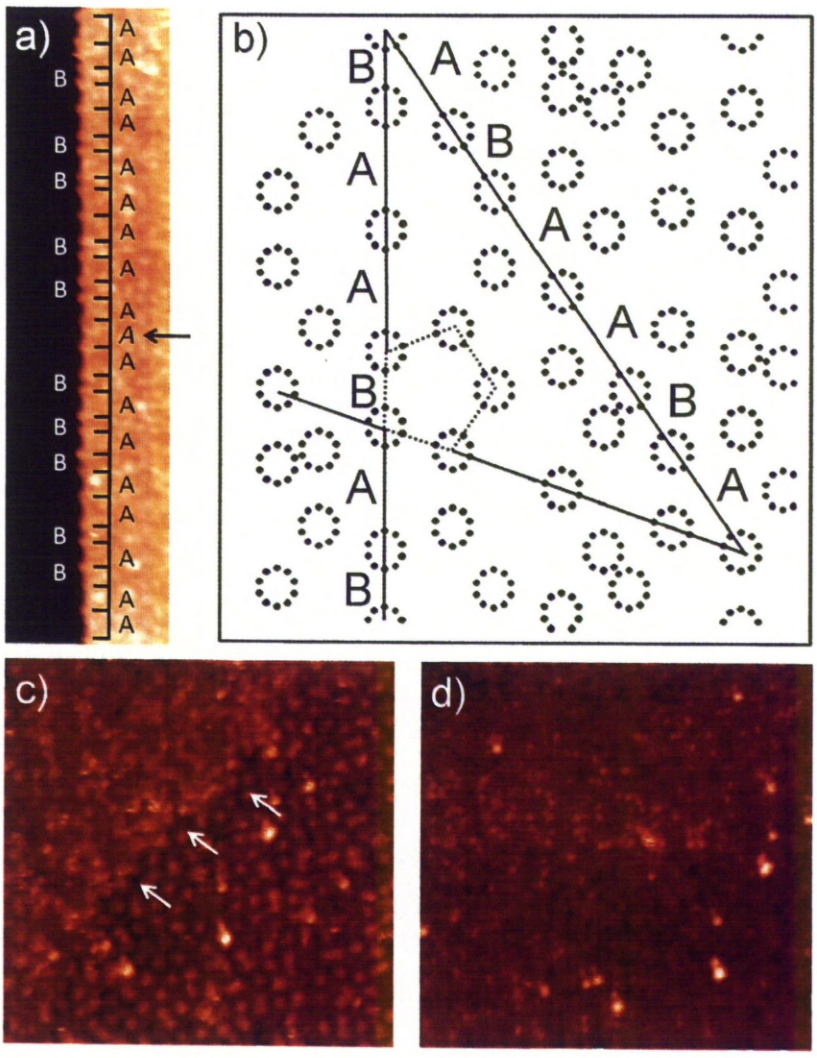

Figure 5.11: (a) A step edge exhibiting protrusions in the form of the Fibonacci sequence. (b) A small section of the *i*-Cd-Yb model, displaying only the Cd atoms present on the surface. (c) A negative bias image and (d) a positive bias image of the same area of the clean surface. (50 nm × 50 nm)

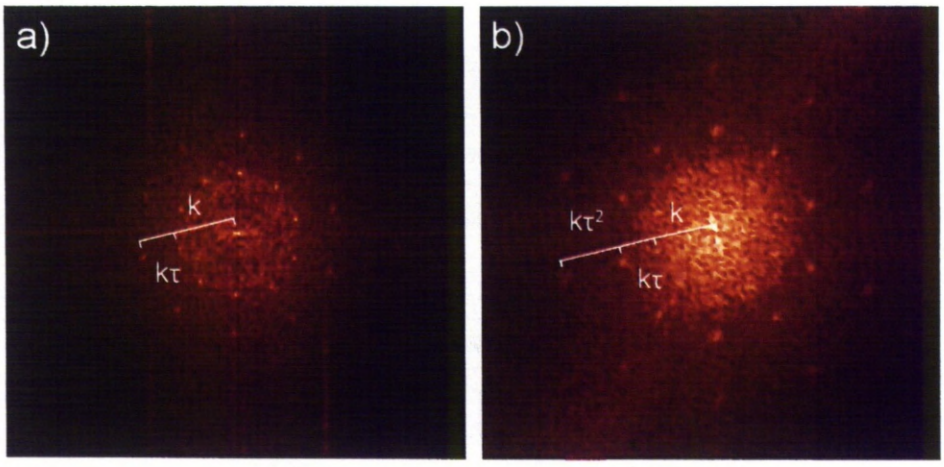

Figure 5.12: (a) Fast Fourier Transform of a negative biased STM image from the fivefold surface of *i*-Ag-In-Yb.(b) Fast Fourier Transform of a positive bias STM image of the same surface.

is shown in figure 5.11 (a), with a triple A defect highlighted. These A and B segments measure 4.24 ± 0.27 nm and 2.53 ± 0.22 nm respectively. These two lengths are τ-related, so that $A = \tau B$. A segments occur more often than B segments, with the ratio of occurrences also being related by τ. The Fibonacci sequence can be explained if the step-edge is parallel to the edge of the pentagon features observed in the model, which corresponds to high symmetry directions as shown in figure 5.11 (b). No individual atoms are imaged at the step edges, and it has not been possible to resolve ring like features at a step edge by probing with a positive bias.

These sequences are only observed on steps of the smallest height. This may be due to the larger step height being the combination of a many atomic planes, with such a high density of atoms being present at various heights obstructing any cluster resolution from being obtainable.

Negative bias images may also exhibit a change in morphology as highlighted in figure 5.11 (c). Areas differing in morphology can occur on the same terrace. The tunneling current of this different morphology is greater and manifests itself as a brighter area on the STM image. However a positive bias image of the same area does not display this change in morphology, as shown in figure 5.11 (d). This indicates that this differing morphology is an electronic effect.

Surface ordering

Fourier transforms of the negative and positive bias' images show ten fold patterns with

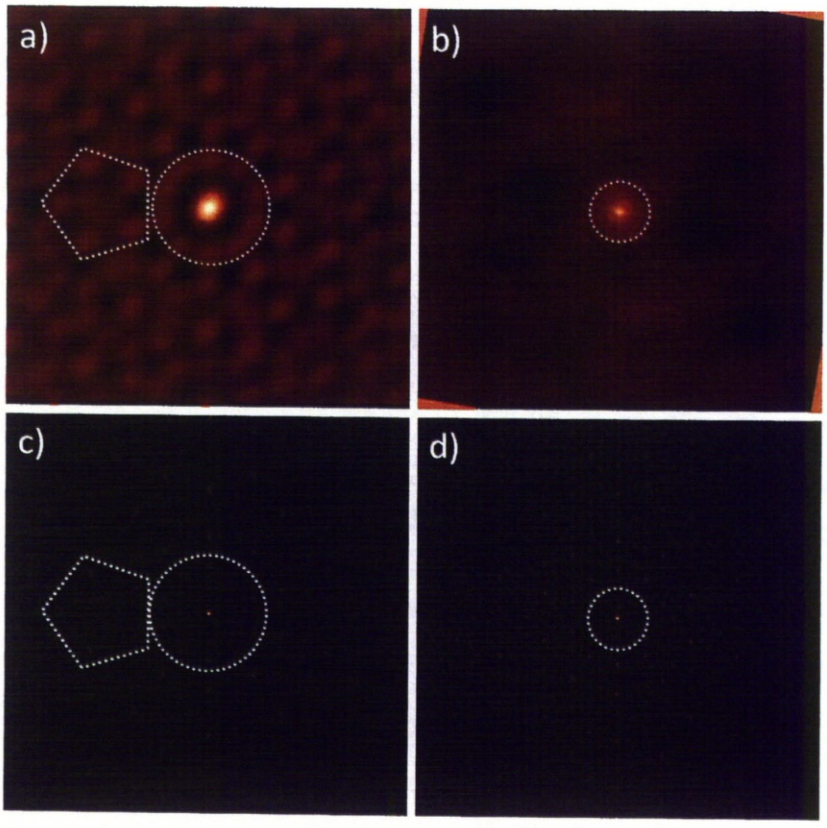

Figure 5.13: (a, b) are auto correlation patterns taken from negative and positive bias STM images respectively. These are accompanied by autocorrelation patterns taken from (c) the positions of clusters and (d) the positions of Yb atoms from the i-Cd-Yb model (20 nm $\times$ 20 nm).

maxima located at τ scaled distances which confirm quasiperiodic order, and are shown in figure 5.12 (a) and (b). The negative bias FFT is scaled down by a factor of τ from the positive bias FFT.

By observing autocorrelations taken from negative and positive biased STM images it is possible to test long range order by displaying the distances between recurring features that occur in the positive and negative biased STM images. Figure 5.13 (a) and (b) demonstrate autocorrelation pattern taken from negative and positive biased STM images, respectively. The autocorrelation patterns from the negative image displays many rings of maxima with radii 2.3 nm, 3.8 nm, 6.1 nm and so on. These are related by 1, τ and τ^2 respectively, and confirm aperiodic order. The first maximum corresponds to the protrusion separations observed by

STM.

The autocorrelation of a positive-bias STM image consists of smaller and more frequent rings of maxima. The first maximum occurs at a radius of 0.6 nm which corresponds to the atomic separation of Yb atoms, 0.6 nm. The radius of the second maxima at 1.1 nm originates from the next nearest neighbour separation of the Yb atoms, and is τ-related to the first maximum. The third maximum of 1.9 nm corresponds to the diameter of the Yb rings.

An autocorrelation pattern from a dense atomic plane from the model structure (shown previously in figure 5.5 (a)) is then compared to the experimental results. The densest plane is chosen as opposed to the other two atomic planes as these are merely inflations of the densest plane which contains more information. Figure 5.13 (c) and (d) are autocorrelation patterns taken from the i-Cd-Yb model. Figure 5.13 (c) has been determined using the positions of the cluster centers which are associated with the positions of the protrusions. These have been modeled as a point source as opposed to larger objects that match the size of these protrusions, so that a clearer, sharper autocorrelation pattern is produced. The pattern produced agrees with that of the negative biased STM image shown in figure 5.13 (a), apart from one feature. The first maximum on the theoretical autocorrelation pattern occurs at 1.4 nm which is smaller than the first maximum from the STM autocorrelation pattern by a factor of τ. This is due to the omission of a small cluster separation occurring in the STM image, due to a lack of resolution

To compare the model structure to the positive biased autocorrelation, the Yb atom placements have been used. This produces a complex pattern similar to that of the experimental autocorrelation pattern, and as with the cluster centre position autocorrelation pattern, matches up well to the experimental data with maxima at similar positions. The positive bias autocorrelation patterns are a factor of τ^2 smaller than the negative bias autocorrelation patterns. This is consistent with the autocorrelation patterns from the model, and also consistent with fast Fourier transform (FFT) patterns obtained from the respective STM images (see figure 5.12 (a) and (b)).

Impurity phases

It was mentioned previously that sample 1 is not a single grain quasicrystal, and contains two periodic domains. These domains offer many examples of periodic features, of which two examples are shown in figure 5.14 (a) and (d). Auto correlations and FFT's are used to determine

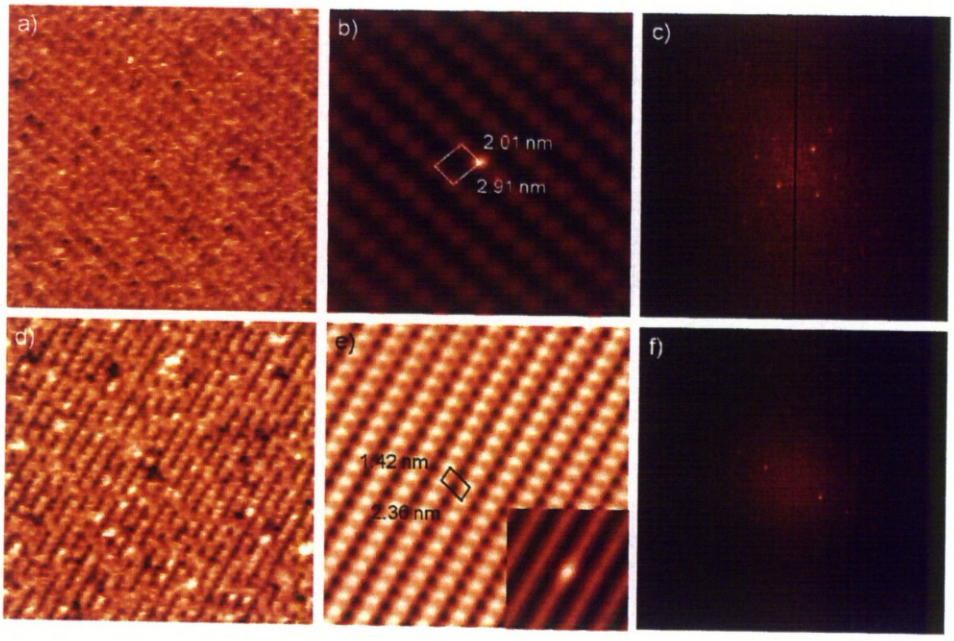

Figure 5.14: (a) and (d) Negative bias STM images of areas of periodic domains of the clean fivefold *i*-Ag-In-Yb quasicrystal. (50 nm × 50 nm) (b) Autocorrelation of (a) with the unit cell highlighted. (25 nm × 25 nm) (e) Fourier pass filter of (d) with the unit cell highlighted. (25 nm × 25 nm) Inset: Autocorrelation of (d). (10 nm × 10 nm) (c) and (f) FFT's of (a) and (d) respectively.

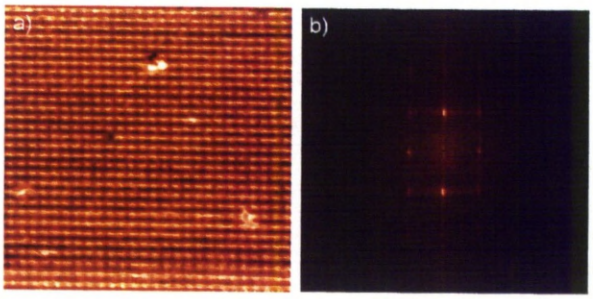

Figure 5.15: (a) An STM image of the 1/1 approximant of the Ag-In-Yb system (40 nm × 40 nm). (b) An FFT pattern taken from (a).

the sizes of the unit cells expressed by these structures. Many examples of periodicity of this surface produce autocorrelations that exhibit rod features. This makes the measuring of the unit cell problematic. Figure 5.14 (a) produces a clear autocorrelation which is shown in Figure 5.14 (b). Figure 5.14 (d) does not produce a similar autocorrelation, and instead the Fourier pass filter is shown in figure 5.14 (e) is used to determine the unit cell size. The autocorrelation for (d) is shown in the inset of (e).

The structure shown in figure 5.14 (a) has a unit cell of size 2.01 nm × 2.91 nm, and is a near perfect rectangle (a distortion has been incurred from thermal drift encountered during STM measurements). The structure shown in figure 5.14 (d) has a unit cell of size 1.42 nm × 2.36 nm. Both these structures are accompanied by step heights of 1.7 nm, which is similar to the unit cell length of the 1/1 approximant of Ag-In-Yb of 1.57 nm [48] with an example of the 1/1 Ag-In-Yb approximant shown in figure 5.15. The periodic nature of these STM images are emphasised in their FFT patterns, which are shown in 5.14 (c) and (f).

Occasionally periodic structures in the quasicrystalline domain can be observed which coexist with the present aperiodic structure. An example of this is shown in figure 5.16 (a). This structure has a unit cell of 2.47 nm × 1.3 nm. A second periodic domain occurs adjacent to the first, with this domain and a domain boundary featured in figure 5.16 (b). This structure has a unit cell of 2.7 nm × 2.3 nm. Both these domains are accompanied by step heights of 0.5 nm. This step height is consistent with the periodicity of the 1/1 approximant along the [110] direction. The distances between clusters along this direction is related to the unit cell, a, by $\frac{a}{\sqrt{2}} = 0.53$. This is not conclusive proof that this structure is related to the 1/1 approximant.

Firstly, the encountered unit cell sizes of all 4 structures do not match up to the unit cell of the

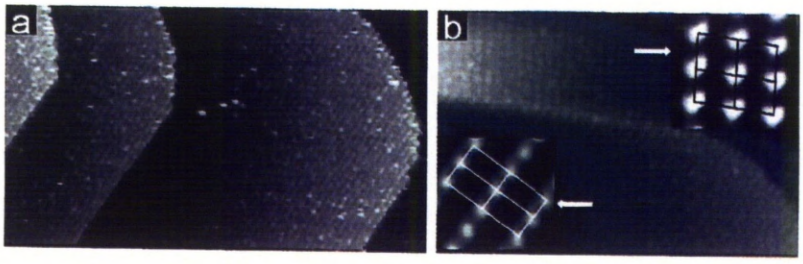

Figure 5.16: (a) An STM image taken from the quasiperiodic domain of sample 1 that displays local periodic ordering (160 nm × 90 nm) (b) An STM image taken from the same domain showing coexisting periodic structures, with Fourier pass filters of both domains included in inserts. The lower part of (b) corresponds to the same structure observed in (a). (97 nm × 65 nm). Reprinted from [128]

1/1 or 2/1 approximants, of 1.57 nm and 2.53 nm. Also, while the step height of 0.5 nm agrees with that of the 1/1 approximant along the [110] direction, analysis of the 1/1 approximants bulk structure prohibits this [138]. Bulk truncations along the [110] surface produces a step height distribution that does not conform to the observed values.

As no correlation is found between these periodic phases and the approximant phases, there are several speculations as to what is being observed. Firstly, it is possible that we are looking at a surface projection of the approximant, but along a low symmetry direction. Secondly, it is possible that we are observing an unknown phase of the quasicrystal. Known periodic phases of this system are $AgIn_2$ (tetragonal; $a = 0.688$ nm, $c = 0.562$ nm), In_4Ag_9 (cubic; $a = 0.992$ nm), $InAg_3$ (hexagonal; $a = 0.295$ nm, 0.786 nm), Ag_3In (hexagonal; $a = 0.299$ nm, 0.480 nm) and $YbAg_{5.4}In_{6.6}$ (tetragonal; $a = 0.973$ nm, 0.571 nm) [139], but all these phases have unit cells that are not related to the observed measurements. By observing the partial phase diagram of Ag-In-Yb in figure 5.17 it is clear that these periodic phases do not occur within the vicinity of the quasicrystal. Thirdly, it is possible that the periodic surface has reconstructed from the known theoretical structures.

5.4.2 LEED

Low Energy Electron Diffraction have been performed on sample 2. Patterns are observed only at a range of low energies for this surface, appearing at $\sim$ 10 eV and persisting to an energy

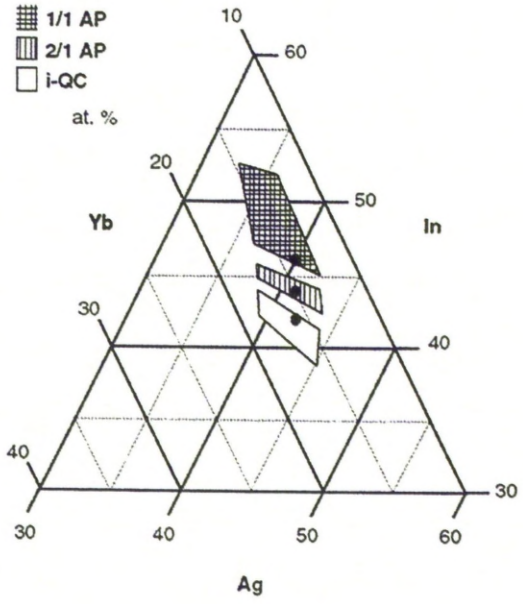

Figure 5.17: Partial phase diagram of the Ag-In-Yb system. Reprinted from [130]

of $\sim$ 80 eV. Diffraction patterns for a variety of energies are displayed in figure 5.18. These patterns demonstrate a well ordered surface displaying a five fold symmetry. Successive orders of diffraction spots are related by factors of τ. The first order of a second distinct set of rings has a distance from the reflected beam of $k\chi$. k is the two dimensional projection of the three dimensional reciprocal lattice vector $k = \frac{a_i^*}{\cos\theta}$, $i = 2...6$ where $\theta = 31.72°$ for icosahedral geometry. The ratio edge length, t, to radius R of a pentagon is denoted by $t = \chi R$ where $\chi = 1.175$.

Reciprocal lattice vectors are compared with that of LEED patterns of Cu(111). Patterns at the same energies are compared using the k-vector of Cu calculated from its lattice parameter [140]. This is then used to calibrate spot separation measurements while analysing the i-Ag-In-Yb LEED patterns. X-ray diffraction has been performed multiple times on the bulk material [52, 130, 131], which has led to a calculated lattice constant of $a \simeq 0.559$ nm. This translates to a reciprocal lattice vector of $a^* \simeq 15.86$ nm^{-1} where

$$a_i^* = \frac{2\pi}{a}\sqrt{2} \tag{5.1}$$

A LEED pattern from Cu(111) becomes observable at around 45 eV. This does not leave

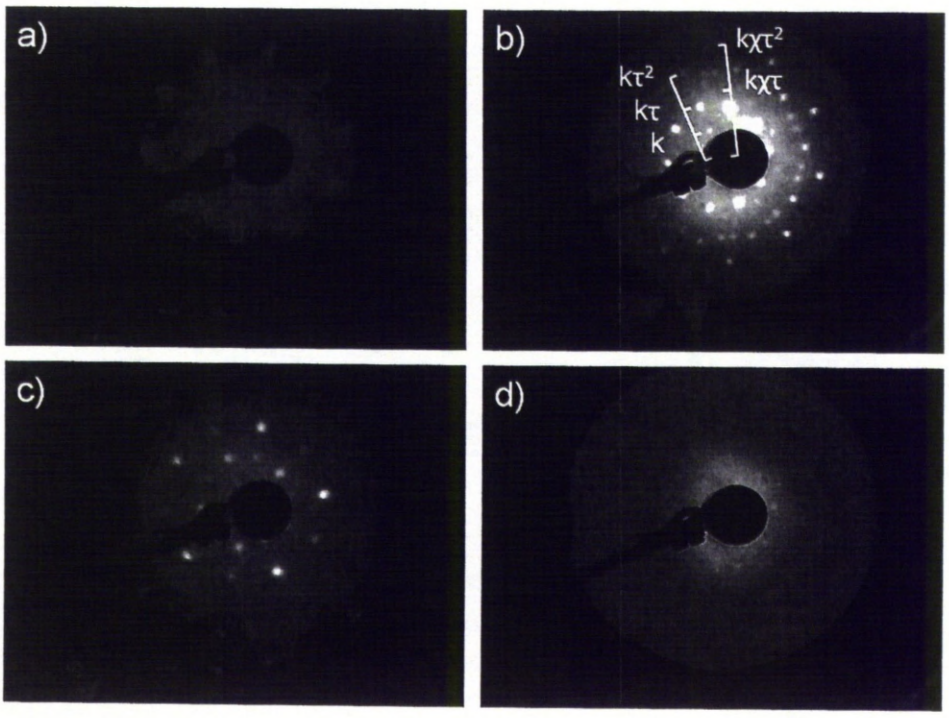

Figure 5.18: LEED images of the fivefold *i*-Ag-In-Yb surface taken at; (a) 10.5 eV, (b) 15 eV, (c) 33 eV and (d) 64.6 eV.

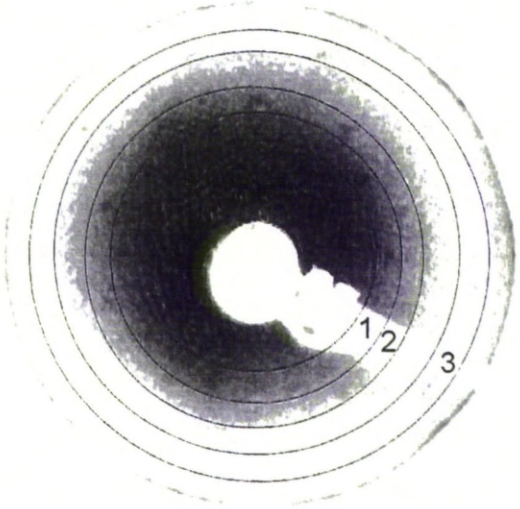

Figure 5.19: LEED image of the fivefold *i*-Ag-In-Yb surface taken at 45 eV.

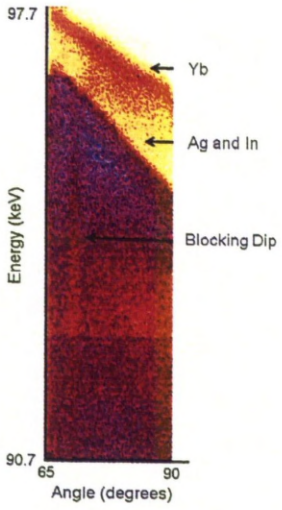

Figure 5.20: Two dimensional MEIS spectra obtained from the clean *i*-Ag-In-Yb surface.

many coinciding energies at which patterns from both Cu (111) and *i*-Ag-In-Yb are observable, and will exclude the use of the sharper LEED patterns observed from *i*-Ag-In-Yb at energies of 15 - 35 eV. At 45 eV there are at least 3 rings of spots observable from the *i*-Ag-In-Yb surface, highlighted in figure 5.19. Spots of ring 1 yield a reciprocal lattice constant $a^* = (13.854 \pm 1.222)$ nm^{-1} which translates to a lattice constant $a = (0.642 \pm 0.056)$ nm. This value is consistent with the lattice constant derived from the bulk.

5.4.3 MEIS

By employing MEIS it is possible to determine the surface composition and surface structure of the fivefold plane of *i*-Ag-In-Yb. The acquired spectra, of which an example is given in figure 5.20, can then be compared to previous XPS results in regards to composition. For the structure determination, a Monte Carlo simulation is employed using the *i*-Cd-Yb model to generate a theoretical MEIS spectrum, which has then been compared to experimental data.

Composition Analysis

The initial compositional MEIS results were taken on *i*-Ag-In-Yb sample 1. MEIS spectra were taken after annealing at various temperatures, and are shown in figure 5.21 (a). The lower energy section is associated with the signal from the bulk, and originates from scattered ions that have undergone many inelastic collisions. Due to the spread of energy from emerging ions it is not possible to determine the bulk composition from this data.

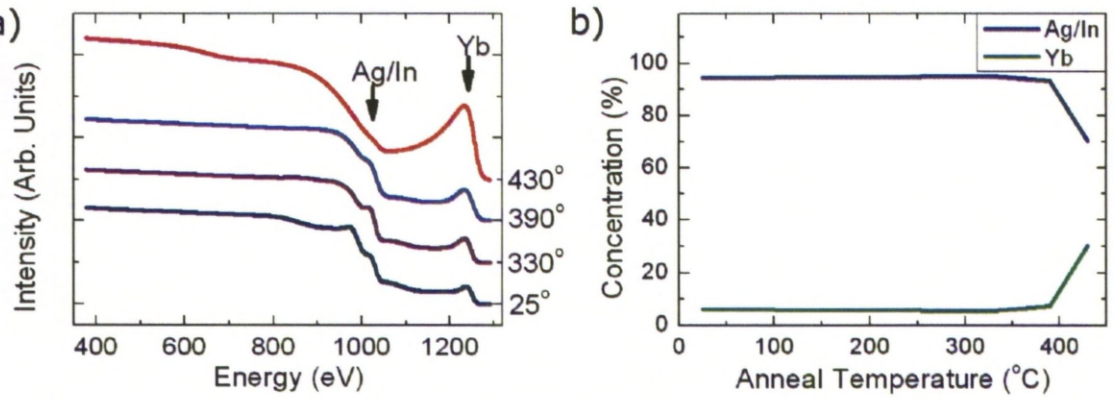

Figure 5.21: (a) One dimensional spectra taken from sample 1 along the energy axis, showing the intensity of scattered ions as a function of energy. Peaks relating to the presence of Yb and Ag/In are highlighted. (b) Concentrations of Yb and Ag/In as a function of anneal temperature.

Signals at higher energies of the spectrum originate from the surface, and elements can be characterised from the energies of the measured peaks. Yb produces a strong signal at a high energy due to it being the heaviest element present, while Ag and In feature at a lower energy. Due to their similar sizes and masses, ions scattered by Ag and In have similar energies leading to one indistinguishable peak. As such the concentrations of both elements are counted as one species.

Figure 5.21 (b) shows the normalised intensities of these elements with respect to the square of their atomic number Z^2, as a function of anneal temperature. As the anneal temperature increases, the concentration of Yb increases. At 430°C the amount of Yb at the surface is roughly 30%. This value is slightly higher than the expected value of bulk concentrations for Yb, due to the fact that the top-most surface plane is composed mainly of Yb. The average Yb concentration over all potential surface planes of the *i*-Cd-Yb model (shown in figures 5.4 and 5.7) varies between 31% and 75%, with an average value of 46%. As MEIS will detect an average composition over an area of several μm^2, the detected Yb concentration is consistent with that indicated by the model at surface terminations.

An energy spectrum from sample 2 has also been obtained. This spectrum has yet to be fully analysed due to the complex nature of fitting a theoretical scattering plot. However it is possible to see that there is a large contribution of Yb on the surface. The Yb signal intensity from sample 2 is comparable to that of the intensity recorded on sample 1. This indicates that

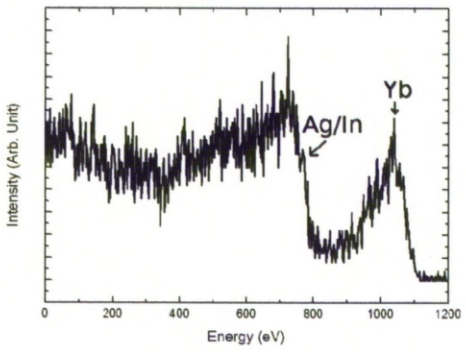

Figure 5.22: (a) One dimensional spectra taken from sample 2 along the energy axis.

if single grain quasicrystalline *i*-Ag-In-Yb sample is studied using MEIS, the surface will be composed mainly of Yb.

Structure Analysis

By taking angle resolved information from the 2D spectra, the surface structure of a material can be compared to the theoretical model. Figure 5.23 shows a comparison of the experimental data taken from sample 2 and theoretical scattering spectra. The theoretical spectrum was determined by taking a small slice from the unrelaxed *i*-Cd-Yb model and simulating a MEIS experiment using appropriate software packages. Due to the complexity of the model and lack of a unit cell, the theoretical spectrum is limited to an angular resolution of 0.5°. Although the *i*-Cd-Yb model does not feature Ag and In, the average mass and size of these two atoms is similar to Cd. Another issue is that the populations of these two differing atoms cannot be identified, so using Cd in every Ag/In position produces a reasonable estimate.

In both experimental and theoretical spectra, three major blocking dips occur at angles of 69°, 90° and 110.5°. The theoretical data also shows blocking features at angles of 75°, 79°, 83°, 102° and 121.5°.

Due to the low flux of ions incident to the surface, a significant signal to noise ratio was produced. However the coincidence of major blocking dips provides good evidence of the surface of the *i*-Ag-In-Yb quasicrystal is bulk terminated and undergoes no reconstruction.

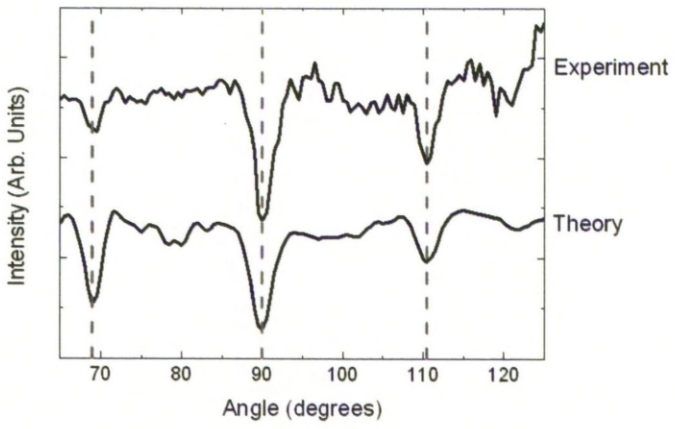

Figure 5.23: The experimental and theoretical structural spectra from the clean fivefold i-Ag-In-Yb surface.

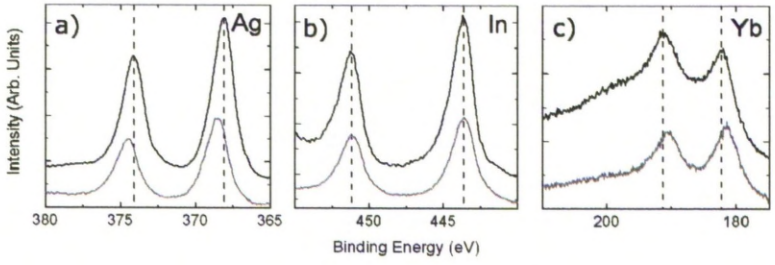

Figure 5.24: XPS spectra of the clean fivefold surface of i-Ag-In-Yb (indicated by a grey line) and pure metals (indicated by a black line) core levels for (a) Ag, (b) In and (c) Yb.

5.4.4 XPS

XPS spectra of the clean fivefold surface for Ag $3d$, In $3d$ and Yb $4d$ core levels are shown in figure 5.24 (a), (b) and (c) respectively. These are compared with the core level spectra of a Ag(111) crystal and pure (99.9%) metallic foils of In and Yb. The binding energies for Ag and Yb from the fivefold surface are slightly different to their pure versions. The Ag $3d$ peaks are shifted to higher binding energies by 0.5 eV, while the Yb $4d$ peak are shifted by about 0.7 eV to lower binding energies, while the binding energy for In remains unchanged from its pure metallic form. This suggests that there is a charge transfer occurring between Ag and Yb in the quasicrystal, and that the two elements are bonded. Charge transfer as a result of bonding may leave an atom with a partial positive or negative charge. The Columbic interaction between

the core levels of a charged atom and it's nucleus will cause an energy shift of the core level electrons, to a higher binding energy for a positive charge, and a lower binding energy for a negative charge. The line shapes of Ag and In are unchanged from their pure counterparts. The Yb $4d$ line shape from the quasicrystal also exhibits its characteristic spin-orbit doublet shape, which is observed in other Yb compounds [141].

Previous XPS studies [64] have shown that sputtering preferentially removes In and Yb from the surface leading to a surface composition of $Ag_{71}In_{24}Yb_5$. After annealing the composition is restored close to that of the bulk resulting in a surface composition of $Ag_{40}In_{45}Yb_{15}$, which is close to the bulk composition. The previous study was performed using sample 1.

A compositional analysis using sample 2 has also been completed. The surface composition after sputtering was found to be $Ag_{62.1\pm0.8}In_{28.4\pm0.6}Yb_{9.4\pm0.3}$. After annealing the surface composition changed to $Ag_{35.6\pm0.4}In_{44.3\pm0.8}Yb_{20.0\pm0.6}$.

5.5 Summary

The comparison of STM, LEED, MEIS and XPS studies performed on the fivefold i-Ag-In-Yb surface with that of the model of i-Cd-Yb have yielded results consistent with the theory that the surfaces exhibited by this material are bulk terminated. The surfaces produced by preparation conditions yield an atomically flat step terraced structure. Comparing the step sizes to the bulk model of i-Cd-Yb imply that the surface forms at atomic planes that intersect the center of the Rhombic Triacontrahedral atomic clusters that construct the bulk material. These planes are not the most dense atomic planes, but contain high concentrations of Yb and In. The most dense planes however are accompanied by gaps of atomic density but are absent at potential surface termination planes. This provides us with the understanding that bulk terminations for this system are not chosen purely for their atomic density or gap sizes in the atomic model, but that the surface free energy is a major determining factor. Such surfaces will have low surface free energies as Yb and In have lower surface free energies than that of Ag [142].

This surface exhibits a bias dependence when viewed by STM. At a negative bias large protrusions indicating the positions of clusters of atoms are visible. The sizes of these clusters coincide with the diameter of the ten fold Cd ring that encircles a cluster center, which is formed by an icosidodecahedron or the fourth shell of an RTH cluster. This indicates that these

protrusions are truncated RTH clusters. The inability to gain atomic resolution is possibly caused by the electronic coupling of Ag and In atoms. A pentagonal tiling can be superimposed onto this image with the vertices of such a tiling lying on the cluster center. A tiling of identical edge length can be superimposed upon the model structure also.

At a positive bias decagonal rings are observed. The diameter of these rings matches up to the diameter of a decagonal ring of Yb atoms present on the i-Cd-Yb model, which are shared between different clusters. The same tiling as described for images at a negative bias can be superimposed onto this image, with the vertices placed at the center of the ring features.

Autocorrelations of negative biased images resemble autocorrelations taken from the i-Cd-Yb model with the cluster center positions highlighted. Another similarity is also shared by comparing an autocorrelation between positive biased images and the positions of Yb atoms from the model structure. This gives further proof to STM images at negative bias showing states enhanced around Ag/In positions and positive bias showing states enhanced around Yb positions.

LEED patterns taken from the surface demonstrate fivefold symmetry. K-vectors obtained from these images match reciprocal lattice vectors measured from X-ray diffraction, and suggest that the bulk structure is present at the surface. Compositional MEIS analysis concludes that the annealed surface has a high concentration of Yb. This also agrees with predictions that the surfaces occur on atomic planes rich in Yb. Analysis of the angle resolved MEIS spectrum compares well with the theoretical spectrum obtained from the model structure.

XPS spectra show no changes in the line forms of the core level peaks from the quasicrystal when compared to their pure metal counterparts. The Ag $3d$ and Yb $4d$ core levels undergo an energy shift suggesting a charge transfer indicating bonding between these two elements. The surface composition is found to be similar to the bulk composition.

This system shares many similarities with the i-Al-Pd-Mn system. Both systems exhibit a step terraced structure, where step heights may be identified in their model structures. They also display many fivefold features upon their terraces which can be identified in their models, but the bias dependency when observed by STM is only exhibited to the i-Ag-In-Yb quasicrystal. It is possible to pick out atomic arrangements on the Al-Pd-Mn surface at either bias, which led to the designation of features such as dark stars and white flowers, which are formed from truncated Bergman and pseudo-Mackay clusters respectively. The i-Ag-In-Yb surface is different in terms

of visible features, with the predominant surface features being purely protrusions for negative bias and rings for positive bias, both of which conform to the same pentagonal tiling. These features may be considered to be truncated RTH clusters. Both systems are also considered to exhibit surfaces that are bulk terminated [11,143]. The *i*-Al-Pd-Mn system is reported to adhere to all three factors that govern the formation of a stable surface plane; high atomic density [144], being composed of elements that have a low surface free energy and each termination being accompanied by a large gap in atomic density [88,89]. Surfaces of the *i*-Ag-In-Yb quasicrystal are, however, determined primarily by the fact that a surface is composed of elements that have a low surface free energy. While there are gaps in atomic density that do accompany the highest density atomic planes in the model, these planes do not contribute surfaces.

Chapter 6

Structural characterisation of the two and threefold surfaces of the *i*-Ag-In-Yb quasicrystal

6.1 Introduction

This chapter deals with the characterisation of the three and twofold surfaces of the *i*-Ag-In-Yb quasicrystal. This characterisation follows a similar approach to the methods used for the fivefold sample. The surfaces of the three and twofold crystals are initially studied using STM. The results from this technique are then related to the model structure in an effort to discover which surface planes are responsible for the observed surface structures. The long range order is then tested using LEED, and finally XPS is utilised to analyse the chemical compositions of the surface. These two surfaces are also oxidised and their behaviour studied. This is elaborated on in chapter 8.

6.2 Experimental Details

Preparation of these samples was similar to that of the fivefold sample. These samples were cut from the same ingot that produced fivefold sample 2 after their symmetry planes were identified by Laue backscattering [131]. Preliminary surface preparation involved the same process to

remove residue left over from the cutting process. This produced samples of size and appearance similar to the fivefold sample 2. Further preparation of hand polishing with varying grades of diamond paste was performed in the same way as the fivefold sample, before they were mounted onto suitable plates and entered into UHV. Preparation *in situ* featured sputtering for 30 mins and annealing for 2 hours using similar conditions of those used for the fivefold sample. The only difference was that both the two and threefold samples were only heated to 420°C. The samples were then left to cool for 15 minutes after annealing.

STM experiments were conducted in three different laboratories. The microscopes used to study these samples are Omicron variable temperature STM's operating at room temperature in two different laboratories, Liverpool and Tsukuba, Japan. XPS measurements were performed with unmonochromatised AlK_α radiation ($h\nu = 1486.6$ eV) using a PSP Vacuum Technology hemispherical electron-energy analyser. Results from the two and threefold sample were treated in a similar way to that of the fivefold sample, in how peak intensities and binding energies were measured. LEED measurements were performed using an Omicron Specta LEED optic and source, using a LaB_6 filament. During LEED measurements the samples were kept at room temperature.

6.3 Results

6.3.1 STM: Threefold Surface

Step heights

The threefold surface exhibits an atomically flat surface consisting of steps and terraces as shown in figure 6.1 (a). Terraces range in size from several hundred nanometres to half a micron. Two step heights are observed which have been measured from a total of 199 steps; a small step $S = 0.12 \pm 0.02$ nm and a larger step $L = 0.44 \pm 0.03$, with relative occurrences of 15% and 85% respectively. The small step height is encountered relatively rarely, and is indicated in 6.1 (b), and also in figure 6.2 (b) by white arrows. In these figures, the small step is part of a layer of atoms that only partially covers the terrace, which will be detailed in a later section.

High resolution STM images

Like the fivefold surface, the threefold surface exhibits a degree of bias dependency. Cluster

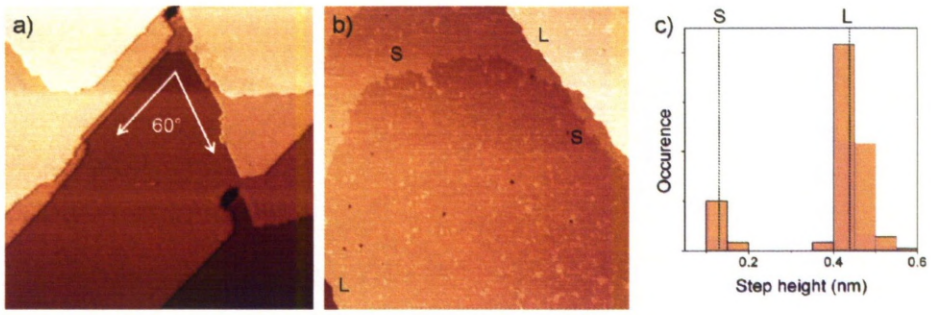

Figure 6.1: (a) Large scale image of the threefold surface, enhanced to distinguish step edges. (300 nm × 300 nm) (b) A larger terrace with the terraces bordering an S step indicated by white arrows (500 nm × 500 nm). (c) A distribution of measured step heights with the S and L step heights indicated.

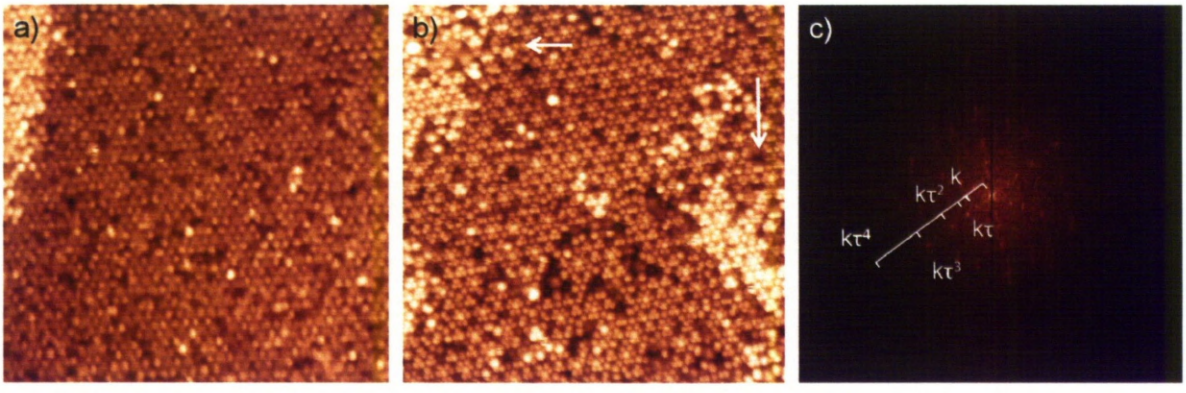

Figure 6.2: (a) A negatively biased STM image of the threefold surface (-1.0 V bias, 80 nm × 80 nm). (b) A positively biased STM image of the same surface, detailing atomic positions (+1.1 V bias, 50 nm × 50 nm). (c) An FFT taken from image (b).

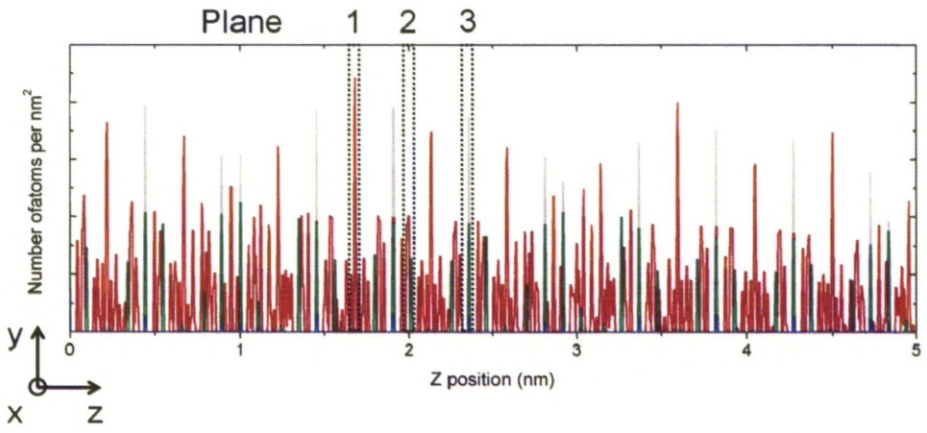

Figure 6.3: Variation in the atomic density in layers perpendicular to the threefold axis using a step size of 0.005 nm. Red indicates Cd, green indicates Yb, blue indicates cluster centers (which has been increased by a factor of 100) and the grey line represents the overall atomic density.

resolved images, shown in figure 6.2 (a), were visible when the sample was biased negatively with respect to the tip. Atomic resolution, shown in figure 6.2 (b), was only observed when the sample was biased positively with respect to the tip. Atomic resolution was difficult to obtain, and was only witnessed after the tip underwent a voltage pulse in an attempt to sharpen it. This inadvertently changed the tip shape, either through picking up material from the surface or by the tip losing part of itself, increasing its sharpness to such a level where individual atoms can be imaged. In other instances when using a positive bias, the clusters as seen in figure 6.2 (a) were slightly more resolved.

The surface is shown at both of these resolutions in an attempt to provide a clear view of the surface over a small scale, and over a larger scale; it is difficult to pick out the positions of the clusters in the atomic resolution image, for example. The sizes, and atomic and cluster separations are investigated below. An FFT generated from figure 6.2 (a) is shown in 6.2 (c), which demonstrates the 3 fold ordering and τ scaling exhibited by this surface.

Comparison with the *i*-Cd-Yb model

By searching through each atomic plane in the *i*-Cd-Yb model, it is possible to identify many potential planes that might present a possible surface. In figure 6.3 the atomic density along the threefold axis is presented. This figure shows that there are several atomic planes of

high density present. Each of these atomic planes will be considered to discern which atomic plane can be feasibly related to experimental results. None of these planes are accompanied by significant gaps in atomic density.

Before comparing the model to the STM results, several features are identified from the experimental results. These features are discussed in greater detail below. The features are the shapes of several atomic arrangements that come in the form of a distorted hexagon, large triangles, small triangles, and the configuration of these features in relation to each other.

Three atomic planes identified from the model that have high atomic densities are presented in figure 6.4. These are; plane 1 shown in figure 6.4 (a), plane 2 shown in figure 6.4 (b) and plane 3 shown in figure 6.4 (c). Comparing these planes to an atomically resolved STM image shown in figure 6.4 (d) indicates the presence of, or the lack of, comparative features. Specific feature sizes and separations, which are detailed later, are compared in the elimination of these atomic planes. Plane 1, (figure 6.4 (a)) which is composed entirely of Cd, exhibits several rows of atoms in a triangular structure. Such features are not observed by STM and as a result this plane is discounted. Plane 2 (figure 6.4 (b)) shows several Cd distorted hexagons, which are indicated by black circles. However these features are not of a similar size to the distorted hexagons observed by STM, but are instead a factor of τ smaller. There are triangular arrangements of Yb atoms, indicated by broken black circles, which have similar separations as the small triangles imaged by STM. Plane 2 is eliminated however, due to the lack of distorted hexagons of similar sizes. Also, the selection of either plane 1 and plane 2 as a surface would create step heights which are not compatible with those observed by STM.

Plane 3 is the final atomic plane to be considered. This atomic plane intersects the RTH cluster centers. Initially there does not seem to be any matching features if the RTH cluster center positions are regarded as being responsible for a distorted hexagon. By removing the RTH cluster center positions and the Cd atoms, it becomes possible to identify every feature observed by STM.

The first feature, shown in figure 6.6 to be considered is the distorted hexagon. This feature has two differing atomic separations measured experimentally to be 0.93 ± 0.07 nm (1) and 0.68 ± 0.07 nm (2). These match up to the separations from the model of 0.97 nm and 0.67 nm respectively.

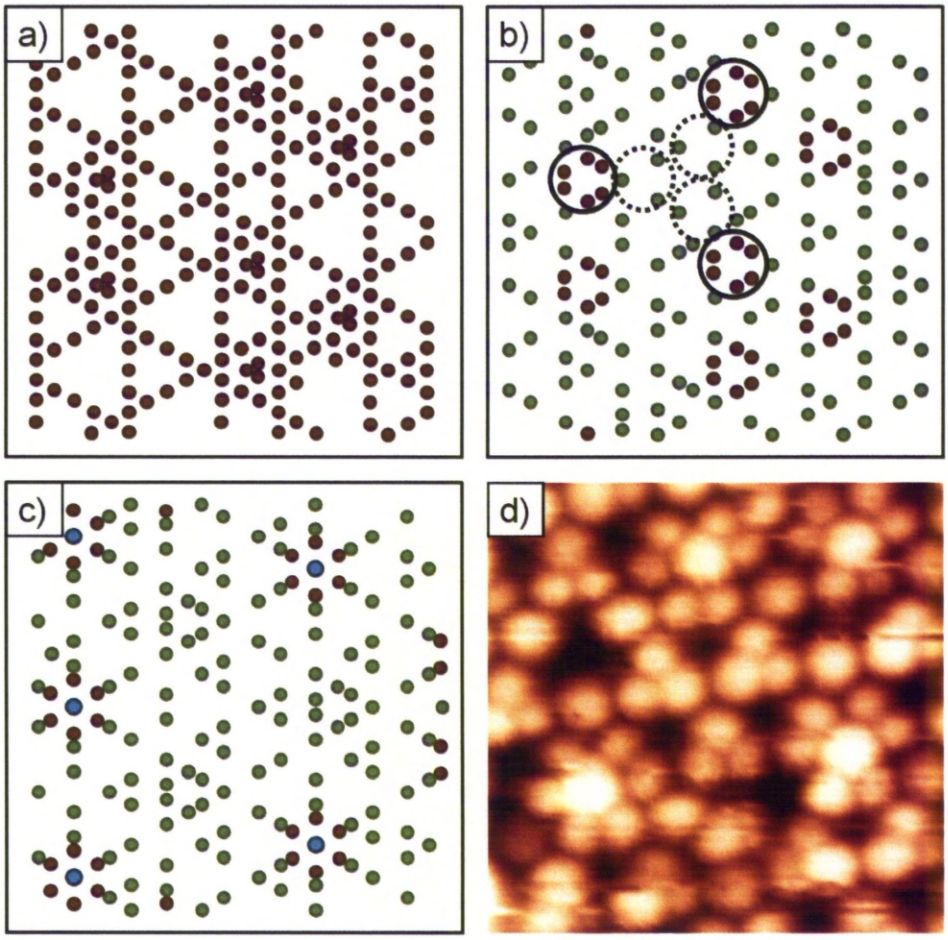

Figure 6.4: Atomic planes from the Cd Yb model normal to the 3 fold axis. Each plane features relatively high atomic densities, indicated as (a) plane 1, (b) plane 2 and (c) plane 3. Positions of these planes are indicated in figure 6.3. (d) A comparative STM image displaying atomic resolution is included. Red dots indicate Cd atoms, green dots indicate Yb atoms, while blue dots indicate the centre of an RTH cluster. (8 nm × 8 nm)

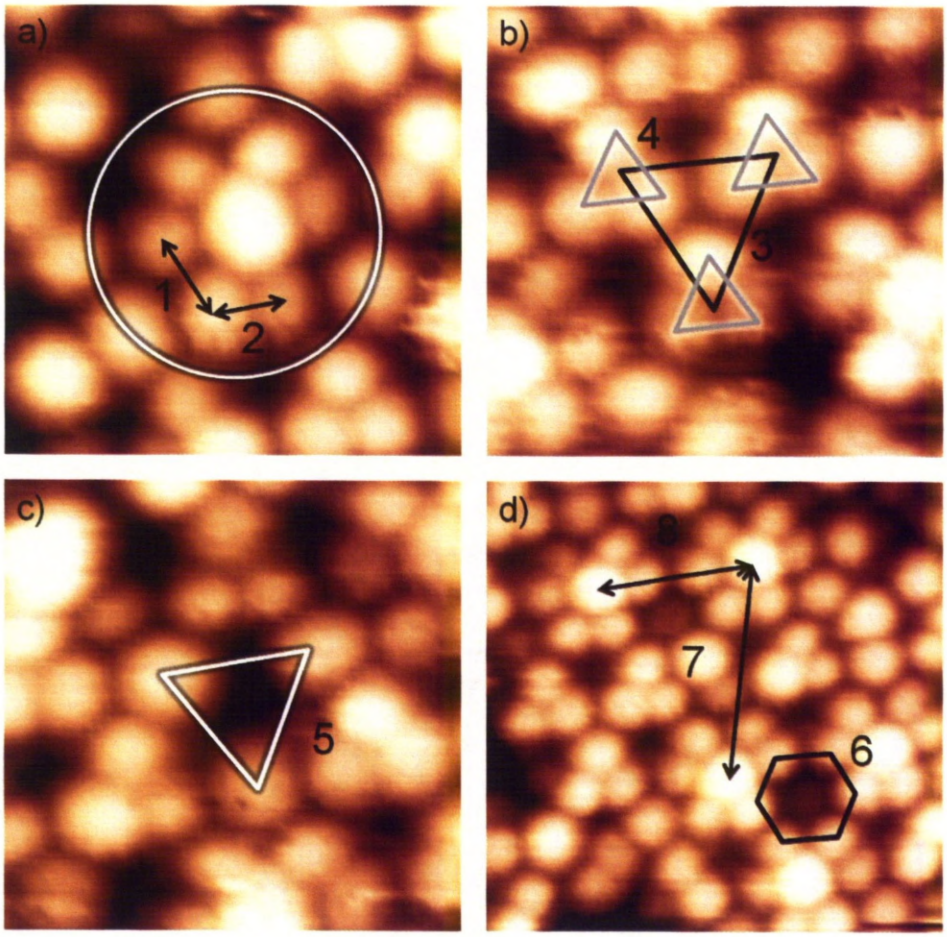

Figure 6.5: Features from STM images of the threefold *i*-Ag-In-Yb surface which include (a) A distorted hexagon, (b) an arrangement of small triangles, (c) a large triangle. (5 nm × 5 nm) (d) Shows these features together. (8 nm × 8 nm). Features have been highlighted with a variety of shapes, to make the identification with the model structure shown in figure 6.6 easier.

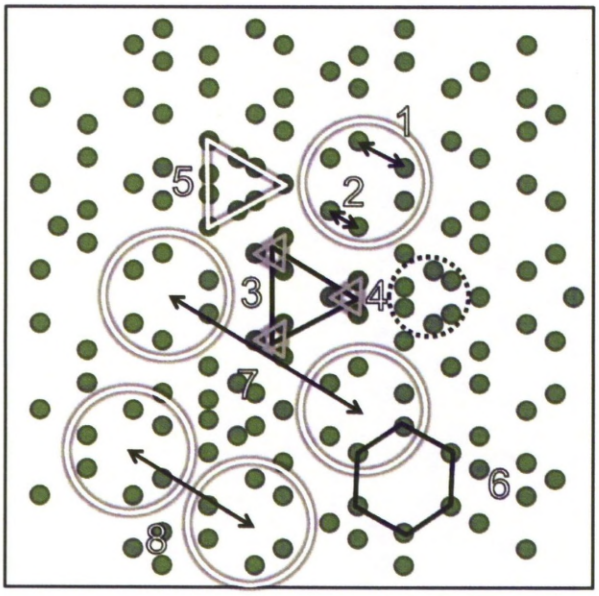

Figure 6.6: Plane 3 with the cluster center and Cd positions omitted. Shapes corresponding to those used to identify features observed by STM in figure 6.5 are also included.

The next features observed are the triangular arrangements of small atomic triangles. The distances between the triangles of 1.69 ± 0.07 nm (black triangle (3)) are slightly larger than those of the model value of 1.57 nm, although these values still reasonably agree with each other. The orientation of this triangular arrangement is 180° to the overall triangular arrangement of the distorted hexagons, in both the experimental and model observation. The small triangles have an edge length of 0.68 ± 0.07 nm (grey triangle (4)) as observed by STM and of 0.60 nm as measured from the model, which is in agreement. The orientation of the small triangles is parallel to the distorted hexagon triangular arrangement in both STM results and the model.

The large triangle has an edge length of 1.61 ± 0.09 nm (white triangle (5)) when measured by STM, and of 1.57 nm from the model. These triangles are aligned at 180° to the overall triangular arrangement of the distorted hexagons in both examples. For the model however, there is a small distorted hexagon in the middle of the large triangle, which is not observed by STM. These atoms are glue atoms however, so it is possible that they are not present on the surface. Glue atoms are found to play an important role in the appearance of the surface of quasicrystals and their approximant phases. For example, when the surface of the *i*-Al-Pd-Mn crystal is prepared by fracture, the fracture plane is forced to circumvent the clusters, due to

Table 6.1: Size and separations of features observed on plane 3, and comparative measurements of features observed by STM of the threefold *i*-Ag-In-Yb surface.

Feature		Model size	Experimental size
Distorted hexagon	(1)	0.97	0.93 ± 0.07
(atomic separations)	(2)	0.60	0.68 ± 0.07
Small triangle	(3)	1.57	1.69 ± 0.07
	(4)	0.60	0.68 ± 0.07
Large triangle	(5)	1.57	1.61 ± 0.09
Regular hexagon	(6)	0.97	0.93 ± 0.07
Distorted hexagon	(7)	4.10	4.20 ± 0.14
(hexagon separations)	(8)	2.53	2.51 ± 0.17

their stability [145], producing a corrugated surface. This indicates that the intervening atoms between the clusters (the glue atoms) exhibit less stability than atoms that are contained within a cluster.

The relative stability of the clusters does not only depend on the positions of glue atoms within them, but also the positions of glue atoms in the surrounding environment.

From the model, a cluster center is encircled by a regular hexagon of edge length 0.97 nm (black hexagon (6)). It is possible to identify these regular hexagons from the model, which share an edge length distance with the larger edge length of a distorted hexagon of 0.93 ± 0.07 nm.

The final characteristic to be measured are the separations of the distorted hexagon arrangements. Two separations of 4.20 ± 0.14 nm (7) and 2.51 ± 0.17 nm (8) are observed by STM, which match separations observed in the model of 4.10 nm and 2.53 nm respectively.

The partial terrace (which borders an S step) has a slightly different density to the terrace it sits upon (which borders an L step). A typical S step terrace contains 0.72 ± 0.19 atoms per nm^2 while a typical L terrace contains 1.08 ± 0.14 atoms per nm^2. These densities were calculated by highlighting a 10 nm $\times$ 10 nm area on an STM image of both an S step terrace and an L terrace and counting the protrusions that relate to atomic positions.

The densities of the L terraces and S terraces as measured by STM are less than the densities

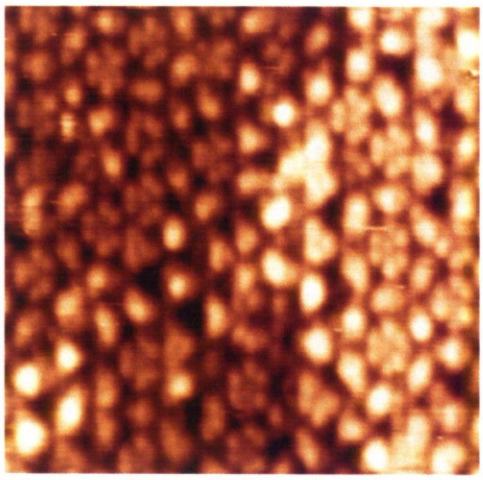

Figure 6.7: An STM of the threefold *i*-Ag-In-Yb surface taken at at Ecole des Mines, a separate experiment to the one that recorded the threefold information already presented. (25 nm × 25 nm) The image is distorted along the horizontal axis due to tip drift.

of the L terraces and S terraces as calculated from the model, of 1.15 ± 0.12 atoms per nm^2 and 0.87 ± 0.12 atoms per nm^2 respectively. Although they are still similar, the lower densities as observed by STM indicate that there are atoms missing at the surface, which is consistent with the conclusions that certain glue atoms are not present on these terraces.

A feature that can be observed by STM that cannot be explained by the model is the existence of an object in the middle of a distorted hexagon that has a greater height than the atoms that make up the distorted hexagon of 0.05 nm. Very rarely a non-centered distorted hexagon is observed. The layers above or below plane 3 do not contain any atom that could reasonably situate itself in these sites. However, figure 6.7 shows STM data observed during a separate experiment conducted at Ecole des Mines of near-atomic resolution showing non-centered distorted hexagons. It is possible that these sites are highly active when exposed to contaminants, and that the chamber used for the initial experiment was subjected to a source of contamination [127]. In the chamber used in the experiment conducted at Ecole des Mines, only a small amount of oxygen was detected after several hours of STM data collection. It was not possible to check oxygen levels in the chamber used in the initial experiment. However, it was found during an oxidation study (presented in chapter 8) that the threefold surface is highly reactive to oxygen.

By considering only the atomic planes that intersect RTH clusters, it is possible to determine what step sizes and sequence will be established from this surface selection. This is shown in figure 6.8. Two steps of size $S = 0.107$ nm and $L = 0.452$ nm with occurrences of 19% and 81% respectively, are formed from this selection of surface planes. The sizes of both steps, and their

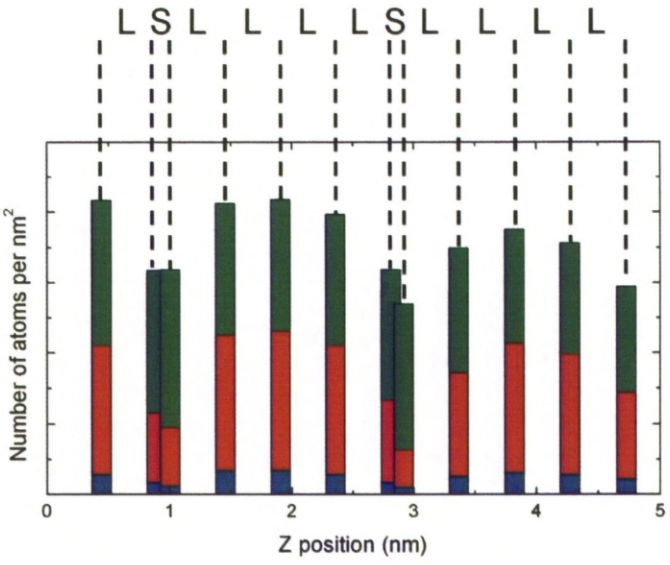

Figure 6.8: The atomic density of viable surface terminations along the threefold axis using a step size of 0.005 nm. Blue indicates the amount of cluster centers (which has been increased by a factor of 100), red indicates the amount of Cd and green indicates the amount of Yb.

frequency match STM measurements. Combinations of these steps are also scaled by factors of τ, such that $\frac{2L}{S+L} = \tau$.

The instability of a terrace bordering an S step, shown in figure 6.1 (b) as an incomplete terrace, can be explained by the relative densities of each surface plane, as well as the glue atom content. The atomic planes bordering an S step in the model have relatively lower atomic densities to those planes bordering an L step. There is also a contribution to the surfaces from glue atoms. While the behaviour of glue atoms is not fully known, it is possible that some of these atoms are not present at the surface, as explained above in regards to the lack of a small distorted hexagon formation being present on the surface, and differing atomic densities between experimental and theoretical results. This would lead to a lower stability of the atomic plane. An atomic plane that borders an S step has $\sim 27\%$ of its Yb atomic positions belonging to glue atoms. This is greater than a 5-20% of Yb atomic positions belonging to glue atoms from the atomic planes that border an L step.

As mentioned above, this surface exhibits a degree of bias dependency when observed by STM. As discussed in chapter 5, at a negative bias the STM will detect the density of states of

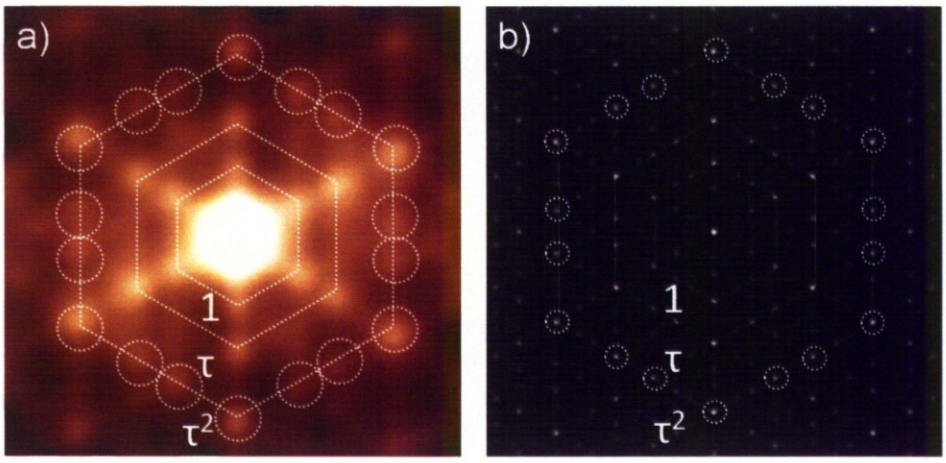

Figure 6.9: Autocorrelations of (a) the atomically resolved STM of the threefold surface (b) plane 3 with no contribution from Cd atoms. (10 nm × 10 nm)

Ag, In and Yb. At a positive bias, only the Yb states will be detected. This would indicate that at a negative bias it is more likely to observe the larger clusters, as the density of states at such a bias are not purely concentrated around the Yb atoms. However at a positive bias, the visible states are firmly concentrated on Yb atoms which makes their resolution more obtainable.

The identification of atomic features from STM results and the similarities of features expressed from atomic planes that intersect the centers of the RTH clusters, as well as the produced step heights and sequences, gives reasonable evidence that these atomic planes are responsible for surface terminations for the threefold surfaces of i-Ag-In-Yb.

Surface ordering

To further give evidence for plane 3 being responsible for the observed surfaces, autocorrelations from the atomically resolved STM and plane 3, with only the contribution of the Yb atoms considered, are compared. Figure 6.9 (a) shows the autocorrelation from the atomically resolved threefold surface and figure 6.9 (b) shows the autocorrelation taken from the Yb atoms of plane 3. Only the Yb atoms are considered due to the matching of features observed by STM to the Yb atoms of atomic planes that intersect the RTH clusters. Figure 6.9 (a) displays τ scaled maxima in sixfold directions. The first maxima of 1.53 nm relate to the size of the triangular arrangements of small triangles, and the size of the larger triangles, while the second and third maxima of 2.69 nm and 4.19 nm relate to the positions and separations of the distorted hexag-

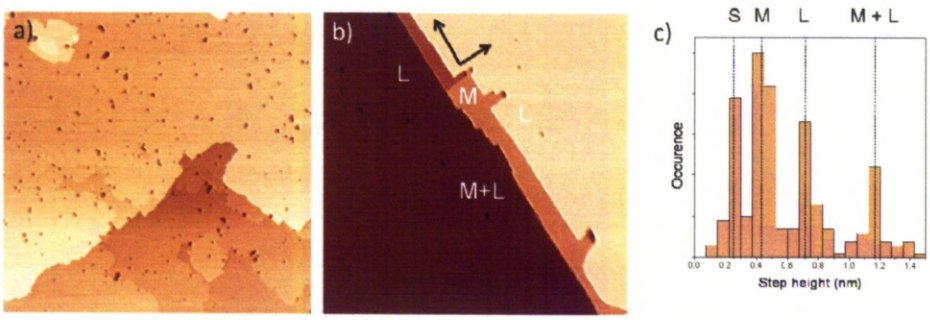

Figure 6.10: (a) A large scale STM image detailing the size of the terraces present on the twofold i-Ag-In-Yb surface, enhanced to distinguish step edges. (1.5 μm$\times$ 1.5 μm) (b) Another large scale image showing the twofold angles encountered from the step and terraced structure, as well as some locations of the more frequently encountered step heights, enhanced to distinguish step edges. (500 nm $\times$ 500 nm). (c) A histogram of the encountered step heights on this surface, with the S, M, L and bunched $M + L$ steps indicated.

onal clusters. The specular feature obscures any maxima that relate to any atomic separations. The autocorrelation in figure 6.9 (b) displays maxima at the same distances as those observed in STM, although it is possible to see other maxima that relate to atomic separations. The brightest maxima that occur in figure 6.9 (a) are highlighted in both images. The similarity of the autocorrelations of both experimental and model results gives further confirmation for the threefold surfaces of i-Ag-In-Yb being formed at atomic planes that intersect cluster centers.

6.3.2 STM: Twofold Surface

Step Heights

After preparation, the twofold surface exhibits an atomically flat surface featuring steps and terraces, shown in figure 6.10 (a) and (b). Three unique step heights are observed which are measured from 265 steps; a small step $S = 0.27 \pm 0.03$ nm, a medium step $M = 0.45 \pm 0.04$ nm and a large step $L = 0.73 \pm 0.06$ nm. A histogram of measured step heights is shown in figure 6.10 (c). Steps of greater heights are also observed. The occurrence of the basic steps heights S, M and L are 25%, 47% and 28% respectively. The fourth step height indicated in the step height histogram is due to a bunching of an M and an L step. Other bunched steps of greater height are observed in rare occasions that can be combinations of any of the three basic step heights.

During the initial scans of the twofold sample the terraces appeared pitted, as shown in figure 6.10 (a). The condition of the terraces improved over the course of the experiment, as shown in figure 6.10 (b). The occurrence of pits can be related to two factors; firstly, the preparation conditions were changed at the commencement of this study. Previous preparation had the crystal being mechanically polished using alumina paste. This was changed to hand polishing using diamond paste. Secondly, as a sample is subjected to preparation procedures, bulk vacancies migrate to the surface. This occurs more readily with a newer sample.

High resolution STM images

During this study several different structures from the twofold surface have been observed. These can be categorised into two different groups: a crowded surface which features rows and a surface which displays an arrangement of protrusions. The surface displaying rows was observed when applying a bias voltage of ~ -1 to $+1.5$ V, while the protrusion structure was only observed when using larger positive bias of $\sim +1$ to $+3$ V.

The first surface to be considered is the crowded example, referred to as twofold surface 1, and is shown in figure 6.11 (a). This STM image has been enhanced with a Fourier pass filter. After enhancing the image a row like structure becomes apparent, with the distance between the rows being 1.52 ± 0.17 nm. These rows are linked occasionally, with the intervals between these links being 2.03 ± 0.16 nm. The presence of these links gives the the occasional appearance of a zig zag motif, highlighted by a broken black line in figure 6.11 (a). The angle between the row and the linkage is 90°. An autocorrelation of this image displays rows containing maxima at various points. The distance between the rows is 1.55 nm, while the distance between maxima is 2.22 nm, indicating that these features originate from the presence of the rows and their linkages observed in the STM images.

The second surface, defined by the arrangement of protrusions and referred to as twofold surface 2, is shown in figure 6.11 (d). Like the first surface it is still possible to observe the presence of rows and their linkages, as highlighted by broken black lines, but the majority of these features is obscured by the protrusions. The protrusions have a FWHM of 1.30 ± 0.04 nm. By creating a unit cell, the protrusion separations are measured as 2.55 ± 0.15 nm and 3.03 ± 0.13 nm, with a lateral separation of 3.38 ± 0.17. The internal angles of this parallelogram are 65°and 115°.

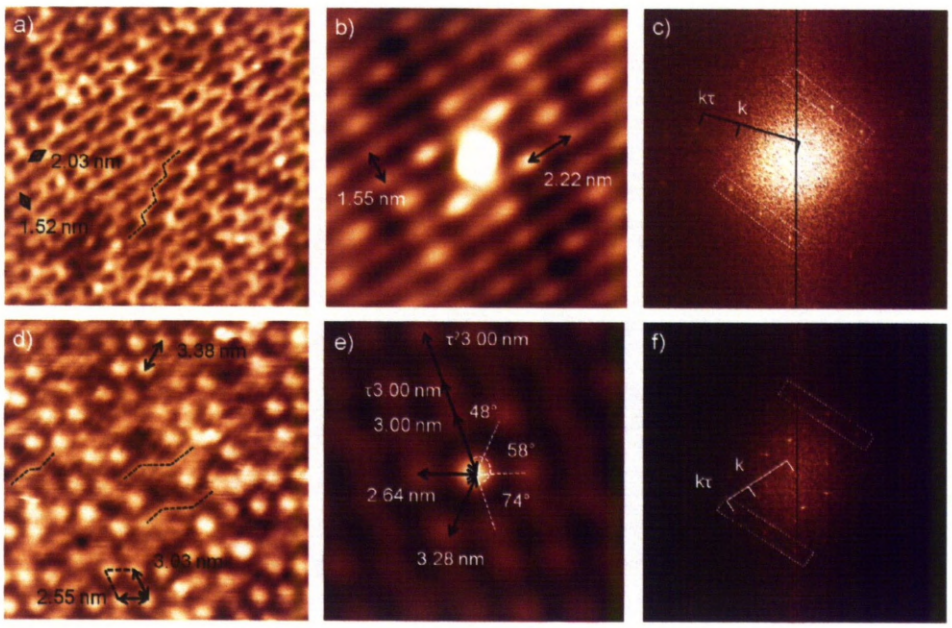

Figure 6.11: (a) An STM image of the clean twofold surface displaying a row like structure, enhanced by a Fourier pass filter (+1.1 V, 30 nm × 30 nm). (b) An autocorrelation of image (a) (15 nm × 15 nm) (c) An FFT pattern of a larger STM image displaying the same structure as seen in (a). (d) An STM image displaying a surface structure composed of protrusions (+1.8 V, 30 nm × 30 nm) (e) An autocorrelation of image (d) (15 nm × 15 nm). (f) An FFT pattern of a larger STM image displaying the same structure as seen in (d).

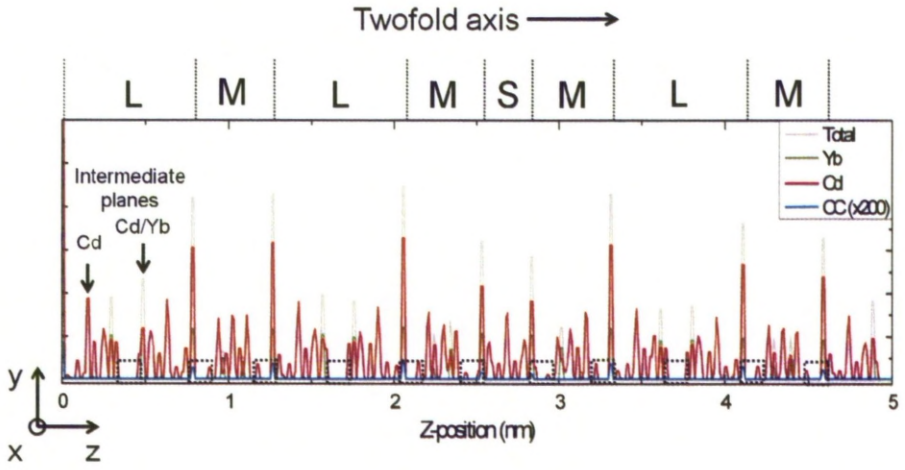

Figure 6.12: Variation in the atomic density in layers along the twofold axis using a step size of 0.01 nm. Red indicates Cd, green indicates Yb, blue indicates cluster centers (which has been increased by a factor of 200) and the grey line represents the overall atomic density.

The autocorrelation of this surface, shown in figure 6.11 (e) shows a pattern displaying maxima in three different directions. The first maxima have varying distances of 2.64 nm, 3.00 nm and 3.28 nm which relate to the separations of the protrusions in the STM images. Successive maxima in each of these directions have separations that are related by a factor of τ. The internal angles of the positions of the maxima are measured to be 74°, 58° and 48°. The separations of the rows and linkages in twofold surface 1 are related to the separations of the protrusions in twofold surface 2 by a factor of τ.

An FFT calculated from figure 6.11 (d) is shown in figure 6.11 (f). This FFT confirms a twofold ordering, as well as τ scaling indicating the presence of aperiodicity. For both FFT's two groups of spots have been highlighted by a broken white box. These boxes indicate corresponding maxima that have the same k-values.

Comparison with the *i*-Cd-Yb model

Like the five and threefold surfaces, there are a number of atomic planes that occur on the *i*-Cd-Yb model that could potentially be responsible for the surfaces observed by STM. Figure 6.12 shows the distribution of atoms along the twofold axis. Immediately it is possible to identify several high density and moderate density planes. Several gaps in atomic density have also been

highlighted by broken black boxes.

Figure 6.13 shows the atomic planes that could potentially be responsible for a surface. Firstly, the planes of moderate density that occur between atomic planes that intersect the center of the RTH clusters are considered. Figure 6.13 (a) displays a low density plane composed entirely of Cd, while figure 6.13 (b) shows a low density plane composed of both Cd and Yb. While the image in figure 6.13 (a) shows a row structure, the row spacings are too large. Also, the density of atoms in this image could not be responsible for the crowded nature of the STM images. Figure 6.13 (b) features rows of Yb atoms, which have spacings similar to those observed by STM. However, the density of this plane is again too sparse to be responsible for the observed STM images. Also, selecting either of these planes as a surface termination produces step heights that are much smaller than those observed by STM. As such, both planes are discounted.

Figures 6.13 (c) and (d) both show atomic planes that intersect the RTH cluster centers, with (c) displaying a less dense version of (d). The most striking feature of these planes are the bands of Cd atoms. The structure of these bands features Cd atoms adopting a zig zag motif. The separation of these bands varies from 1.27 nm to 1.57 nm. This range of separations encompasses the observed row separation from twofold surface 1. The distances between clusters along a direction parallel to these bands is 2.05 nm, which matches the distances of the linkages from twofold surface 1. The angle between the Cd row and the linkage formed by a cluster center is 90°. Figure 6.13 (d) also exhibits the same features and separations, of bands of Cd atoms and of cluster center separations along a direction parallel to these bands. There are, however, smaller cluster center separations along a direction parallel to the Cd bands, which are not observed by STM. However, while the linkages observed by STM occur often, they do not always occur when expected. It is highly likely that linkages that exhibit smaller distances than 2.05 nm are not observed by STM. This is described in more detail below.

The origin of the protrusion structure of twofold surface 2 is unclear when considering the entirety of the atomic planes that intersect the RTH cluster. By considering only the cluster center positions in figure 6.13 (c), it is possible to construct a rhombus of edge length 2.41 nm. This edge length agrees with one of the cluster separations as seen in figure 6.11 (d). This does not explain the larger edge length however. This time, considering the cluster center positions in figure 6.13 (d) is is possible to create a parallelogram of edge lengths 2.41 nm and 2.98 nm, with both edge lengths similar to the protrusion separations in figure 6.11 (d). This indicates

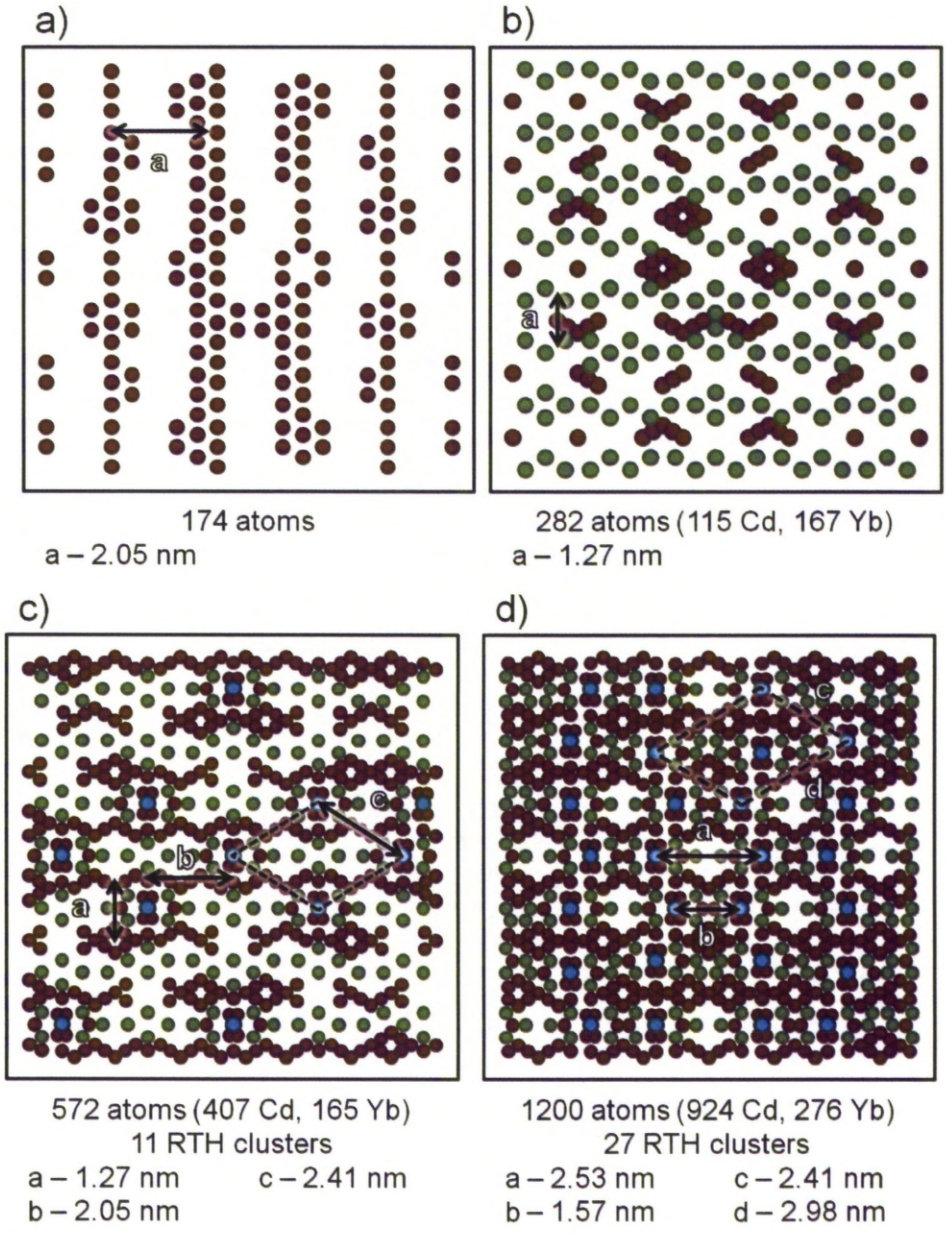

Figure 6.13: Four atomic planes that could potentially create a surface plane. These planes are, (a) a Cd plane, (b) a Cd/Yb plane, (c) a lower density plane intersecting an RTH cluster and (d) a dense plane intersecting RTH clusters and (10 nm × 10 nm) Red dots represent the positions of Cd, green dots the position of Yb, and blue dots the center of the RTH clusters.

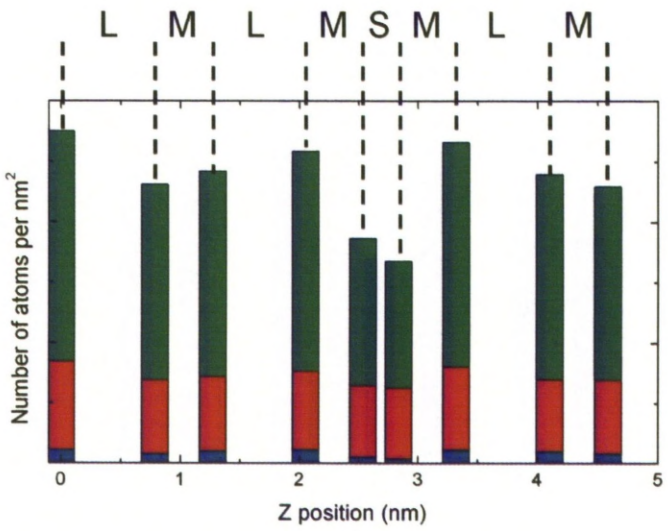

Figure 6.14: The atomic density of viable surface terminations along the twofold axis using a step size of 0.01 nm. Blue indicates the amount of cluster centers (which has been increased by a factor of 100), red indicates the amount of Cd and green indicates the amount of Yb.

that the protrusions and linkages occur at the positions of the RTH cluster centers.

By considering only the atomic planes that intersect RTH clusters, it is possible to determine what step sizes and sequence will be established from this surface selection. This is shown in figure 6.14. Three steps of size $S = 0.30$ nm, $M = 0.48$ nm and $L = 0.78$ nm and occurrences of 13%, 50% and 37% respectively, are formed from this selection of surface planes. The sizes of all three steps and their frequency match STM measurements. Also, the plane separations formed form this surface selection are related to each other by a factor of τ, such that $\frac{M}{S} = \frac{L}{M} = \tau$.

Due to the distribution of step heights and density occurring from the atomic planes that intersect RTH cluster centers, it is determined that these atomic planes are responsible for surface terminations. The step height distribution, low density and lack of features relatable to the STM precludes the selection of the intermediate atomic planes.

The STM results indicate that while being observed by this technique, the surface exhibits a bias dependency. A negative bias image can be considered to be a crowded twofold surface 1. At a negative bias the density of states of all three elements, Ag, In and Yb, are probed. Since there is a high density of all three species at the surface, an STM image will be composed of a large amount of features, giving an overall crowded appearance. The Cd atoms form bands across the

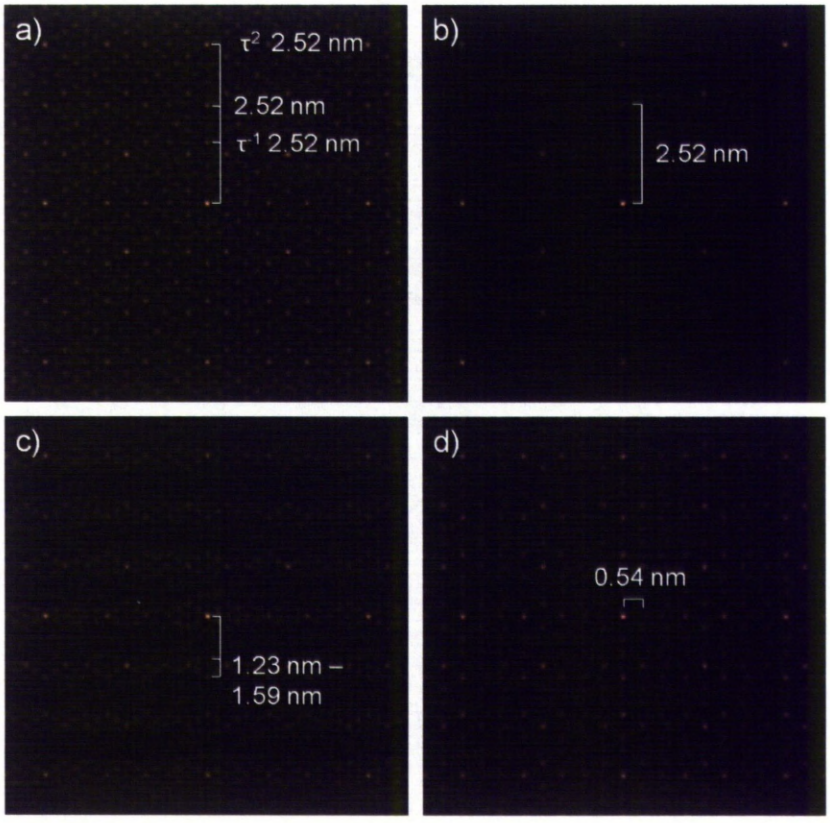

Figure 6.15: Autocorrelations of a high density plane from the i-Cd-Yb model along the twofold axis concentrating on specific features; (a) Cd and Yb atoms, and cluster center positions. (b) Cluster center positions. (c) Cd atoms only. (d) Yb atoms only. (All images 10 nm × 10 nm)

surface which will have a density of states concentrated about them, which is consistent with the observed STM results. At a positive bias, the visible states around the Yb atoms are emphasised. Although there is no particular concentration of Yb atoms about an RTH cluster center position, the density of Yb on these planes (elaborated below) would mean that the tunneling current from other species is also contributed at this bias. Hence, when considering Cd, there is an overall concentration of atoms about the RTH cluster center positions, and it is also possible to sometimes measure a contribution from the bands of Cd atoms.

Surface ordering

To provide further evidence that these atomic planes are responsible for the surfaces observed, autocorrelations of the model are considered. The least dense atomic plane that intersects the

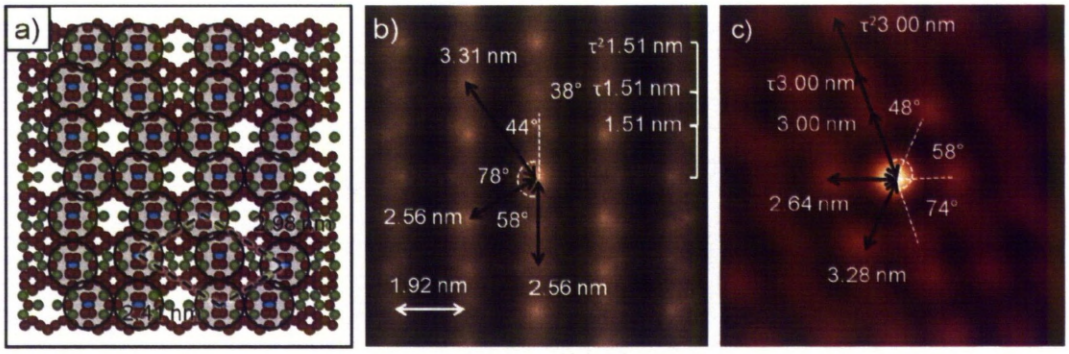

Figure 6.16: (a) An atomic plane intersecting RTH clusters along the twofold axis with an area of $\sim$ 1.30 nm around the positions of the cluster centers emphasised. (10 nm $\times$ 10 nm) (b) An autocorrelation of image (a). (10 nm $\times$ 10 nm) (c) A copy of figure 6.11 (e) (15 nm $\times$ 15 nm)

RTH cluster centers was chosen due to the clarity in the produced patterns when compared to autocorrelations taken using the higher density atomic plane. The autocorrelations are shown in figure 6.15. Firstly the autocorrelation calculated from the contribution of all present atoms and cluster center positions, shown in figure 6.15 (a), shows a τ scaling of successive bright maxima. The autocorrelation taken from the cluster center positions (figure 6.15 (b)) demonstrates a first order maximum whose separation from the center agrees with the smaller separation of clusters observed on twofold surface 2. The autocorrelation taken from just the Cd atoms (figure 6.15 (c)) Displays bands of maxima across the image. The separation of these bands is between 1.23 nm and 1.59 nm, which agrees with the model and STM observations of rows on twofold surface 1. The Yb placements (figure 6.15 (d)) generate an autocorrelation which features rows of bands. The separation of these bands of 0.54 nm does not correspond to any separations observed by STM.

To further explain the origin of the protrusions displayed on twofold surface 2, only the cluster center positions are considered. The positions of the center of the RTH clusters is no longer envisioned as a point source, but is instead increased in size to match that of a protrusion, of $\sim$ 1.30 nm. This is shown in figure 6.16 (a). The size of these protrusions encompasses several Cd and Yb atoms. The autocorrelation of this is shown in figure 6.16 (b). Rows of maxima are observed that have distances that are τ scaled. The highlighted distances from the specular to the maxima are 2.56 nm and 3.11 nm, with angles of 44 °, 58° and 78°. Both the distances and angles are observed in the comparative autocorrelations taken from STM images, as shown

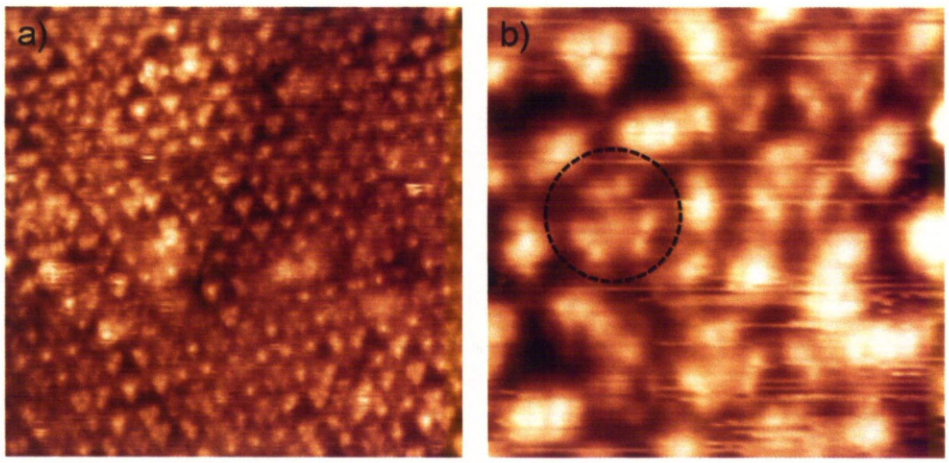

Figure 6.17: (a) an STM image taken from the clean twofold *i*-Ag-In-Yb surface (35 nm × 35 nm). (b) A close up of an area from (a) (10 nm × 10 nm)

again in figure 6.16 (c).

It is possible to create parallelograms using the positions of cluster centers as the vertices, and an example is shown in figure 6.11 (a). The edge lengths of this parallelogram are 2.41 nm and 2.98 nm, and internal angles are 64°and 116°. These edge lengths and internal angles match up with the parallelogram created in the previous STM image shown in figure 6.11 (a), of 2.55 ± 0.15 nm and 3.03 ± 0.13 nm, and 65°and 115°. Angles observed in the autocorrelations of 44 °, 58° and 78° are present when considering the next nearest cluster center position.

It was mentioned previously that in some instances linkages do not appear on twofold surface 1 as shown in figure 6.11 (a). It is possible that these features are not appearing at the surface for similar reasons to why certain Yb atoms do not appear on the threefold surface. However these atoms are not glue atoms, so the reason why they may not be at the surface has yet to be confirmed. The current understanding suggests that some feature relating to the position of the cluster center is responsible for the protrusions. But, due to the lack of atomic resolution obtained in the STM images, it is problematic to identify features observed in experiment with features occurring on the model with a large degree of certainty.

Impurity phases

During a separate experiment at Ecole des Mines conducted by Sharma *et al.*in Nancy, a structure on the twofold crystal that is more closely related to the threefold surface was

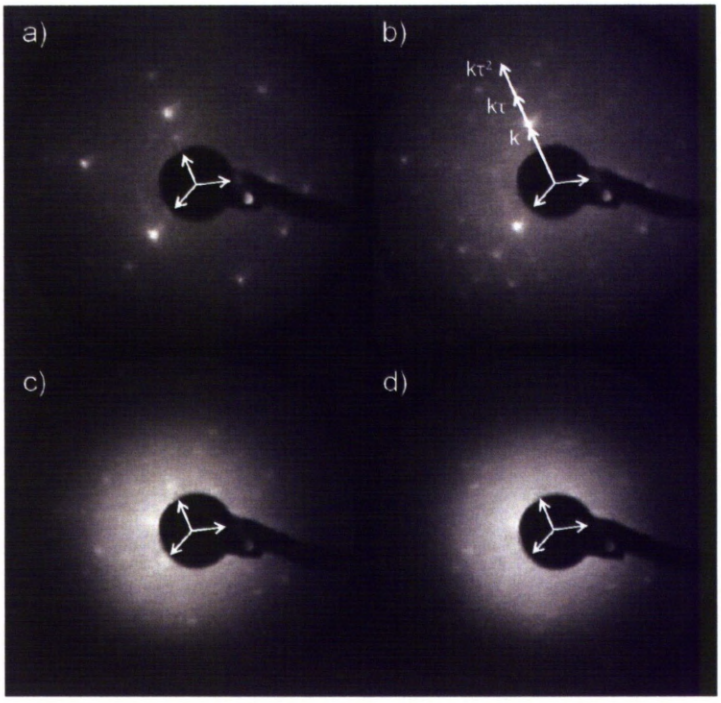

Figure 6.18: LEED patterns taken from the threefold *i*-Ag-In-Yb surface at energies of (a) 15 eV, (b) 20 eV, (c) 40 eV and (d) 50 eV.

observed. Figure 6.17 (a) shows an example of the images taken during this experiment. The surface appears predominantly threefold in its ordering, which is emphasised in FFT patterns. A closer look at the protrusions, as seen in figure 6.17 (b), shows a triangle arrangement of distorted hexagons. These formations appear as a principle feature on the threefold surface. It is likely that this impurity was formed during the crystal's growth, or manifested during a preparation cycle.

6.3.3 LEED

Both high symmetry surfaces give well defined and strong LEED patterns. These occur at energy ranges of around 10 eV up to around 60 eV. Threefold LEED patterns are shown in figure 6.18 and twofold LEED patterns are shown in figure 6.19.

The threefold surface LEED patterns show a clear threefold symmetry. The LEED patterns exhibit many diffraction spots, indicating the well ordered three and six fold symmetries that are present on the surface. This also shows that the ordering is well preserved over long distances.

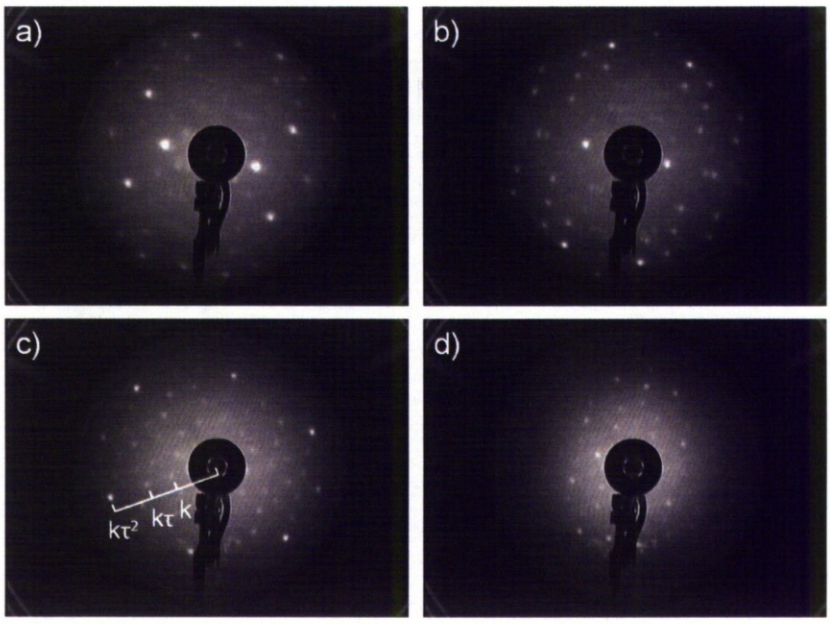

Figure 6.19: LEED patterns taken from the twofold i-Ag-In-Yb surface at energies of (a) 15.7 eV, (b) 20 eV, (c) 26 eV and (d) 35 eV.

Increasing orders of maxima are also τ scaled, shown in figure 6.18 (b).

The twofold surface LEED patterns show a clear twofold symmetry. The LEED patterns displays a greater number of diffraction spots. This indicates that there is atomic ordering on the surface that has yet to be observed with STM. Increasing orders of maxima are also τ scaled, shown in figure 6.19 (c). This confirms the presence of aperiodicity expected from the icosahedral geometry present.

6.3.4 XPS

XPS spectra of the clean two and threefold surface for Ag 3d, In 3d and Yb 4d are shown in figure 6.20 (a), (b) and (c) respectively. Like the fivefold system, these are compared with the core levels of a Ag(111) crystal and pure (99.9%) metallic foils of In and Yb. The surface compositions have been found to be; threefold $Ag_{63.0\pm1.4}In_{27.3\pm1.0}Yb_{9.7\pm0.6}$ and twofold $Ag_{62.1\pm1.1}In_{27.8\pm0.8}Yb_{10.1\pm0.5}$ after sputtering, and threefold $Ag_{37.9\pm0.9}In_{43.5\pm1.4}Yb_{18.7\pm1.0}$ and twofold $Ag_{34.7\pm0.5}In_{45.5\pm1.0}Yb_{19.8\pm0.7}$ after annealing. This indicates that the annealed surface composition is comparable to that of the bulk, and similar to the composition of the fivefold surface.

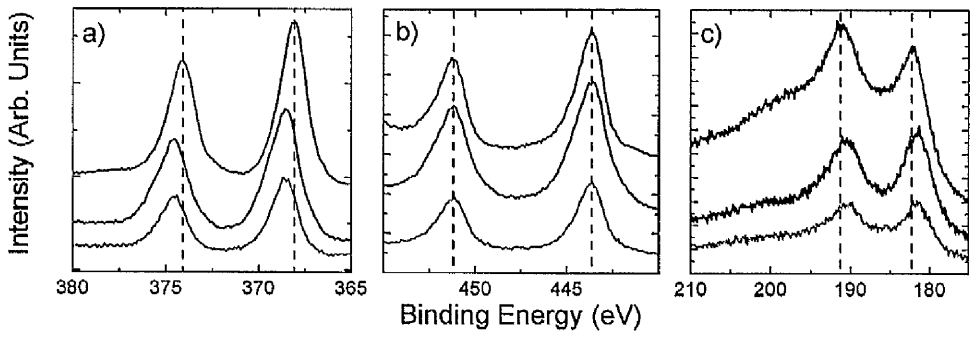

Figure 6.20: XPS spectra of the clean two and three fold surface of *i*-Ag-In-Yb and pure metal core levels for (a) Ag 3*d*, (b) In 3*d* and (c) Yb 4*d*. Twofold spectra are represented by blue lines, threefold spectra by green lines, and spectra from the pure metals are represented by black lines.

The binding energies for Ag 3*d*, In 3*d* and Yb 4*d* from the two and threefold surfaces are similar. Indium binding energies for both surfaces are unchanged from that of the pure metal, while Ag binding energies for both materials have undergone an energy shift to a higher binding energy, while the Yb binding energies for both materials have undergone a shift to a lower binding energy. These results are in agreement with those from the fivefold surface.

6.4 Relative stabilities

The twofold and threefold surfaces demonstrate comparable stability to the fivefold surface. The samples yield surfaces that are atomically flat and composed of steps and terraces and display no evidence of faceting. The formation of these surfaces is in contrast to that of the *i*-Al-Pd-Mn system. The surface of the twofold *i*-Al-Pd-Mn system does not exhibit the same stability as that of the fivefold *i*-Al-Pd-Mn surface [129, 146]. This surface produced LEED patterns that match that expected from a twofold face centered icosahedral phase and the surface composition is more closely matched to that of the bulk. However there is evidence of facetting on the surface, with domains roughly 150 Å in size being present. These facets are closely related to the proximity to the edge of the sample, and orientations along the threefold and fivefold symmetry axes. The threefold *i*-Al-Pd-Mn surface exhibits similar behaviour to the twofold *i*-Al-Pd-Mn surface [129], in that it produces the expected threefold diffraction patterns for this phase. Facetting also occurs for this surface, with facets oriented along the fivefold

axis and an unknown axis. This also indicates that the threefold surface is less stable than the fivefold *i*-Al-Pd-Mn surface. Such facetting was however not observed on any of the high symmetry surfaces of *i*-Ag-In-Yb when examined with STM or LEED, indicating that all three surfaces have similar stabilities.

Table 6.2: Atoms per nm^2 of a typical atomic plane that constitutes surface terminations for the five, three and twofold surfaces of the *i*-Ag-In-Yb quasicrystal.

Atomic density		5f	3f	2f
Yb	3rd shell	1.50	1.24	1.82
	Glue atom	0.61	0.22	0.58
	Total	2.11	1.46	2.40
Ag/In	1st shell	-	-	1.62
	2nd shell	-	-	1.62
	4th shell	1.71	0.32	1.58
	5th shell	-	-	3.27
	Total	1.71	0.32	8.09
Overall total		3.82	1.78	10.49
Overall total (no glue atoms)		3.21	1.56	9.91

The selection of a surface plane is dictated by three rules as mentioned previously; The atomic density of the surface plane, the surface free energy of the elements that constitute the surface plane, and the presence of a gap in the atomic density of sufficient size adjacent to the surface plane. For the first factor, the densities of typical atomic planes giving rise to five, three and twofold surfaces are presented in table 6.2. The atomic densities of Ag(111), In(100) and Yb(111) crystals are 11.89, 9.43 and 6.62 atoms nm^{-2}. These orientations were chosen as they yield the greatest atomic densities of all possible orientations for these specific species. By considering these densities and the composition of each surface (specified previously), the surface atomic density can be considered to be 8.10 atoms nm^{-2}, 7.21 atoms nm^{-2} and 9.69

Table 6.3: Percentages of Ag and In in the 1st, 2nd, 4th and 5th shells of the RTH cluster, from the 1/1 approximant. The 3rd shell is composed of 100% Yb. Values provided courtesy of Cesar Pay Gómez [137].

Shell		In	Ag
1st		100%	0%
2nd		40%	60%
4th		80%	20%
5th	Vertex	63%	37%
	Midedge	0	100%
	Total	22%	78%

atoms nm^{-2} for the five, three and twofold surfaces respectively. These densities are similar to those exhibited by the surfaces of the crystalline constituents of this quasicrystal.

Table 6.4: Overall percentage populations of In and Yb in a typical surface for the five, three and twofold planes.

Symmetry plane	Ag	In	Yb	In and 3rd shell Yb
5f	9-12 %	37-55%	31-54%	80-85%
3f	5-10 %	19-40%	50-77%	84-89%
2f	37-42 %	25-41%	23-33%	52-57%

While the pure metals have no other factor for the density of their surface planes other than at which angle a surface is created at, the quasicrystal surfaces exposed surface planes are influenced heavily by what atomic species make up the surface plane as well as the density. Figure 6.4 shows the percentages of elements that occur at potential surfaces for all three high symmetry planes, as calculated from the model. The surfaces of each three planes are dominated by Yb and In, while having relatively smaller amounts of Ag. The surface free energies of surfaces of Ag, In amd Yb are 1.302 Jm^{-2}, 0.591 Jm^{-2} and 0.428 Jm^{-2} respectively [142]. While surface free energy is determined by the density of the packed atoms, there is a coincidence that the potential surfaces are made from planes that have high concentrations of elements which have

lower surface free energies.

For the third factor of surface selection, gaps in atomic density are observed for the five and twofold planes, although only a small gap occurs at an atomic plane responsible for a threefold surface plane. The appearance of these atomic gaps at a surface plane is consistent with the provision of an interlayer spacing occurring with a surface termination for an icosahedral quasicrystal [16]. However, it appears that the most influential factors are the surface free energy of the plane, followed by the atomic density, and finally the presence of a gap accompanying a surface termination.

It is generally regarded from STM and LEED observations that the five, three and twofold surfaces all have comparable stabilities. This is evidenced by the step terraced structure presented by STM, and the clear and sharp diffraction patterns they produced. On the macroscopic scale, it is a reasonable to estimate that a crystal grown by a suitable method (for example, the flux method) will exhibit facets relating to the most stable plane. This is the case for *i*-Al-Pd-Mn which only expresses fivefold facets [147]. For this crystal, the fivefold plane is the most stable plane. For the *i*-Ag-In-Yb quasicrystal, an ingot grown by the flux method, as shown in chapter 5 figure 5.1 (a), exhibits five, three and twofold facets. Assuming that the facets yielded by an ingot of this method are indicative of the stability of the high symmetry planes, then for *i*-Ag-In-Yb the five, three and twofold surface planes offer comparative surface stabilities.

6.5 Summary

The two and threefold surfaces have been investigated by STM. Both surfaces yield atomically flat step terraced structures that, like the fivefold surface, exhibit a degree of bias dependency. The threefold surface is composed of terraces that originate from atomic planes that intersect the center of the RTH clusters, which exhibit aperiodicity as observed from FFT patterns. These atomic planes present Yb configurations that match the distorted and regular hexagon, and other triangular arrangements observed on the surface by STM. The twofold surface also presents large terraces, which are also formed on atomic planes that intersect the center of the RTH clusters. Two structures have been measured from the surface; a dense crowded surface where surface features are hard to image, and a surface featuring an arrangement of protrusions. Both of the twofold surfaces observed exhibit twofold ordering and aperiodicity as indicated

by their respective FFT patterns. These surfaces can be explained using the same atomic planes, by considering the singular atomic arrangements in the case of the crowded surface, and considering larger objects at the positions of the center of the RTH clusters for the surface displaying protrusions.

Both surfaces produce good quality LEED diffraction patterns that emphasize the ordering present on the surfaces, as well as the aperiodicity inherent in this system. Surface composition as measured by XPS is similar to that of the bulk.

The stability of all three surfaces can now be understood in terms of their elemental composition and density. On the nanoscale all three surfaces exhibit the same stability as is indicated by the presence of large terraces for all three surfaces. On a macroscopic scale, the primary factor for stability is the surface free energy, with a contribution from the atomic density of the surface plane. This is shown by observing the shape of an ingot of *i*-Ag-In-Yb which exposes large fivefold surfaces, moderate sized threefold facets and small twofold facets.

Chapter 7

Growth of thin films on the icosahedral Ag-In-Yb quasicrystal

7.1 Introduction

The growth of thin films is an important technique in several applications such as electronics. The ability to coerce an element to grow in a manner that it classically does not adopt also allows the study of the interactions between substrates and adsorbates. Antimony provides a potential candidate for the formation of a single element quasicrystalline overlayer on the *i*-Ag-In-Yb crystal. This element is similar to others that have successfully formed quasiperiodic overlayers on other quasicrystals, as it has a similar size to Sn and has a similar electronic configuration to Bi, two elements that have previously been seen to form quasiperiodic overlayers [39, 92]. Antimony has been shown to form quasiperiodic overlayers on *i*-Al-Pd-Mn and *d*-Al-Ni-Co [30] and as such the evidence for it adopting an aperiodic structure is promising.

There are also other potential candidates for the growth of single element quasiperiodic overlayers. A current study by the Liverpool quasicrystal group featured the deposition of Pb on the clean fivefold surface of *i*-Ag-In-Yb. A summary of this work is shown in figure 7.1. At sub-monolayer coverages the Pb atoms form localised fivefold features on top of the truncated RTH clusters. Upon completion of the monolayer, a bilayer begins to form. This second layer takes the formation of an aperiodic arrangement of decagonal rings of Pb atoms. Further growth leads to the formation of Pb(111) islands whose orientation is modulated by the quasiperiodic

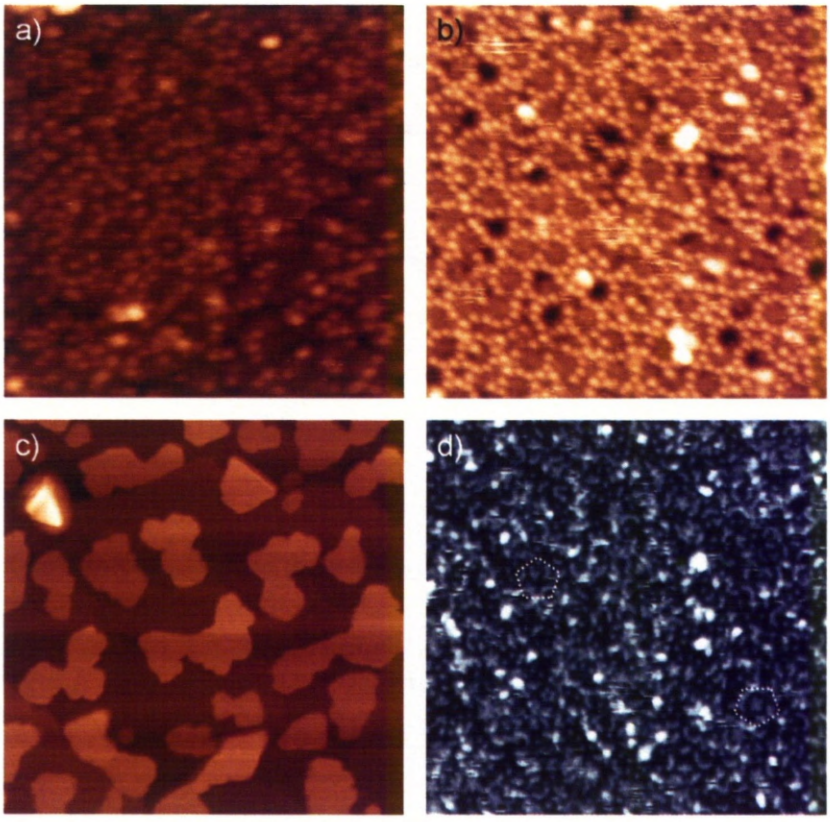

Figure 7.1: STM images of the deposited Pb thin film on the clean fivefold surface of the *i*-Ag-In-Yb quasicrystal. (a) Monolayer (30 nm × 30 nm), (b) Bilayer (30 nm × 30 nm) and (c) Triangular Pb islands (400 nm × 400 nm). (d) An STM image of a bilayer of Bi on the same surface. (50 nm × 50 nm)

substrate.

Another current study features the growth of Bi on the same surface with an example shown in figure 7.1 (d). Initial results show sub-monolayer depositions of Bi atoms forming pentagons on the truncated RTH clusters in a similar way to sub-monolayer coverages of Pb. The Bi thin film only forms up to a monolayer, with this monolayer resisting the growth of a bilayer, islands, or any disordered growth.

While it is possible to grow single element quasiperiodic overlayers, interest lies with replicating such growth using molecules. Buckminsterfullerene has an a truncated icosahedron structure made up from 60 carbon atoms, and essentially behaves like a large atom. This provides an excellent candidate in probing the adsorption properties of a surface using a molecule. C_{60}

is also a P-type semiconductor material, and provides a potential choice in the application of growing optically active layers on top of other materials in an attempt to create new types of photo-sensitive materials.

7.2 Experimental Details

Sample 2 was used in the studies of Sb deposition for this system. The fivefold sample was treated in the same way for this experiment as it was when it was characterised. This involves the same cleaning method using diamond paste, and the same parameters when sputtering and annealing. STM measurements were performed using an Omicron variable temperature STM operating at room temperature and at constant current mode. The surface was prepared until it presented flat terraces of sizes greater than 200 nm. This was to ensure that time was not wasted finding a flat area in between depositions.

Sb was deposited using an Omicron triple cell EFM-3 electron-beam evaporator. The evaporant was placed within a molybdenum crucible which was then inserted into the evaporator. A high voltage was applied until a flux was detected, and the current adjusted until the required flux was obtained. A flux of 120 nA/sec provided a deposition rate of 0.05% of a monolayer per second on the clean surface. Pressure during deposition was 2×10^{10} mbar. C_{60} was deposited using a home built evaporator comprising a tungsten filament wrapped tightly around a Pyrex crucible containing C_{60} powder. The sample remained at room temperature during deposition. The evaporator was operated at temperatures of 485-495K.

For XPS measurements, the growth of Sb was with non-monochromatised Mg K_α radiation ($h\nu$ =1486.6 eV) using a PSP Vacuum Technology hemispherical electron-energy analyzer. UPS measurements were performed with non-monochromatised He I radiation (21.2 eV) at normal emission. Helium pressure in the analysis chamber was kept constant (3×10^{-8} mbar) for all UPS measurements. All XPS and UPS measurements were performed at room temperature with the sample oriented normal to the analyser. Photoemission experiments were conducted in a different chamber to STM measurements. The surface was oxidised by gradual contamination from the residual gases within the chamber.

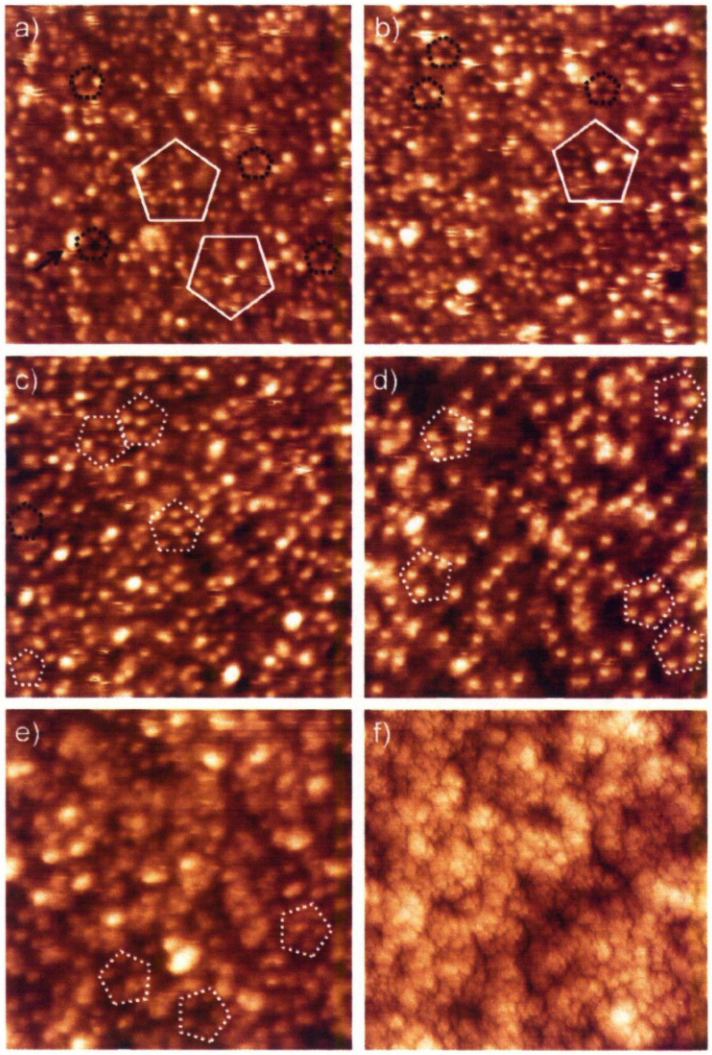

Figure 7.2: Negative bias STM images of Sb deposited on the fivefold *i*-Ag-In-Yb surface at 0.15 ML (a), 0.30 ML (b), 0.85 ML (c), 1.25 ML (d), 1.65 ML (e) and 15.5 ML (f). Image (f) Has been superimposed on its derivative to enhance the present features (all images are 30 nm × 30 nm, except for (f) which is 150 nm × 150 nm)

7.3 Results

7.3.1 STM

High resolution STM images

The deposition of Sb on the fivefold clean surfaces has been investigated at several coverages, ranging from sub-monolayer to several monolayers of deposited material, and at positive and negative bias. STM images of specific coverages and bias are elaborated upon here. Coverages are calculated by analysing the area of substrate that is covered by the adsorbed material. Figure 7.2 shows negative biased STM images at coverages of 0.15 ML up to 15.5 ML.

At a coverage of 0.15 ML the substrate is still visible as shown in figure 7.2 (a). The brighter

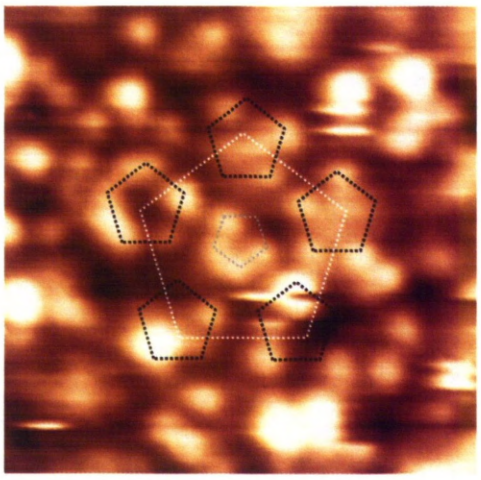

Figure 7.3: Deposition of 0.30 ML of Sb on the clean fivefold surface of *i*-Ag-In-Yb. A small pentagonal feature is highlighted by a grey broken pentagon.

spot-like features are related to the positions of Sb atoms with a height of 0.06 ± 0.01 nm. The Sb atoms form pentagons of edge length 0.97 ± 0.04 nm which are all oriented in the same direction. Several incomplete pentagons and the pentagonal tiling of the substrate are highlighted by broken black pentagons. Figure 7.2 (b) shows a 0.30 ML deposition of Sb. At this coverage a greater number of complete pentagons are observed.

A 0.85 ML coverage of Sb features the formation of larger pentagonal arrangements shown in figure 7.2 (c) highlighted by broken white pentagons. The pentagons have a height of 0.18 ± 0.02 nm from the substrate and thus are part of a second layer. The larger Sb pentagons have an edge length of 1.60 ± 0.06 nm, which is related to the size of the smaller Sb pentagons of the first layer by a factor of τ, and the larger pentagons have two different orientations, rotated by 36°. Several incomplete small Sb pentagons from the first layer are still observed.

While the majority of Sb atoms form features on top of the truncated RTH clusters, smaller features form within the pentagonal arrangements of cluster centers of the substrate. Figure 7.3 shows a pentagonal arrangement of RTH clusters with forming Sb pentagons on top of them. In the center of this arrangement, another Sb pentagon begins to form. The atoms that form this pentagon express the same height as the atoms forming pentagons on the truncated RTH clusters. While these features are seen to form readily, a complete pentagon has yet to be observed, with incomplete pentagons being predominantly present. The size of these smaller Sb

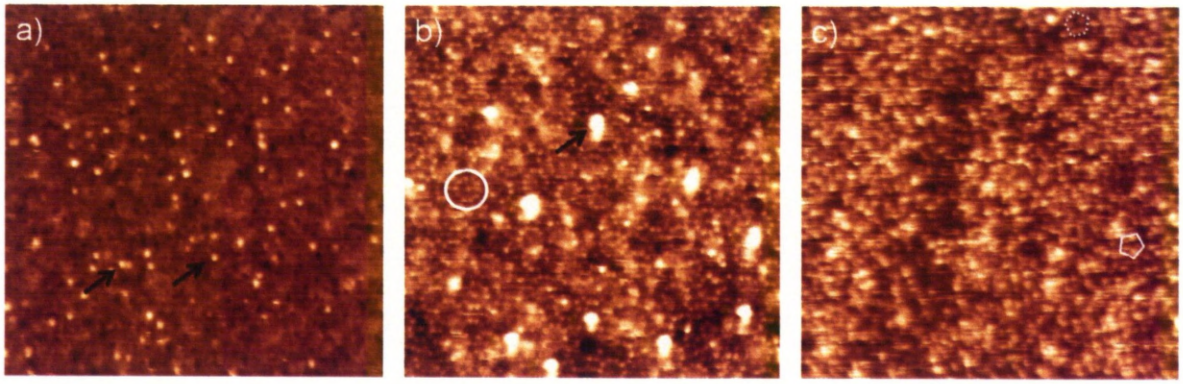

Figure 7.4: Positive bias STM images of Sb deposited on the fivefold *i*-Ag-In-Yb surface at coverages of (a) 0.15 ML (75 nm × nm) (b) 0.85 ML (30 nm × 30 nm) and (c) 1.70 ML (75 nm × 75 nm). Arrows indicate the positions of protrusions unrelated to the Sb monolayer.

pentagons is roughly 0.57 nm, which is scaled down in size by a factor of τ when compared to the other first layer Sb pentagons. Due to the rarity of these features it is not possible to conclude whether they only form in one orientation of pentagonal features formed by the truncated RTH clusters of the substrate. These formations are also observed during the growth of the Bi thin film on the fivefold surface of *i*-Ag-In-Yb. The small pentagons are mainly observed in only one orientation of larger pentagons formed by the truncated RTH clusters. For the Pb system these smaller pentagons are not observed.

Depositing up to 1.25 ML of Sb yields a layer containing more complete pentagons as shown in figure 7.2 (d). There are many complete and incomplete larger Sb pentagons at this coverage. At a coverage of 1.65 ML, the structure becomes obscured by clumps of disordered Sb (figure 7.2 (e)) but it is possible to observe larger Sb pentagons as well as the disordered Sb. A deposition of 15.5 ML of Sb leads to disordered growth covering the terraces as shown in figure 7.2 (f). Annealing high coverages produced an overlayer that was too rough to scan by STM.

Figure 7.4 features STM images taken at a positive bias at different coverages. Unlike the images taken at a negative bias, no Sb pentagons are observed at low coverages. This was attempted during repeat experiments with the same outcome. Instead, it is possible to image the substrate directly with no intervening adsorbed structures present. For example, figure 7.4 (a) shows an image at a 0.15 ML coverage of Sb. In this image black dots are observed which are related to the middle of the Yb rings, which is the expected structure of the clean substrate

at this bias. Also, several protrusions are imaged, indicated by black arrows. The height of these protrusions is 0.149 ± 0.03 nm, and have a FWHM of 0.99 ± 0.27 nm determined using a line scan as detailed in chapter 5. These protrusions are also observed on negative bias images. These features are considered to be related to Sb and are not encountered on the clean surface.

Figure 7.4 (b) shows an STM image at a 0.85 ML deposition of Sb. In this image, the density of states attributed to the Yb atoms has been enhanced, with the decagonal arrangement of atoms within the rings observable. More protrusions are also observed. Figure 7.4 (c) demonstrates an STM image at a deposition of 1.70 ML. The adsorbate appears as a disordered layer, with FFT's of the adsorbate appearing diminished when compared to FFT's taken from a deposition of 1.65 ML. Some areas of fivefold structure observable in the form of pentagons of edge length comparable to the pentagons encountered on the 2nd layer of Sb as observed at negative bias. Depositing more Sb yields disordered layers comparable to images taken at a negative bias, indicating the bias dependency is not observed at higher coverages.

Ordering of the thin film

By studying the FFT patterns of the STM images, the presence of long range ordering can be ascertained. Figure 7.5 (a) shows an FFT pattern of this surface after the deposition of Sb, but with the contribution from the substrate removed. This denotes an FFT pattern that arises from the adsorbate only. The resulting pattern mimics that of the clean fivefold surface indicating that the Sb pentagons are forming on the repeating features of the substrate, namely the truncated RTH clusters. The subsequent maxima of this pattern are τ scaled. An FFT from the second layer is shown in figure 7.5 (b), again with the contribution from the substrate removed. The inner maxima correlate to that of the clean surface and are again τ scaled, and higher orders of maxima are now observable. Both films share the same k-vector value.

The autocorrelations of the monolayer and second layer after height filtering to remove the contribution of the substrate are shown in figure 7.5(c) and (d) respectively, after the contribution of the substrate has been removed. Both patterns are reminiscent of clean surfaces autocorrelation explained earlier in chapter 5, with τ scaled maxima separations comparable to cluster separations measured by STM. This indicates that the Sb thin film's structure is dictated by that of the substrates structure. For the monolayer autocorrelation a ring is observed around the specular. This ring is related to the edge length of the Sb pentagons, with a spec-

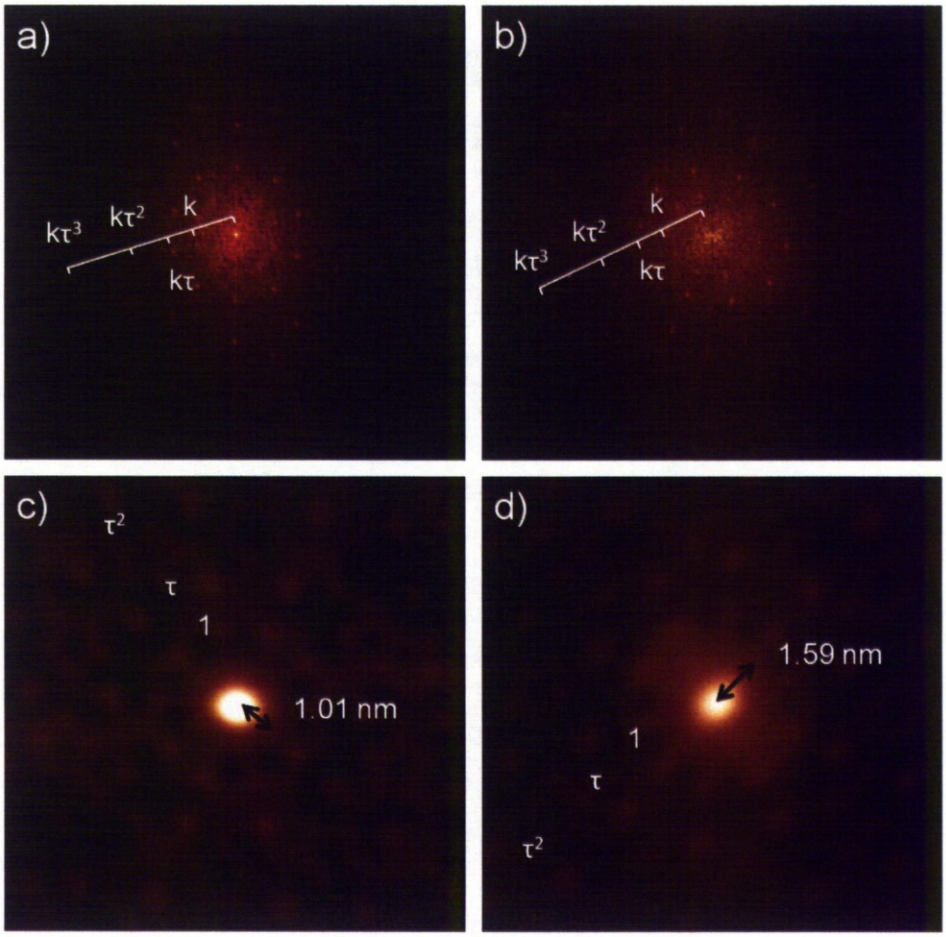

Figure 7.5: (a) Fast Fourier Transforms of the (a) monolayer (0.85 ML) and (b) bilayer (1.65 ML) of Sb deposited on the clean fivefold surface of *i*-Ag-In-Yb. (c) and (d) Autocorrelation of the Sb monolayer and the Sb bilayer at the same coverages as the respective FFT's (a) and (b) (15 nm × 15 nm). The contribution of the substrate was removed prior to the calculation of the FFT's and autocorrelations.

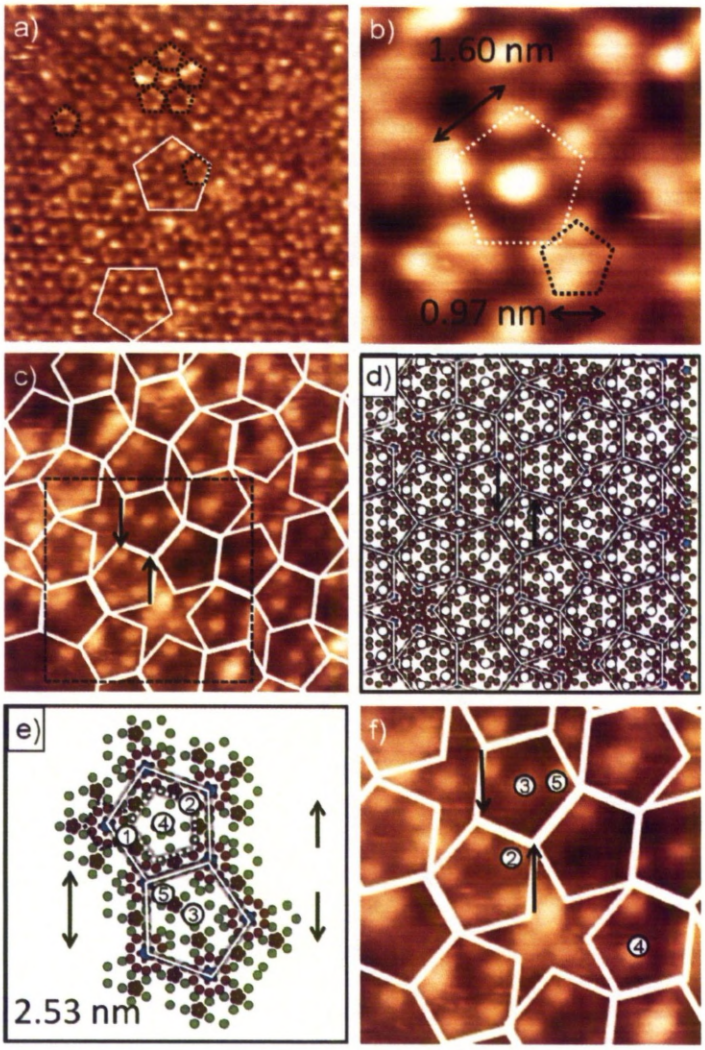

Figure 7.6: STM and model images showing the positions of Sb atoms on the clean fivefold surface of *i*-Ag-In-Yb. (a) Fourier filter enhance STM image at a coverage of 0.85 ML of Sb (30 nm × 30) nm). (b) Close up of a partially formed large Sb pentagon at a coverage of 1.25 ML of Sb. (c) Tiling super imposed on a coverage of 1.65 ML of Sb (20 nm × 20 nm) (d) Model structure of *i*-Cd-Yb with a super imposed P1 tiling, decorated with the theoretical positions of Sb (20 nm × 20 nm. Cluster centres, Cd (Ag/In) atoms, Yb atoms and Sb atoms indicated by blue, green, red and white sots respectively. Smaller and darker red spots indicate Cd (Ag/In) atoms on lower atomic planes). (e) A pentagonal arrangement of 8 RTH clusters taken from the *i*-Cd-Yb model detailing specific absorption sites.

ular to ring distance of 1.02 nm. This agrees with the atomic separation of Sb as measured by STM. For the bilayer autocorrelation this ring is now more diffuse and has a radius of 1.59 nm. This is scaled larger by a factor of τ when compared to the ring observed for the monolayer autocorrelation. The size of this ring corresponds to the edge length of a second layer Sb pentagon.

Comparison with the *i*-Cd-Yb model

Comparing STM images with the model structure, adsorption sites can be identified. Figure 7.6 (a) shows a Fourier pass filter enhanced STM image of the fivefold *i*-Ag-In-Yb surface at a coverage of 0.85 ML. The enhancements added to this image assist in identifying the positions of the RTH clusters, with the monolayer Sb pentagons decorating the top of the substrate features.

This observation is evaluated in relation to a simple configuration of one up and one down pentagon constructed from RTH clusters from the substrate, with the atomic positions of the surface atoms and the two underlying layers considered also, with these atomic layers positioned at a distance of 0.40 Å and 0.51 Å from the surface termination respectively. This is shown in Figure 7.6 (e). Equivalents of these adsorption sites as seen experimentally are shown in Figure 7.6 (f), which is used to deduce the positions of the bilayer Sb atoms below. These subsequent layers must be considered as they add chemical uniqueness to several adsorption sites and hence will modify their adsorption potential. Firstly the adsorption sites of the first layer of Sb must be determined. Sites 1 and 2 are positioned between a decagon of Ag/In atoms and a decagon of Yb atoms. On the surface plane these two sites are equivalent to each other, but when atoms from the next underlying plane is considered they become distinct. As well as this adsorption site a smaller first monolayer Sb pentagon forms in the middle of this pentagonal arrangement of RTH clusters and oriented at 36°

For a clean surface the middle of the RTH cluster pentagon features a pentagon of Yb decorating adsorption sites 3 and 4. If adsorbing Sb atoms form a feature inside this Yb pentagon around sites 3 and 4 a smaller pentagon will be created that matches STM results.

The determination of second layer Sb atoms provides a more complex selection of possible adsorption sites. It is possible to see both small pentagons from the first layer and larger pentagons from the second layer in figure 7.6 (b), which has a coverage of 1.25 ML. This image indicates that the position of the bottom right vertex of the larger Sb pentagon is located between the two Sb atoms of the smaller pentagon.

For determining the adsorption sites of the second layer, site 1 is no longer considered as it is assumed these are filled with Sb atoms attributing to the 1st layer. Site 2 now appears to be the most preferential adsorption site. This site lies in between two underlying first layer Sb atoms. If all site 2s in a pentagonal arrangement of RTH clusters of a certain orientation are filled, a pentagon of edge length 1.57 nm is formed, agreeing with experimental observations. However the differing orientation of a pentagonal arrangement does not have equivalent distributions of atomic species. As such, to form the same arrangement on an RTH cluster oriented at 36° would mean the 2nd layer of Sb adsorbs directly on top of 1st layer Sb atoms, shown as site 5. This is not preferred and is explained in more detail below. The next preferential site for adsorption of a 2nd layer Sb atom appears to be site 3 which creates the pentagonal tile featuring an Sb

atom in the centre. This position will be modified by the presence of an underlying monolayer Sb pentagon. Site 4 is also seen to feature a 2nd layer Sb atom, being in an equivalent position as site 3 and will also be modified by the presence of a monolayer Sb pentagon. Site 5 is a seemingly unstable adsorption site. If occupied in the model, the interatomic distances exhibited are slightly smaller than those measured between pentagons constructed using site 2. As such, when encountered in STM images, these Sb atoms appear to be in positions around site 5 in an attempt to maintain the interatomic distance exhibited by the pentagonal features.

A pentagonal tiling (consisting of two pentagons oriented at 36° to each other, two stars oriented at 36° to each other, rhombi and boats) has been superimposed over an STM image displaying the Sb bilayer at a coverage of 1.65 ML shown in figure 7.6 (c). Up and down pentagons are indicated by accompanying arrows. The up and down pentagons express motifs that are encountered throughout the tiling, with the up pentagon containing a large Sb pentagon and the down pentagon containing a single Sb atom. The stars oriented in the same direction as the up pentagons contain no Sb atoms, while stars oriented in the same direction as the down pentagons contain an Sb pentagon. The same tiling has been super-imposed onto the model structure shown in Figure 7.6 (d), and theoretical positions of the second Sb layer decorated onto it adhering to the decorations encountered in the STM images (however only 1 orientation of star is encountered in the current size of the model). This creates a sparse aperiodic arrangement of Sb atoms.

Star features occur in the experimental results in two orientations as expected from a P1 tiling. Star formations that are parallel to the down pentagon tiles are occupied by a pentagon of 2nd layer Sb atoms. Stars parallel to the up pentagon tiles do not display a stable configuration of 2nd layer Sb atoms. Comparing this to the model, we find that stars parallel to the up pentagon tiles do not demonstrate any stable adsorption sites. Anti-parallel stars are observed on other atomic planes (not shown here) and do feature adsorption sites to create a pentagon of edge length 1.57 nm.

Calculations of the adsorption potential for Pb, Sb and Bi on the clean fivefold surface of *i*-Ag-In-Yb are presented in figure 7.7 [148]. A line is projected along a fivefold axis and the adsorption potential for each element is calculated along it. Considering the area inside the decagonal Yb ring, there are two potential adsorption sites that would give rise to a pentagon. These sites are indicated by an orange circle and a black circle. A pentagon created from orange

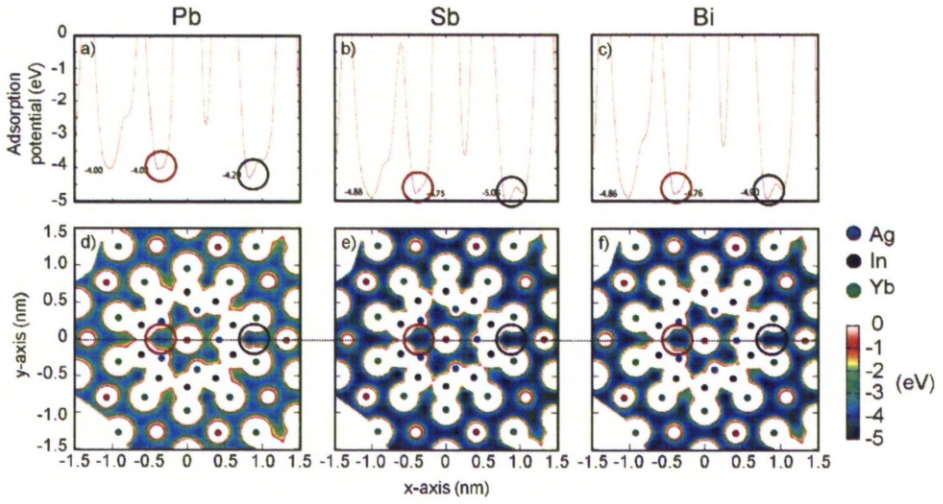

Figure 7.7: Adsorption potential calculations for Pb, Sb and Bi for the clean fivefold surface of *i*-Ag-In-Yb. (a) Pb, (b) Sb and (c) Bi adsorption potentials along the projected line indicated in (d), (e) and (f) respectively. The Ag atoms present are on an atomic layer beneath that of the atomic layer that constitutes the surface. Courtesy of Kazuki Nozawa of Chuo University, Tokyo, Japan.

adsorption sites would yield an edge length that is not encountered by STM. However, using the black adsorption site, which is equivalent to adsorption site 1 in figure 7.6, does create a pentagonal feature that matches experimental results. For Pb, Sb and Bi the adsorption potential for the black site is lower than that for the orange site, indicating a preference for adsorption for all three elements.

7.3.2 Sb growth on the threefold surface

A preliminary study on the growth of an Sb overlayer on the threefold surface has been completed. Figure 7.8 shows the threefold surfaces over a range of coverages of Sb from submonolayer to several monolayers. At sub-monolayer coverages, shown in figure 7.8 (a), no Sb formations are present. However, the STM image is enhanced considerably and obtaining similar resolution is relatively easy. Depositing more Sb, shown in figure 7.8 (b) continues to show no apparent Sb structures. However, protrusions are present on the surface, highlighted by white circles. These protrusions have a width of 1.50 ± 0.26 nm width and a height of 0.15 ± 0.05 nm when measured from the top of an Sb atom. As this image was taken at a positive bias, it is assumed that

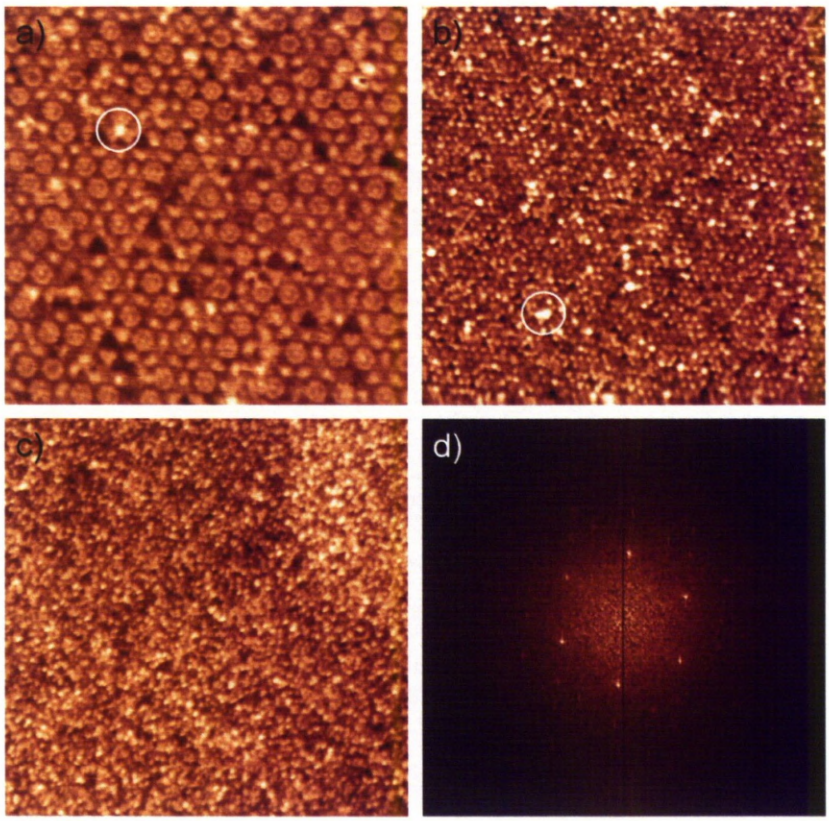

Figure 7.8: STM images showing the growth of Sb on the threefold *i*-Ag-In-Yb surface. Images taken after a depositions of (a) 0.03 ML (40 nm × 40 nm), (b) 0.12 ML (100 nm × 100 nm) (c) 6.12 ML (200 nm × 200 nm). (d) An FFT pattern generated from (b). Coverages are calculated in reference to fivefold deposition times and coverages where 1 min at 60 nA gives 0.015 ML. (a) was taken at a negative bias, while (b) and (c) were taken at a positive bias.

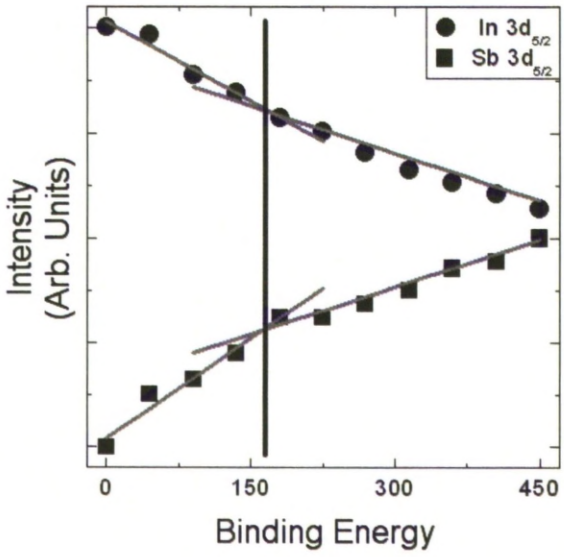

Figure 7.9: Variation of intensity (as measured by the area under the peaks) in In $3d_{5/2}$ and Sb $3d_{5/2}$.

single Sb atoms are not visible as evidenced for the fivefold surface, and instead only significant concentrations of Sb can be imaged. This is indicated by the similarities in protrusion heights for both five and threefold surfaces, although the widths vary between both surfaces. However such a large error is recorded for the widths it is expected that the formation of these protrusions have random sizes. At a greater coverage, as shown in figure 7.8 (c), a rough layer forms.

Taking an FFT pattern of figure 7.8 (b), shown in figure 7.8 (d), produces a pattern related to the threefold surface (which can be viewed in chapter 6. Removing the contribution from the substrate from 7.8 (c) and calculating an FFT produces a no overall pattern.

7.3.3 XPS

XPS has been utilised to explore the growth mode of Sb and how the growth affects the core levels of *i*-Ag-In-Yb. Sb was dosed at a constant rate of 120 nA for 45 second deposition intervals. XPS spectra of the Ag 3*d*, In 3*d*, Sb 3*d* and Yb 4*d* core levels were then collected after each deposition. As Sb is dosed, the Sb signal increases, while the In signal decreases as seen in figure 7.9. A comparison was accomplished by placing linear fits across the first 5 data points and the latter 8 data points, and an inflection point is observed. Inflection points occur for both Sb and

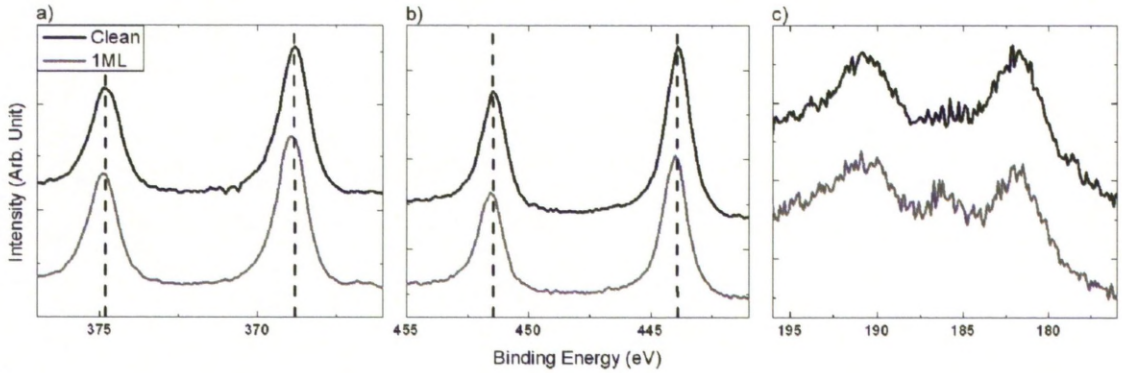

Figure 7.10: Comparison of the core levels of clean fivefold *i*-Ag-In-Yb and at a coverage of 1 ML of Sb. (a) Ag 3*d*, (b) In 3*d* and (c) Yb 4*d*.

In at the same coverage. Comparing these results with STM observations, it is concluded that the Sb grows as a monolayer, and then grows as a disordered 3D layer.

The core level peaks of the substrate were recorded before and after Sb deposition. XPS of the clean substrate peaks and after a deposition of 1 ML are compared in figure 7.10. The line shapes of the core levels are unchanged after deposition. The 3rd peak located between the Yb $4d_{3/2}$ and Yb $4d_{5/2}$ peaks is due to a slight oxygen contamination of the surface [127]. The lack of change in binding energy, FWHM or line shapes of the substrate spectra indicates that Sb is not alloying with the substrate. However, calculations have indicated that there is the presence of a strong adsorbate-substrate interaction.

7.3.4 UPS

UPS spectra have been taken at specific deposition times to identify any changes that occur within the valence band. Spectra were taken at coverages of 0 ML, 1 ML, 2 ML, 3 ML and 10 ML and are shown in figure 7.11 (a) and (b). The clean surface displays Yb 4*f* and Ag 4*d* peaks whose line shapes agree with previous work by Sharma *et al.* [83], with the Yb 4*f* peaks being close to the Fermi edge. Upon dosing Sb, the Yb 4*f* and Ag 4*d* peaks begin to diminish. The Fermi edge remains relatively unchanged until a large amount of Sb is deposited, with the Fermi edges spectral intensity decreasing when large amounts of Sb are present.

Annealing a heavily Sb deposited surface to 400°C for 15 minutes results in a complete change of the valence band as shown in Fig. 7.11 (c). The Yb 4*f* and Ag 4*d* peaks disappear

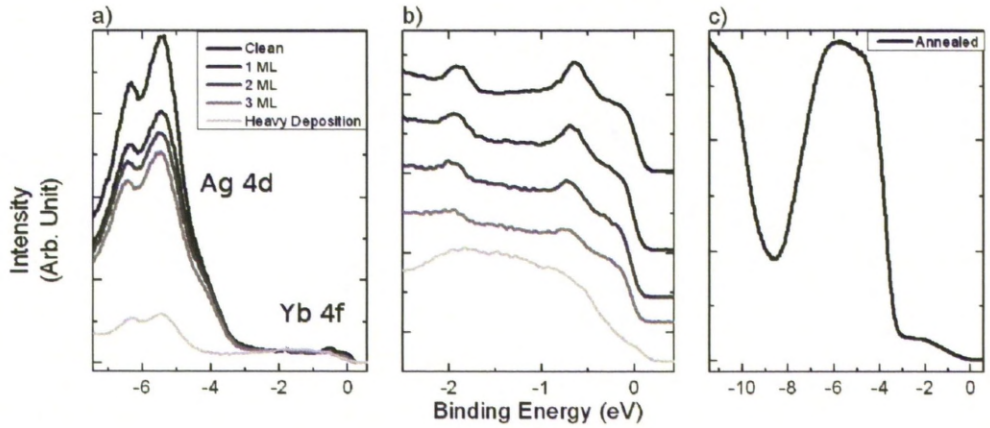

Figure 7.11: (a) UPS spectra of Sb deposited on fivefold *i*-Ag-In-Yb at several stages of deposition (b) Spectra focused on the Yb peaks at the Fermi edge (c) UPS spectra of a heavily Sb dosed annealed surface.

and a large peak occurs at a binding energy of -5.5 eV. This behaviour is indicative of oxygen present on the surface, which has affected the annealed surface such that the original metallic peaks are no longer present. This behaviour has been observed after the oxidised clean surface has been annealed [83].

7.3.5 Oxidation of Sb overlayer

Table 7.1: Binding Energies for the Sb3*d*, In3*d* and O1*s* core levels, for the oxidised fivefold *i*-Ag-In-Yb surface, heavily Sb dosed Ge(110) and Sb dosed fivefold *i*-Ag-In-Yb

	Sb		In		O 1s		
	3/2	5/2	3/2	5/2	In oxide	Yb oxide	Sb oxide
Oxidised fivefold	-	-	451.5	443.8	529.6	530.8	-
Sb on Ge (110)	537.7	528.3	-	-	-	-	-
Sb dosed fivefold	537.0	527.6	451.5	443.8	530.4	531.3	532.4

The grown Sb monolayer was exposed to oxygen, and binding energies were compared to a heavy Sb deposition on a Ge(110) crystal. Germanium was chosen as a comparison due to its resistance to oxidation. After deposition the binding energies of the Ge 3*d* peaks remain

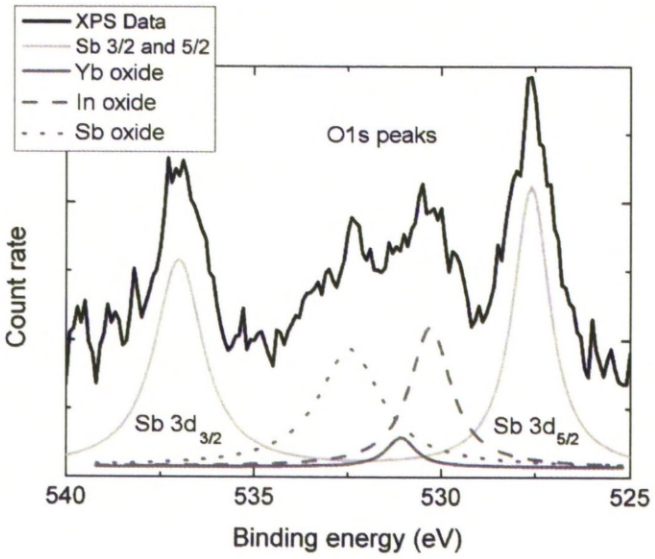

Figure 7.12: XPS spectrum of the Sb3$d_{3/2}$, Sb3$d_{5/2}$ and O1s peaks.

unchanged from those of the clean semiconductor indicating no alloying has occurred. The Ge crystal with Sb overlayer was then oxidised to 2000L, after which no O 1s peak was observed. When the clean fivefold surface is exposed to oxygen the In and Yb components of its surface oxidise, with the Yb oxidising more readily than In [127]. After exposing the Sb overlayer to oxygen, three oxide peaks are observed as shown in figure 7.12. These peaks have been fitted using a Gaussian line form. The peaks due to In oxide and Yb oxide are identified at 530.4 eV and 531.3 eV. These values are shifted to a higher oxide binding energy from the values observed by Nugent *et al.* The 3rd oxide peak is observed at a binding energy of 532.4 eV.

For the oxidised Sb deposited layer, the peaks due to Sb $3d_{3/2}$ and Sb $3d_{5/2}$ occur at 537.0 eV and 527.6 eV respectively. These are shifted to a lower binding energy by 0.7 eV from the Sb $3d_{3/2}$ and Sb $3d_{5/2}$ peaks observed on Sb deposited on Ge(110) of 537.7 eV and 528 eV respectively. The In oxide and Yb oxide components of the surface behave in a similar way on the clean surface and when a monolayer of Sb is present.

7.4 Growth of C_{60}

During the course of the clean fivefold study presented previously, and the Sb study, C_{60} was deposited on the surface in an attempt to create a quasiperiodic molecular overlayer. This was

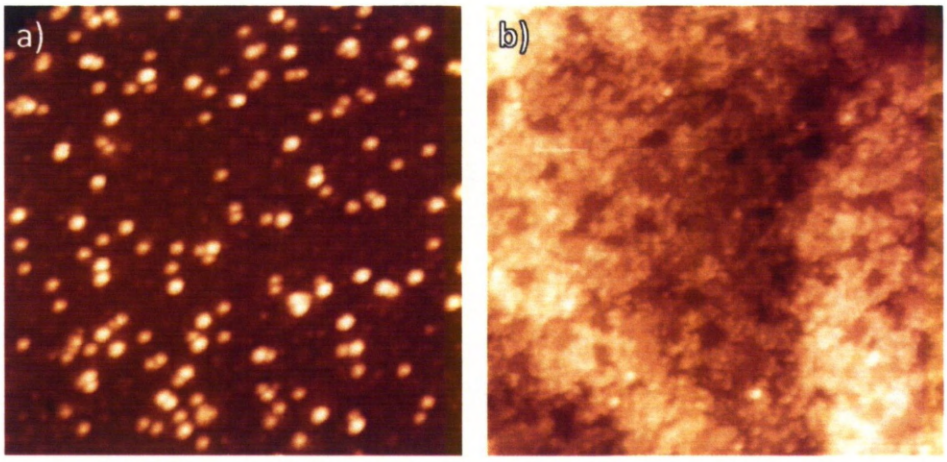

Figure 7.13: Two different depositions of C_{60} on the clean *i*-Ag-In-Yb surface. (a) demonstrates a 0.1 ML deposition (50 nm × 50 nm). (b) Shows the same surface after a deposition of 1 ML of C_{60}. (100 nm × 100 nm)

attempted initially on the clean surface, but was repeated on the clean surface after a predeposition of Sb, in an attempt to modify the behaviour between the substrate and C_{60}.

Clean surface

Figure 7.13 (a) shows the clean surface with a deposition of 0.1 ML of C_{60}. The protrusions have heights that occur around two values, heights of 0.46 ± 0.04 nm and of 0.65 ± 0.04 nm. The protrusions have a FWHM of 1.2 ± 0.1 nm determined using line profiles as specified in chapter 5, which is consistent with the van der Waals size of a C_{60} molecule of 1.02 nm [149]. The smaller scaled heights of C_{60} molecules relates to a molecule being absorbed in the space between protrusions, while the larger scaled heights of C_{60} molecules relate to a molecule absorbed on the top of a protrusion.

The bunching of protrusion heights into two groups suggest that there are preferred adsorption sites present on this surface. However when measuring the distances between successive C_{60} molecules, no relationships are observed indicating that their adsorption sites are random. Figure 7.13 (a) does not provide any autocorrelation patterns. This is the case for both the raw image, and the image with the substrates contribution removed. Taking an FFT pattern of figure 7.13 (a) of both the raw image and with the contribution from the substrate removed, yields FFT patterns displaying no overall ordering.

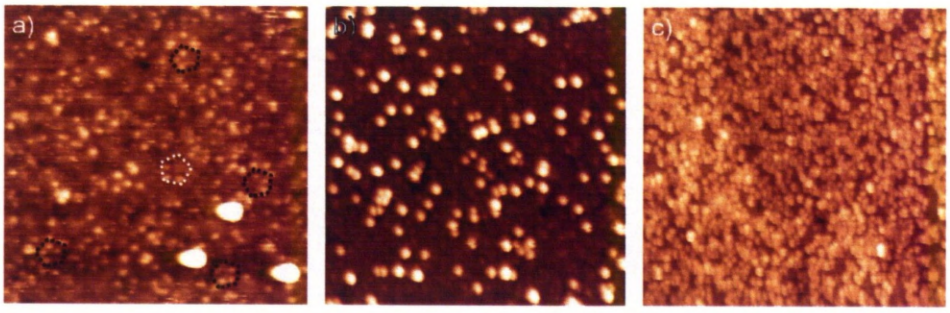

Figure 7.14: STM images of the fivefold *i*-Ag-In-Yb surface at a coverage of 0.17 ML of Sb and subsequent deposition of C_{60} at coverages of (a) 0.01 ML (30 nm × 30 nm) (b) 0.2 ML (50 nm × 50 nm) and (c) 0.9 ML. (75 nm × 75 nm)

Depositing more than one layer of C_{60} as shown in figure 7.13 (b) creates a rough layer of no apparent order. This is further evidenced by its FFT pattern which displays no overall ordering. LEED patterns of depositions up to a monolayer show a LEED pattern related to the substrate, which becomes suppressed until no pattern is viewable indicating the monolayer of C_{60} exhibits no order.

Clean surface modified by Sb

Figure 7.14 (a) shows an STM image after depositing 0.17 ML of Sb on the clean fivefold *i*-Ag-In-Yb with a subsequent 0.01 ML deposition of C_{60}. The fivefold Sb features are clearly visible and are highlighted. A further deposition leads to the appearance of several protrusions, shown in figure 7.14 (b). The protrusions have heights occurring in the range of 0.44 ± 0.03 nm and 0.62 ± 0.04 nm. They have a FWHM of 1.26 ± 0.1 nm, which is consistent with the van der Waals size of a C_{60} molecule. Taking autocorrelations and calculating an FFT from 7.14 (b), for conditions of no substrate contribution and the raw image, the resultant patterns indicate no long range order.

As for the clean surface, C_{60} heights occur in the same two ranges. As these are similar to the heights seen on the clean surface, and with no emergence of ordering, the predeposition of Sb onto the fivefold *i*-Ag-In-Yb surface has not modified the interactions between it and C_{60}.

Forming a 0.9 ML C_{60} layer as shown in figure 7.14 (c) creates a disordered 3D over layer. This coverage of C_{60} was annealed to 500 K for 10 minutes, after which no STM images were obtainable due to instabilities in the tip and surface induced by the rough nature of the overlayer.

7.5 Summary and comparisons

By employing STM and XPS we have studied the deposition of Sb on the clean *i*-Ag-In-Yb surface. The analysis of STM images taken from a range of coverages indicated that the Sb first grows as a sparse monolayer up to partial second layer, after which an amorphous growth mode becomes prevalent. Comparing the STM images to the theoretical substrate structure, it was possible to identify the adsorption sites of the first Sb layer being located between the 3rd shell of the RTH cluster which is composed mainly of I [137] and the Yb ring that is shared between many RTH clusters [48]. The second layer Sb atoms were observed adsorbing in sites that formed pentagons in the middle of truncated RTH cluster pentagonal arrangements.

X-ray Photoemission Spectroscopy was then employed to verify the monolayer growth of the system. A monolayer break was observed during steady amounts of growth, after which simultaneous multilayer behaviour was observed. UPS shows the same valence structure as expected from the clean surface. This structure is not drastically modified at increasing levels of In, with only the metallic Ag and Yb peaks diminishing in intensity as more Sb is deposited.

Oxidation of the system has shown that an Sb oxide peak forms as well as the expected indium oxide and ytterbium oxide peaks. The metallic In peaks continue to shift in the same way for both the clean system and Sb overlayer system, suggesting overall that the oxidation behaviour does not change in the presence of Sb [127].

The growth of Sb on the clean fivefold surface of *i*-Ag-In-Yb is similar to the growth of Pb and Bi on the same surface. The first layer of all three materials share similar adsorption sites, with pentagonal features forming on top of the truncated RTH clusters. These sites have the lowest adsorption potentials for all three elements, of all the possible adsorption sites identified within the Yb ring that surrounds an RTH cluster center. This adsorption potential is the greatest for Sb, then Bi, with Pb having the weakest. This indicates that Sb interacts more strongly with the substrate than Bi and Pb. However Bi forms the densest monolayer, while Sb is the next densest and Pb exhibits the sparsest monolayer. It is then not possible to observe the growth of a second layer of Bi; the monolayer resists the growth of any structures upon it, be it a wetting layer, island growth or the formation of a disordered three dimensional layer. This is in contrast to both Sb and Pb, which form second layers. However Sb does not complete a second layer, with a disordered growth mode occurring. Pb forms a complete second layer, of a greater

density of that of its monolayer. After the completion of the second layer, Pb begins to grow as hexagonal (111) islands whose orientations are modulated by the underlying quasiperiodic order.

Depositing C_{60} on both the clean surface and the clean surface modified by a predeposition of Sb yields a thin film with no ordering. This is unlike the deposition of C_{60} at low coverages on the fivefold surface of the *i*-Al-Pd-Mn quasicrystal [150]. At low coverages ($\sim$ 0.065 ML) it is possible to observe local τ scaled ordering. This however was not observed for C_{60} on *i*-Ag-In-Yb. Although C_{60} has not been observed to form a quasiperiodic overlayer on *i*-Ag-In-Yb, current experiments that involve the use of pentacene have been successful in forming quasiperiodic features using organic molecules.

Chapter 8

Oxidation of the high symmetry surfaces of the *i*-Ag-In-Yb quasicrystal

8.1 Introduction

With the structure of the fivefold surface now understood, as well as the structures of various epitaxially grown over layers, it is possible to study the interactions of these systems when exposed to more complex adsorbates. A common chemical any material is exposed to is oxygen. This chemical is responsible for the corrosion experienced by many different materials, such as iron. For *i*-Ag-In-Yb to be considered for applications in atmospheric conditions, the reactivity of its surfaces to oxygen must first be observed to identify any changes in structure, composition and properties.

The oxidation behaviour for all three high symmetry surfaces is compared to that of the pure forms of the constituents of the quasicrystal, namely Ag, In and Yb. The stability of the oxide layer for the fivefold surface is then tested, as well as calculations of its thickness. Finally, the method of oxidation is tested, by oxidising the fivefold surface and pure metal foils in both atmosphere and pure water.

8.2 Experimental Details

All three surfaces were prepared as stated in previous chapters, using fivefold sample 2 and two and threefold samples cut from the same ingot. One main difference however is the preparation time. After the samples yielded surfaces that were lacking of the presence of oxygen, preparation times were lowered to 15 minutes of sputtering and an hour of annealing. This process yielded surfaces that when measured by XPS were devoid of contamination and presented compositions similar to the bulk. The samples were only left to cool for 5 minutes between the end of their anneal cycle and the commencement of XPS, ensuring that oxidation due to residual gases in the chamber was kept to a minimum.

Surface composition and cleanness of the oxidation experiments were monitored by XPS with unmonochromatised AlK_α radiation ($h\nu$ = 1486.6 eV) using a PSP Vacuum Technology hemispherical electron-energy analyser. For studies of the pure elements, 99.9% pure In and Yb foils and a Ag(111) single crystal were used. Each sample was cleaned by Ar^+ sputtering with XPS used to monitor their cleanness. The Yb foil was difficult to prepare, with a trace amount of oxygen detectable by XPS after many cycles of sputtering. These reference samples were used to calibrate the XPS core-level binding energies while oxygen adsorption on these surfaces was useful in identifying the oxidation states on the quasicrystal surface.

Oxidation in vacuum was carried out by introducing 99.6% pure oxygen gas through a leak valve directly into the XPS chamber. Oxidation was performed at different exposures, ranging from sub-Langmuir (L) to 1000 L, where 1 L is equal to the exposure of 1×10^{-6} mbar of gas per second. For exposures of $>$ 10 L an oxygen pressure of 1×10^{-8} mbar was used, for 10 - 100 L exposure an oxygen pressure of 5×10^{-7} mbar was used and for larger exposures an oxygen pressure of 1×10^{-6} mbar was used. For air oxidation the samples were exposed to atmosphere in the fast entry load-lock chamber for 15 hours. The samples were cleaned prior to air exposure. Yb and In foils were exposed to the atmosphere for longer than 15 hours. For oxidation in water the samples were submerged into distilled pure water. Exposure time for the quasicrystal was 24 hours, and for Yb and In 15 hours. Prior to water exposure the samples were sputter annealed and briefly exposed to atmosphere while being transferred to water. All XPS measurements and oxygen exposures were performed at room temperature. XPS measurements were made at an angle of 15° to the normal emission, except polar angle-dependent measurements for which the

angle was varied from 15° to 75° at intervals of 10°. Peak properties such as binding energy and intensity were recorded in the same way as the core levels from the clean five, three and twofold samples as detailed in chapter 5.

Determining the error on binding energy was possible in several ways. The simplest way is to assume that the error on the binding energy is limited by the resolution of the detector of 0.1 eV. The second way is to vary a peak fit from the experimental data by shifting the value of the peak binding energy to a higher or lower energy until the standard deviation of the peak approaches a value of three. The second method was employed to calculate uncertainties in this chapter and these are included in the appropriate tables.

The binding energy shift in XPS contains contributions from both initial and final state effects [151]. Initial state effects originate from the local Madelung potential and the ground state valence levels, reflecting the ground state chemistry. Additionally, final state effects arise from charge redistribution or relaxation around the core hole following the photoemission process. In XPS analysis of oxides, the final state and Madelung potential contributions to the binding energies are often neglected and it is assumed that the shift predominantly reflects the initial state chemistry. In our measurements, it is not possible to separate the initial and final state contributions to the shift in binding energies, but we consider the shift to be dominated by the initial state effect.

STM experiments were performed in Ultra High Vacuum (UHV) using an Omicron variable temperature STM operating at room temperature. LEED measurements were performed using an Omicron SpectaLEED optic and source, using a LaB_6 filament, also at room temperature.

8.3 Results

8.3.1 XPS

Clean surfaces review

Previous chapters have reported the composition of the surface as studied through XPS. The compositions of the two, three and fivefold surface sample 2 after sputtering were found to be in the ranges of 62 - 63% Ag, 27 - 28% In and 9 - 10% Yb, while annealing recovered the compositions to ranges of 35 - 38% Ag, 43 - 45% In and 19 - 20% Yb. The surface composition after preparation, using the conditions stated in the experimental details, are identical to that

Table 8.1: BE and FWHM of the core-level peaks for pure elements and the fivefold, threefold and twofold *i*-Ag-In-Yb surfaces after annealing and their values after oxidation in vacuum. The values are in units of eV with an uncertainty of $\pm 0.1 - 0.2$ eV as specified above. The FWHM were determined from the spectra taken with 10 eV pass energy. FWHM of the Yb peaks for the clean, threefold and twofold samples after oxidation are not given due to the complex nature of spectra after oxidation.

	Ag $3d_{5/2}$		In $3d_{5/2}$		
	BE	FWHM	BE	FWHM	Yb $4d$
Pure element	368.1	1.0	443.6	1.1	182.3, 191.3
Fivefold	368.5	1.1	443.6	1.1	181.5, 190.6
Threefold	368.5	1.1	443.6	1.2	181.7, 190.6
Twofold	368.6	1.2	443.5	1.2	181.6, 190.6
			After oxidation		
Pure element	368.1	1.0	444.0	1.5	-
Fivefold	368.5	1.1	443.9	1.4	181.6, 185.0
					189.65, 199.0
Threefold	368.6	1.1	443.9	1.7	-
Twofold	368.6	1.2	443.9	1.5	-

of the bulk. This is in agreement with previous results for sample 1 by Sharma *et al.* [64].

A summary of core levels for the clean surface are shown in table 8.1. Core levels for Ag, In and Yb are displayed for each high symmetry surface of the quasicrystal, and for pure metal versions of each element (in the form of a Ag(111) crystal and In and Yb foils), for reference. The core levels analysed are the $3d$ peaks for Ag and In, due to their large intensities, and the $4d$ peaks for Yb. A summary of peak binding energies and FWHM is given in table 8.1.

Core levels for the two, three and fivefold samples are identical in position and width after preparation conditions. However the positions of the Ag and Yb peaks in comparison to the pure versions are shifted to higher binding energies and lower binding energies respectively. Indium

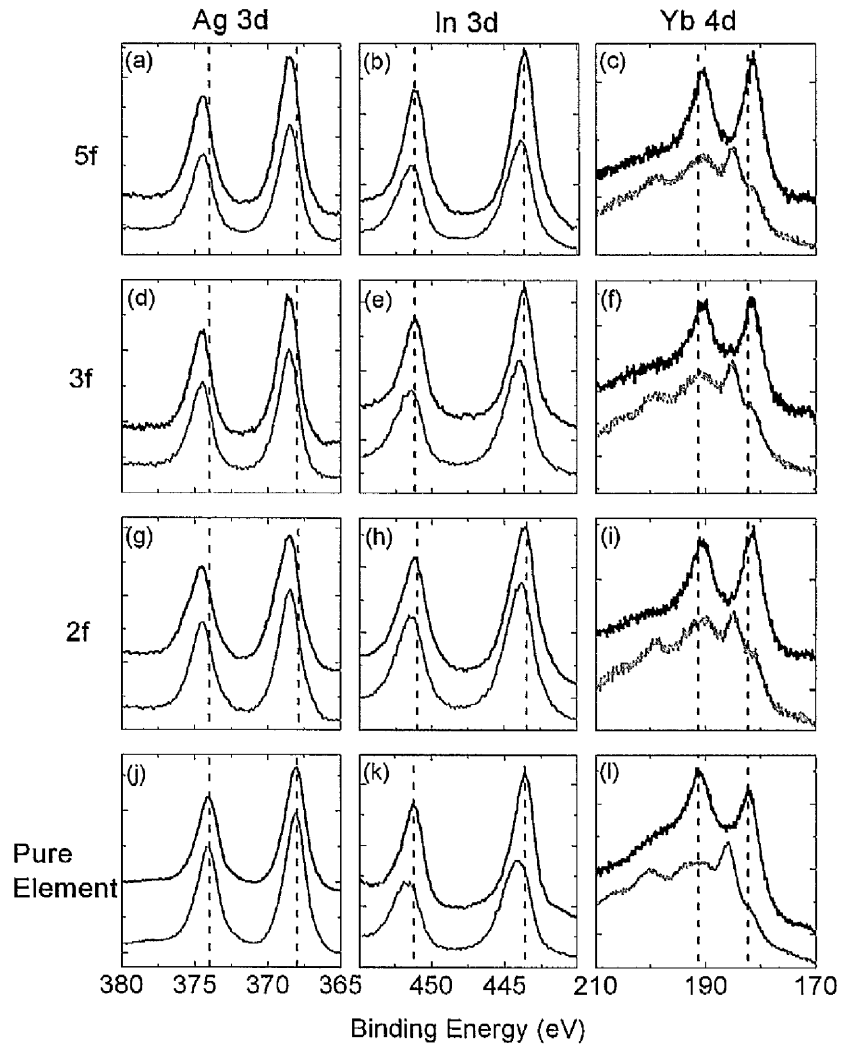

Figure 8.1: XPS spectra of the *i*-Ag-In-Yb high symmetry surfaces and pure elements. Black lines represent a clean surface and grey lines represent an oxidised surface. The first column shows Ag $3d$ second column shows In $3d$ peaks and the third column shows Yb $4d$ peaks. Spectra (a)-(c) are taken from the clean fivefold surface, (d)-(f) from the clean threefold surface, (g)-(i) from the clean twofold surface and (j)-(l) from the pure elements. Oxygen exposure was 1000 L for all surfaces except for the Yb foil, which was exposed to 10 L. Vertical dotted lines represent the peak positions of the pure elements. Spectra were taken with 50 eV pass energy at the analyser.

for both quasicrystal surfaces and the pure foil is unchanged. Yb displays the same divalency characteristic for the quasicrystal surfaces as it does for other Yb compounds [141].

The similarities of the three surfaces is not surprising. As photons used for XPS penetrate several layers into the material, combined with the low resolution of the system, means the contribution of the surface layer will be negligible. This is shown by comparing the annealed core levels to the sputtered core levels. Apart from relative intensities, the core levels are identical after each process, indicating that the surface contribution is negligible.

The clean surfaces have also been investigated using synchrotron radiation...

Oxidation in vacuum

A summary of before and after core level spectra from the high symmetry quasicrystal surfaces and pure elements are shown in figure 8.1, with a summary of binding energies in table 8.1. The surfaces were oxidised to 1000 L, with the exception of Yb which was oxidised to 10 L. The oxidation behaviour of Ag is unchanged for each surface and the pure metal version, in that it is not affected by the presence of oxidation at all, apart from a decrease of intensity for the quasicrystal as is expected for an intervening oxide layer forming in the path of incident photons and escaping electrons.

The In component of each surface reacts to the presence of oxygen. The pure metal version shows a shift in binding energy to a higher energy level. This behaviour also occurs for the quasicrystal surfaces. The Yb foil undergoes a profound change in the presence of oxygen, as its line shape changes drastically. This is also observed for each other surface.

The evolution of the Ag $3d$, In $3d$, Yb $4d$ and O $1s$ core levels for the fivefold surface are shown in figure 8.2 (a)-(d), with comparative spectra from the evolution of the In and Yb foils are shown in figure 8.2 (e) and (f). Spectra were taken at several exposure levels up to 1000 L, except for Yb which was oxidised to 10 L. The Ag(111) is not displayed due to its unreactive nature to oxygen.

The signals from the core levels shown in figure 8.2 (a)-(c) decrease with oxygen exposure, as expected when an oxide layer forms. Ag core levels are unchanged throughout, while In shifts to a higher binding energy. Yb undergoes a significant change.

The Yb component of the quasicrystal surfaces oxidises readily in the presence of small amounts of oxygen. The Yb $4d$ core levels are shown in figure 8.2 (c). The clean surface exhibits

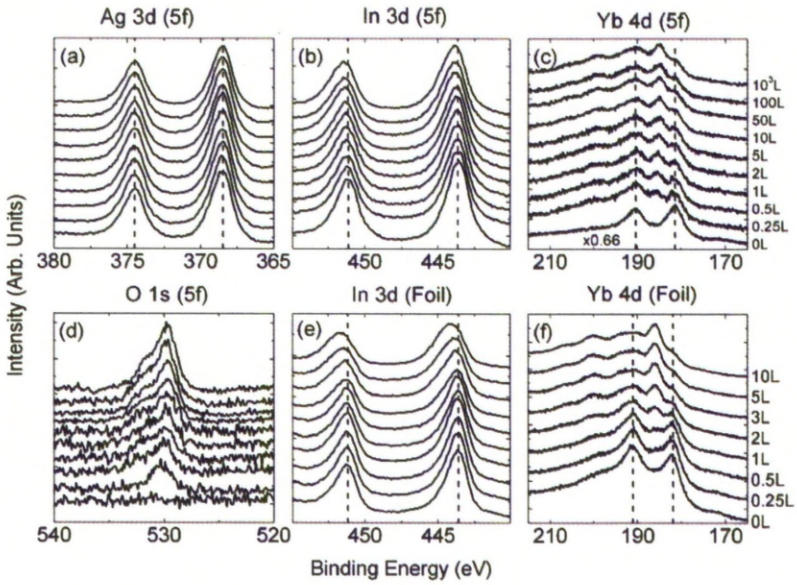

Figure 8.2: XPS spectra from the fivefold *i*-Ag-In-Yb surface ((a)-(d)) and In (e) and Yb (f) foils with increasing exposures (bottom to top). The exposure began at 0.25 L and ended at 10^3 L for all samples, except Yb foil where the exposure finished at 10 L.

spin orbit doublets at 181.5 and 190.6 eV. Upon exposure to oxygen, these are accompanied by oxide peaks at around 185 and 199 eV. The intensity of the oxide peaks increases with increasing oxygen exposure, while the metallic peaks are suppressed. A trace amount of the metallic peaks are still detectable at 1000 L. Previous studies on an Yb thin film indicate that there is a total of five oxidation states in addition to the original metallic peaks, relating to the oxidation of Yb [152] in the given range of binding energies. However with the resolution of the system used it was not possible to observe them all which hinders a quantitative analysis of the Yb $4d$ metallic and oxide core levels. Over increasing levels of oxidation, the intensity of the Yb $4d$ peaks is found to be invariant. This indicates that there is no Yb segregation to the surface during this process.

The behaviour of the Yb core levels is different for that of Al based quasicrystals. For Al based quasicrystals, oxide peaks arising from the Al $2p$ core levels are distinct from each other and the metallic peak [153]. This causes some issues when attempting to determine the thickness of the oxide layer, which is done below using a different method. The lack of Yb segregation upon oxidation is also in contrast to Al base quasicrystals, as oxidation induces segregation of Al to the surface which then forms a passivating oxide layer [154, 155].

The oxidation behaviour of Yb in the quasicrystal is very similar to that of pure Yb. As shown in figure 8.2 (f). Pure Yb oxidises at a very low exposure yielding additional peaks at higher binding energies. The separation of the metallic peaks is the same as it is for the quasicrystal. High exposure produces a complex structure with a remnant of metallic peaks as in the quasicrystal.

The O $1s$ core level is shown in 8.2 (d). At low levels of oxygen exposure a peak at 529.6 eV is present. However, at increasing levels of oxygen exposure a second peak develops at a slightly higher binding energy.

Overall, the increase in FWHM, peak shift and modification of the Yb core levels indicate that these elements are being oxidised. The behaviour of the individual constituents upon exposure to oxygen are identical to that of their metal foils.

The results of the gradual oxidation are examined quantitatively and presented in figure 8.3, in which the change in FWHM, binding energy and intensity are considered. The FWHM of the Yb $4d$ levels is not displayed due to the complex nature and hence difficulty in reliably determining its value.

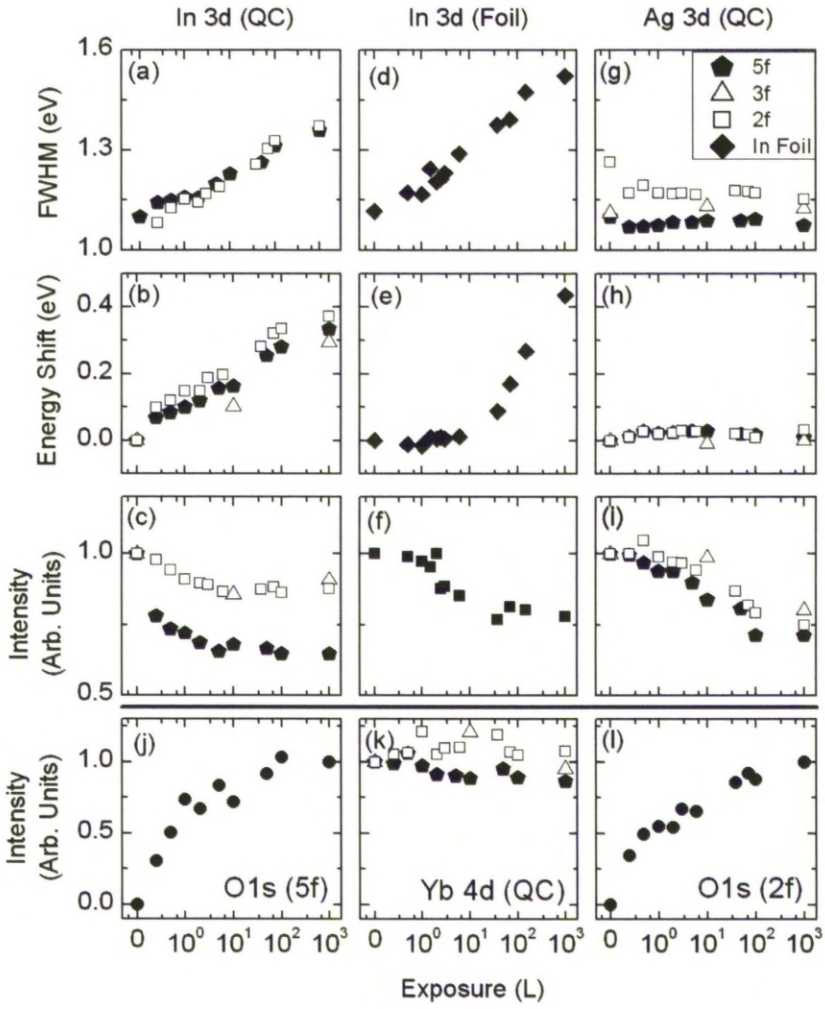

Figure 8.3: Change in the FWHM, position and intensity of core level peaks as a function of oxygen exposure for the fivefold, threefold and twofold Ag-In-Yb surfaces, as well as for the pure Ag and In materials. (a)-(c) In $3d$ for the quasicrystal surfaces, (d)-(f) In $3d$ for the In foil and (g)-(i) Ag $3d$ for the quasicrystal surfaces. (j) and (l) O $1s$ intensity for the fivefold and twofold surfaces. (k) Yb $4d$ intensity for the quasicrystal surfaces. The intensities of the In $3d$ Ag $3d$ and Yb $4d$ peaks are normalised with respect to the clean surface whereas the O $1s$ peaks are normalised to the value obtained at an exposure of 10^3 L. Note the log scale on the x axis.

The variation of FWHM, peak position and intensity of the In $3d_{5/2}$ peak is shown in figure 8.3 (a)-(c). Upon increasing exposures of oxygen the FWHM gradually increases as the peak shift occurs and the overall intensity drops, which almost saturates at an oxygen exposure of 100 L. The peak shift after an oxygen exposure of 1000 L is 0.3 eV, which is expected if In oxide forms. This is then compared to the variation in the In $3d_{5/2}$ peak during the oxidation of the pure In foil, shown in 8.3 (d)-(f). As for the quasicrystal surfaces, the FWHM increases at higher levels of oxygen exposure. However as the exposure increases, the core level peak grows asymmetrically, featuring a tail at the higher binding energy side. This increases the FWHM at a greater rate. At high levels of oxidation, the FWHM only increases slightly, indicating that the process of oxidation begins at low exposures and saturates at a higher exposure. For the binding energy of the pure foil, the shift occurs only slightly at small levels of oxygen exposure, which then increases rapidly when it reaches a certain exposure level. This is in contrast to the gradual change in binding energy expressed by the quasicrystal surfaces. The overall energy shift and FWHM is greater at 1000 L for the pure foil than the quasicrystal surfaces.

A more recent study conducted at Ecole des Mines, Nancy by Sharma *et al.*, has evidenced behaviour contradictory to that seen for the results presented in this chapter. Chambers used for both experiments had similar base pressures. Over the course of the experiment conducted in Ecole des Mines, the clean two, three and fivefold crystals were contained in a UHV chamber for durations exceeding 8 hours. During this time the surfaces were subjected to STM measurements, with XPS spectra recorded before and after, which after 8 hours showed only a small amount of oxidation on the surfaces. This suggests that during the experiments where the results presented in this chapter were taken, there was a source of oxygen contamination in the chamber.

The quantitative analysis of Ag $3d$ levels for the quasicrystal surfaces are shown in figure 8.3 (g)-(i). the FWHM and binding energy are unchanged at all levels of oxygen exposure, confirming the same inert behaviour for this species at these conditions. The sticking coefficient of Ag in the Ag(111) crystal at the pressures employed has been found to be negligible [156]. However, if oxygen exposure is carried out at temperatures greater than room temperature and at high exposures, the oxidation of Ag(111) can be induced [157]. For this study the Ag(111) crystal was limited to room temperature.

Figure 8.4 shows the O $1s$ levels for the fivefold quasicrystal surface, the In foil and the Yb

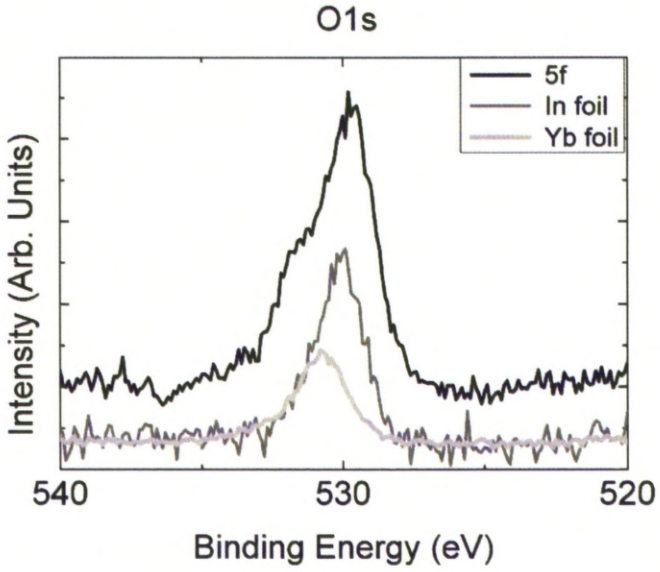

Figure 8.4: O 1*s* spectra from the fivefold *i*-Ag-In-Yb surface (black), In foil (dark grey) and Yb foil (light grey) after oxygen exposure. Exposure for the quasicrystal and In was 10^3 L for the Yb foil was 10 L.

foil. At greater levels of oxygen exposure, two distinct peaks are seen to form for the quasicrystal surface. By comparing the oxide peaks from both the pure In and Yb foils, we can determine which peak originates from specific compounds for the quasicrystal. The peak at 529.6 eV is determined to be caused by In oxide, while the peak at 530.8 eV is determined to be Yb oxide. The In oxide peak is in good agreement with that expected [119,158], while the Yb oxide peaks binding energy is close to the expected binding energy for that compound [152]. The intensity of O 1*s* peak has a larger contribution from In oxide than Yb oxide, as expected from the composition of the surface.

Stability of the oxide layer

To test the thermal stability of the oxide layer, the system was annealed to various temperatures and spectra recorded. The anneal temperature however could not exceed that used for the preparation, as above this temperature the surface reconstructs, potentially permanently. Pre oxidised core levels for O 1*s*, In 3*d* and Yb 4*d*, and at two anneal temperatures are shown in figure 8.5. The time for each anneal was 15 minutes. After annealing the oxidised surface to 250°C, the oxide peak relating to In oxide disappears shown in figure 8.5 (a), indicating that

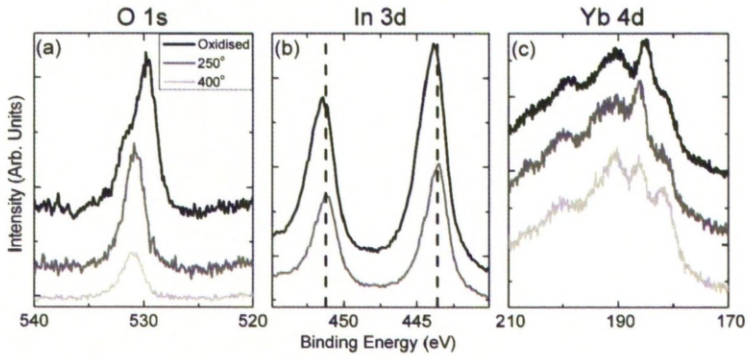

Figure 8.5: (a) O 1s, (b) In 3d and (c) Yb 4d spectra from the fivefold i-Ag-In-Yb surface after an exposure of 10^3 L, and after annealing at different temperatures (key given in insert). The vertical dotted line marks the peak positions for the clean surface.

oxygen bound to In has desorbed at this temperature. However, the O 1s peak arising from Yb oxide has increased in intensity. This can be explained if the oxygen bound to In is transferred to Yb at this temperature. This is confirmed by considering the In spectra in figure 8.5 (b), where the In 3d binding energy reverts to its non oxidised value. The previously shifted binding energy and increased FWHM for In expected from oxidation have reverted to their pre-oxidation values.

The O 1s peak from Yb oxide can still be detected after annealing the oxidised surface to 400°C. This suggests that oxygen is more strongly bound to Yb than to In. This is expected from the heats of formation of bulk oxides which are -1815 kJ mol^{-1} for Yb_2O_3 and -926 kJ mol^{-1} for In_2O_3 at room temperature [159]. Since the heat of formation for Ag_2O is -31 kJ mol^{-1}, which is much less than that for ytterbium and indium oxides, Ag is expected to be inert.

Thickness of the oxide layer

A specific method for calculating the oxide thickness for Al alloys requires the comparison of the ratio of the metallic and oxidic Al 2p core levels [160]. While this method can be used for other metallic alloys, the lack of a distinguishable oxide peak for In, and the difficulty in quantifying the oxidised Yb 4d core level make this method impractical. Instead, an angle resolved approach is considered for determining the thickness of the oxide layer. Polar angle dependent XPS measurements were performed on the fivefold surface after an exposure to 1000 L of oxygen. The overall intensities of the Ag 3d and O 1s peaks as a function of the polar angle

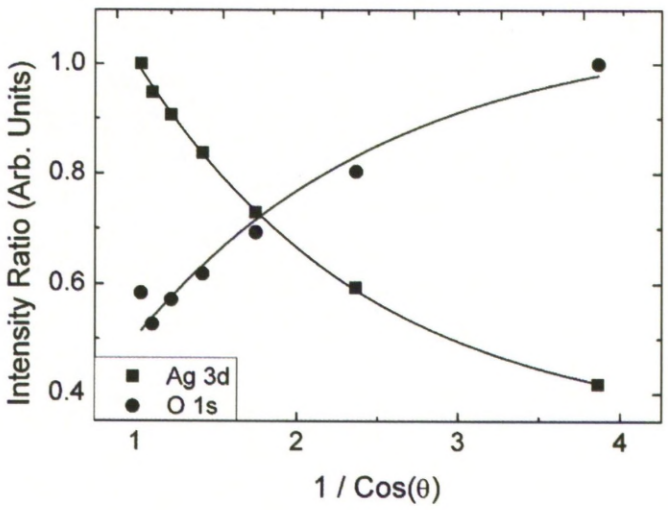

Figure 8.6: XPS intensities of the O $1s$ and Ag $3d$ peaks as a function of polar angles (θ) taken from the fivefold i-Ag-In-Yb surface after an oxygen exposure of 10^3 L. the O $1s$ intensity is the total of indium oxide and ytterbium oxide. Solid curves are results of the best fit with exponential functions.

θ are shown in figure 8.6. The intensity of the O $1s$ peak increases exponentially with increasing grazing angle, while the intensity of the Ag $3d$ peak decreases exponentially. The exponential decay of the Ag $3d$ peak can be modeled using the Beer-Lambert formula:

$$I_{Ag3d} \propto e^{-d/\lambda_{Ag3d}\cos\theta} \tag{8.1}$$

Where λ_{Ag3d} is the inelastic mean free path of the Ag $3d$ photoelectrons and d is the thickness of the oxide layer if a uniformly thick oxide layer is formed. Similarly, the increase in the O $1s$ intensity is expected to be

$$I_{O1s} \propto (1 - e^{-d/\lambda_{O1s}\cos\theta}) \tag{8.2}$$

The observed variations of peak intensities fit well with the Beer-Lambert formula, shown by the exponential curve fits in figure 8.6. The thickness calculated from these fits is (1.1 ± 0.1) nm. The value of λ used in the calculation was determined using the Tanuma-Powell-Penn equation [120] assuming that the photoelectrons travel through a layer of In oxide and Yb oxide of composition similar to the relative amounts of In and Yb present in the bulk. This value

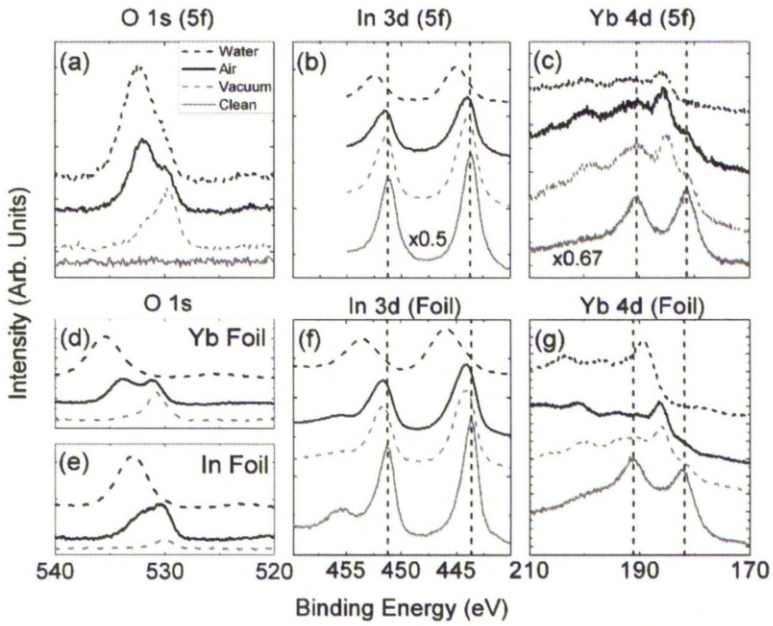

Figure 8.7: O 1*s*, In 3*d* and Yb 4*d* spectra form the clean surface (solid grey) and after exposure to oxygen in vacuum (dotted black), air (solid black) and water (dashed black). (a)-(c) fivefold *i*-Ag-In-Yb; (d) and (g) Yb foil and (e) and (f) In foil. The vertical dotted lines mark the peak position for the clean surface.

was cross checked by comparing the intensity of the Ag 3*d* core level at a specific polar angle before exposure to oxygen and after 1000 L of exposure to oxygen. For this, the intensity for the clean surface (I°_{Ag3d}) and after oxidation (I_{Ag3d}) were measure for two polar angles, 15° and 45°, and compared. The value for the thickness is calculated using the Beer-Lambert formula and determined to be (1.3 ± 0.3) nm, which is consistent with the previous method.

The oxide layer thickness of this system is similar to that of the oxide layer on the fivefold surface of *i*-Al-Pd-Mn [155]. The oxide thickness for *i*-Al-Pd-Mn varies due to the segregation of Al to the surface during the process; a greater degree of Al segregation leads to the formation of a thicker oxide layer. The oxide layers thickness varies from 0.5 nm to 3.0 nm. At an Al concentration similar to that of the bulk ($\sim 70 - 80$ at.%) the thickness of the oxide layer of *i*-Al-Pd-Mn is similar to that of the oxide layer for *i*-Ag-In-Yb.

Oxidation in air and water

While oxidation in vacuum gives an indication of how the surface behaves in the presence of minute levels of oxygen, it does not show the behaviour of the materials when exposed to conditions encountered in atmosphere. The oxidation of the fivefold quasicrystal surface was carried out in atmosphere and pure water, and is shown in figure 8.7 (a)-(c). These are compared to the in-vacuum oxidation spectra. These are then compared to the oxidation of the In and Yb foils in the same environments, shown in figure 8.7 (d)-(g). A summary of peak positions is given in table 8.2. The Ag core levels remain unchanged for both methods of oxidation, and are not displayed.

For oxidation in atmosphere, the In $3d$ peaks and Yb $4d$ peaks (figure 8.7 (b) and (c)) are identical in positions, and for the case of In, identical in FWHM when they are oxidised in vacuum. This suggests that the same degree of oxidation occurs in both environments. This is also true for the In and Yb foils (figure 8.7 (f) and (g)), which display similar behaviours when oxidised in both vacuum and atmosphere.

The O $1s$ spectrum after oxidation in atmosphere still exhibits two peaks, as it does after oxidation in vacuum. However, the peak at a higher binding energy relating to Yb oxide is larger than peak relating to In oxide, after atmospheric oxidation. The increase in the intensity of the Yb oxide oxide peak is due to a hydroxide species and physisorbed oxygen. This is expected due to presence of water vapour in the atmosphere. The O $1s$ spectra from the In and Yb foils after air exposure also exhibit hydroxide species at higher binding energies.

After exposing the quasicrystal to water, the Yb $4d$ core levels showed no remnants of the metallic peaks. This indicates that oxidation is more effective in water than it is in air or vacuum. The In $3d$ core levels are shifted to higher binding energies by 1.3 eV. This is comparable within experimental uncertainty to the binding energy shift observed for the pure In foil, and is caused by the formation of the hydroxide species. The Ag core levels remain unaffected by exposure to water.

The O $1s$ spectra for the quasicrystal and pure In foil are dominated by the presence of the hydroxide species after water exposure. The Yb $4d$ and O $1s$ spectra from the Yb foil after water exposure are shifted to higher binding energies, with the O $1s$ peak now located at a binding energy of 535.5 eV. This shift is larger than expected and could be caused by the charging of the insulating oxide layer. After water exposure, the Yb foil was found to be corroded and discoloured, while the other samples suffered no major surface discolourations.

Table 8.2: Binding energies of the In $3d$ and O $1s$ core levels for the fivefold i-Ag-In-Yb surface, In foil and Yb foil after oxidation in vacuum, air and water. The data for clean samples has also been included. The values are in units of electron volts (eV). uncertainty in the peak position is $\pm 0.1 - 0.2$ eV except for values marked with *, which have a large degree of uncertainty due to the low intensity and overlap with neighbouring oxide peaks.

	In $3d_{5/2}$	O $1s$(oxide)		
		In oxide	Yb oxide	O $1s$ (hydroxide)
5f i-Ag-In-Yb				
Clean	443.6			
O_2 exposed	443.9	529.6	530.8	
Air exposed	444.0		*529.7	531.9
Water exposed	444.9		*530.0	532.4
In foil				
Clean	443.6			
O_2 exposed	444.0	530.2		
Air exposed	444.1		530.4	531.9
Water exposed	444.9			533.0
Yb foil				
Clean				
O_2 exposed			530.7	
Air exposed			531.0	533.7

8.3.2 STM and LEED

The surface ordering techniques of STM and LEED were employed to study the surface ordering after oxidation. The experimental set up allowed the measurement of the surface by STM after different oxygen exposures. The tenfold FFT patterns from the clean surface images disappear soon after oxidation starts (< 1 L) suggesting that the oxidation destroys the quasicrystalline order on the surface. However, the step terraced structure could be observed even after an oxygen exposure of 10^4 L. The terraces were found to be very rough after oxidation and produced FFT patterns indicating no overall long range order. No LEED patterns were observed from the surface after oxidation suggesting that oxidation has destroyed the surface structure and agreeing with STM results.

8.4 Summary

The oxidation behaviour of the fivefold, threefold and twofold surfaces have now been compared. The variation in FWHM and chemical shift of In $3d$, Ag $3d$ and Yb $4d$ with increasing oxygen exposure is identical for all three surfaces. The variation in the O $1s$ intensity is also similar for the three surfaces. This, as well as the fact that experiments were carried out under the same oxygen pressure and substrate temperature, suggests that the sticking coefficient is very similar for all three high symmetry surfaces. The intensity of the In $3d$ peaks decreases faster for the fivefold surface than for the other two surfaces. This could be due to differences in surface roughness: if a surface is flat and oxygen is adsorbed on top, a unform layer of oxide species would be formed. Photoelectrons would have to pass through the layer and thus intensity would decrease. The observed contamination was evidenced by the change in line shape of the Yb $4d$ level and also in the valence band structure when studied by UPS [83]. For the initial experiment it was found that the threefold surface was very difficult to clean. This could be due to a source of contamination in the chamber used, as this did not occur for a more recent experiment.

The quasicrystal responds to oxygen in a similar manner to that of its separate constituents. Ag remains widely unreactive to the presence of oxygen, while In shows a moderate sensitivity to oxygen and Yb is very reactive to the presence of oxygen. This is expected from the heats of formation of the bulk oxides of these elements. Upon oxidation the binding energy of In shifts to higher energies, while the Yb $4d$ core level undergoes a more significant change. The metallic

Yb peaks diminish while oxidic peaks emerge. Exposure to oxygen in vacuum and in air produce similar behaviour. Oxidation in pure water is more effective. Subsequent STM and LEED of the surface after oxidation suggests that this process destroys the quasicrystalline order of the substrate.

Chapter 9

Summary and outlook

A quasicrystal is a material that exhibits long range order but no periodicity, and as a result can express previously thought forbidden symmetries. This discovery caused the definition of a crystal to change, as these new materials did not conform with previous ideas of solid state physics and how only a periodic system could constitute a crystal. Over a relatively short time these new materials have been widely investigated, with atomic structures being probed, physical properties being catalogued and new structures and behaviours being observed using elemental species and materials that do not classically accommodate aperiodicity.

The introduction of a stable binary quasicrystal system removes some of the issues encountered when studying materials for which all stable species are composed of three metallic elements. The problem of chemical complexity has proven an issue when determining these materials atomic structures. A binary system alleviates this issue. Although this binary system itself cannot be studied in UHV, a daughter material, *i*-Ag-In-Yb can. In order to study the binary system, the isostructural ternary alloy must be investigated in its place. This has been studied using various techniques such as STM, LEED, MEIS, XPS and UPS in an effort to characterise its structure and properties. The surface of this system has also been modified by depositing various materials upon it, studying the effects of an aperiodic structure on elements that do not classically conform to such ordering.

STM provides a technique that can study the atomic structures of a material down to the atomic scale. This technique enabled the characterisation of the five, three and twofold surfaces through comparisons of experimental data to that of the model structure. STM has shown that

all three surfaces exhibit terminations that occur at atomic planes that intersect the rhombic triacontrahedral clusters. Atomic resolution combined with techniques such as LEED, MEIS and XPS show that the fivefold surface exhibits no evidence of reconstruction. The compositions of all three surfaces has been found to be similar to the bulk. The stability of all three surfaces has found to be comparable on the nanoscale, although at the macroscopic level surface free energy, with a small contributing factor from atomic density, seems to dictate the most stable high symmetry plane as indicated by the size of the facets on an *i*-Ag-In-Yb ingot.

With the structures of the surface characterised it was then possible to conduct more complex experiments. The growth of single element quasicrystals provides the challenge of coercing elements that normally form periodic structures to adopt one that it would not normally exhibit. Sb was chosen due to its similarity in size and electronic configuration to previously grown single element quasicrystals, and also because Sb has been observed forming quasiperiodic overlayers when studied by diffraction techniques on *i*-Al-Pd-Mn. It has been observed to form a quasiperiodic partial second layer of which adsorption sites can be identified, until during the growth of the second layer a disordered growth mode becomes prevalent. The next step up from single element epitaxy would be the growth of a molecular quasiperiodic layer. The deposition of C_{60}, which can be modeled as a large atom, was attempted on the clean fivefold *i*-Ag-In-Yb surface, as well as on the same surface modified by a predeposition of Sb. However, for both cases a film of no resulting ordering was produced.

With the study of single element quasicrystals being of great interest, the reactivity of the clean surface also has a great relevance, mainly to potential applications that would involve the material being exposed to atmospheric conditions. The oxidation of the three high symmetry surfaces was investigated and compared to the oxidation of the three constituent species which were oxidised as pure metal foils. The behaviour of all three quasicrystal surfaces are identical under oxidation conditions, and are also similar to that of their pure metal forms. The method of oxidation was then changed from in vacuum to that of atmosphere and water. While oxidation in atmosphere produced similar results to oxidation in vacuum, oxidation in water was far more effective, and the inclusion of hydroxide species emphasised the effects of the process. The oxide layer was found to be stable up until anneal temperatures used in the preparation cycle with the contribution from In oxide becoming reduced. The released oxygen appears to have become bound to Yb producing more Yb oxide.

This new species of quasicrystal offers many new and different features that are not encountered in the *i*-Al-Pd-Mn system. These include, and are not limited to:

- The higher order structures of *i*-Al-Pd-Mn are formed from an F-type lattice, while *i*-Ag-In-Yb is formed from a P-type lattice.
- Both materials can be considered as an aperiodic stacking of atomic clusters. However the atomic clusters that make up *i*-Al-Pd-Mn are known as Mackay clusters while the clusters that make up *i*-Ag-In-Yb are known as Rhombic Triacontrahedral clusters. Both clusters have varying numbers and geometries of atomic shells. The surfaces of these materials are considered to be the truncation of their respective clusters.
- Sputter treatment of *i*-Ag-In-Yb leaves an amorphous surface while a sputter treatment of *i*-Al-Pd-Mn forms a periodic structure.
- Under study by STM, *i*-Ag-In-Yb exhibits a bias dependency, while *i*-Al-Pd-Mn does not.
- Surfaces of *i*-Al-Pd-Mn are chosen from high density, Al rich atomic planes that occur after a large gap in the model, or in other words suitable atomic planes adhere to all three bulk termination selection rules. *i*-Ag-In-Yb surfaces are chosen from only moderately dense planes that are In and Yb rich, meaning that surface free energy of the surface plane is the more important factor, as is expected for any surface.
- The stability of the two and threefold surfaces of *i*-Ag-In-Yb is comparable to that of the fivefold surface, and feature atomically flat surfaces and no evidence of faceting. The two and threefold surfaces of *i*-Al-Pd-Mn are less stable than that of the fivefold surface, and undergo faceting in order to obtain stability.

While the studies listed here may be comprehensive, there is still a great deal of work that could be done on this system. The major assumption of this study is that the atomic model of *i*-Cd-Yb is acceptable as the atomic model of *i*-Ag-In-Yb. While this is true for the atomic positions, the distribution of Ag and In are not yet included in this model. However, recent calculations have begun to determine the probability of occupation of Ag and In at each atomic position that is known to be a Cd atom in the *i*-Cd-Yb model. It is therefore not unreasonable to estimate that at some point in the near future, a specific model relating to *i*-Ag-In-Yb will

become available. When this does manifest itself, the task for this system then lies in relating all the experimental evidence gathered thus far to the *i*-Ag-In-Yb model.

In conclusion, the high symmetry surfaces of the *i*-Ag-In-Yb surface have been characterised, with surfaces being identified in the bulk model as atomic planes that intersect the center of the RTH clusters. The epitaxy of Sb has been observed to form a quasiperiodic film up until the partial formation of the bilayer. Oxidation experiments discovered similar behaviours between all three high symmetry surfaces and the pure metal forms of the quasicrystals constituents, where water was the most effective environment for oxidation. The deposition of C_{60} produced disordered films on several variations of the fivefold surface.

Principal studies

- H.R. Sharma, M. Shimoda, K. Sagisaka, H. Takakura, J.A Smerdon, P.J. Nugent, R. McGrath, D. Fujita, S. Ohhashi, A.P. Tsai, *Structure of the fivefold surface of the Ag-In-Yb quasicrystal*, Physical Review B, Volume 80, Issue 12, 2009

- P. J. Nugent, J. A. Smerdon, R. McGrath, M. Shimoda, C. Cui, A. P. Tsai and H. R. Sharma, *Step-terrace morphology and reactivity to C_{60} of the five-fold icosahedral Ag-In-Yb quasicrystal*, Philosophical Magazine, Volume 91, Issue 19 & 21, 2011

- P. J. Nugent, G. Simutis, V. R. Dhanak, R. McGrath, M. Shimoda, C. Cui, A. P. Tsai, and H. R. Sharma, *Surface oxidation of the icosahedral Ag-In-Yb quasicrystal*, Physical Review B, Volume 82, Issue 1, 2010

- *Structure of the two and threefold surfaces of the Ag-In-Yb quasicrystal*, P.J. Nugent, C. Cui, H.R. Sharma, R. McGrath, A. P. Tsai and M. Shimoda, *to be published*

- P.J. Nugent, V.R. Dhanak, M. Shimoda, C. Cui, R. McGrath, A. P. Tsai and H. R. Sharma, *Growth of the Sb thin film on the fivefold surface of the i-Ag-In-Yb quasicrystal, to be published*

Contributed studies

- H.R. Sharma, P.J. Nugent, J.A. Smerdon, M. Shimoda, S. Ohhashi, V. Fourne, J Ledieu, and A.P. Tsai, *Impurity phases in the icosahedral Ag-In-Yb quasicrystal: influence in surface structure*, Journal of Physics: Conference Series, Volume 226, Number 1, 2010

- H.R. Sharma, G. Simutis, V.R. Dhanak, P.J. Nugent, C. Cui, M. Shimoda, R. McGrath, A.P. Tsai, and Y. Ishii, *Valence band structure of the icosahedral Ag-In-Yb quasicrystal*, Physical Review B, Volume 81, Issue 10, 2010

- H.R. Sharma, J.A. Smerdon, P.J. Nugent, M. Shimoda, H. Takakura, S. Ohhashi, A.P. Tsai, and R. McGrath, *Quasicrystalline Pb film Formed on the Fivefold Surface of a Primitive Type Icosahedral Quasicrystal, to be published*

- H.R. Sharma, J.A. Smerdon, P.J. Nugent1 I. McLeod, A. Ribeiro, V.R. Dhanak, M. Shimoda, A.P. Tsai and R. McGrath, *Growth Pb thin film on the fivefold surface of the i-Ag-In-Yb quasicrystal, to be published*

- H.R. Sharma, J.A. Smerdon, P.J. Nugent, K. Nozawa, Y. Ishii, M. Shimoda, A.P. Tsai and R. McGrath, *Formation of a pseudomorphic Pb bilayer on the fivefold surface of the i-Ag-In-Yb quasicrystal, to be published*

- H. R. Sharma, J.A. Smerdon, P.J. Nugent, I. McLeod, A. Ribeiro, V.R. Dhanak, M. Shimoda, A.P. Tsai, and R. McGrath, *Growth and reactivity to C60 of Pb thin film on various quasicrystal surfaces, to be published*

Bibliography

[1] D. Shechtman, I. Blech, D. Gratias and S. Cahn, Phys. Rev. Lett. 53 (1984) p.1941–1953.

[2] R. Executive Committee.of the , Acta. Cryst. 48 (1992) p.922–946.

[3] R. Penrose, Bull. Inst. Math. Appl. 10 (1974).

[4] P.A. Thiel, A.I. Goldman and C.J. Jenks *Physical Properties of Quasicrystals*, Springer, 1999.

[5] M. Krajci and J. Hafner, Phys. Rev. B 71 (2005) p.054202.

[6] Y. Muro, T. Sasakawa, T. Suemitsu, T. Takabatake, R. Tamura and S. Takeuchi, Jpn. J. Appl. Phys. 41 (2002) p.3787–3790.

[7] A. Pope, T. Tritt, R. Gagnon and J. Strom-Olsen, Appl. Phys. Lett. 76 (2001) p.2345–2347.

[8] R. Tamura, Y. Murao, S. Takeuchi, K. Tokiwa, T. Watanabe, T. Sato and A. Tsai, Jpn. J. Appl. Phys. 40 (2001) p.L912–L914.

[9] J.M. Dubois *Useful Quasicrystals*, World Scientific Publishing, 2005.

[10] T. Schaub, D. Burgler, H. Guntherodt and J. Suck, Phys. Rev. Lett. 73 (1994) p.1255–1258.

[11] L. Barbier, D. Le Floc'h, Y. Calvayrac and D. Gratias, Phys. Rev. Lett. 88 (2002) p.085506.

[12] Z. Papadopolos, G. Kasner, J. Ledieu, E.J. Cox, N.V. Richardson, Q. Chen, R.D. Diehl, T.A. Lograsso, A.R. Ross and R. McGrath, Phys. Rev. B 66 (2002) p.184207.

[13] Z. Shen, C.R. Stoldt, C.J. Jenks, T.A. Lograsso and P.A. Thiel, Phys. Rev. B 60 (1999) p.14688–14694.

[14] B. Unal, T.A. Lograsso, A. Ross, C.J. Jenks and P.A. Thiel, Phys. Rev. B 71 (2005) p.165411.

[15] R.S. Becker, A.R. Kortan, F.A. Thiel and H.S. Chen, Journal of Vacuum Science Technology B: Microelectronics and Nanometer Structures 9 (1991) p.867 –873.

[16] H.R. Sharma, V. Fourne, M. Shimoda, A.R. Ross, T.A. Lograsso, A.P. Tsai and A. Yamamoto, Phys. Rev. Lett. 93 (2004) p.165502.

[17] T. Cai, F. Shi, Z. Shen, M. Gierer, A.I. Goldman, M.J. Kramer, C.J. Jenks, T.A. Lograsso, D.W. Delaney, P.A. Thiel and M.A.V. Hove, Surface Science 495 (2001) p.19 – 34.

[18] T. Cai, V. Fourne, T. Lograsso, A. Ross and P.A. Thiel, Phys. Rev. B 65 (2002) p.140202.

[19] R. McGrath, J. Ledieu, E.J. Cox, S. Haq, C.J.J. R. D. Diehl, I. Fisher, A.R. Ross and T.A. Lograsso, J. Alloys Compounds 342 (2002) p.432–436.

[20] N. Ferralis, K. Pussi, E.J. Cox, M. Gierer, J. Ledieu, I.R. Fisher, C.J. Jenks, M. Lindroos, R. McGrath and R.D. Diehl, Phys. Rev. B 69 (2004) p.153404.

[21] J. Yuhara, J. Klikovits, M. Schmid, P. Varga, Y. Yokoyama, T. Shishido and K. Soda, Phys. Rev. B 70 (2004) p.024203.

[22] M. Gierer, M.A. Van Hove, A.I. Goldman, Z. Shen, S.L. Chang, C.J. Jenks, C.M. Zhang and P.A. Thiel, Phys. Rev. Lett. 78 (1997) p.467–470.

[23] M. Gierer, M.A. Van Hove, A.I. Goldman, Z. Shen, S.L. Chang, P.J. Pinhero, C.J. Jenks, J.W. Anderegg, C.M. Zhang and P.A. Thiel, Phys. Rev. B 57 (1998) p.7628–7641.

[24] Z. Shen, M. Kramer, C. Jenks, A. Goldman, T. Lograsso, D. Delaney, M. Heinzig, W. Raberg and P. Thiel, Phys. Rev. B 58 (1998) p.9961–9971.

[25] Z. Shen, P.J. Pinhero, T.A. Lograsso, D.W. Delaney, C.J. Jenks and P.A. Thiel, Surface Science 385 (1997) p.L923 – L929.

[26] F. Shi, Z. Shen, D.W. Delaney, A.I. Goldman, C.J. Jenks, M.J. Kramer, T. Lograsso, P.A. Thiel and M.A.V. Hove, Surface Science 411 (1998) p.86 – 98.

[27] H. Sharma, K. Franke, W. Theis, A. Riemann, S. Flsch, P. Gille and K. Rieder, Phys. Rev. B 70 (2004) p.235409.

[28] M. Gierer, A. Mikkelsen, M. Grber, P. Gille and W. Moritz, Surface Science 463 (2000) p.L654 – L660.

[29] H. Sharma, M.Shimoda and A. Tsai, Adv. Phys. 56 (2007) p.403–464.

[30] K. Franke, H.R. Sharma, W. Theis, P. Gille, P. Ebert and K.H. Rieder, Phys. Rev. Lett. 89 (2002) p.156104.

[31] J. Smerdon, J. Ledieu, J. Hoeft, D. Reid, L. Wearing, R. Diehl, T. Lograsso, A. Ross and R. Mcgrath, Phil. Mag. 86 (2006) p.841–847.

[32] J. Ledieu, J. Hoeft, D. Reid, J. Smerdon, R. Diehl, T. Lograsso, A. Ross and R. McGrath, Phys. Rev. Lett. 92 (2004) p.135507.

[33] J. Ledieu, J. Hoeft, D. Reid, J. Smerdon, R. Diehl, N. Ferralis, T. Lograsso, A. Ross and R. McGrath, Phys. Rev. B 72 (2005) p.035420.

[34] J.A. Smerdon, J. Ledieu, R. McGrath, T.C.Q. Noakes, P. Bailey, M. Draxler, C.F. McConville, T.A. Lograsso and A.R. Ross, Phys. Rev. B 74 (2006) p.035429.

[35] J. Ledieu, P. Unsworth, T.A. Lograsso, A.R. Ross and R. McGrath, Phys. Rev. B 73 (2006) p.012204.

[36] D. Reid, J. Smerdon, J. Ledieu and R. McGrath, Surface Science 600 (2006) p.4132 – 4136 Berlin, Germany: 4-9 September 2005, Proceedings of the 23th European Conference on Surface Science.

[37] T. Cai, J. Ledieu, R. McGrath, V. Fournee, T. Lograsso, A. Ross and P. Thiel, Surface Science 526 (2003) p.115 – 120.

[38] H.R. Sharma, M. Shimoda, J.A. Barrow, A.R. Ross, T.A. Lograsso and A.P. Tsai, Mat. Res. Soc. Symp. Proc. 805 (2004) p.273 – 280.

[39] H. Sharma, M. Shimoda, A. Ross, T. Lograsso and A. Tsai, Phys. Rev. B 72 (2005) p.045428.

[40] H.R. Sharma, M. Shimoda, A.R. Ross, T.A. Lograsso and A.P. Tsai, Philosophical Magazine 86 (2006) p.807–812 Berlin, Germany: 4-9 September 2005, Proceedings of the 23th European Conference on Surface Science.

[41] M. Krajci, J. Hafner and M. Jahnatek, Phys. Rev. B 73 (2006) p.184202.

[42] L. Leung, J. Ledieu, P. Unsworth, T. Lograsso, A. Ross and R. McGrath, Surface Science 600 (2006) p.4752 – 4757.

[43] M. Shimoda, J. Guo, T. Sato and A.P. Tsai, Journal of Non-Crystalline Solids 334-335 (2004) p.505 – 508 8th International Conference on Quasicrystals.

[44] J.A. Smerdon, N. Cross, V.R. Dhanak, H.R. Sharma, K.M. Young, T.A. Lograsso, A.R. Ross and R. McGrath, J. Phys.: Condens. Matt. 22 (2010) p.345002.

[45] H.R. Sharma, V. Fourne, M. Shimoda, A.R. Ross, T.A. Lograsso, P. Gille and A.P. Tsai, Phys. Rev. B 78 (2008) p.155416.

[46] B. Unal, C. Jenks and P. Thiel, Journal of Physics: Condensed Matter 21 (2009) p.055009.

[47] A. Tsai, J. Guo, E. Abe, H. Takakura and T. Sato, Nature 408 (2000) p.537–538.

[48] H. Takakura, C. Gómez, A. Yamamoto, M.D. Boissieu and A. Tsai, Nature Materials 6 (2007) p.58–63.

[49] M. Shimoda, H. Sharma and A.P. Tsai, Surface Science 598 (2005) p.88 – 95.

[50] M. Boudard, M. Boissieude , C. Janot, G. Heger, C. Beeli, H. Nissen, H. Vincent, R. Ibberson, A. M and J. Dubois, Journal of Physics: Condensed Matter 4 (1992) p.10149–10168.

[51] A. Mackay, Acta. Cryst. (1962) p.916–918.

[52] J. Guo and A. Tsai, Phil. Mag. Lett. 82 (2002) p.349–352.

[53] L. Pauling, Nature 317 (1985) p.512–514.

[54] B. Dubost, J. Lang, M. Takana, P.Sainfort and M. Audier, Nature 324 (1986) p.48–50.

[55] S. Burkov, Phys. Rev. Lett. 67 (1991) p.614–617.

[56] K. Fung, C. Yang, Y. Zhou, J. Zhao, W. Zhan and B. Shen, Phys. Rev. Lett. 56 (1986) p.2060–2063.

[57] L. Bendersky, Phys. Rev. Lett. 55 (1985) p.1461–1463.

[58] N. Wang, H. Chen and K. Kuo, Phys. Rev. Lett. 9 (1987) p.1010–1013.

[59] Z. Mai, L. Xu, N. Wang, K. Kuo, Z. Jin and G. Cheng, Phys. Rev. B 40 (1989) p.12183–12186.

[60] J. Jiang, K. Fung and K. Kuo, Phys. Rev. Lett. 68 (1992) p.616–619.

[61] Q. Yang and W. Wei, Phys. Rev. Lett. 58 (1987) p.1020–1023.

[62] H. Chen, D. Li and K. Kuo, Phys. Rev. Lett. 60 (1988) p.1645–1648.

[63] P.A. Thiel, Progress in Surface Science 75 (2004) p.69 – 86 Quasicrystals.

[64] H.R. Sharma, M. Shimoda, S. Ohhashi and A.P. Tsai, Phil. Mag. 87 (2007) p.2989–2994.

[65] L. Bindi, P. Steinhardt, N. Yao and P. Lu, Science 324 (2009) p.1306–1309.

[66] A. Yamamoto and S. Weber, Phys. Rev. Lett. 78 (1997) p.4430–4433.

[67] P. Wolffde , Acta Cryst. A 30 (1974) p.777–785.

[68] A. Yamamoto, H. Takakura, T. Ozeki, A.P. Tsai and Y. Ohashi, Journal of Non-Crystalline Solids 334-335 (2004) p.151 – 155 8th International Conference on Quasicrystals.

[69] D. Sands *Introduction to Crystallography*, W.A. Benjamin Inc., 1969.

[70] A. Yamamoto and H. Takakura, Ferroelectrics 305 (2004) p.197–211.

[71] V. Elser, Phys. Rev. B 32 (1985) p.4892–4898.

[72] A. Conrad, F. Krumeich and B. Harbrecht, Angew. Chem. Int. Ed 37 (1998) p.1383–1386.

[73] J. Guo, E. Abe and A. Tsai, Phys. Rev. B 62 (2000) p.605–608.

[74] A. Tsai, Journal of Non-Crystalline Solids 334-335 (2004) p.317 – 322 8th International Conference on Quasicrystals.

[75] A. Yamamoto, H. Takakura and A. Tsai, Phys. Rev. B 68 (2003) p.094201.

[76] C. Gómez and S. Lidin, Angew. Chem. Int. Edn. Engl. 40 (2001) p.4037–4039.

[77] C. Gómez and S. Lidin, Phys. Rev. B 68 (2003) p.024203.

[78] C. Henley and V. Elser, Phil. Mag. B 53 (1986) p.59–66.

[79] B. Biggs, S. Poon and N. Munirathnam, Phys. Rev. Lett. 65 (1990) p.2700–2703.

[80] G. Laissardieérede , D.N. Manh and D. Mayou, The Science of Complex Alloy Phases (2005) p.345–372.

[81] G. Laissardiérede , D. Nguyen-Manh and D. Mayou, Progress in Materials Science 50 (2005) p.679 – 788.

[82] R. Tamura, T. Takeuchi, C. Aoki, S. Takeuchi, T. Kiss, T. Yokoya and S. Shin, Phys. Rev. Lett. 92 (2004) p.146402.

[83] H.R. Sharma, G. Simutis, V.R. Dhanak, P.J. Nugent, C.Cui, M. Shimoda, R. McGrath, A.P. Tsai and Y. Ishii, Phys. Rev. B 81 (2010) p.104205–104205–7.

[84] H.R. Sharma, K.J. Franke, W. Theis, P. Gille, P. Ebert and K.H. Rieder, Phys. Rev. B 68 (2003) p.054205.

[85] H. Sharma, M. Shimoda and A. Tsai, Jpn. J. of Appl. Phys. 45 (2006) p.2208–2211.

[86] J. Ledieu and R. McGrath, Journal of Physics: Condensed Matter 15 (2003) p.S3113.

[87] A. Yamamoto, H. Takakura and A.P. Tsai, Journal of Alloys and Compounds 342 (2002) p.159 – 163.

[88] Z. Papadopolos, P. Pleasants, G. Kasner, V. Fourne, C. Jenks, J. Ledieu and R. McGrath, Phys. Rev. B 69 (2004) p.224201–224201–7.

[89] B. Unal, C.J. Jenks and P.A. Thiel, Phys. Rev. B 77 (2008) p.195419.

[90] T. Schaub, D. Burgler, H. Guntherodt and J. Suck, Z. Phys. B 96 (1994) p.93–96.

[91] H.R. Sharma, M. Shimoda, K. Sagisaka, H. Takakura, J.A. Smerdon, P.J. Nugent, R. McGrath, D. Fujita, S. Ohhashi and A.P. Tsai, Phys. Rev. B 80 (2009) p.121401–121406.

[92] J. Smerdon, J. Parle, L. Wearing, T. Lograsso, A. Ross and R. McGrath, Phys. Rev. B 78 (2008) p.075407.

[93] D. Gratias, F. Puyraimond, M. Quiquandon and A. Katz, Phys. Rev. B 63 (2000) p.1–16.

[94] T.C. Chiang, Surface Science Reports 39 (2000) p.181 – 235.

[95] M. Milun, P. Pervan and D. Woodruff, Reports on Progress in Physics 65 (2002) p.99.

[96] V. Fourne, H. Sharma, M. Shimoda, A. Tsai, B. Unal, A. Ross, T. Lograsso and P. Thiel, Phys. Rev. Lett. 95 (2005) p.155504.

[97] T. Nagao, J.T. Sadowski, M. Saito, S. Yaginuma, Y. Fujikawa, T. Kogure, T. Ohno, Y. Hasegawa, S. Hasegawa and T. Sakurai, Phys. Rev. Lett. 93 (2004) p.105501.

[98] S. Chey, L. Huang and J. Weaver, Surface Science 419 (1998) p.L100 – L106.

[99] V. Yeh, L. Berbil-Bautista, C.Z. Wang, K.M. Ho and M.C. Tringides, Phys. Rev. Lett. 85 (2000) p.5158–5161.

[100] J. Ledieu, L. Leung, L.H. Wearing, R. McGrath, T.A. Lograsso, D. Wu and V. Fourne, Phys. Rev. B 77 (2008) p.073409.

[101] J. Smerdon, L. Leung, J. Parle, C. Jenks, R. McGrath, V. Fournee and J. Ledieu, Surface Science 602 (2008) p.2496 – 2501.

[102] B. Unal, V. Fournee, P. Thiel and J. Evans, Phys. Rev. Lett. 102 (2009) p.196103.

[103] V. Fournée, T. Cai, A. Ross, T. Lograsso, J. Evans and P. Thiel, Phys. Rev. B 67 (2003) p.033406.

[104] B. Unal, V. Fournée, K.J. Schnitzenbaumer, C. Ghosh, C.J. Jenks, A.R. Ross, T.A. Lograsso, J.W. Evans and P.A. Thiel, Phys. Rev. B 75 (2007) p.064205.

[105] P. Moras, Y. Weisskopf, J. Longchamp, M. Erbudak, P. Zhou, L. Ferrari and C. Carbone, Phys. Rev. B 74 (2006) p.121405.

[106] K. Pussi, M. Grier and R. Diehl, J. of Phys. Con. Matt. 21 (2009) p.1.

[107] H. Luth *Solid Surfaces, Interfaces and Thin Films*, Springer, 2001.

[108] D. Robertson, Journal of Physics D: Applied Physics 5 (1971) p.604–608.

[109] M. Yurechko, B. Grushko and P. Ebert, Phys. Rev. Lett. 95 (2005) p.256105.

[110] R. Young, J. Ward and F. Scire, Phys. Rev. Lett. 27 (1971) p.922–924.

[111] G. Binnig, H. Rohrer, C. Gerber and E. Weibel, Phys. Rev. Lett. 49 (1982) p.57–61.

[112] I. Horcas, R. Fernandez, J. Gomez-Rodriguez, J. Colchero, J. Gomez-Herrero and A.M. Baro, Rev. Sci. Instrum. 78 (2007) p.013705.

[113] C. Davisson and L. Germer, Phys. Rev. 30 (1927) p.705–740.

[114] D. Woodruff and T. Delchar *Modern Techniques of Surface Science*, Cambridge University Press, 1994.

[115] C. Kittel *Introduction to Solid State Physics*, John Wiley and Sons, Inc, 2005.

[116] A. Perez-Rodrguez, A. Cornet and J. Morante, Microelectronic Engineering 40 (1998) p.223 – 237 Electrical and Physical Characterization.

[117] N. Fairley and A. Carrick *The Casa cookbook - part 1: Recipes for XPS data Processing*, Accolyte Science, UK, 2005.

[118] R.H. T., Chasse and R. Szargan, Fresenius' J. Anal. Chem. 365 (1999) p.48–54.

[119] C. Donley, D. Dunphy, D. Paine, C. Carter, K. Nebesny, P. Lee, D. Alloway and N. Armstrong, Langmuir 18 (2002) p.450–457.

[120] S. Tanuma, C. Powell and D. Penn, Surface and Interface Analysis 17 (1991) p.911–926.

[121] W. Theis and K. Franke, Journal of Physics: Condensed Matter 20 (2008) p.314004.

[122] K.J. Franke, P. Gille, K.H. Rieder and W. Theis, Phys. Rev. Lett. 99 (2007) p.036103.

[123] J. Smerdon, Journal of Physics: Condensed Matter 22 (2010) p.433002.

[124] I. McLeod, V. Dhanak, A. Matilainen, M. Lahti, K. Pussi and K. Zhang, Surface Science 604 (2010) p.1395 – 1399.

[125] M. Shimoda, J. Guo, T. Sato and A. Tsai, Surface Science 482-485 (2001) p.784 – 788.

[126] P. Nugent, J. Smerdon, R. McGrath, M. Shimoda, C. Cui, A. Tsai and H. Sharma, Philosophical Magazine 91 (2011) p.2862–2869.

[127] P.J. Nugent, G. Simutis, V.R. Dhanak, R. McGrath, M. Shimoda, C. Cui, A.P. Tsai and H.R. Sharma1, Phys. Rev. B 82 (2010) p.014201–014201 – 8.

[128] H. Sharma, P. Nugent, J. Smerdon, M. Shimoda, S. Ohhashi, V. Fourne, J. Ledieu and A. Tsai, Journal of Physics: Conference Series 226 (2010) p.012004.

[129] Z. Shen, W. Raberg, M. Heinzig, C.J. Jenks, V. Fournee, M.A.V. Hove, T.A. Lograsso, D. Delaney, T. Cai, P.C. Canfield, I.R. Fisher, A.I. Goldman, M.J. Kramer and P.A. Thiel, Surface Science 450 (2000) p.1 – 11.

[130] S. Ohhashi, J. Hasegawa, S. Takeuchi and A. Tsai, Phil. Mag. 87 (2007) p.3089–3094.

[131] C. Cui and A.P. Tsai, J. Cryst. Growth 312 (2009) p.131–135.

[132] P. Ebert, M. Yurechko, F. Kluge, T. Cai, B. Grushko, P.A. Thiel and K. Urban, Phys. Rev. B 67 (2003) p.024208.

[133] T. Noakes, P. Bailey, C. McConville, C. Parkinson, M. Draxler, J. Smerdon, J. Ledieu, R. McGrath, A. Ross and T. Lograsso, Surface Science 583 (2005) p.139 – 150.

[134] T. Noakes, P. Bailey, M. Draxler, C. McConville, A. Ross, T. Lograsso, L. Leung, J. Smerdon and R. McGrath, Journal of Physics: Condensed Matter 18 (2006) p.5017.

[135] H. Sharma, M. Shimoda, V. Fournee, A. Ross, T. Lograsso and A. Tsai, Applied Surface Science 241 (2005) p.256 – 260 The 9th International Symposium on Advanced Physical Fields.

[136] M. Boissieu H. Takakura C.P. Gomez A. Yamamoto A.P. Tsaide , Phil. Mag. (2007) p.2613–2639.

[137] C. Gómez, private communication (2010).

[138] H. Takakura, C. Gomez, A. Yamamoto, M. Boissieu and A. Tsai, to be published .

[139] Crystallographic database of the AgInYb, PDF2, National Institute for Materials Science, Tsukuba, Japan .

[140] M. Straunabus and L. Yu, Acta. Cryst. 25 (1969) p.676–682.

[141] J.S. Chung, E.J. Cho and S.J. Oh, Phys. Rev. B 41 (1990) p.5524–5528.

[142] L.Z. Mezey and J. Giber, Japanese Journal of Applied Physics 21 (1982) p.1569–1571.

[143] J. Ledieu, R. McGrath, R.D. Diehl, T.A. Lograsso, D.W. Delaney, Z. Papadopolos and G. Kasner, Surface Science 492 (2001) p.L729 – L734.

[144] A. Bravais *Etudes Cristallographiques*, Gauthier-Villars, Paris, 1866.

[145] V. Fournée, A.R. Ross, T.A. Lograsso, J.W. Anderegg, C. Dong, M. Kramer, I.R. Fisher, P.C. Canfield and P.A. Thiel, Phys. Rev. B 66 (2002) p.165423.

[146] Z. Shen, C.J. Jenks, J. Anderegg, D.W. Delaney, T.A. Lograsso, P.A. Thiel and A.I. Goldman, Phys. Rev. Lett. 78 (1997) p.1050–1053.

[147] I.R. Fisher, M.J. Kramer, T.A. Wiener, Z. Islam, A.R. Ross, T.A. Lograsso, A. Kracher, A.I. Goldman and P.C. Canfield, Philosophical Magazine B 79 (1 October 1999) p.1673–1684(12).

[148] K. Nozawa, private communication (2011).

[149] A. Pronin, S. Demishev, N. Sluchanko, N. Samarin, D. Konarev and R. Lyubobskaya, Physics of the Solid State 42 (2000) p.586–588.

[150] J. Ledieu, C. Muryn, G. Thornton, R. Diehl, T. Lograsso, D. Delaney and R. McGrath, Surf. Sci. 472 (2001) p.89–96.

[151] P. Bagus, F. Illas, G. Pacchioni and F. Parmigiani, J. of Electron Spectrosc. and Relat. Phenom. 100 (1999) p.215–236.

[152] B.D. Padalia, W.C. Lang, P.R. Norris, L.M. Watson and D.J. Fabian, Proc. R. Soc. London 354 (1977) p.269–290.

[153] V. Demange, J.W. Anderegg, J. Ghanbaja, F. Machizaud, D.J. Sordelet, M. Besser, P.A. Thiel and J.M. Dubois, Appl. Surf. Sci. 173 (2001) p.327–338.

[154] D. Popovic, D. Naumovic, M. Bovet, C. Koitzsch, L. Schlapbach and P. Aebi, Surface Science 492 (2001) p.294–304.

[155] S. Chang, J. Anderegg and P. Thiel, Journal of Non-Crystalline Solids 195 (1996) p.95 – 101.

[156] C. Benndorf, M. Franck and F. Thieme, Surface Science 128 (1983) p.417–423.

[157] A. Boronin, S. Koscheev and G. Zhidomirov, Journal of Electron Spectroscopy and Related Phenomena 96 (1998) p.43–51.

[158] R. Hewitt and N. Winograd, Journal of Applied Physics 51 (1980) p.2620–2624.

[159] D. Wagman, W. Evans, V. Parker, R. Schumm, I. Halow, S. Bailey, K. Churney and R. Nutall, J. Phys. Chem. Ref. Data 11 (1982).

[160] B. Strohmeier, Surface and Interface Analysis 15 (1990) p.51–56.